Satellite and Rocket Measurements of Solar Ultraviolet Flux and Atmospheric Molecular Oxygen Density

by

George William Albert Lockey B.Sc.(Hons.)

Department of Physics

A thesis
presented for the degree of
Doctor of Philosophy
in the
University of Adelaide.

October 1972

CONTENTS

SUMMARY

This thesis describes experiments performed using rocket and satellite-borne ion chambers sensitive to vacuum ultraviolet radiation. The objectives of these experiments were:-

(i) the measurement of molecular oxygen density by the technique of absorption spectroscopy, and

(ii) the measurement of absolute solar flux at the wavelength of hydrogen Lyman-α (1215.7Å) and in the wavelength bands 1420Å to 1480Å and 1550Å to 1690Å.

Ion chambers with both glass bodies and copper bodies have been designed and constructed for use in these experiments. The construction and testing of these detectors are fully discussed.

In the upper mesosphere (70 Km to 90 Km) and lower thermosphere (90 Km to 200 Km), seasonal, geographical and temporal variations in the atmospheric molecular oxygen density profile are still largely unknown. As a result, significant uncertainties still exist with regard to "model" or "standard" atmospheres used to represent the molecular oxygen distribution.

In the present work, five rockets carrying lithium fluoride - nitric oxide ion chambers (which respond mainly to hydrogen Lyman-α radiation) have been launched from Woomera, Australia. The main objective of these experiments was the determination of the nature of seasonal variations in the molecular oxygen density profile in the altitude range 80 Km to 95 Km. Only two of the rockets, HAD 309 and HAD 310, performed satisfactorily. The HAD 309 experiment gave the

first winter measurement of molecular oxygen density in the southern hemisphere in the region of the atmosphere near 90 Km.

A comparison of the HAD 309 and HAD 310 (summer) results with similar measurements by other workers has indicated that the average scale height of the density distribution, in the altitude range 80 Km to 95 Km, is greater in winter than in summer.

Australia's first satellite, WRESAT 1, carried lithium fluoride-nitric oxide, sapphire-xylene and quartz-triethylamine ion chambers. This experiment was designed to measure atmospheric molecular oxygen density at satellite sunrise and sunset, in the altitude range 90 Km to 220 Km. A method of analysis of the ion chamber data has been developed which allows for the effect of the finite size of the solar disk. All of the available WRESAT 1 data has been analysed using this method.

To within the experimental uncertainties, the WRESAT 1 density results show general agreement with the mean 1965 CIRA model atmosphere in the region near 100 Km. However, in the height range 130 Km to 220 Km, the average density values are a factor of two below those of the mean 1965 CIRA model and show day-to-day variations greater than those predicted by the 1965 CIRA models.

The region of the solar temperature minimum, between the upper photosphere and lower chromosphere, is of considerable importance for the theory of the solar atmosphere. The solar flux data obtained from the sapphire-xylene and quartz-triethylamine ion chambers carried on WRESAT 1, indicate a value of $(4570 \pm 50)^{\circ}K$ for the solar minimum brightness temperature. A comparison has been made between this value and the values obtained by workers using dispersive instruments.

PREFACE

This thesis contains no material which has been accepted for the award of any other degree or diploma in any University. To the best of the author's knowledge and belief it contains no material previously published or written by another person, except when due reference is made in the text.

G. Lockey

ACKNOWLEDGEMENTS

The satellite and rocket experiments described in this thesis were carried out in co-operation with the Flight Projects Group, Weapons Research Establishment. The author would like to thank all persons involved with the preparation and launching of the rockets and the WRESAT 1 satellite. In particular the author gratefully acknowledges the considerable assistance given by the late Mr B. Rofe.

Thanks are due to Mr S. Dowden of the Physics Department for his invaluable technical assistance and to Messrs B. Hurn and B. Walker of the Physics Department for designing and constructing the rocket electronic circuitry.

The author would like to thank most sincerely Dr B.H. Horton for the enthusiasm, advice and encouragement he has given during the time the author has worked with him.

The author would also like to thank Mrs P. Clark for her efforts in plotting the satellite data and Mrs R. Willshire for her assistance in proof-reading the typed copy.

Special thanks are due to the author's wife, Rosemary, for the help and support she has given and for her great patience during a trying period.

Finally the author would like to thank his supervisor Professor J.H. Carver for his guidance and encouragement during the experiments and the writing of this thesis.

The author gratefully acknowledges the support provided by a Commonwealth Postgraduate Award.

CHAPTER 1

SOLAR RADIATION FROM 1000Å TO 2000Å

1.1 Previous Measurements

1.1.1 Introduction

Before 1946, knowledge of the solar spectrum was limited to wavelengths longer than 2869Å. Shorter wavelengths are prevented from reaching terrestial or balloon-borne equipment by the strong absorption processes that take place in the upper atmosphere (Section 2.1). The first measurements of the solar spectrum beyond the atmospheric cut-off were made with a normal incidence grating spectrograph carried by a V-2 rocket to an altitude of 88 Km (Baum et al., 1946). A series of 35 spectra were recorded on film and these showed a continuation of the visible continuum down to 2100Å. During the next five years, considerable improvements were made in the speed and resolution of spectrographs. However, extension of the spectrum to wavelengths much below 2100Å was not possible. This was mainly due to the rapid decrease in the continuum intensity below 2100Å and the inability to obtain long exposures on flights where the rocket was unstabilized.

The need for a stabilized rocket-borne platform from which to point a spectrograph at the sun led to the development, by the University of Colorado, of a bi-axial pointing control, suitable for use in the

Aerobee rocket. Before this was achieved however, non-dispersive photometers were applied with success to the detection of solar Lyman-α radiation (Section 1.1.5). Since 1952, when the pointing control was used successfully for the first time, investigations of the solar ultraviolet spectrum have followed two main lines:-

(i) dispersive measurements for which a pointing control is essential, and

(ii) non-dispersive measurements for which a pointing control is not necessary.

1.1.2 Dispersive Measurements

In 1952, with the aid of the bi-axial control, Rense (1953) was able to photograph the Lyman-α resonance line of atomic hydrogen (1215.7Å) for the first time, and to show that it was in emission. From 1952 to 1960, all dispersive measurements of the solar ultraviolet spectrum were made with single dispersion grating spectrographs using photographic recording and operating at either normal or grazing incidence. The spectra from these instruments were generally unsuitable for absolute intensity determinations due to the effects of stray long wavelength light. However, important features of the solar spectrum were observed for the first time in these spectra and so a short description of the most significant measurements will be given. Reviews of these and subsequent measurements up to 1963 have been given by Pagel (1963) and Tousey (1963). A review of the more recent

measurements has been given by Goldberg (1967) and Noyes (1971).

In 1954, Johnson et al. (1954) using a normal incidence instrument obtained many intense images of the Lyman-α line of much better quality than those of Rense (1953). An instrument of the same type was flown in 1955 by Johnson et al. (1958) and many emission lines were recorded, the shortest wavelength being that of the CIII line at 977Å. Also in this flight, the continuum could be traced down to 1550Å and the sudden decrease in the continuum intensity at 2100Å was seen for the first time. A grazing incidence spectrograph was flown in 1958 and 1959 by Violett and Rense (1959) and emission lines were recorded down to 83.9Å. The resonance lines of HeI (584Å) and HeII (304Å) were seen for the first time but strong stray light made interpretation of the spectra very difficult. The best spectra obtained with a single dispersion instrument were those taken in 1959 by Purcell et al. (1960). Although a special coating was used on the grating to reduce the effects of stray light, intensity determinations could only be made at wavelengths longer than 1750Å.

A great improvement was made in the spectra by the use of the double dispersion instrument, first flown in 1960 by Detwiler et al. (1961a). A grating was used to pre-disperse the incident solar radiation along the entrance slit of the main spectrograph. As a result, the stray light from the visible and near ultraviolet portions of the solar spectrum fell beyond the ends of the slit and was rejected from the spectrograph. The final spectrum was rendered stigmatic by

mechanically distorting the pre-dispersing grating in such a way that it compensated for the astigmation of the main grating. With this system, the intensity distribution along a spectral line corresponded to the intensity distribution at that wavelength in a slice along a diameter of the sun. From the spectra obtained during this flight an intensity distribution was derived over the range 850Å to 1550Å. The absolute level of the spectrum was referred to Lyman-α, the intensity of which was measured during the flight by an ion chamber, sensitive to the range 1050Å to 1350Å, attached to the spectrograph housing. By combining the spectral response curve of the ion chamber with the measured intensity distribution of the solar spectrum, a correction of 15% was estimated for the contribution of the continuum and lines other than Lyman-α to the ion chamber signal. The results of this flight have been published by Detwiler et al. (1961b) in the form of the total intensity of continuum plus lines in 50Å intervals and the intensities of the strongest emission lines. The intensity distribution has also been published, in digitalized form, by Brinkman et al. (1966) and these values are used in Section 5.6 to determine the contribution made by emission lines to the signal from an ion chamber sensitive to the range 1420Å to 1480Å. These values are also used in Section 3.8 to estimate the change in sensitivity of this ion chamber due to variations in its temperature during a rocket flight.

Two double dispersion spectrographs covering the ranges 1200Å to 2000Å and 800Å to 1250Å were flown in 1962 by Tousey et al. (1964). The almost complete elimination of stray light enabled the continuum

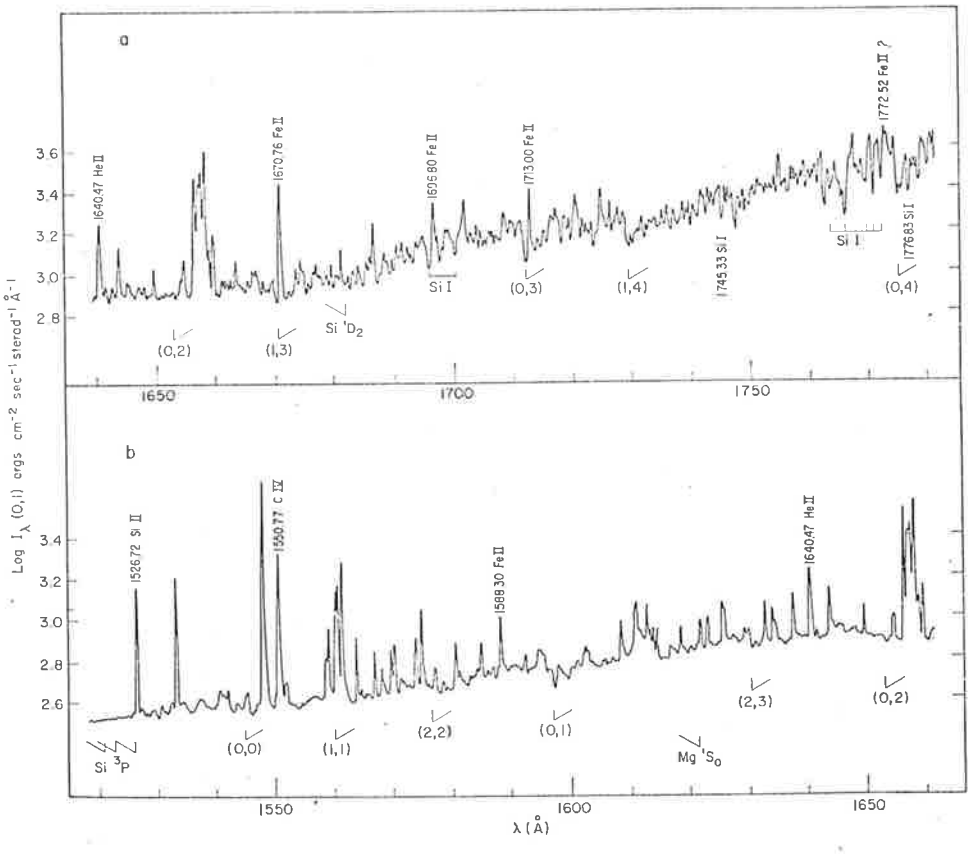

Fig. 1.1 The intensity distribution of the solar spectrum between 1520Å and 1780Å. The spectra were obtained by the density tracing of photographic exposures. No attempt should be made to read line intensities, as the spectra were traced in rapid scan and some of the lines may therefore not have been properly recorded (Widing et al., 1970).

to be traced down to approximately 950Å. The double dispersion instrument was reflown in July 1966 by Purcell, Snider and Tousey and gave spectra that were significantly better for photometry than those of the 1962 flight or those from a flight with a similar instrument in February 1966. Figure 1.1 shows a densitometer trace between 1520Å and 1780Å from one of the spectra taken during the July 1966 flight (Widing et al., 1970). Figure 1.2 is a densitometer trace for the region 1150Å to 1520Å published by Tousey (1964).

The most recent photographically recorded spectra in the 1000Å to 2000Å range were obtained in 1970 by Brueckner and Moe (1972). Unlike earlier instruments, their double dispersion spectrograph accepted radiation only from a localized area on the solar disk. The angular resolution was determined by the size of the entrance slit, which was 2 arc sec by 1 arc min projected on the solar disk, and by the pointing jitter of ± 2 arc sec. Spectra were taken at positions 7, 24, 40 and 300 arc sec distant from the limb, making it possible to study centre to limb variations with a spatial resolution of ± 2 arc sec. The spectra obtained covered the range 1175Å to 1795Å but the instrument was only absolutely calibrated above 1400Å. As the spectral resolution was 0.07Å, it was possible to determine the absolute continuum level in many sections without interference from absorption or emission features.

Burton and his co-workers at the Astrophysics Research Unit, Culham Laboratory, England, using the Skylark rocket fitted with a

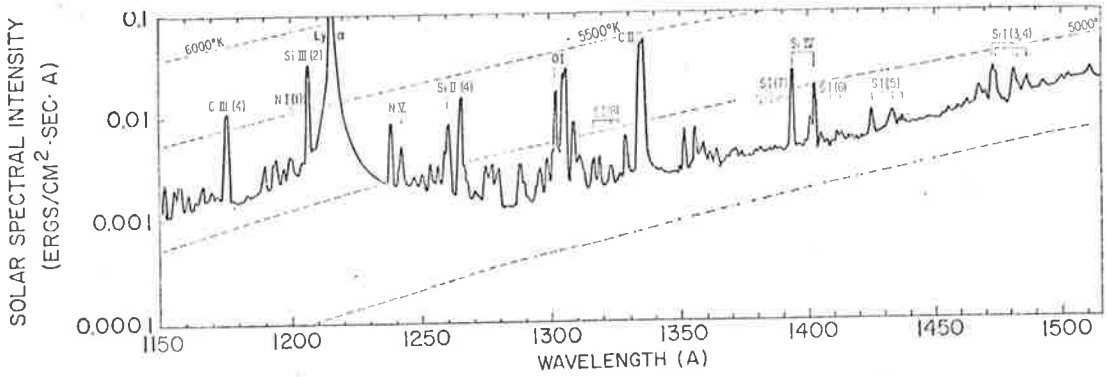

Fig. 1.2 The intensity distribution of the solar spectrum between 1150Å and 1520Å determined by the density tracing of photographic exposures (Tousey, 1964).

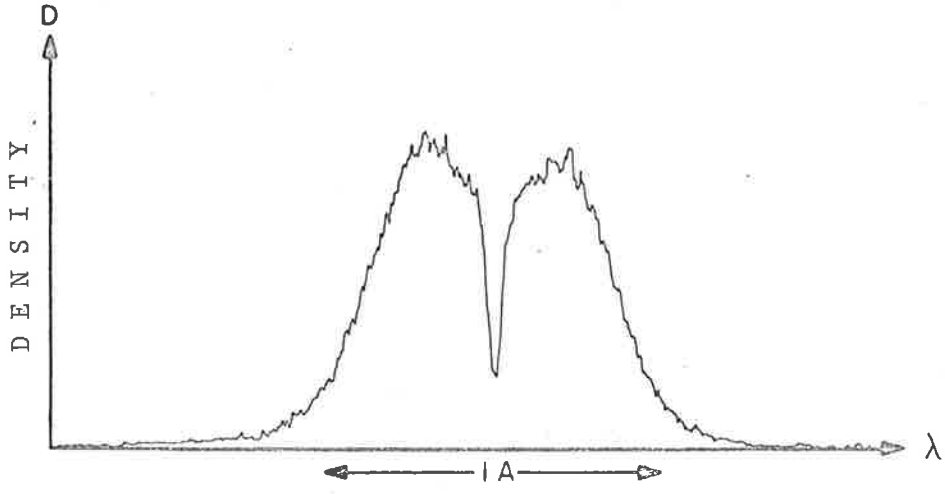

Fig. 1.3 The profile of the solar hydrogen Lyman-α line as measured by Purcell and Tousey (1960) (Friedman, 1961).

tri-axial pointing control, have been able to direct their spectrograph slit 10 arc sec outside the solar limb to an accuracy of ± 2 arc sec. This has enabled them to photograph the chromospheric and coronal emissions in the range 300Å to 2800Å with very little interference from the strong photospheric radiation. Burton and Ridgeley (1970) have published a list of wavelengths and intensities of about 600 emission lines most of which are identified. The chromospheric and coronal spectra have also been observed by Speer et al. (1970) and Brueckner et al. (1970). They carried out separate observations of the "flash" spectrum from 850Å to 2150Å during the total eclipse of March 7th, 1970.

The determination of absolute fluxes when using photographic recording techniques is difficult, as has been pointed out by Rense (1961) and Detwiler et al. (1961b). Both the film sensitivity and the instrument's transmission efficiency must be measured as a function of wavelength. These two quantities can be determined separately but are usually measured simultaneously by placing the instrument in a vacuum chamber and exposing it to an absolutely calibrated source of ultraviolet radiation. This was the method used by Brueckner and Moe (1972). Even when using a source of known absolute intensity distribution, errors can be introduced due to scattered light, spectral impurities in the light source, overlapping orders and the fact that the radiation from the laboratory source may not have the same angular distribution as that from the sun.

In early spectrographic measurements, absolutely calibrated ion chambers were flown with the spectrograph. This method was first used by Byram et al. (1958), who used ion chambers sensitive to the ranges 1050Å to 1350Å and 1220Å to 1350Å to correct the absolute fluxes derived photographically by Johnson et al. (1958). The difficulty with this method is that the integrated intensity from the total solar disk (which is generally not uniformly bright) must be calculated from the spectrographic data before comparisons can be made with the ion chamber data.

Photoelectric recording techniques have also been applied to the measurement of the solar ultraviolet spectrum from both rockets and satellites. Hinteregger and his co-workers have flown a grazing incidence grating monochromator in which the spectrum is scanned by a slit in a moving belt and is detected by a windowless, magnetically focussed, resistance strip photomultiplier. The output of the detector is telemetered directly to ground. Due to the insensitivity of the detector's photocathode to wavelengths longer than approximately 1300Å, background problems, inherent in grazing incidence instruments due to intense long wavelength stray light, have been eliminated. This instrument, which was flown successfully for the first time in 1959, is described in detail by Hinteregger (1961a). The first reliable intensity measurements were taken on a flight in August, 1960. Intensities, extrapolated to the top of the atmosphere, have been given for all of the important lines and the continuum in the range 50Å to 1300Å from both the 1960 flight (Hinteregger, 1961b)

and from later flights in 1963 (Hinteregger and Hall, 1965). A summary of all of the important rocket flights made with this instrument up to 1969 has been given by Hall et al. (1969). In all of these flights the measurements have been of the integrated radiation from the whole solar disk under non-flare conditions.

A scanning monochromator of the same type as that described above has been flown on the NASA satellite OSO 3 and has provided absolute measurements of the total disk radiation in the wavelength range 270Å to 1300Å. As no corrections are needed for residual atmospheric absorption these results are superior to the rocket values. The satellite instrument worked for approximately six months in 1967 during which time its sensitivity gradually decreased. Absolute intensities of the important lines and the continuum have been given by Hall and Hinteregger (1970) for observations taken before appreciable deterioration had occurred. The decrease in sensitivity was slow enough to allow the 27-day variations of the emission line intensities to be clearly seen. Over one 27-day period the intensity of the hydrogen Lyman-α line was found to vary by approximately 30%.

A normal incidence scanning monochromator was launched in 1967 on the satellite OSO 4. This instrument was designed by Goldberg and his co-workers at the Harvard College Observatory to obtain spectral scans over the range 300Å to 1400Å from a 1 arc min square at the centre of the solar disk. A number of scans made in October 1967 have been averaged to give a mean spectrum of the quiet sun (Dupree and

Reeves, 1971). The instrument could also be used as a spectroheliograph and during October and November 1967 approximately 4000 spectroheliograms of the entire disk were obtained in about 50 individual emission lines or continuum wavelengths, with a spatial resolution of about 1 arc min. These results have been published in atlas form by Reeves and Parkinson (1970). A similar instrument, with the somewhat better spatial resolution of 35 arc sec, was orbited in the OSO 6 spacecraft and recorded spectra at many different points on the solar disk (Dupree et al., 1970).

Timothy and Timothy (1970), using a different spectrometer on OSO 4, monitored the intensities of the Lyman-α emission lines of hydrogen and helium over the periods October 1967 to December 1967 and June 1968 to December 1969. As the first of these monitoring periods covers the data acquisition phase of the WRESAT I satellite, the hydrogen Lyman-α intensities obtained by the OSO 4 spectrometer are compared in Section 6.3 with the values obtained in the present work from the WRESAT I ion chambers.

A photoelectric scanning monochromator, which for the first time was not limited to wavelengths less than 1400Å, was flown in 1968 in an Aerobee-150 rocket by Parkinson and Reeves (1969). This instrument was designed to make an accurate determination of the solar continuum level in the range 1400Å to 1875Å, where the radiation is believed to originate in the vicinity of the solar temperature minimum (Section 1.2). To provide better data than existing photographic observations,

high spatial and spectral resolutions were required. This was achieved by using an Ebert spectrometer equipped with a telescope system. The measured spectral response was 0.06Å and the spatial resolution 20 arc min by 7 arc sec. The detector was a photomultiplier with a lithium fluoride window and a calcium iodide photocathode. The photocathode was relatively insensitive to wavelengths longer than 2500Å while the short wavelength cut-off was determined by the detector's window and a calcium fluoride filter placed at the exit slit. The effect of scattered light above 2000Å and below 1300Å was not measurable. Although the bi-axial pointing control operated only intermittently during the flight, many intensity measurements were made near the centre of the solar disk throughout the range 1400Å to 1875Å. Substantial agreement at 1400Å was found between these results and those of the Harvard OSO 4 spectrometer described above. A second flight, in which the pointing control operated correctly, was made with this instrument in September 1969. Hinteregger (1970) has reported that the results of this experiment, which have not yet been published, tend to confirm those of the earlier flight. The continuum intensities derived from the 1968 flight are compared in Section 6.3 with the photographic measurements of Widing et al. (1970) and Brueckner and Moe (1972) (both described above) and with the present WRESAT I ion chamber measurements.

The absolute calibration of photoelectric scanning monochromators has been discussed fully by Hinteregger (1961a, 1965). As the calibration procedure is easier than that used for photographic

instruments, the monochromators allow more precise absolute intensity measurements than the spectrographs. Due to the speed with which a spectral scan can be made, the monochromators are also much better suited to studies of the absorption in the earth's atmosphere of radiation of a particular wavelength. However, in spite of considerable progress in photoelectric recording techniques, the photographic plate remains superior for any precise wavelength measurements as well as for well defined image formation such as that required in spectroheliographs.

1.1.3 Profiles of the Solar Lyman-α Line

The profile of the solar hydrogen Lyman-α line was studied at high resolution in 1959 and 1960 by Purcell and Tousey (1960, 1961). Profiles were also taken in 1962 by Garrett, Purcell and Tousey (Tousey, 1963), in 1966 by Bruner and Parker (1969) and in 1967 by Bruner and Rense (1969). All of these measurements have shown that the line profile is characterized by a half maximum width of about 1Å; a wide shallow self-reversal due to absorption in the solar atmosphere; and a deep, narrow reversal formed by absorption due to atomic hydrogen between the rocket and the sun.

Figure 1.3 shows the line profile as measured in 1959 by Purcell and Tousey (1960), who used the grating of their normal incidence spectrograph in the thirteenth order to obtain a resolution of 0.03Å. From the 1959 and 1960 flights, it was found that the separation between the profile maxima varied from 0.3Å to 0.4Å for plage

regions and from 0.4Å to 0.5Å for quiet regions of the sun. The maximum on the short wavelength side was found to be usually, but not always, higher in intensity than the other. As the value of the absorption cross-section of molecular oxygen changes rapidly near the Lyman-α wavelength, the positions of the maxima and their relative intensities can be of importance when determining the effective absorption cross-section of molecular oxygen for the whole Lyman-α line (Section 2.2).

1.1.4 Solar Images at Lyman-α

In 1956, Mercure et al. (1956) obtained the first image of the solar disk at the wavelength of hydrogen Lyman-α. Although the image was small and the stray light background intense, it was concluded that Lyman-α is emitted from Ca K plage regions with increased intensity. In 1959, when the sun was very active, Purcell et al. (1959) obtained a stigmatic image of the sun at Lyman-α with a spatial resolution of 1 arc min and with a very low stray light background. It was found that the Lyman-α plage regions correlated well with those of Ca K and to a lesser extent with those of H-α. In 1965 spectroheliograms of the sun at Lyman-α were taken from the OSO 3 satellite with a resolution of 1 arc min (Tousey, 1967). These images also showed good correlation between the Lyman-α and Ca K plage regions. Sloan (1968) has mapped the intensity distribution of Lyman-α over small areas of the sun with resolutions of up to 2.5 arc sec. He used as a detector an ion chamber, sensitive mainly to Lyman-α, positioned behind a pin-hole at

the focal plane of a small telescope. Bright features 6 to 20 arc sec in size were found with intensities typically 20% brighter than the background.

Departure of the solar disk from uniform brightness at Lyman-α can lead to serious difficulties when using the atmospheric occultation of the sun, as seen from a satellite, to measure density profiles in the earth's atmosphere (Section 6.2.2).

1.1.5 Non-dispersive Measurements

Before the development of a pointing control, rocket spectrographs were unable to measure the solar spectrum below approximately 2100Å (Section 1.1.1). Because of this, attempts were made to develop non-dispersive detectors which, because of their higher sensitivity, could be used to measure intensities below 2100Å from unstabilized rockets.

The first non-dispersive detectors to be used employed the thermoluminescent properties of the phosphor $CaSO_4$:Mn. Detectors sensitive to the ranges 1050Å to 1340Å and 1220Å to 1340Å were designed and Tousey et al. (1951) have described a number of flights of these detectors that took place from 1948 to 1950. They proved to be unreliable for absolute intensity measurements with the most reliable experiment giving a value of 0.4 erg cm^{-2} sec^{-1} for the Lyman-α flux.

Geiger counters sensitive to the wavelength bands 1100Å to 1350Å, 1425Å to 1650Å and 1725Å to 2100Å were flown in rockets from

1949 to 1952 by Friedman and his co-workers (Friedman et al., 1951 and Byram et al., 1953). The most accurate data were obtained in measurements of Lyman-α intensities using the 1100Å to 1350Å detectors. These detectors also proved unreliable for absolute intensity measurements with the best experiment yielding a value of 0.1 erg $cm^{-2} sec^{-1}$ for the Lyman-α intensity.

The first non-dispersive detectors to give reliable solar flux values were the ion chambers flown in 1955 by Byram et al. (1956). These detectors employed a lithium fluoride window and a nitric oxide filling gas to give a spectral response range from 1050Å to 1350Å. Absolute calibration of these detectors was both simple and accurate (Section 3.6). The Lyman-α line dominates the radiation in the 1050Å to 1350Å range to such an extent that only between 10% and 15% of the ion chamber signal is due to other wavelengths (Section 1.1.2). As a consequence, lithium fluoride-nitric oxide ion chambers have been used extensively for the purpose of measuring solar Lyman-α radiation from both rockets and satellites. A list of most of the rocket measurements up to 1967 has been made by Weeks (1967). He has found a significant solar cycle variation in the Lyman-α level with a mean value for the maximum of the solar cycle of 6.1 ± 0.45 erg cm^{-2} sec^{-1} and a mean value for the minimum of 4.3 ± 0.35 erg cm^{-2} sec^{-1}.

Eight ion chambers sensitive to different narrow wavelength bands between 1050Å and 1680Å were flown on a Long Tom rocket in 1966 by Carver et al. (1969). Sapphire-xylene (1420Å to 1470Å) and

quartz-triethylamine (1570Å to 1680Å) ion chambers were included in this experiment. Their spectral responses lie inside the wavelength band believed to be emitted from the vicinity of the solar temperature minimum (Section 1.2). The intensities derived from these two ion chambers are compared in Section 6.3 with measurements made in the present work with WRESAT I ion chambers of the same types.

Lithium fluoride-nitric oxide ion chambers have been flown in several satellite vehicles with the aim of monitoring continuously the Lyman-α output from the total solar disk. Two of these detectors were launched in the Solrad I spacecraft in June 1960. Some ambiguities in the derived flux levels resulted from the deterioration of the sensitivity of the detectors. However, it was possible to conclude that over the period from July 13th to August 3rd, 1960, the day-to-day variations in solar Lyman-α emission did not exceed 18% (Kreplin et al., 1962). It was also concluded that the Lyman-α emission from a class 2 disk flare does not exceed 11% of the quiet sun total disk emission. The OSO I satellite, launched in March 1962, also carried a lithium fluoride-nitric oxide ion chamber. The average Lyman-α flux was found to be 5.0 erg $cm^{-2}sec^{-1}$ and enhancements were associated with large flares. A 5% enhancement was caused by a class 2^{+} flare and a 7% enhancement was caused by a class 3 flare (Brandt, 1969). Lithium fluoride-nitric oxide ion chambers on the Interkosmos I satellite showed variations in the Lyman-α flux from 3.7 to 4.7 erg cm^{-2} sec^{-1} during the period from October 15th to October 23rd, 1969, with

a mean value of 4.1 erg $cm^{-2} sec^{-1}$ (Felske et al., 1970). In the present work, rocket flights of lithium fluoride-nitric oxide ion chambers on July 24th, 1969 and December 9th, 1969 resulted in Lyman-α flux determinations in substantial agreement with those of the Interkosmos I satellite (Section 4.4.2). The two lithium fluoride-nitric oxide ion chambers on the OSO 4 satellite deteriorated rapidly. However, it was possible to extrapolate the response of one of the ion chambers back to the first orbit (Timothy and Timothy, 1970). Close agreement was found between the value of the Lyman-α intensity determined in this way and that derived from a monochromator also on the OSO 4 satellite (page 9).

An improvement in the spectral resolution of the lithium fluoride-nitric oxide ion chamber has been made on the Solrad 8, 9 and 10 satellites by flying with it another ion chamber sensitive to the range 1220Å to 1350Å. The latter ion chamber enables a calculation to be made of the contribution to the 1050Å to 1350Å detector, due to wavelengths longer than Lyman-α . Although saturation of the Solrad 8 detectors and a gradual decrease in their sensitivity made analysis of the data difficult, it was possible to show that during the period from December 1965 to July 1966 day-to-day variations were less than 10% (Fossi et al., 1970). The Solrad 9 ion chambers deteriorated rapidly and no useful data were obtained.

The Solrad 10 satellite also carried an ion chamber sensitive to the wavelength band 1440Å to 1660Å. Privately communicated intensity

measurements obtained with this detector are compared with those obtained in the present work with ion chambers on the WRESAT I satellite (Section 5.6).

The measurement of absolute intensities using satellite-borne ion chambers has not yet proved to be very satisfactory, mainly due to the loss of instrument sensitivity. The satellite experiments have been valuable, however, in showing that the day-to-day variations in the Lyman-α flux level appear to be small with the greatest changes being less than 10%. Also enhancements in the total Lyman-α flux due to large flares have been shown to be too small to cause significant geophysical changes (such as an increase in D-region ionization). However, these enhancements imply very large local increases in Lyman-α brightness and may therefore make significant contributions to the energy lost from flares.

1.2 The Nature and Origin of the Solar Ultraviolet Spectrum

Observations of the solar spectrum have led to a description of the solar atmosphere in terms of three emitting zones:-

(i) The photosphere. This is the innermost zone and it extends from the limb of the visible solar disk down to the deepest observable layers. It is about 350 km thick and its temperature decreases from about 9000°K at the bottom to about 4500°K at the top.

(ii) The chromosphere. This zone lies immediately above the photosphere and is about 20,000 Km thick. Its temperature increases from 4500°K where it meets the photosphere to about 40,000°K where it meets the corona.

(iii) The corona. This is the outermost zone and during total solar eclipse it has been seen to extend to a distance of at least 40 solar radii. Between the chromosphere and the corona there is a very narrow transition region where the temperature rises from 40,000°K to about 1 million degrees. The general coronal temperatures are between 1 and 2 million degrees.

The visible solar radiation comes almost entirely from the photosphere and consists of a continuum, with a radiation temperature* of about 6300°K, crossed by numerous Fraunhofer absorption lines. The continuous opacity of the solar gases is a minimum in the visible spectral range where it is predominantly due to the free-free and bound-free transitions of the negative hydrogen ion. At wavelengths both longward and shortward of the visible spectrum, the continuous opacity increases, with the result that the emergent solar continuum originates in progressively higher layers. In particular, we expect that in both the far infra-red and the extreme ultraviolet, the

---

* The radiation temperature of the sun at a particular wavelength is the temperature of a black body which would emit the same intensity of radiation at that wavelength as the sun.

radiation temperature of the continuum will pass through a minimum at some wavelength for which the radiation is emitted from the temperature minimum region between the photosphere and chromosphere.

Beginning in the near ultraviolet, the continuous opacity increases towards shorter wavelengths as the ionization limits of the abundant neutral metals are crossed. As a result the radiation temperature of the continuum drops from 6300°K to about 5500°K at 2100Å. Near 2087Å the character of the solar spectrum undergoes a rapid change with the continuum intensity falling by a factor of five in the space of about 15Å (Boland et al., 1971). At 2000Å the radiation temperature has dropped to 5000°K while the cores of the absorption lines follow a 4900°K black body curve both above and below the continuum discontinuity. The conclusion is that the continuum radiation below about 2080Å arises only a short distance below the region of the temperature minimum, while the absorption lines are formed slightly closer to the temperature minimum where the temperature is a little lower.

The most recent measurements of the continuum intensity below 2000Å are those of Widing et al. (1970), Parkinson and Reeves (1969) and Brueckner and Moe (1972) all of which are described in Section 1.1.2. These measurements are generally in close agreement in terms of the wavelength dependence of the intensity but there are still large discrepancies between the various measurements of the absolute intensity level (Section 6.3). Qualitatively, below 2000Å the

continuum follows a descending black body curve down to 1700Å. Between 1700Å and 1400Å there is a broad radiation temperature minimum. Below 1400Å (Figure 1.2), the temperature begins to slowly rise with a more rapid increase occurring as the wing of the very intense Lyman-α line begins to dominate. On the short wavelength side of the Lyman-α line the radiation temperature falls to another minimum at 1180Å but never reaches a temperature as low as the minimum on the long wavelength side. Below 1180Å the radiation temperature of the continuum rises again to a maximum at 970Å.

In the 2000Å to 1000Å range the type of line seen against the continuum changes from absorption to emission. The first emission lines appear just below 2000Å and towards shorter wavelengths the absorption lines progressively disappear as the emission lines become more numerous. Below 1682Å (which corresponds to the ^1D absorption edge of Si I) there are no atomic absorption lines and the only absorption features are the band heads of CO. All of the emission lines show limb brightening in keeping with their origin in the chromosphere where the temperature is increasing outwards.

The spectral range from 1682Å to 1525Å is of particular interest because the emergent continuum radiation can be shown from observations to arise from the region of the temperature minimum. Above 1682Å the continuum is still photospheric in origin. This is shown by the continued presence of shallow absorption lines (Figure 1.1) which, as mentioned above, indicates that the emergent continuum arises from

just below the temperature minimum region where the temperature is still decreasing outwards. Additional confirmation of this is given by the fact that above 1682Å the continuum is still limb darkened. There is a small but rapid change in the continuum intensity at 1525Å which coincides with the ^3P absorption edge of Si I. The intensity is highest to the short wavelength side of the edge and this, coupled with the strong limb brightening observed below 1525Å, implies that the continuum radiation below 1525Å is chromospheric in origin. Between 1682Å and 1525Å there are no atomic absorption lines and the centre to limb variations are small (Brueckner and Moe, 1972). Both of these characteristics are expected for radiation arising from the region across the temperature minimum.

Recent theoretical models (Cuny, 1971, Gingerich et al., 1971) are in agreement with the observations in suggesting that the region between 1525Å and 1682Å is particularly significant for investigations of the temperature minimum. A comparison of the various measurements of the radiation temperature in this wavelength band is made in Section 6.3.

CHAPTER 2

THE ATMOSPHERIC ABSORPTION OF SOLAR ULTRAVIOLET RADIATION

2.1 Introduction

Although considerable effort has been expended in measuring the properties of the total neutral atmosphere, relatively few measurements have been made of the properties of the individual atmospheric constituents. This is especially true with regard to molecular oxygen above about 90 Km, where both its dissociation into atomic oxygen and diffusion begin to become important. Seasonal, latitudinal and temporal variations in the molecular oxygen density profile are still largely unknown and significant uncertainties exist with regard to models used to represent the distribution of molecular oxygen. At lower altitudes, where molecular oxygen is a well-mixed species, more information is available from measurements of the total neutral atmosphere. However, even here more information is needed on the molecular oxygen distribution and its variations with season, latitude and time of day. Such measurements in the upper mesosphere (70 Km - 90 Km) and lower thermosphere (90 Km - 200 Km) will be helpful in understanding atomic oxygen and ozone photochemistry as well as vertical and horizontal transport mechanisms in a region where several of these problems are probably important. These measurements will also be helpful in improving existing "standard or reference

atmospheres", that attempt to give a dynamic interpretation of the behaviour of the real atmosphere. As pointed out by Schilling (1968), even minor variations in the properties of a reference atmosphere in the upper mesosphere - lower thermosphere region can lead to very large variations in its properties at higher altitudes. Therefore, a proper interpretation of the variations of the upper thermosphere, as detected by earth-orbiting satellites, depends upon a thorough knowledge of the variations in these lower regions.

The two basic methods for determining the concentration of different neutral species in the upper atmosphere are absorption spectroscopy and mass spectroscopy. At present, absorption spectroscopy is preferred for accurate quantitative determinations because the data interpretation is relatively straightforward and unambiguous. The accuracy of the various mass spectrometric methods is compromised by effects associated with motion of the rocket and reactions at the walls of the instrument (Section 6.1.3). In addition, mass spectrometers can only be operated above about 100 Km. Both dispersive instrumentation, such as spectrographs, and wider band non-dispersive instrumentation, such as Geiger counters and ion chambers, are useful in the application of absorption spectroscopy. In the present work, the study of molecular oxygen densities is based on experiments using ion chambers carried on sounding rockets and on one satellite vehicle. Within the wavelength range 1000Å to 1700Å, it can be shown that atmospheric absorption is due almost entirely to molecular oxygen. However, the minor atmospheric constituents do

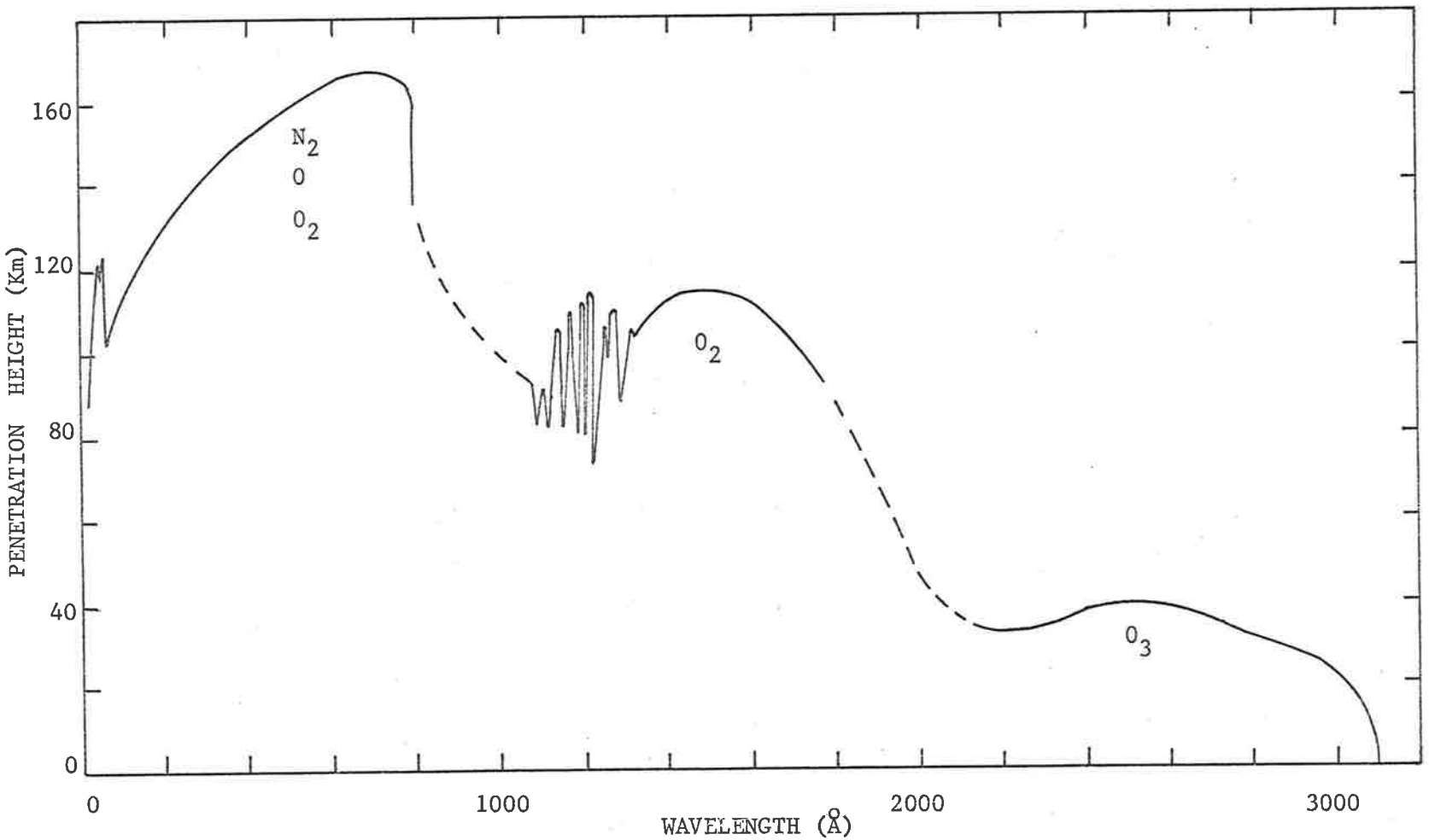

Fig. 2.1 The variation of penetration height with wavelength (Friedman, 1960).

absorb to a small extent and this can be of importance at the wavelength of the solar Lyman-α line (Section 2.5).

Figure 2.1 shows the variation of the atmospheric penetration height* as a function of wavelength (Friedman, 1960b). From 2000Å to 3000Å the radiation is absorbed almost entirely by ozone, which reaches its peak concentration at an altitude of about 25 Km. At wavelengths shorter than 2000Å, molecular oxygen absorbs strongly and the absorption takes place at higher altitudes. The absorption by molecular oxygen leads to its dissociation and the production of atomic oxygen. At wavelengths shorter than 1000Å, molecular nitrogen also absorbs strongly and atomic oxygen, which is the principal atmospheric constituent above about 150 Km, contributes to the absorption of wavelengths shorter than about 900Å.

2.2 The Absorption Cross-Section of Molecular Oxygen

The absorption of vacuum ultraviolet radiation by molecular oxygen has been investigated by a number of workers. Detailed measurements using photoelectric techniques have been made by Watanabe et al. (1953a), Metzger and Cook (1964) and Blake et al. (1966). These measurements are substantially in agreement with one another. Figure 2.2 shows the absorption spectrum of molecular oxygen as given

---

*The atmospheric penetration height is the height above the earth's surface at which the solar flux has been attenuated to 1/e of its value above the atmosphere.

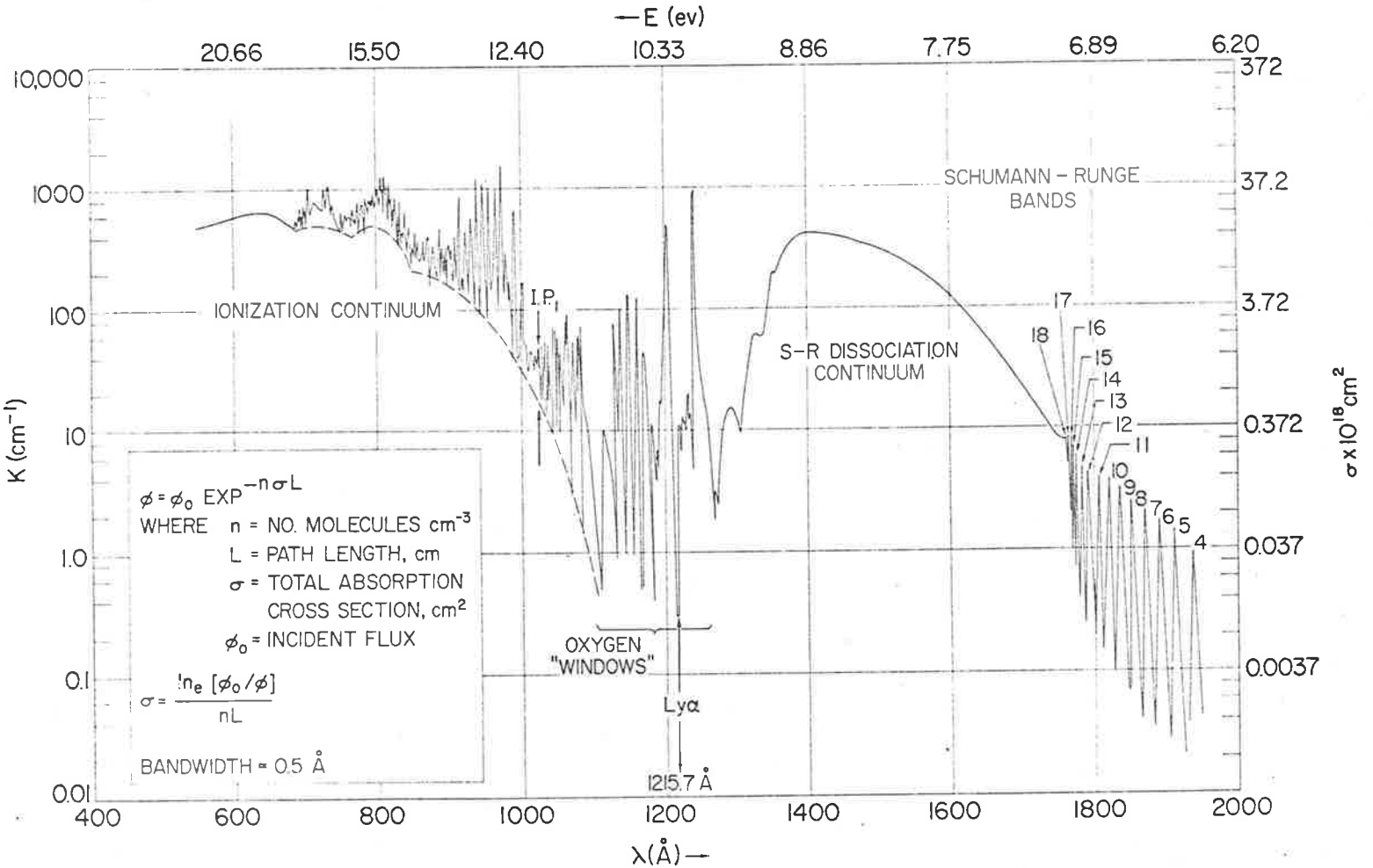

Fig. 2.2 The absorption spectrum of molecular oxygen (Cook and Ching, 1965).

by Cook and Ching (1965). The Schumann-Runge dissociation continuum extends from about 1300Å to about 1750Å with the maximum cross-section of $1.48 \times 10^{-17} cm^2$ occurring at 1425Å. The Schumann-Runge bands are at wavelengths longer than 1750Å. The cross-sections of these bands decrease with increasing wavelength until they merge into the weak Hertzberg continuum. At wavelengths shorter than 1300Å, the spectrum shows a number of strong absorption bands separated by "windows" where the cross-section is much lower. The most important of these windows is the one that almost exactly coincides with the very strong solar Lyman-α line. The shape of this window is shown in Figure 2.3 (Ogawa, 1968) which also indicates the approximate positions of the two maxima in the solar Lyman-α line (Section 1.1.3). Although the window is very narrow, the close proximity of the Lyman-α line to the centre of the window means that the variation of the absorption cross-section across the line is small. The absorption cross-section at the bottom of the window has been found to be pressure dependent with a rate of change of about $1.7 \times 10^{-23} cm^2 torr^{-1}$ (Blake et al., 1966, Shardanand, 1967). As the value of the cross-section is about $1.0 \times 10^{-20} cm^2$ at Lyman-α, the pressure dependence is negligible for the range of pressures encountered in the region of the atmosphere where absorption of solar Lyman-α radiation takes place.

Table 2.1 shows the values of the absorption cross-section at Lyman-α that have been obtained by various workers using photoelectric techniques. The two measurements of Ogawa (1968) refer to the cross-section at the wavelengths of the two maxima of the solar Lyman-α line.

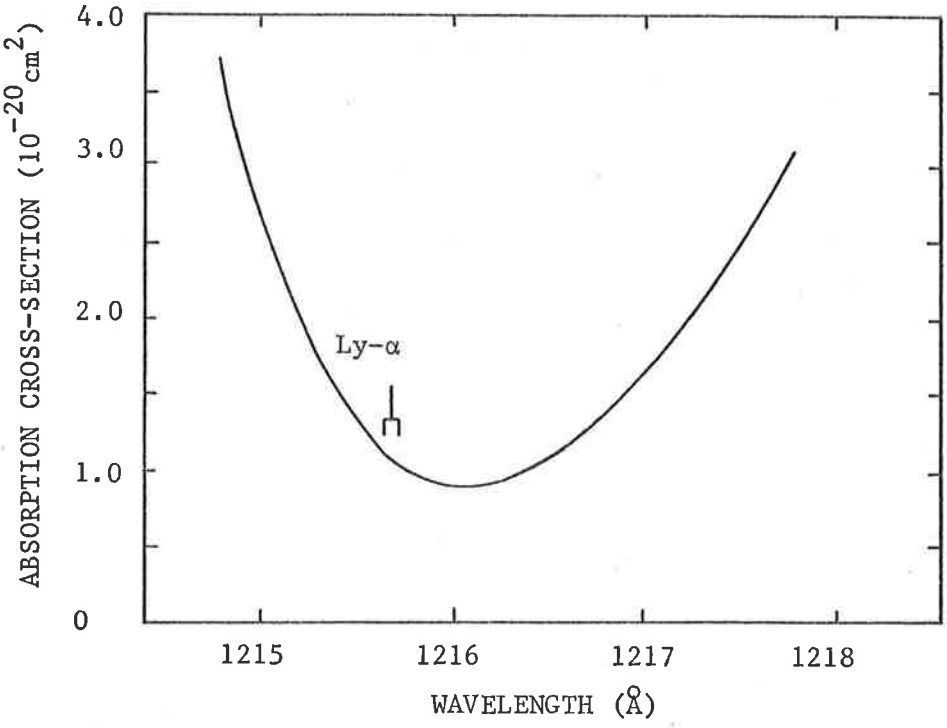

Fig. 2.3 The shape of the molecular oxygen window near Lyman-α (Ogawa, 1968).

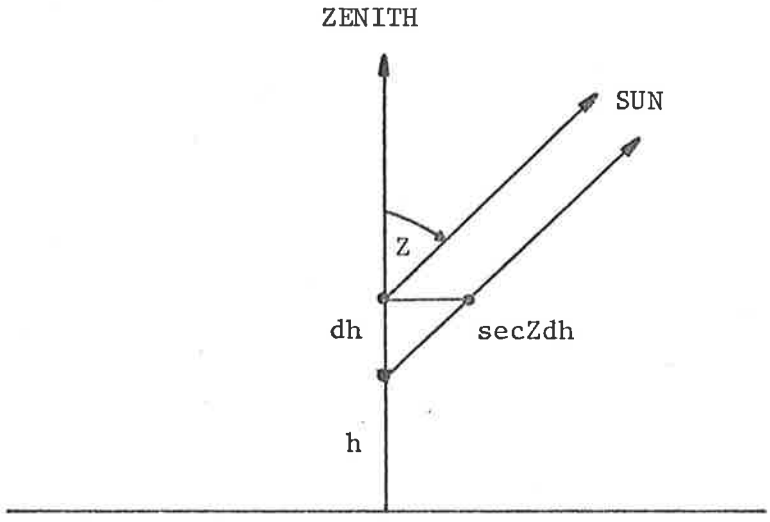

Fig. 2.4 Geometry for the flat-earth approximation.

TABLE 2.1

Reference	Cross-Section
Preston (1940)	$1.04 \times 10^{-20} cm^2$
Watanabe et al. (1953a)	1.00
Metzger and Cook (1964)	1.04
Blake et al. (1966)	1.12
Shardanand (1967)	1.08
Ogawa (1968)	1.03 1.13

More recently, Gaily (1969) (also using a photoelectric technique) has studied the pressure dependence of the cross-section at Lyman-α and at several shorter wavelengths nearby. His results at Lyman-α are in substantial agreement with those of Watanabe et al. (1953a).

Ditchburn et al. (1954) and Lee (1955) used photographic techniques to obtain values for the cross-section of $0.84 \times 10^{-20} cm^2$ and $0.85 \times 10^{-20} cm^2$. In the present work a value of $1.0 \times 10^{-20} cm^2$ has been adopted for the Lyman-α cross-section. The values quoted above indicate an uncertainty of ± 14% in the adopted value and this uncertainty must be taken into account when deriving molecular oxygen densities from atmospheric Lyman-α absorption profiles (Section 2.3).

2.3 Molecular Oxygen Densities from Absorption Measurements Between 1000Å and 1700Å

A reasonably complete treatment of the derivation of atmospheric neutral particle densities, from measurements of the attenuation of solar ultraviolet radiation, has been given by Hinteregger (1962). In this chapter, the discussion will only apply to the absorption of radiation in the wavelength range from 1000Å to 1700Å. In this wavelength range, the absorption due to atmospheric constituents other than molecular oxygen can be ignored (Section 2.5). The discussion will also be restricted to the case where the solar zenith angle*, Z, is less than 90°. The situation where Z is greater than 90° is considered in detail in Section 5.3.

Under the above restrictions, the flux in photons $cm^{-2}sec^{-1}$, of parallel monochromatic radiation of wavelength, λ, at a height, h, above the earth's surface, is given by the Beer-Lambert law

$$\phi(\lambda,h) = \phi'(\lambda) \exp[-\sigma(\lambda)N(h)] \qquad \ldots(1)$$

where $\phi'(\lambda)$ is the flux above the atmosphere in photons $cm^{-2}sec^{-1}$,

$\sigma(\lambda)$ is the absorption cross-section of molecular oxygen in cm^2,

and N(h) is the columnar density above a height, h, i.e. the number of oxygen molecules in a column of area $1cm^2$ along the path of the radiation.

---

*The solar zenith angle is the angle between the direction of the sun and the local zenith.

If $\sigma(\lambda)$ is also dependent on temperature or pressure it may, as a result, show an indirect height dependence. For molecular oxygen, in the height and wavelength ranges applicable in the present work, these effects may be neglected.

In practice, any radiation detector will have a finite bandwidth, $\Delta\lambda$, within which it will respond. From equation (1), the flux, in photons $cm^{-2}sec^{-1}$, within the instrumental bandwidth, from λ to $\lambda + \Delta\lambda$ is given by

$$\phi(\lambda,\Delta\lambda,h) = \int_{\lambda}^{\lambda+\Delta\lambda} \phi_o(\lambda)\exp[-\sigma(\lambda)N(h)]d\lambda \qquad ...(2)$$

where $\phi_o(\lambda)$ is the differential photon flux above the atmosphere in photons $cm^{-2}sec^{-1}$ Å^{-1}. If $\varepsilon(\lambda)$ represents the spectral response function of the detector (Section 3.6) then the detector's signal at the height, h, is given by

$$I(h) = \int_{\lambda}^{\lambda+\Delta\lambda} \varepsilon(\lambda)\phi_o(\lambda)\exp[-\sigma(\lambda)N(h)]d\lambda \qquad ...(3)$$

If $\sigma(\lambda)$ can be replaced by a constant cross-section, σ, then equation (3) can be simplified to the form

$$I(h) = I = I_o \exp[-\sigma N(h)] \qquad ...(4)$$

where $I_o = \int_{\lambda}^{\lambda+\Delta\lambda} \varepsilon(\lambda)\phi_o(\lambda)d\lambda$ is the ion chamber signal above the atmosphere. This simplification is possible in two cases.

(i) A solar emission line may dominate the radiation within the bandwidth of a detector to such an extent that the

bandwidth, $\Delta\lambda$, can be reduced to the bandwidth across the line. This is the case for the ion chamber with a lithium fluoride window and nitric oxide filling gas, which responds over the wavelength range 1050Å to 1350Å (Chapter 3). As mentioned in Section 1.1.2, the Lyman-α emission line at 1215.7Å accounts for approximately 85% of the output of this detector. Also, the Lyman-α line lies close to the centre of a window in the molecular oxygen absorption spectrum where the cross-section is very low (Section 2.2). This means that most of the other wavelengths within the 1050Å to 1350Å range will be absorbed at much higher altitudes. Therefore, in the region where the total solar radiation in the bandwidth 1050Å to 1350Å has been reduced by about 15% or more, the ion chamber can be considered to be responding purely to Lyman-α radiation. As the variation of the absorption cross-section of molecular oxygen is small over the wavelength range covered by the Lyman-α line (Section 2.2), equation (4) is a good approximation with σ equal to $1.0 \times 10^{-20} cm^2$.

(ii) The absorption cross-section may be constant, or nearly so, throughout the bandwidth of a detector. An example of this behaviour is provided by the ion chamber with a sapphire window and xylene filling gas (Chapter 3). The bandwidth of this detector is 1420Å to 1480Å. As can be seen from

Figure 2.2, the variation of the molecular oxygen absorption cross-section across this wavelength range is small. Equation (4) is therefore a good approximation, with σ having the value $1.45 \times 10^{-17} cm^2$ which is the average value across the bandwidth. The estimated probable error in this value is ± 10%.

The third type of ion chamber used in the present work has a quartz window and triethylamine filling gas and a bandwidth extending from 1550Å to 1690Å. As can be seen from Figure 2.2, the absorption cross-section of molecular oxygen varies somewhat over this wavelength range. Therefore, the simplification of equation (3) used above is not applicable to this detector.

Let us consider the change in the signal of a quartz-triethylamine chamber over the height range $h + \Delta h$ to h. The differential photon flux at the height $h + \Delta h$ is given, by comparison with equation (1), as

$$\phi(\lambda, h+\Delta h) = \phi_o(\lambda)\exp[-\sigma(\lambda)N(h+\Delta h)]$$

Equation (3) can therefore be rewritten as

$$I(h) = \int_{\lambda}^{\lambda+\Delta\lambda} \epsilon(\lambda)\phi(\lambda, h+\Delta h)\exp[-\sigma(\lambda)\Delta N(h)]d\lambda \qquad \ldots(5)$$

where $\Delta N(h) = N(h) - N(h+\Delta h)$.

If Δh is sufficiently small, we may neglect the changing distribution of the radiation as it passes through the layer. We may then

approximate equation (5) by

$$I(h) = I(h+\Delta h)\exp[-\sigma_{eff}(h+\Delta h)\Delta N(h)] \qquad \ldots(6)$$

where $\sigma_{eff}(h+\Delta h)$ is the "effective absorption cross-section" and is defined by

$$\sigma_{eff}(h) = \frac{\int_{\lambda}^{\lambda+\Delta\lambda}\varepsilon(\lambda)\phi(\lambda,h)\sigma(\lambda)d\lambda}{I(h)} \qquad \ldots(7)$$

The value of σ_{eff} can only decrease or remain constant as the radiation penetrates down through the atmosphere. It will decrease when $\sigma(\lambda)$ varies across the bandwidth of a detector because the radiation of wavelengths where $\sigma(\lambda)$ is larger will be absorbed more quickly, leaving a higher proportion of the radiation of wavelengths at which σ is smaller. This changing distribution of the radiation within a detector's bandwidth is known as "radiation hardening".

The variation of σ_{eff} with height was investigated for the quartz-triethylamine ion chamber using the following assumptions.

(i) The vertical distribution of molecular oxygen was assumed to be that given by the 1965 mean CIRA atmosphere (CIRA 1965).

(ii) The solar zenith angle was taken to be 0^{o}.

(iii) The variation of the molecular oxygen absorption cross-section between 1550Å and 1690Å was assumed to be that

given by Blake et al. (1966).

(iv) The spectral distribution of the solar flux was taken to be that of a black body at a radiation temperature of 4600°K (Section 6.3).

(v) The spectral response used was that shown in Figure 3.12 which is a typical example.

Equation (7) was used to calculate values of σ_{eff} for various heights. These values are listed in Table 2.2 along with the corresponding values of the attenuation of the ion chamber's signal $((I_o-I)/I_o)$. The values of σ_{eff} and attenuation, given in Table 2.2, are independent of the assumed density distribution and the solar zenith angle. The height values, however, depend on both of these parameters. The values of σ_{eff} are not strongly dependent on the assumed solar flux distribution. As shown in Section 6.3, the solar spectrum in the wavelength range from 1550Å to 1670Å is closely represented by that of a black body with a radiation temperature of 4600°K. If, however, the solar flux is assumed to be constant over this wavelength range, the value of σ_{eff} above the atmosphere is changed by less than 8% from the value given in Table 2.2.

As expected, the values of σ_{eff} decrease as the radiation penetrates deeper into the atmosphere, due to the effect of radiation hardening. However, over the height range where the attenuation of the ion chamber's signal is less than 80%, the values of σ_{eff} are

greater than 80% of the value above the atmosphere. Therefore, over this range, σ_{eff} can be taken to have the value $3.2 \times 10^{-18} cm^2$ with a maximum error of 12%. The values of $\sigma(\lambda)$ used in the above calculations have a probable error of about ± 5% (Blake et al., 1966). The probable random error in the values of σ_{eff} given in Table 2.2, due to the errors in the values of $\sigma(\lambda)$, $\varepsilon(\lambda)$ and $\phi(\lambda)$, is not expected to exceed ± 8%.

TABLE 2.2

Height	σ_{eff}	Signal Attenuation $(I_o-I)/I_o$
100	2.2	0.97
105	2.8	0.82
110	3.2	0.58
115	3.4	0.37
120	3.4	0.24
	3.6	0.00

To within the above accuracy limitations we may therefore assume σ_{eff} to be a constant, σ, with the value $3.2 \times 10^{-18} cm^2$. Equation (6) therefore becomes

$$I(h) = I(h+\Delta h)\exp[-\sigma \Delta N(h)]$$

which, by a simple iteration procedure, leads to the equation

$$I(h) = I_o \exp[-\sigma N(h)]$$

Therefore, equation (4) is valid for all three of the ion chamber types used in the present work.

Up to this point, the theory developed in this chapter is valid for solar zenith angles up to 90°. In fact, if the variable, h, is regarded as a minimum ray height (Section 5.3) rather than a rocket height, this theory also applies for zenith angles in excess of 90°. However, the remainder of the theory in this chapter will be concerned with the situation where the solar zenith angle is sufficiently small for the flat-earth approximation to be used. The geometry of this situation is shown in Figure 2.4.

The differential form of equation (4) is

$$\frac{1}{I}\frac{dI}{dh} = \frac{d}{dh}(\ln I) = -\sigma \frac{dN(h)}{dh} \qquad \ldots(8)$$

From Figure 2.4, it can be seen that

$$\frac{dN(h)}{dh} = -n(h) \sec Z \qquad \ldots(9)$$

where n(h) is the number density of molecular oxygen in molecules cm^{-3} and Z is the solar zenith angle. Therefore, substituting into equation (8) and rearranging we have

$$n(h) = \frac{1}{\sigma \sec Z}\frac{d}{dh}(\ln I) \qquad \ldots(10)$$

The number density at any height is therefore proportional to the slope, at that height, of a semi-logarithmic plot of the ion chamber's signal versus the height of observation. It should be noted that density determinations do not depend upon an absolute measurement of the signal.

For solar zenith angles in excess of about 73^{o}, equation (9) (and hence equation (10)) begins to become inaccurate due to the effect of the curvature of the earth. In the satellite atmospheric occultation experiment described in Section 5.3, where the absorption measurements are made at satellite sunrise and sunset, both the curvature of the earth and the finite size of the sun must be considered when deriving density profiles. For the rocket experiments described in Section 4.3, the solar zenith angles were such that equation (10) could be used with negligible error.

2.4 Height Range for Determining Molecular Oxygen Densities

Equation (4) may be rewritten as

$$I = I_o \exp[-\tau(h)] \qquad \ldots(11)$$

where the optical depth for the wavelength band λ to $\lambda + \Delta\lambda$ is given by

$$\tau(h) = \sigma N(h) \qquad \ldots(12)$$

Therefore,

$$\tau(h^*) = \sigma N(h^*) = 1 \qquad \ldots(13)$$

where h^* is the penetration height (Section 2.1).

If the number density of molecular oxygen varies exponentially with height, x, with a scale height, H, we have

$$n(x) = n_o \exp(-x/H)$$

This will be a good approximation over a limited height range. Therefore, from equation (9),

$$N(h) = -\int_h^\infty n_o \exp(-x/H) \sec Z \, dh$$
$$= N_o H \exp(-h/H) \sec Z$$

and so, from equation (12),

$$\tau(h) = \sigma n_o H \exp(-h/H) \sec Z \qquad \ldots(14)$$

Using equations (14) and (11) the variation of I with height can be determined as shown in Table 2.3.

TABLE 2.3

h	τ	I/I_o
h^*-H	2.7	0.07
h^*	1.0	0.37
h^*+H	0.37	0.67
h^*+2H	0.14	0.87
h^*+3H	0.05	0.95

As can be seen from Table 2.3, the absorption takes place over a height range equal to about 4H. This represents the practical limit to the range over which densities can be determined by the measurement of absorption at one value of σ. The range is limited in the region of low attenuation by the difficulty in measuring the very small changes in I with height, and is limited in the region of high attenuation by the difficulty in measuring very small values of I. In general, the most accurate densities will be obtained near the penetration height, where the rate of change of signal with height is a maximum and the errors due to data reduction therefore a minimum.

From equation (13),

$$\sigma n_o H \sec Z \exp(-h^*/H) = 1 \qquad \ldots(15)$$

Therefore, the value of h* will be increased as Z is increased, but the values in Table 2.3 will remain unaltered. As a result, the absorption takes place higher up but over the same height range. From equation (15), it can be seen that as the zenith angle changes from 0 to Z, the value of h* is increased by an amount h_1, such that $\sec Z = \exp(h_1/H)$. Values of h_1/H are given in Table 2.4 for various values of Z.

It can be seen from Table 2.4, that even for large changes in the zenith angle the height range over which oxygen densities can be determined is not shifted by a large amount. This statement is

TABLE 2.4

Z	h_1/H
0^o	0.00
20^o	0.06
40^o	0.27
60^o	0.69
70^o	1.07

strictly true only when the flat-earth approximation is valid. In fact, due to the curvature of the earth the range is not raised more than several scale heights for zenith angles up to 90^o. Nevertheless, observations at large zenith angles provide a useful way of extending, significantly, the range of heights over which densities can be measured at one value of σ. For zenith angles less than 70^o, the normal height range for determining molecular oxygen densities with the lithium fluoride-nitric oxide ion chamber is 70 Km to 90 Km. Weeks and Smith (1968), using large zenith angles by making rocket flights near sunrise and sunset, have raised this height range considerably. For example, at a zenith angle of 95^o they have determined molecular oxygen densities over the height range 94 Km to 112 Km. Similarly in the satellite experiment described in Chapter 5, molecular oxygen densities have been measured above 90 Km by using lithium fluoride-nitric oxide ion chambers to measure the atmospheric attenuation of Lyman-α radiation at satellite sunrise and sunset.

2.5 Absorption of Lyman-α by Constituents other than Molecular Oxygen

In general, throughout the wavelength range 1000Å to 1700Å and in the height range near where $\frac{dI}{dh}$ is a maximum, atmospheric absorption is due almost entirely to molecular oxygen. Therefore,

$$\sigma_{O_2} n_{O_2}(h) >> \sigma_2(\lambda) n_2(h) + \sigma_3(\lambda) n_3(h) + \ldots$$

where the cross-sections σ_2, σ_3 etc. and the number densities n_2, n_3 etc. refer to the constituents other than molecular oxygen. However, Lyman-α radiation almost exactly coincides with a window in the molecular oxygen absorption spectrum where the cross-section is particularly low (Figure 2.2). Also, as can be seen from Table 2.5, all the other constituents except molecular nitrogen have higher absorption cross-sections at this wavelength. Therefore, even small concentrations of these constituents may make some contribution to the absorption of Lyman-α radiation. In the following, the absorption of Lyman-α radiation by each atmospheric constituent, σn, will be expressed as a fraction of the absorption due to molecular oxygen, $\sigma_{O_2} n_{O_2}$. The results of these calculations are shown in Table 2.5.

(a) Molecular nitrogen

Above 1000Å the absorption spectrum of molecular nitrogen consists only of the very weak band systems corresponding to several forbidden transitions. Upper limits that have determined for the cross-section at Lyman-α are $2 \times 10^{-22} cm^2$ (Preston, 1940), $3 \times 10^{-22} cm^2$

TABLE 2.5

Constituent	Cross-Section Relative to O_2, σ/σ_{O_2} (1)	Number Density Relative to O_2, n/n_{O_2} (2)		Absorption of Lyman-α Relative to O_2, $n/\sigma_{O_2} n_{O_2}$	
		70Km	90Km	70Km	90Km
O_2	1	1	1	1	1
N_2	$<6\times10^{-3}$	3.73	3.73	$<2.2\times10^{-2}$	$<2.2\times10^{-2}$
CO_2	7.4	1.5×10^{-3}	1.5×10^{-3}	1.1×10^{-2}	1.1×10^{-2}
H_2O	1.4×10^{3}	2.7×10^{-5}	7.6×10^{-7}	3.8×10^{-2}	1.0×10^{-3}
O_3	2.3×10^{3}	1.3×10^{-6}	4.4×10^{-7}	3.0×10^{-3}	1.0×10^{-3}
NO	2.7×10^{2}	3.5×10^{-6}	4.4×10^{-6}	9.4×10^{-4}	1.2×10^{-3}

(1) The cross-sections at Lyman-α (see text) are relative to the value 1.0×10^{-20} cm^2 taken for molecular oxygen.

(2) The densities are relative to that of molecular oxygen as given by the U.S. Standard Atmosphere (1962). The values for N_2 and CO_2 apply for the homosphere (i.e. below about 90 Km where the atmosphere is well mixed). The values for the other constituents are taken from the sources quoted in the text, the first value being that at 70 Km and the second value that at 90 Km.

(Watanabe et al., 1953b) and $6 \times 10^{-23} cm^2$ (Ditchburn et al., 1954). Using the lowest upper limit of the cross-section the absorption due to molecular nitrogen, at heights below 90 Km, is less than 2% of that due to molecular oxygen (Table 2.5). At greater heights, this percentage will be slightly greater due to the more rapid fall-off in molecular oxygen density due to dissociation.

(b) Carbon dioxide

The absorption cross-section of carbon dioxide at Lyman-α has been measured as $7.33 \times 10^{-20} cm^2$ (Inn et al., 1953). This value agrees closely with the value of $7.47 \times 10^{-20} cm^2$ determined by Preston (1940). There is no experimental evidence concerning the distribution of carbon dioxide in the region above 70 Km. However, Bates and Witherspoon (1952) have concluded that the rate of dissociation of carbon dioxide is appreciable only above 100 Km and so it seems likely that the fraction of carbon dioxide in the atmosphere is constant up to 100 Km. Under this assumption the absorption of carbon dioxide relative to that of molecular oxygen is 1.1% below 100 Km (Table 2.5) and less than this at greater heights.

(c) Water Vapour

The absorption spectrum of water vapour is shown in Figure 2.5 (Watanabe and Zelikoff, 1953). It can be seen from Figure 2.5 that Lyman-α occurs near a maximum in the absorption spectrum. The values of the cross-section obtained at Lyman-α by various workers are $1.45 \times 10^{-17} cm^2$ (Preston, 1940), $1.45 \times 10^{-17} cm^2$ (Watanabe and Zelikoff, 1953) and $1.34 \times 10^{-17} cm^2$ (Ditchburn et al., 1954). As

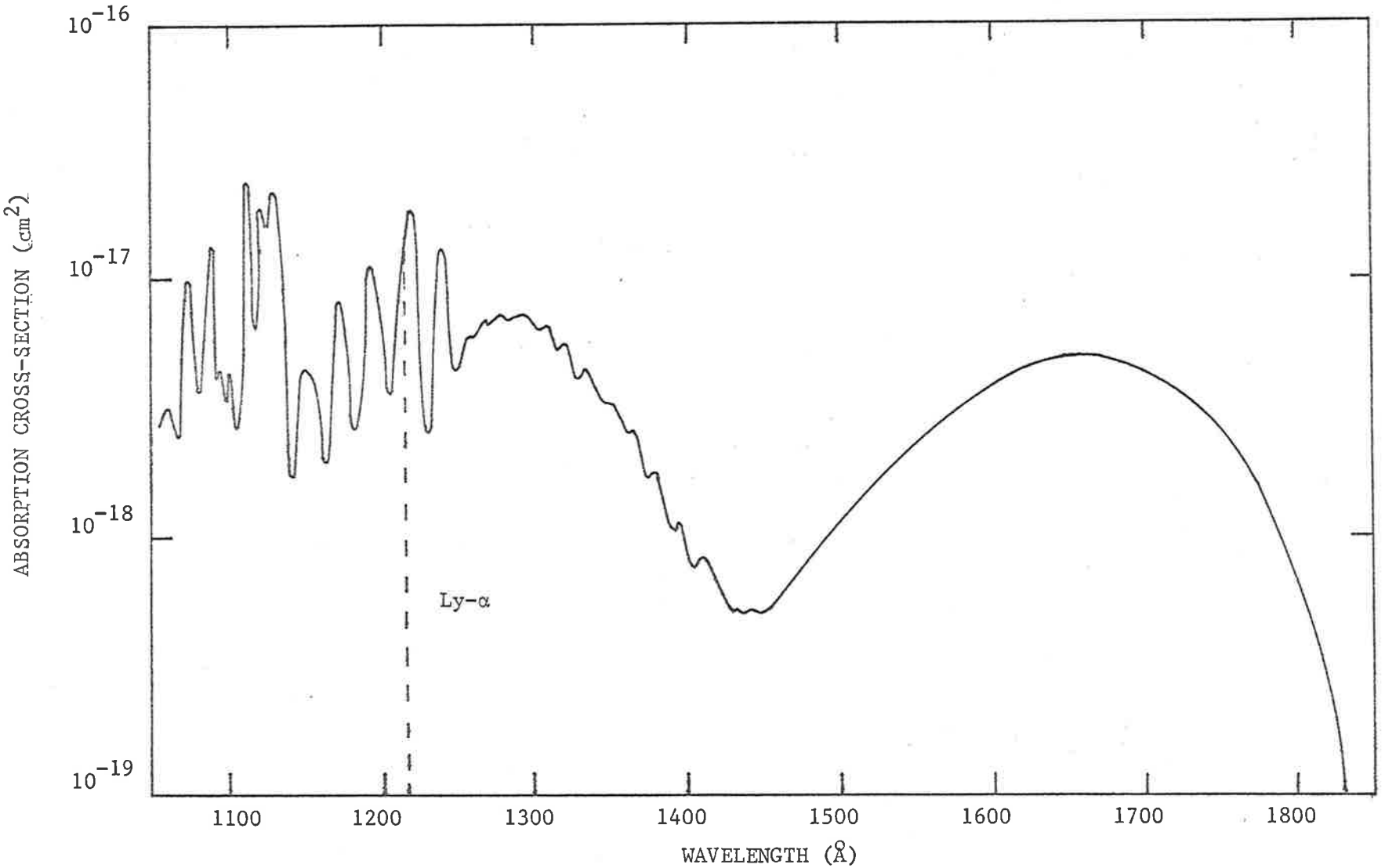

Fig. 2.5 The absorption spectrum of water vapour (Watanabe and Zelikoff, 1953).

these values are more than a thousand times the value for molecular oxygen, even very small concentrations of water vapour above 70 Km could contribute significantly to the absorption of Lyman-α radiation. The very strong band structure in the water vapour absorption spectrum occurs within the 1050Å to 1350Å bandwidth of the ion chamber used in the present work to detect Lyman-α radiation. Due to the very high cross-section values at the peaks of these bands, even very small traces of water vapour in the nitric oxide filling gas of this detector can seriously affect its operation (Section 3.6.3).

There have been no experimental determinations of water vapour concentrations above 70 Km but a theoretical profile has been obtained by Bates and Nicolet (1950), as a result of an analysis of the photo-chemistry of a hydrogen-oxygen atmosphere. The formation of noctilucent clouds near an altitude of 80 Km, in summer and at latitudes above 45^{o}, has been studied by Chapman and Kendall (1965). They have concluded that these clouds are formed when water vapour is carried (by convection at night) up to 80 Km, where it condenses on dust particles. As these clouds appear infrequently, it must be assumed that the transport of water vapour to these heights is a rare phenomenon. It should not therefore affect the overall concentration of water vapour at these heights.

There is obviously still a great uncertainty in the concentration of water vapour above 70 Km but for the present work it was

assumed that the water vapour concentration is as calculated by Bates and Nicolet (1950). Under this assumption the absorption due to water vapour, relative to that due to molecular oxygen is 3.8% at 70Km, 0.57% at 80Km, 0.10% at 90Km and less at greater heights (Table 2.5).

(d) Ozone

Tanaka et al. (1953) have obtained a value of $2.3 \times 10^{-17} cm^2$ for the absorption cross-section of ozone at Lyman-α. The only experimental determination of the concentration of ozone above 70Km is that of Rawcliffe et al. (1963). They have determined the density to be 4.5×10^8 mols.cm^{-3} at 70Km and 8×10^6 mols.cm^{-3} at 90Km. Therefore the absorption due to ozone relative to that due to molecular oxygen is 0.30% at 70Km and 0.10% at 90Km (Table 2.5).

(e) Nitric oxide

A value of $2.5 \times 10^{-18} cm^2$ has been obtained for the absorption cross-section of nitric oxide at Lyman-α (Marmo, 1953). Pearce (1969) has determined the concentration of nitric oxide to be 1.2×10^9 mols.cm^{-3} at 70Km, 2.8×10^8 mols.cm^{-3} at 80Km and 8×10^7 mols.cm^{-3} at 90Km. Using these values the absorption of nitric oxide relative to that of molecular oxygen is negligibly small (Table 2.5).

Atomic oxygen and atomic nitrogen exhibit continuous absorption only below their first ionization limits which are at 910Å and 852Å respectively. They can therefore be neglected when considering

absorption processes above 1000Å. Similarly, the inert gases which have ionization limits at 886Å (Kr), 787Å (A) and 575Å (Ne) need not be considered.

In the present work no corrections have been made for absorption due to constituents other than molecular oxygen. From the values given in Table 2.5 it may be concluded that the total contribution due to constituents other than molecular oxygen is not more than seven percent. The exact contribution is uncertain due to the uncertainty in the concentrations of some of the constituents, particularly water vapour.

In the wavelength bands 1420Å to 1480Å and 1550Å to 1690Å (which are the bandwidths of the other ion chambers described in Chapter 3), the effective absorption cross-section of molecular oxygen is respectively 1.45×10^3 times and 300 times the value at Lyman-α (Section 2.3). As a result, the contribution to the absorption of radiation in these wavelength bands, due to atmospheric constituents other than molecular oxygen, is negligible.

CHAPTER 3

THE CONSTRUCTION AND TESTING OF VACUUM ULTRAVIOLET ION CHAMBERS

3.1 Introduction

In principle, it is possible to fly dispersive instruments to measure the transmission of solar radiation by the atmosphere (Section 6.1). However, especially when using unstabilized rocket vehicles, a simpler and more practicable method is to use non-dispersive but spectrally selective detectors.

The broad-band non-dispersive detectors used for the detection of ultraviolet radiation, in the range 1000Å to 2000Å, can be put into two broad categories:-

(i) photomultipliers or photodiodes having high work function photocathodes that restrict their sensitivities to regions below approximately 2000Å, and

(ii) detectors utilizing the photoionization of gases and having relatively narrow band-passes in the range 1050Å to 1700Å.

The short wavelength limits of both types of detector are determined by the use of various window materials that can only transmit radiation of wavelengths longer than some definite value.

Detectors of the first type have been described by Dunkelman et al. (1962) who have detailed a variety of high work function photocathodes, both opaque and semitransparent, that have been developed to produce detectors spectrally selective to the vacuum ultraviolet. Typical examples of such materials are Cu-I, Cs-I and K-Br. However, the nature of the photoemissive process is such that the decrease in sensitivity towards longer wavelengths is only gradual. As the intensity of solar radiation increases rapidly towards longer wavelengths, these detectors have poor spectral selectivity when used in experiments where the sun is the source of radiation.

In contrast, detectors of the second type have quite a definite upper limit, or cut-off, to their long wavelength sensitivity. This limit is set by the energy needed to ionize any molecule of the filling gas. Apart from a small low energy tail, mainly due to the thermally excited vibrational and rotational states of the neutral molecules (Watanabe, 1957), this energy corresponds to the adiabatic ionization potential (IP) of the gas. Watanabe et al. (1962) have given the IP values of about 300 molecules in the range 7 to 15 eV. The gases most suitable for use in radiation detectors will be those for which the photoionization efficiency (defined as the number of ion-electron pairs produced for each photon absorbed in the gas) rises rapidly at the photoionization threshold. A sharp long wavelength cut-off will be prevented if there is appreciable photoelectric emission from the cathode (Section 3.9).

The earliest detectors employing the photoionization of a gas were the Geiger counters described by Chubb and Friedman (1955). These counters proved unreliable and were replaeed by ion chambers (Friedman et al., 1958). Ion chambers with machined copper bodies have been used at the U.S. Naval Research Laboratory (Friedman et al., 1964) and at University College, London (Willmore, 1961). An internally plated ceramic form has been used at NASA Goddard Space Flight Centre (Stober, 1962, Dunkelman et al., 1963) and at the Meteorological Office, Bracknell (Wildman et al., 1969). Ion chambers with bodies of extruded copper tubing have been used at the University of Adelaide (Carver and Mitchell, 1964, Carver et al., 1969) and are described in Section 3.2.

These detectors, with their wide field of view, excellent spectral selectivity, ruggedness and small size have proved to be well suited for use in geophysical experiments designed to be flown in small unstabilized rocket vehicles.

3.2 Construction of the Ion Chambers

3.2.1 Copper-Bodied Ion Chambers

Figure 3.1 shows a cross-sectional diagram of a copper-bodied ion chamber identical to those described by Carver and Mitchell (1964). Detectors of this type were used in the Skylark rocket experiment described in Section 4.2 and in the satellite experiment described in Chapter 5. The body of the chamber consisted of a

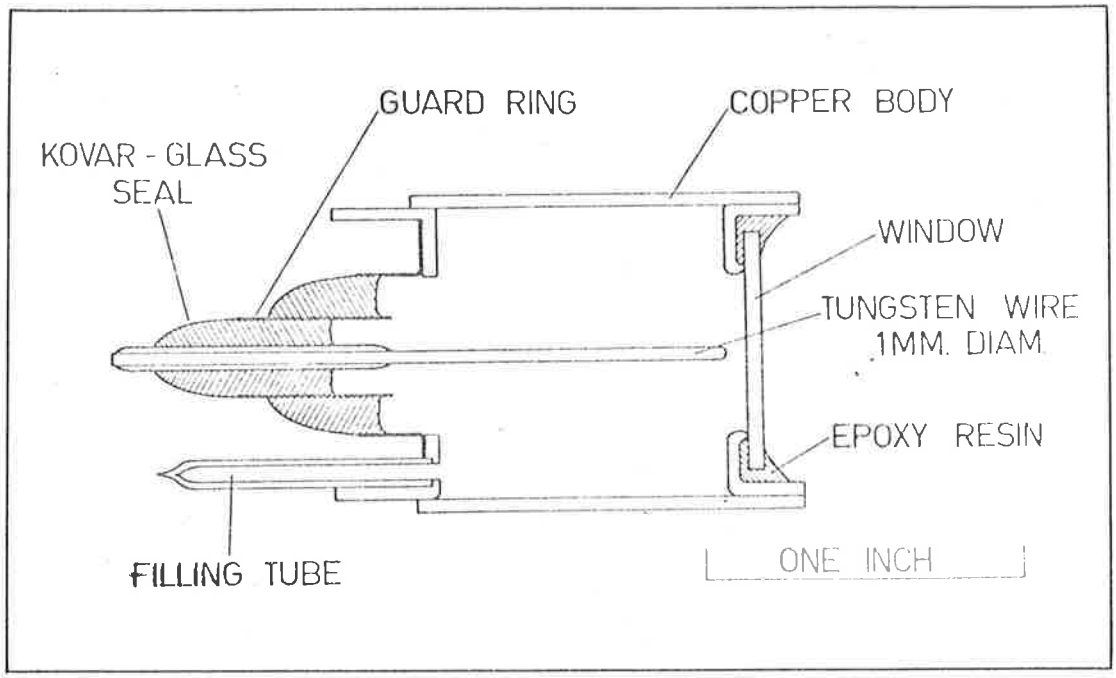

Fig. 3.1 A cross-sectional diagram of a copper-bodied ion chamber of the type first used by Carver and Mitchell (1964).

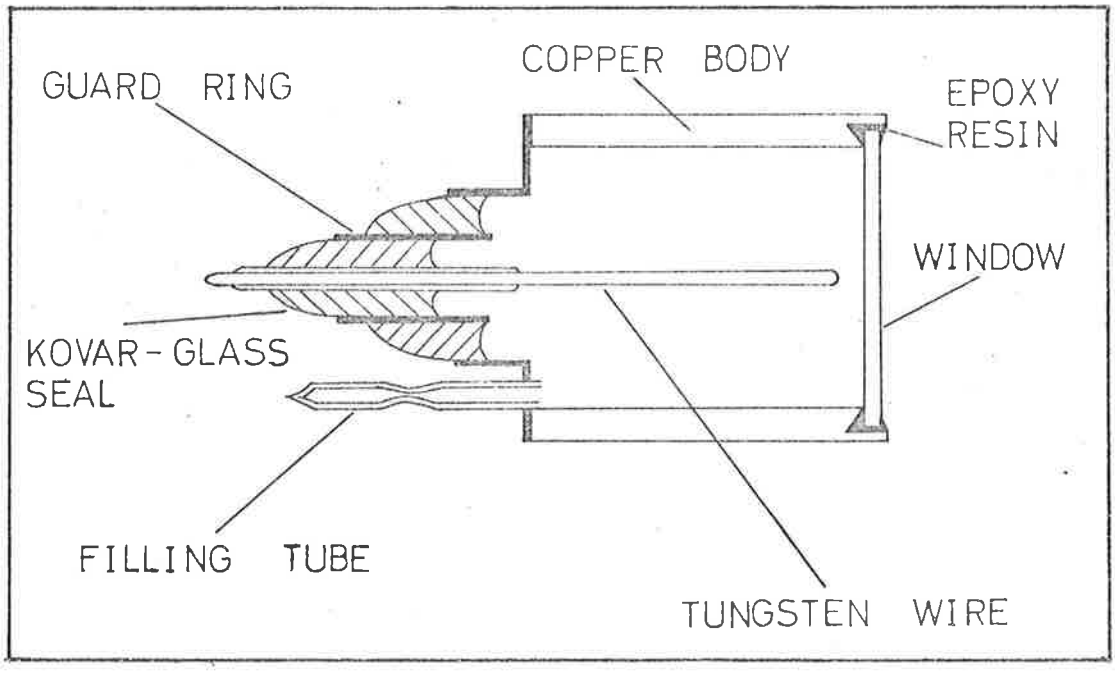

Fig. 3.2 A cross-sectional diagram of a more recently designed copper bodied ion chamber.

length of 1 inch copper tubing, into which copper end pieces were soldered. The cathode was a 1 mm diameter tungsten rod supported by a kovar-glass seal. A length of annealed copper tubing was soldered into the back of the chamber and acted as an evacuating and filling tube. Soft silver solder was used in assembling the chamber and the window materials were attached with epoxy resin.

In the present work, some difficulties were experienced in the manufacture of ion chambers with lithium fluoride windows and nitric oxide filling gas (LiF-NO ion chambers) due to contamination of the filling gas by water vapour. This was thought at first to be due to the migration of water through the epoxy window seal and so silver chloride was investigated as a sealing material. Silver chloride cannot be applied directly to copper and so glass-bodied chambers were constructed (Section 3.2.2) to enable this seal to be used. As a result of investigations using glass-bodied ion chambers it was found that the source of water vapour was the lithium fluoride windows. Due to their ease of manufacture, copper-bodied chambers were again constructed.

Figure 3.2 shows a cross-sectional diagram of the more recently designed copper-bodied chamber. It is similar in design to the ion chamber shown in Figure 3.1 but has the advantage of being simpler to construct and much easier to clean. The body consisted of a 1 inch length of copper tubing with an outside diameter of 0.813 inch and a wall thickness of 0.094 inch. The support for the centre electrode

was a kovar-glass seal which incorporated a guard ring. After cleaning in an ultrasonic bath, the leakage resistance between the guard ring and the centre electrode was always greater than $5 \times 10^{13}\Omega$. The seal was soft soldered on to the back of the copper tube and at the same time a filling tube was soft soldered into the metal flange of the seal. The cathode was a length of solid, ground tungsten rod of 1mm diameter which was hard soldered on the tip and then soft soldered into the back seal. The assembled chambers were cleaned in nitric acid and then boiled in detergent. They were then scrubbed with steel wool, washed in distilled water and finally washed in acetone.

Both ion chamber and window were heated in an oven to a temperature of approximately $90^{\circ}C$ and the window then attached with the epoxy resin Araldite AV100. At the same time, a glass extension was joined on to the copper filling tube with epoxy resin, so that the ion chamber could be connected to the glass manifold of the filling system (Section 3.5.1).

3.2.2 Glass-Bodied Ion Chambers

Glass-bodied ion chambers were used in the HAD 309 and HAD 310 rocket flights described in Sections 4.3.5 and 4.3.6 respectively. Figure 3.3 shows a cross-sectional diagram of a typical glass-bodied chamber. The body consisted of a length of glass tubing, with an outside diameter of 19mm and a standard wall thickness, which was open at the front end and had a domed seal at the rear end. The front

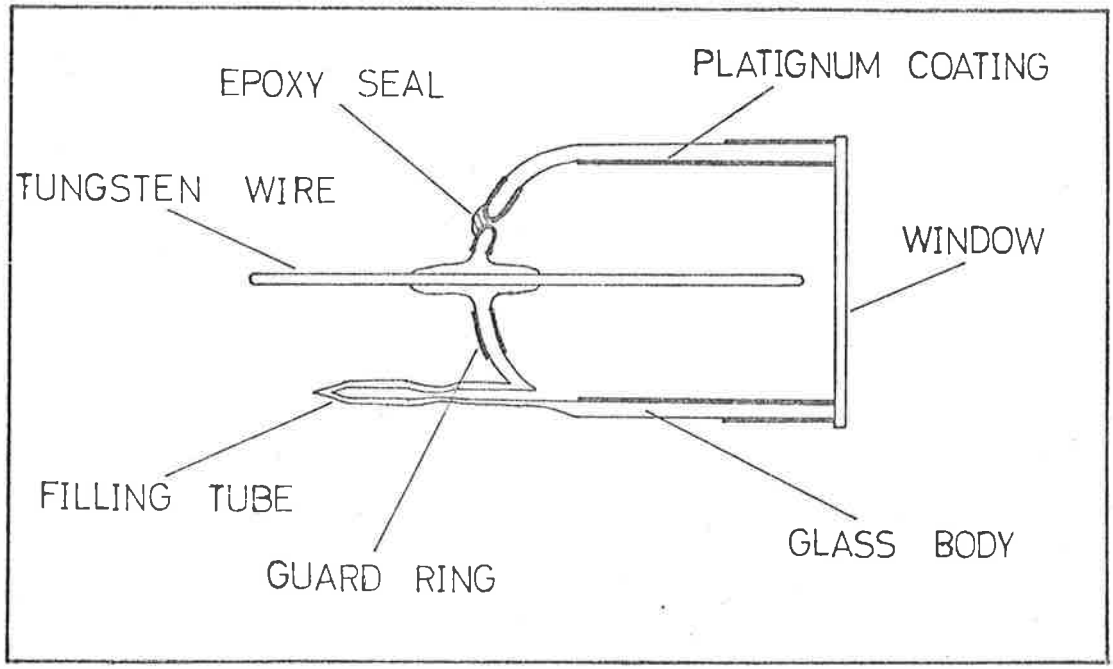

Fig. 3.3 A cross-sectional diagram of a glass-bodied ion chamber.

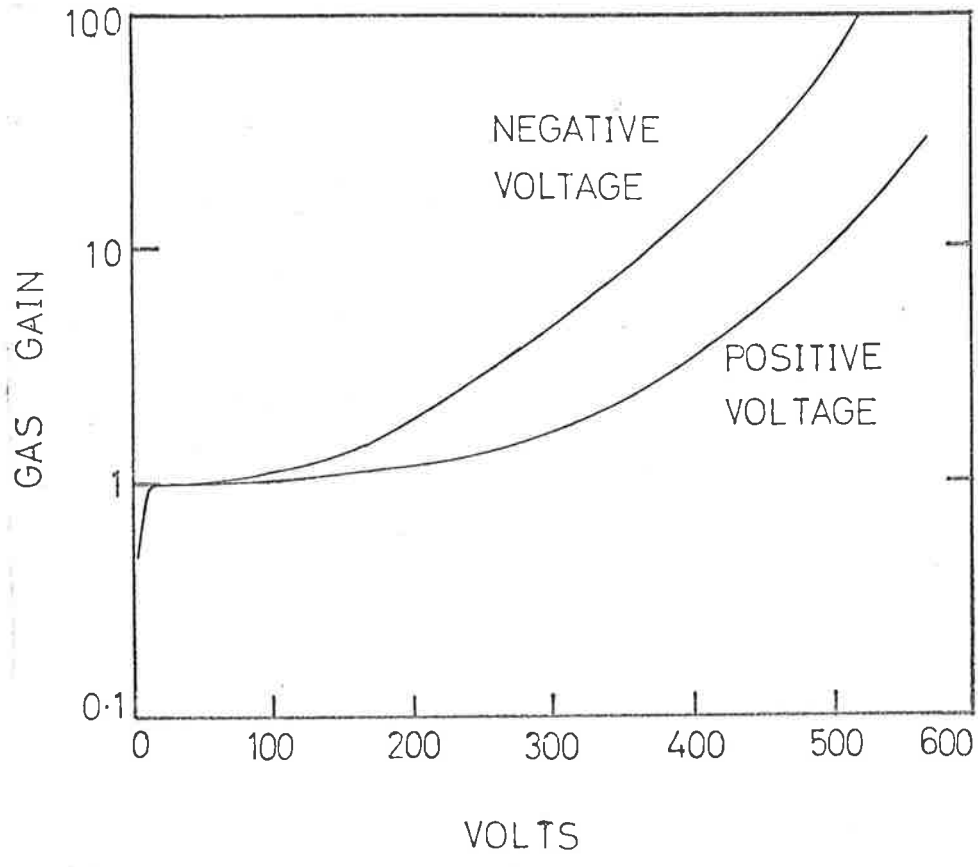

Fig. 3.4 Typical ion chamber gas-gain curves for negative and positive voltage applied to the chamber body.

surface was ground flat, and square to the tubing walls, on a lathe. A length of glass tubing with an outside diameter of 4mm was sealed into the rear of the chamber and served as an evacuating and filling tube. A glass to metal seal was made on a 1.25 inch length of solid ground tungsten rod of 1mm diameter and the rod was then sealed into the back of the chamber. The assembled chamber was cleaned in the same way as described above for the copper-bodied chambers.

To provide a second electrode, platinum was coated on the inside wall of a glass chamber in the following way. After the chamber had been cleaned, the inside wall, except for a small area around the centre electrode, was painted with Mathey Bright Platinum Solution. This coating was continued across the front face and on to the front ½ inch of the outside wall. The chamber was then gently heated inside and outside with a gas flame until a bright platinum surface became apparent. A second coat of platinum was applied in the same manner.

For those chambers requiring a higher leakage resistance a guard ring was incorporated. This was done by depositing a ring of platinum on the glass around the back seal of the centre electrode, on both the inside and outside walls, in the same way as described above. These two layers were then joined through a fine hole in the chamber wall which was later sealed with silver chloride and covered with epoxy resin.

The window was coated with platinum around the edge of the inside face and then sealed on to the body with silver chloride.

3.3 Window Materials

The properties of the window materials used in this work are listed in Table 3.1.

TABLE 3.1

WINDOW PROPERTIES

Material	Size	Transmission limit
Lithium fluoride	3/4 inch diameter x 3/4 mm thick	1035Å
Lithium fluoride	3/4 inch diameter x 1½ mm thick	1045Å
Sapphire	3/4 inch diameter x 0.02 inch thick	1415Å
Quartz	3/4 inch diameter x 0.063 inch thick	1545Å

The transmission limit, as given in Table 3.1, represents the shortest wavelength transmitted by the window. The lithium fluoride windows were unpolished, cleaved crystals, while the sapphire and quartz windows were polished plates. A highly refined variety of quartz known as Spectrosil A was used to obtain a transmission limit at a much shorter wavelength than the nominal 1800Å limit of naturally occurring quartz.

3.4 Baking the Lithium Fluoride Windows

Contamination by water vapour of a LiF-NO ion chamber could be easily detected by the appearance of absorption dips in its spectral response (Section 3.6.3). The contamination was found to be prevented by baking the window to a high temperature for a period of several hours before attaching it to the chamber. This generally produced a marked change in the transmission of the window. Figure 3.5 shows the transmission, as a function of wavelength, of a 1.5mm thick cleaved lithium fluoride window, both before and after baking for two hours at a temperature of 300°C in an electric oven. It can be seen that the transmission was improved at all wavelengths as a result of heating. This improvement was found to be permanent provided the window was kept in a dry atmosphere or under vacuum. Baked windows left exposed to the laboratory atmosphere deteriorated to their original condition over a period of three to four weeks. The conclusion is that when a lithium fluoride window is exposed to the atmosphere it takes up a surface layer of water. Baking the window drives off the layer and so the window transmission is improved. If the window is not baked before its attachment to a chamber, the water layer on the inner surface of the window subsequently out-gases into the nitric oxide and so reduces the quantum efficiency of the ion chamber at Lyman-α (Section 3.6.3). When filled (Section 3.5) LiF-NO ion chambers were stored in a desiccator to prevent the formation of a water layer on the outer surface of the window. Not only would such a layer lower the sensitivity of the ion chamber by

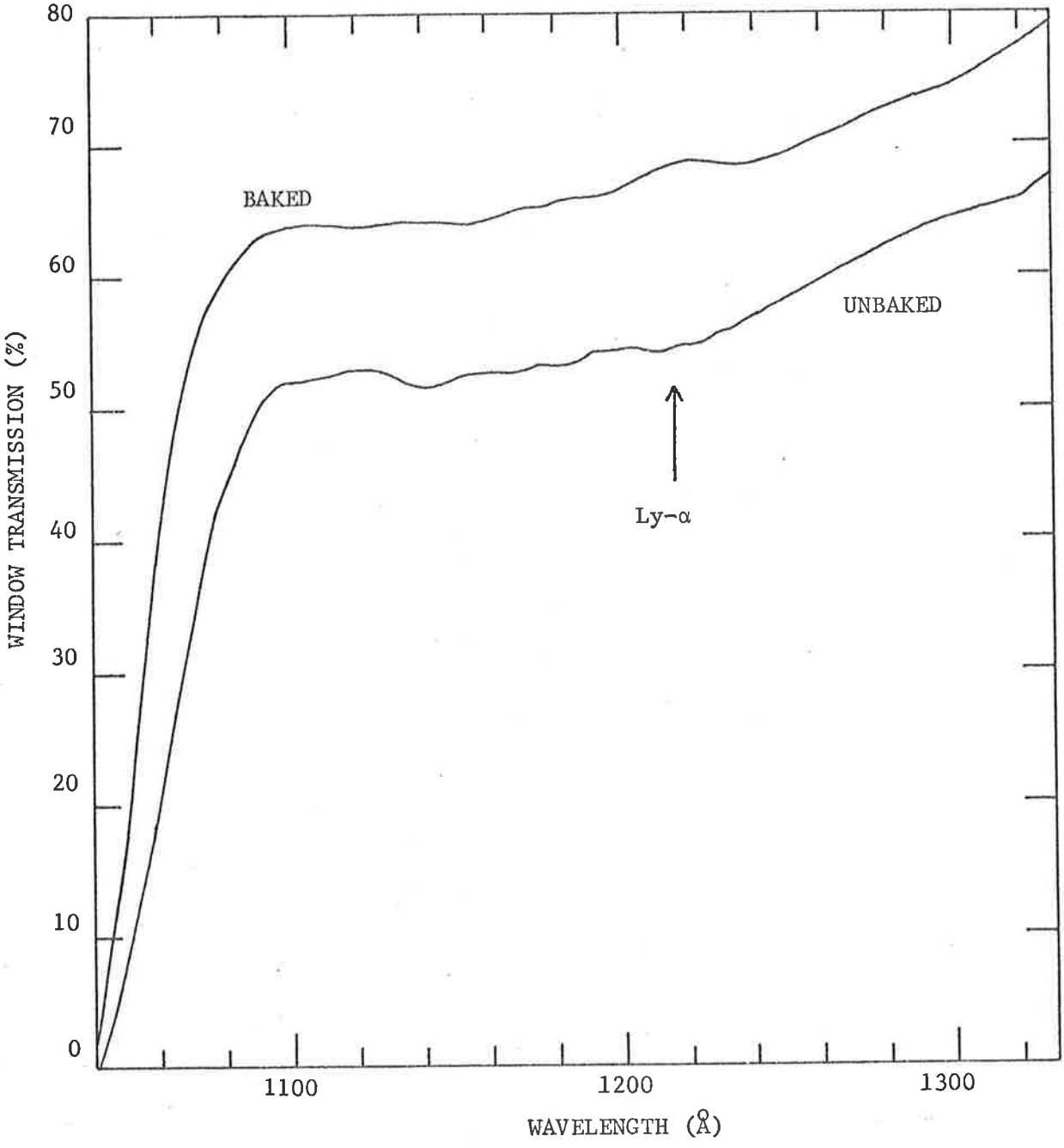

Fig. 3.5 The transmission of a lithium fluoride window as a function of wavelength, both before and after baking.

reducing its window transmission, but subsequent out-gassing of the layer during a rocket or satellite flight would cause its sensitivity to vary.

3.5 Filling the Ion Chambers

3.5.1 The Filling System

The glass filling system consisted of a manifold, mercury manometer, cold trap and sections to which pressure gauges, gas flasks and liquid containers could be attached. The manifold had several glass stems to which the glass filling tubes of the ion chambers could be easily joined. A 2 inch diffusion pump, backed by a rotary pump, was used to evacuate the detectors to pressures below 10^{-5} torr. The pressure was monitored by means of an ionization gauge mounted above the butterfly valve that isolated the diffusion pump from the glassware. The various sections of the glassware were separated by bakeable taps and the whole glass system, other than the mercury manometer, was enclosed in an asbestos-walled oven. Baking the system while evacuating the ion chambers resulted in a more complete removal of contaminants.

Table 3.2 lists the three different combinations of window material and filling gas employed in the ion chambers used in the present work. Also shown are the filling pressures of the gases and the spectral responses of the ion chambers.

TABLE 3.2

ION CHAMBERS

Window	Gas	Filling pressure	Spectral response
Lithium fluoride	Nitric oxide (NO)	15-20mm of Hg	1050-1350Å
Sapphire	p-Xylene (C_8H_{10})	4mm of Hg	1420-1480Å
Quartz	Triethylamine ($C_6H_{15}N$)	9.5mm of Hg	1550-1690Å

The ion chambers with sapphire windows and p-xylene filling gas will be referred to as S-X ion chambers, and those with quartz windows and triethylamine filling gas as Q-T ion chambers.

3.5.2 The Filling Procedure

The ion chambers to be filled were evacuated and maintained at a pressure less than 10^{-5} torr for several days. They were periodically heated to a temperature of approximately 90°C to assist in the removal of contaminants. Nitric oxide (purified as described in Section 3.5.3), which is a gas at room temperature, was introduced into the filling system from a 1 litre glass flask. A mercury manometer was used to ensure that the filling pressure was in the range of 15mm to 20mm of mercury. As the other gases were liquids at room temperature, they were introduced into the filling system from a small glass phial containing approximately 5 ml of liquid. The air in the phial was pumped away by the rotary pump, before the gas was

admitted into the manifold. The filling pressures of these gases were monitored by connecting a calibrated oil filled manometer to the filling system.

Chubb and Friedman (1955) have shown that pre-treatment of a chamber with an electronegative gas like nitric oxide increases the work function of the metal surfaces and so reduces photoemissive effects. For that reason, any chamber to be filled with p-xylene or triethylamine was first filled with nitric oxide, to a pressure of 30mm of mercury, and left for an hour. The nitric oxide was then pumped away and the required filling gas admitted.

Each glass ion chamber was removed from the filling system by sealing its filling tube with a gas flame, approximately six inches from the back of the chamber. This avoided the decrease in filling pressure that would occur during seal off, if the ion chamber was heated while still connected to the manifold. The filling tube was later sealed off closer to the back of the chamber.

Before removing a copper-bodied ion chamber, its copper filling tube was compressed in two places approximately ½ inch apart. A seal was then made between these compressions by cutting the filling tube with a pair of pincers. This formed a vacuum-tight cold weld provided the copper tubing had been well annealed. The seal was coated with epoxy resin to give it mechanical strength.

For maximum efficiency, the filling pressure should be high enough to ensure that the incident radiation is completely absorbed in the gas. Table 3.2 lists the filling pressures needed to ensure that most of the ultraviolet radiation entering the detectors is absorbed by the gas.

Figure 3.6 shows the three different types of glass and copper-bodied ion chambers after assembly and filling. The earlier type of copper-bodied ion chamber is shown with the back seal and leads potted in silicone rubber for protection. For mechanical protection and electrical isolation, the glass-bodied ion chambers are later potted in silicone rubber inside a copper holder suitable for mounting in the rocket.

3.5.3 The Purification of Nitric Oxide

Nitric oxide was obtained commercially in storage cylinders or prepared chemically in the laboratory. In either case, the impurities expected were the other oxides of nitrogen, water vapour and nitrogen. The technique used to remove these impurities was to pass the nitric oxide over silica gel cooled to $-80^{\circ}C$. Hughes (1961) has shown this to be as effective as twenty fractional distillations in removing all the impurities except nitrogen.

The nitric oxide container was connected to two U-tubes filled with silica gel which were in turn connected to a 1 litre glass flask fitted with taps. The U-tubes and the flask were then evacuated to a pressure less than 10^{-3} torr while being heated. This helped in the

Fig. 3.6 The three different types of ion chamber shown after assembly and filling. The earlier type of copper-bodied ion chamber is shown with the back seal and leads potted in silicone rubber for protection.

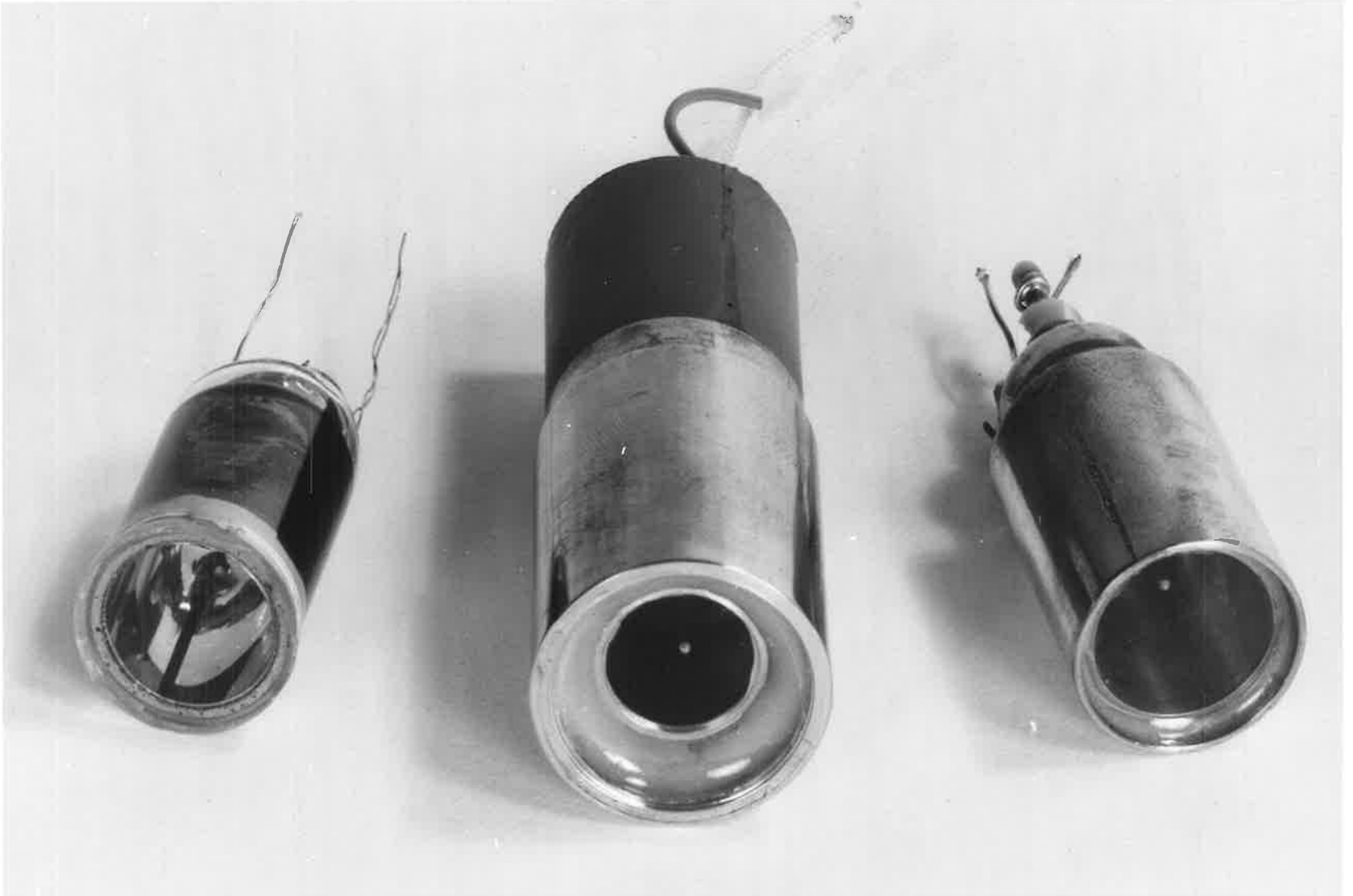

removal of water vapour and other gases that would contaminate the nitric oxide. The vacuum system was then closed off and the U-tubes surrounded by a 'slush' mixture consisting of 50% cloroform and 50% carbon tetrachloride partially solidified by the addition of liquid air. Nitric oxide was then allowed to flow slowly through the U-tubes until the pressure in the glass flask was approximately equal to the atmospheric pressure.

3.6 Absolute Calibration of the Ion Chambers

3.6.1 Introduction

Each ion chamber was calibrated by measuring its quantum efficiency* as a function of wavelength. The ion chambers used in this work were run at unity gas gain, that is with no gas multiplication, and so the quantum efficiency was given by the product of the window transmission, the fraction of the photons absorbed by the gas and the photoionization efficiency (Section 3.1) of the gas. Figure 3.4 shows typical gas gain curves for both positive and negative voltage applied to the chamber body. The applied voltage was always such that the detector operated in the 'plateau' region, between approximately 10V and 90V, where the current was almost independent of the voltage and the ion collection efficiency close to 100%. To minimize photoelectric

---

*The quantum efficiency of an ion chamber, at a given wavelength, is defined as the number of ions collected at the cathode, divided by the number of photons of that wavelength incident on the window.

effects (Section 3.9) the ion chambers were operated with positive voltage on the case.

The dispersed ultraviolet radiation used for the calibrations was obtained from an half metre McPherson vacuum monochromator. A grating with 1200 lines mm^{-1} gave a dispersion of 60μ $Å^{-1}$ at the exit slit. The intensity of the monochromator beam was monitored by means of a photomultiplier that viewed the fluorescent radiation from a sodium salicylate-coated wire grid placed in the beam (Ditchburn, 1962). The photomultiplier current was taken to be proportional to the beam intensity. The assumption made was that the intensity of the fluorescent radiation was independent of the incident wavelength. Watanabe and Inn (1953) and Allison et al. (1964) reported that the quantum yield (the number of fluorescent photons produced per incident photon) of sodium salicylate, in the range 1000Å to 1700Å was constant. However, Knapp and Smith (1964) and Samson (1964) have shown that a fresh layer has a constant quantum yield from 900Å to 1250Å with a rise of approximately 20% up to a maximum at approximately 1500Å. They have also shown that prolonged exposure to the atmosphere of a monochromator produces a slow decrease in quantum yield with the greatest effect occurring at short wavelengths. In this work, salicylate layers were always less than three days old, and so the quantum efficiency between 1050Å and 1700Å was assumed to be constant to at least ± 10%. No corrections were made for such variations.

3.6.2 Spectral Response

The experimental arrangement for determining the shape of the spectral response of an ion chamber is shown in Figure 3.7. Radiation from the exit slit of the monochromator passed through the salicylate-coated grid (0.5mm spacing) and entered the ion chamber which was electrically insulated from the monochromator. A voltage of + 30V was applied to the ion chamber body which meant that the ion chamber operated at unity gain. The fluorescent radiation from the sodium salicylate was transmitted to a type EMI 9514S photomultiplier by a polished perspex light pipe. New salicylate layers were deposited on the grid by placing it in a stream of warm air and spraying it with a saturated solution of sodium salicylate in methyl alcohol. Old layers were simply removed by washing the grid in water.

The currents from the ion chamber and photomultiplier were monitored on Keithley micro-microammeters, and the ratios of these currents, as a function of wavelength, gave the shape of the spectral response curve independent of the lamp spectrum. An absolute efficiency scale was derived for this curve as described in Section 3.6.3.

3.6.3 Absolute Quantum Efficiency

The quantum efficiency of a LiF-NO ion chamber was calculated at Lyman-α by comparing its ion current with that from a standard parallel plate ion chamber filled with nitric oxide and subjected to the same beam of radiation from the monochromator. The quantum efficiency of any other ion chamber was obtained by comparison with

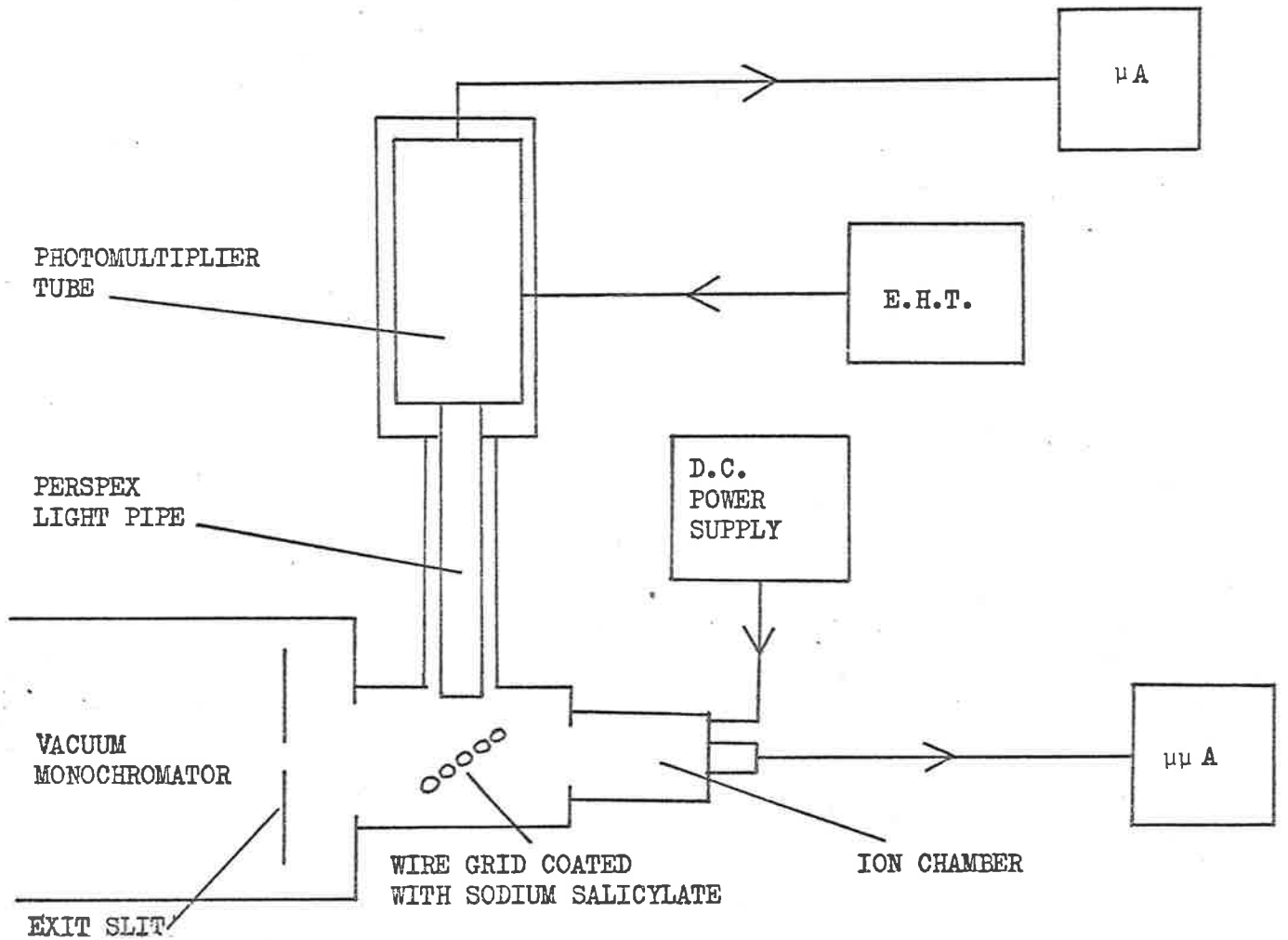

Fig. 3.7 Experimental arrangement for measuring the spectral response of an ion chamber.

Inclusion to Section 3.6

By moving windows with various short wavelength cut-offs in and out of the monochromator beam in the region between the monochromator exit slit and the salicylate coated grid (figure 3.7), the following facts were ascertained:-

(i) The percentage of the signal of photomultiplier P.M. 2 (figure 3.8) due to stray light was always less than ½% of the signal due to the main beam.

(ii) Almost all of the stray light was at wavelengths greater than those to which the ion chambers responded.

These facts show that the stray light produced by the monochromat had no significant effect on the calibration of the ion chambers.

the calibrated one. Nitric oxide was used in the standard ion chamber as its photoionization efficiency has been calculated to be 81% by Watanabe et al. (1967).

Figure 3.8 shows the standard ion chamber in position at the exit port of the monochromator. The lithium fluoride window was attached to a brass plate that was insulated from the monochromator. An adequate collecting field was provided for ions formed close to the window by electrically connecting the window mount to the positive plate of the standard ion chamber. Suppose that i_o is the ion current from the standard ion chamber (operated at unity gain) when all of the Lyman-α photons entering it are absorbed by the nitric oxide. Then, $i_o/0.81$ represents the ion current that would be produced by the standard ion chamber if all of the photons produced an ion-electron pair. If i_L is the ion current from a LiF-NO ion chamber subjected to the same beam of radiation as the standard ion chamber, then the quantum efficiency of the ion chamber at Lyman-α is given by:-

$$Q_L = \frac{0.81\ i_L}{i_o}$$

An absolute scale for the spectral response curve of any ion chamber (obtained as described in Section 3.6.2) was determined in the following way. The ion chamber was positioned on the monochromator, as shown in Figure 3.7. The photomultiplier current, I_λ, and the ion chamber current i_λ, were noted for any wavelength, λ, within the sensitive range of the detector. This ion chamber was then replaced

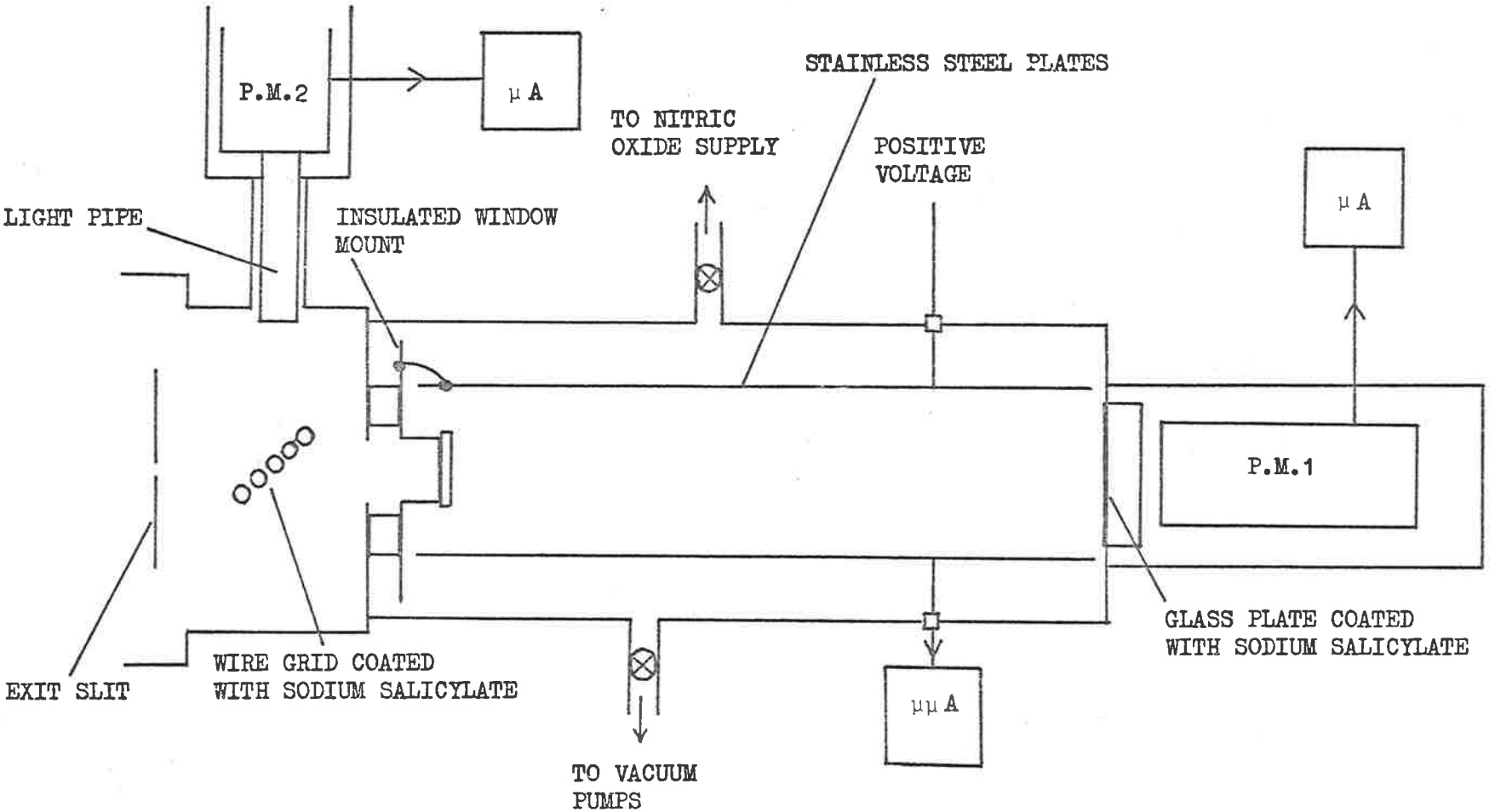

Fig. 3.8 Experimental arrangement for absolutely calibrating ion chambers.

with a LiF-NO ion chamber, calibrated at Lyman-α as described above, and the corresponding currents at Lyman-α, I_L and i_L, were noted. The quantum efficiency, of the uncalibrated ion chamber, at the wavelength λ, was then calculated from the expression:-

$$Q_\lambda = Q_L \times \frac{i_\lambda \, I_L}{i_L \, I_\lambda}$$

where Q_L is the quantum efficiency of the LiF-NO ion chamber at Lyman-α.

Figure 3.9 shows the spectral response curve of a typical LiF-NO ion chamber. The window of this chamber had been baked, as described in Section 3.4. The curve follows closely that obtained by multiplying the measured window transmission by the values of the photoionization efficiency of nitric oxide, as measured by Watanabe et al. (1967). Figure 3.10 shows the spectral response curve of a LiF-NO ion chamber contaminated by water vapour. As the window of this chamber was not baked, subsequent out-gassing of water vapour from the window into the nitric oxide (Section 3.4) has produced prominent absorption dips in the spectral response. The centres of the strong water vapour absorption bands between 1040Å and 1350Å are indicated in Figure 3.10 by small arrows. It can be seen that the wavelength of Lyman-α lies close to the centre of a strong water vapour absorption band (Figure 2.5). The degree of contamination of the nitric oxide was found to increase rapidly with increasing temperature. The rapid change in the quantum efficiency at Lyman-α that would therefore occur during a

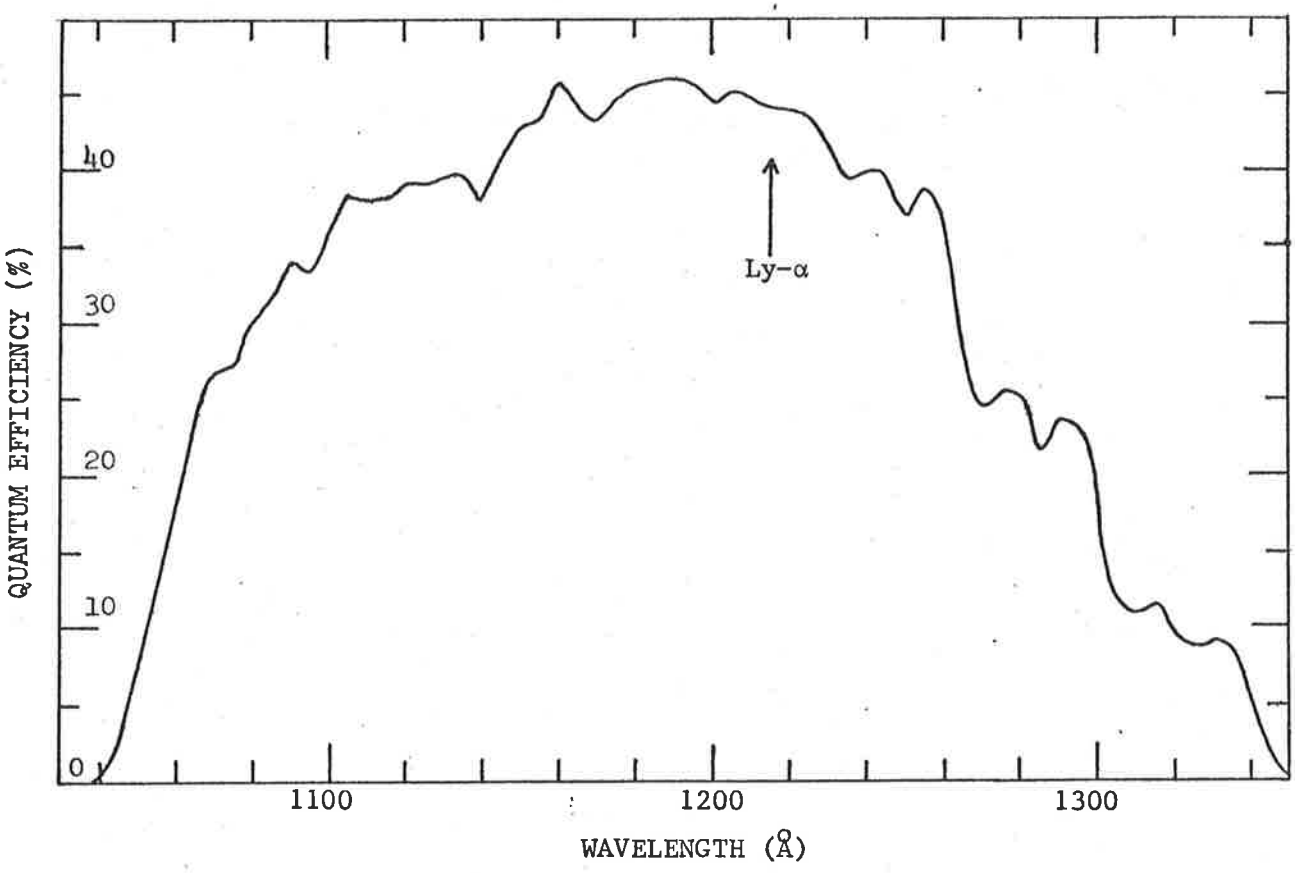

Fig. 3.9 Spectral response curve of an uncontaminated LiF-NO ion chamber

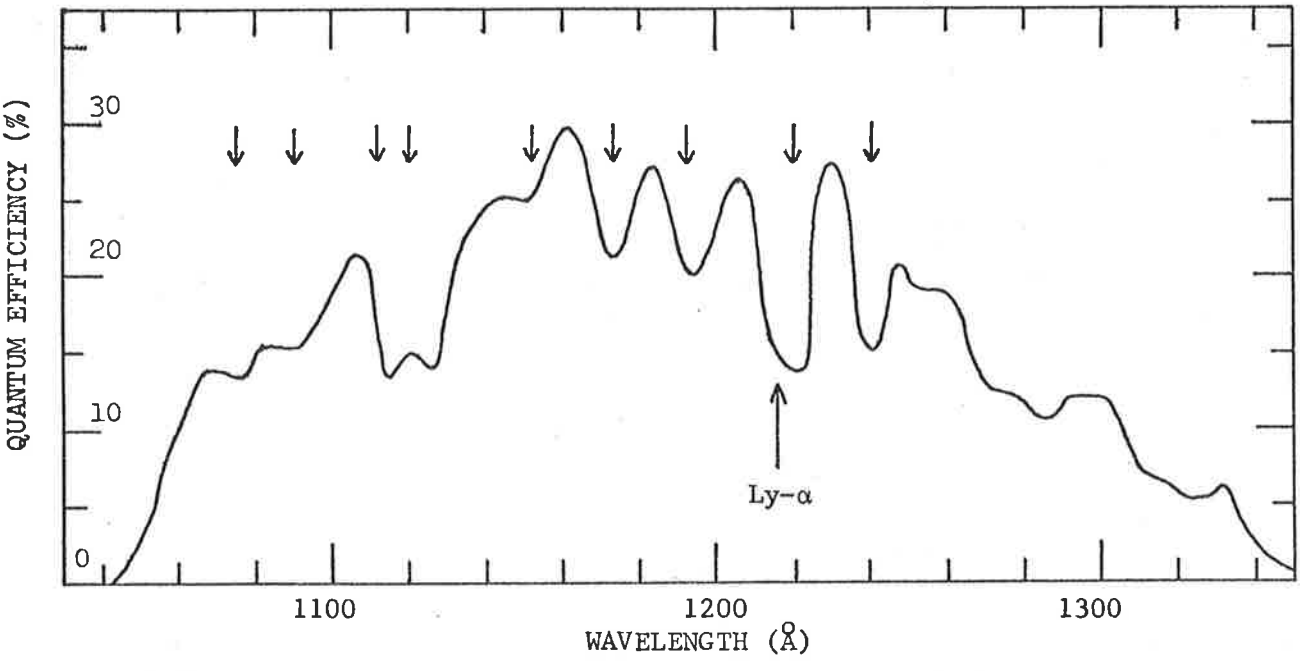

Fig. 3.10 Spectral response curve of a LiF-NO ion chamber contaminated by water vapour. The peaks of the strongest bands in the water vapour absorption spectrum (Fig. 2.5) are indicated by small arrows.

rocket flight, renders such an ion chamber useless.

For the LiF-NO ion chambers, the monochromator exit slit was set to give a resolution of 5Å and values of quantum efficiency were measured at 5Å intervals. For the S-X and Q-T ion chambers the beam resolution was set to 2Å and the quantum efficiency measured at 2Å intervals. Room temperature spectral response curves are shown for these chambers in Figure 3.11 and Figure 3.12 respectively.

3.7 Angular Response

When measuring the intensity of solar radiation with a rocket-borne ion chamber, corrections must be made to the ion chamber's output to allow for variations in the angle of incidence*, α, of the radiation. As an in-flight measurement of an ion chamber's angular response (Section 4.3.6) could not be relied upon, each detector was calibrated in the laboratory.

The ion chamber to be calibrated was mounted in a chamber on the end of a rotatable shaft that passed through an O-ring seal in the top of the chamber. The source of ultraviolet radiation was a portable hydrogen discharge lamp with a lithium fluoride window. A 100cm long glass tube mounted into the side of the chamber was used to provide a vacuum-tight connection between the chamber and the lamp.

---

*The angle of incidence is the angle between the normal to the detector's window and the direction of the sun.

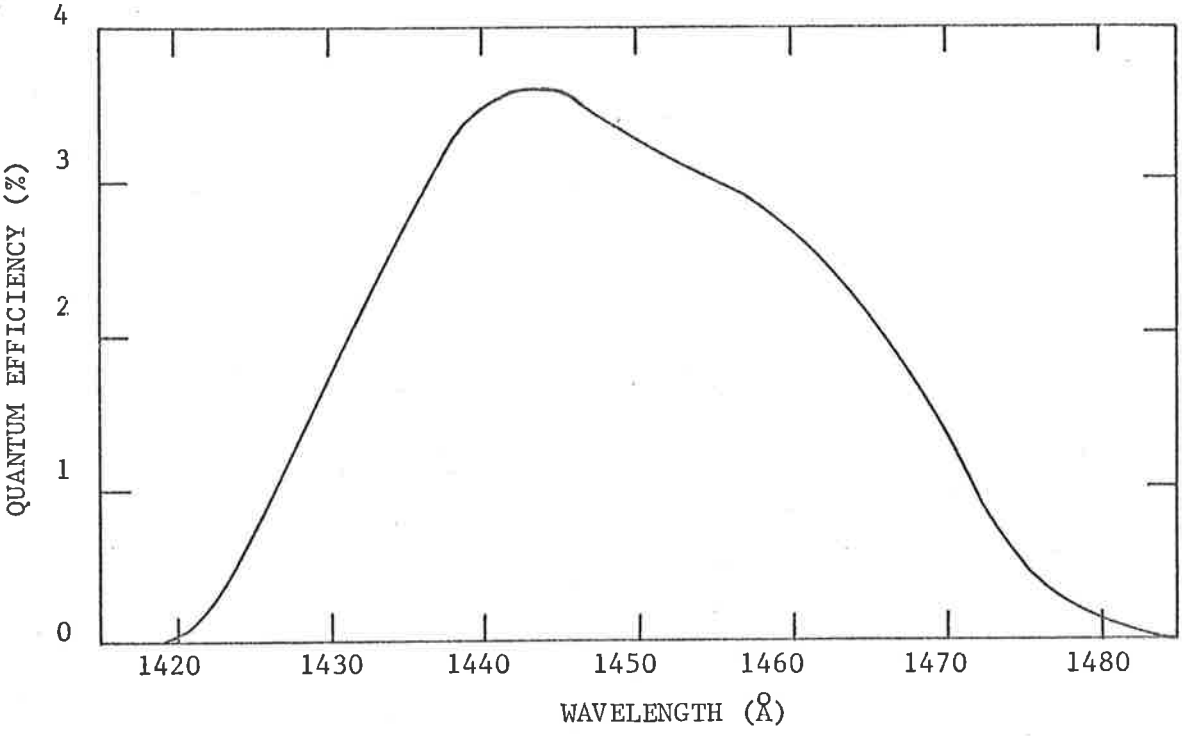

Fig. 3.11 Spectral response curve of a S-X ion chamber.

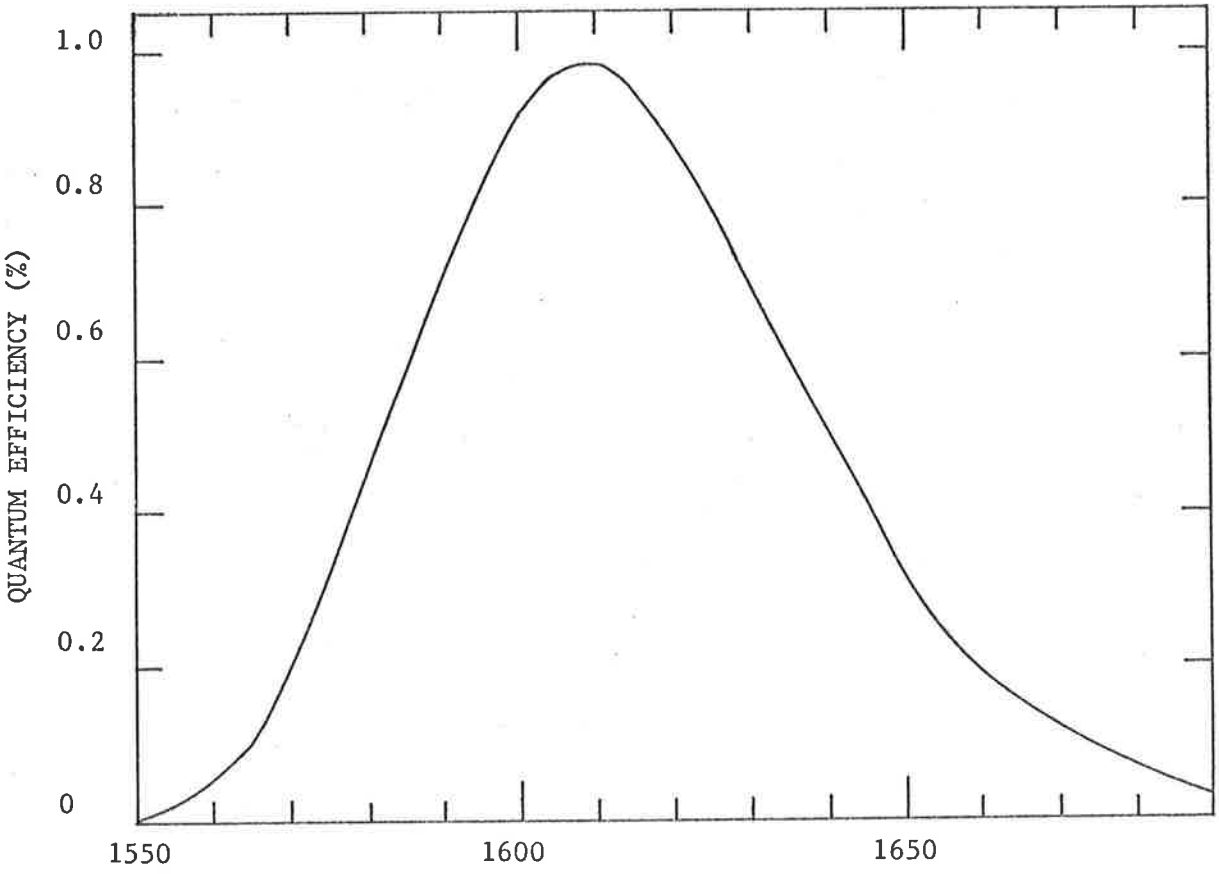

Fig. 3.12 Spectral response of a Q-T ion chamber.

Inclusion to Section 3.7

Fluctuations in the lamp output were checked by making a minimum of three consecutive angular response determinations for each ion chamber. The final angular response curve used was an average of these curves. The scatter of the individual points about the final smooth curve was always found to be within that expected from the other experimental uncertainties. Continuous monitoring of the lamp, by the use of a chart recorder to monitor the output of an ion chamber exposed to the lamp, revealed that short period fluctuations in lamp output were negligible. There was a gradual decrease in lamp output with significant changes occurring over a period of about an hour. This slow decrease had no effect on the angular response measurements. Typical errors on the individual points of an angular response curve such as that shown in figure 3.13 ranged from ±1% near normal incidence to ±3% for angles of incidence near 40°.

Inside the tube was a series of baffles designed to prevent reflections from the walls of the tube and to ensure that the radiation reaching the ion chamber was almost parallel. The chamber and the glass connecting tube were evacuated and the signal from the ion chamber monitored as it was rotated in the beam. Figure 3.13 shows a typical angular response curve.

As the angular divergence of the laboratory beam was not exactly the same as that from the sun, it was expected that the laboratory calibration would be slightly in error. However, a comparison between the laboratory angular response curves and in-flight curves taken during the HAD 310 flight (Section 4.3.6) showed that the differences were about 3% for angles near 40° and less than this for smaller angles. As corrections were not made for values of α greater than about 40° the laboratory calibrations were quite adequate.

3.8 Temperature Effects

The ion chambers used in rocket and satellite vehicles are subjected to a wide range of temperatures. Because of this, Carver and Mitchell (1967) investigated the effects of temperature variations from $15^{\circ}C$ to $100^{\circ}C$ on the sensitivities of several different types of ion chambers. They found that the main effect of an increase in temperature was a shift to longer wavelengths of both the short and long wavelength limits of the spectral range. In all cases the shifts in the short wavelength limit, due to variations in the window

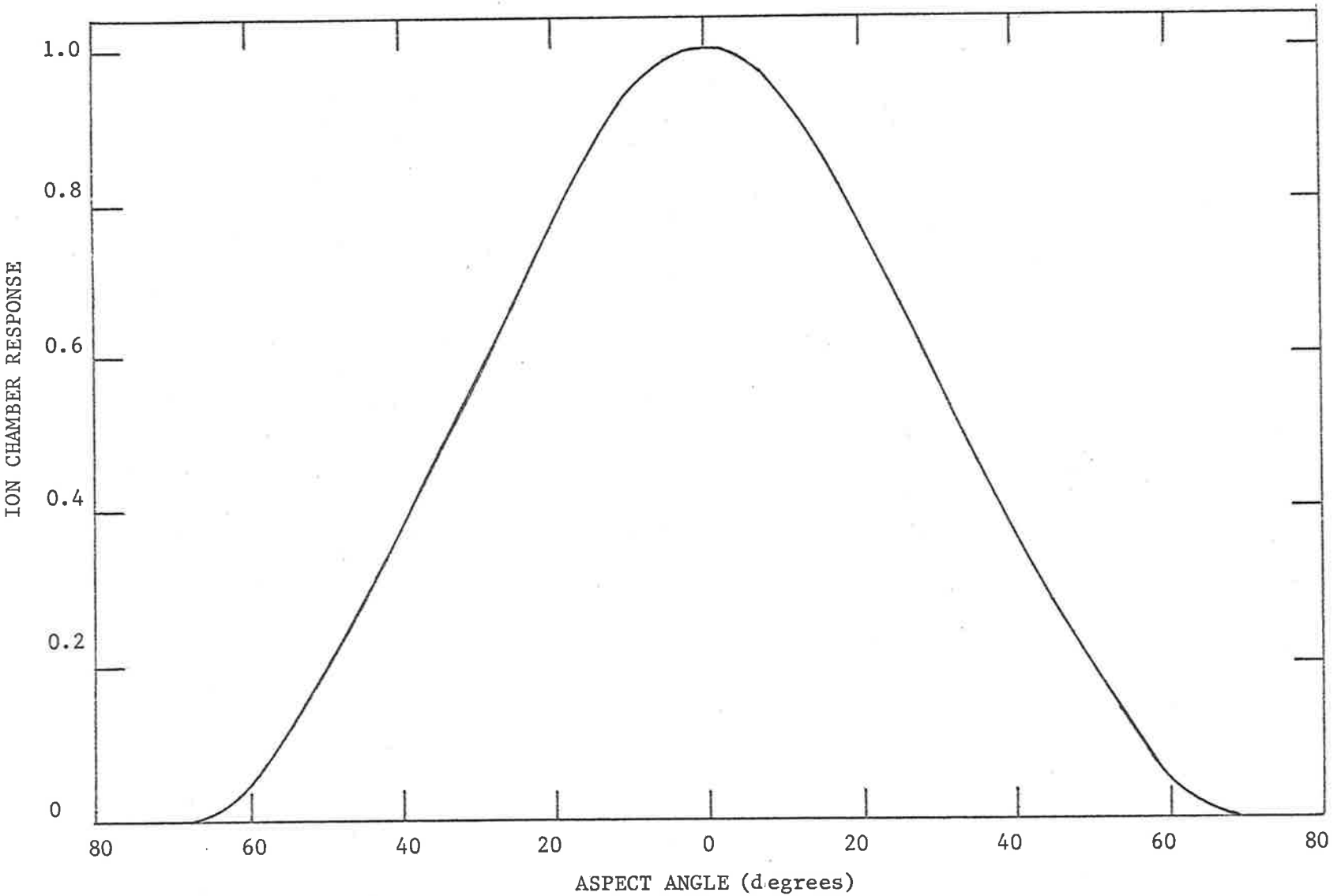

Fig. 3.13 A typical ion chamber angular response curve.

Inclusion to Section 3.8

To avoid contamination of the window, a thermistor was not attached to the window of the S-X ion chamber used in the experiment described. Initially however an old S-X ion chamber was tested with thermistors attached to both the window and the chamber body. The temperature difference indicated by the two thermistors fluctuated but never exceeded $2^{o}C$ over the temperature range $5^{o}C$ to $90^{o}C$. As the accuracy of the calibration of each thermistor was $\pm 1.5^{o}C$, it was concluded that no significant error would be produced by taking the window temperature to be that indicated by the thermistor attached to the chamber wall.

transmission, were larger than the shifts in the long wavelength limit caused by thermal excitation of the ground state gas molecules. The results of Carver and Mitchell (1967) show that while the sensitivity changes of the LiF-MO and Q-T ion chambers are small, S-X ion chambers can be expected to show significant changes in their sensitivity in the temperature range 15°C to 100°C.

To investigate the magnitude of the temperature induced sensitivity changes that could occur during a rocket flight, the spectral response of a S-X ion chamber was measured at several temperatures from 15°C to 87°C. The ion chamber to be tested was mounted at the exit port of the monochromator as shown in Figure 3.7, with the difference that a water-cooled brass mounting plate was included between the insulated ion chamber mount and the end of the monochromator. This plate prevented the conduction of heat to the monochromator and photomultiplier. A calibrated M53 thermistor was attached to the wall of the ion chamber. The ion chamber was then surrounded by a heating jacket and its spectral response measured, as described in Section 3.6.2, at several temperatures in the range 15°C to 87°C. After each increase in the current passing through the coil of the heating jacket, sufficient time was allowed for the temperature of the ion chamber to stabilize before the spectral response was measured. The ion chamber was finally allowed to cool down and its spectral response again measured at room temperature to ensure that no permanent change had occurred.

The spectral response curves obtained are shown in Figure 3.14, superimposed on the solar spectrum as given by Brinkman et al. (1966) (page 4). It can be seen that both the absolute quantum efficiency at the peak of the response, and the band-pass, change considerably above about 40°C. The peak sensitivity is shifted towards longer wavelengths as the temperature increases, being at 1445Å at 15°C and at 1460Å at 87°C.

The change with temperature of the output of a S-X ion chamber, directly viewing the sun above the earth's atmosphere, can be determined in the following way. Let $Q_{\lambda,T}$ represent the quantum efficiency of the ion chamber at the wavelength λ and for a temperature of T°C. Let ϕ_λ represent the number of photons sec^{-1} unit $wavelength^{-1}$ incident on the ion chamber's window at the wavelength λ. Then, if q is the electronic charge, and λ_1 and λ_2 are the wavelength limits of the spectral range, the ion chamber current is given by:-

$$i_T = q\int_{\lambda_1}^{\lambda_2} Q_{\lambda,T}\, \phi_\lambda \, d\lambda.$$

We may define the sensitivity of the ion chamber at the temperature T°C, S_T, by the expression:-

$$S_T = \frac{i_T}{F} \quad ,$$

where F represents the total radiant energy in the band-pass of the detector, incident on the detector's window per second. Hence,

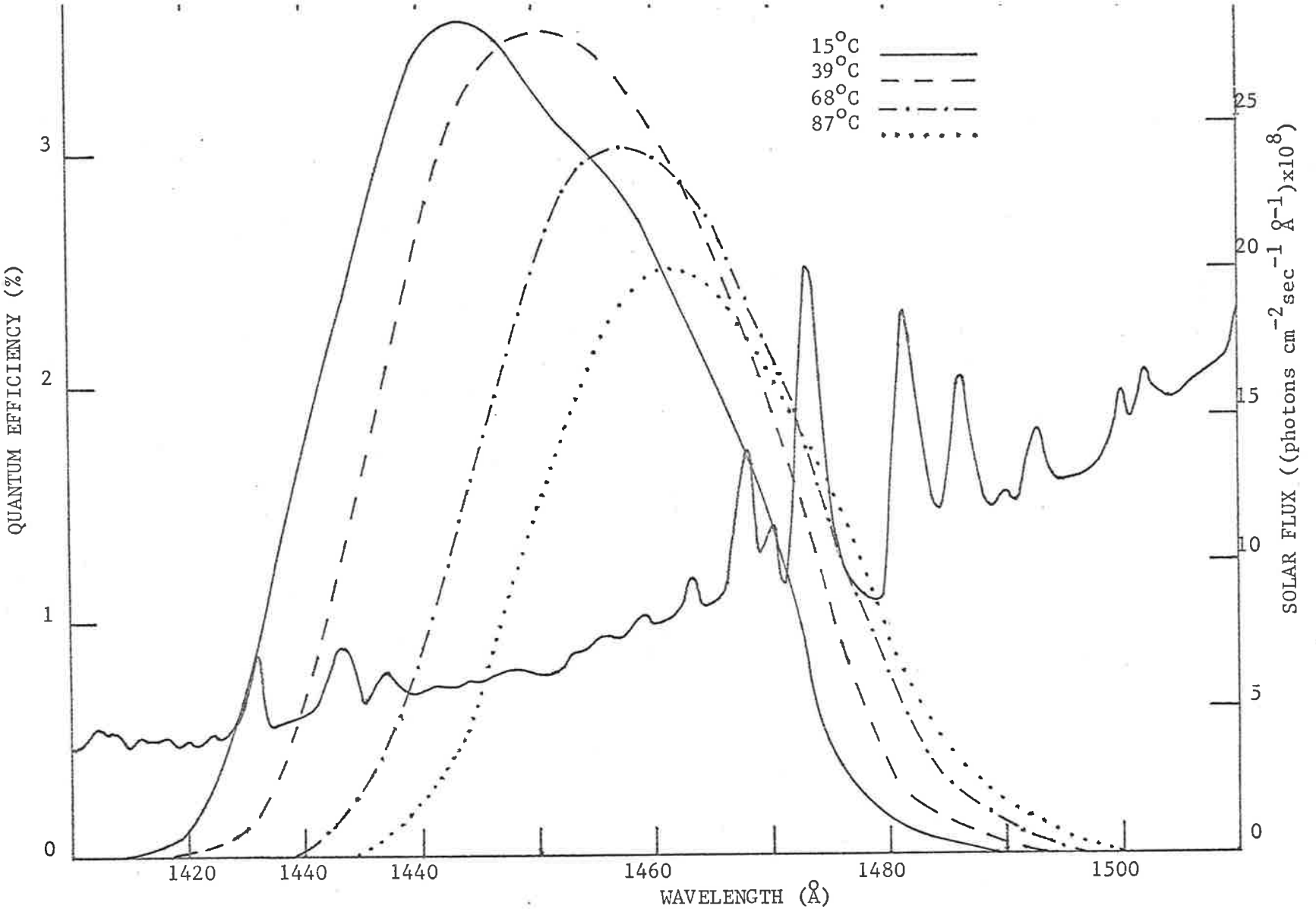

Fig. 3.14 Spectral response curves of a S-X ion chamber at various temperatures. Also shown is a plot of the digitalized solar spectrum given by Brinkman et al. (1966).

$$F = \int_{\lambda_1}^{\lambda_2} \phi_{\lambda,T} E_\lambda \, d\lambda$$

where E_λ is the energy per photon of wavelength λ. A list of values of S_T and the corresponding values of temperature is given in Table 3.3. The values of S_T have been normalized to 1 at 15°C.

TABLE 3.3

S-X TEMPERATURE SENSITIVITY

Sensitivity (S_T)	Temperature (°C)
1.00	15
0.97	39
0.80	68
0.68	87

In flights on unstabilized rocket vehicles such as the Long Tom, the ion chambers (which are mounted near the skin of the rocket to give a wide field of view) may reach temperatures in excess of 80°C.

It can be seen from the values given in Table 3.3 that under such circumstances the in-flight sensitivity will be much less than that measured in the laboratory at room temperature.

Figure 3.14 shows that the contribution to the ion chamber signal due to the emission lines between 1465Å and 1500Å, increases as the temperature is raised. This complicates any attempt to interpret the level of the solar continuum from the ion chamber signal (Section 5.6).

3.9 Long Wavelength Sensitivity

If the spectral response of an ion chamber is to have a sharp long wavelength cut-off, its response due to photoelectric emission from the cathode must be negligible. This is usually so, as the filling gas absorbes strongly at wavelengths greater than its photo-ionization threshold wavelength. Therefore, as the photoelectric yield of metal surfaces decreases rapidly with increasing wavelength, the radiation most efficient at producing photoelectrons is absorbed before it can reach the exposed surfaces. To reduce the possibility of long wavelength sensitivity even further, the ion chambers used in the present work were operated with the chamber walls as the anode. The centre electrode and back seal were then the only possible emitters of photoelectrons. In addition, before being filled, each ion chamber was pre-treated with nitric oxide to increase the work function of its metal surfaces (Section 3.5.2).

CHAPTER 4

ROCKET MEASUREMENTS OF MOLECULAR OXYGEN DENSITIES AND SOLAR VACUUM ULTRAVIOLET RADIATION

4.1 Introduction

Five rocket vehicles were instrumented with ion chambers of the types described in Chapter 3. Each experiment had two objectives:-

(i) the measurement of molecular oxygen density profiles by the technique of absorption spectroscopy described in Section 2.3, and

(ii) the measurement of the intensity of solar radiation in one or more wavelength bands in the range 1050Å to 1680Å.

The Skylark rocket, SL 781, was instrumented with LiF-NO, S-X and Q-T ion chambers. However, no useful information was obtained as the rocket failed to reach an altitude at which solar ultraviolet radiation could be detected. This experiment is described briefly in Section 4.2.

Three HAD rockets were used to carry LiF-NO ion chambers to heights in excess of 70 Km. The experiments flown in the vehicles designated HAD 309 and HAD 310 were successful and are described in detail in Section 4.3. The third of these rockets, HAD 311, failed to reach an altitude of 70 Km and so no useful data were obtained.

The Cockatoo rocket, COCK 113, was used to carry an experiment identical to that flown in the HAD rockets. Due to the very large aspect angles, which resulted from excessive precession of the rocket roll axis, the data was not reduced.

4.2 The Skylark Experiment

A section of the Skylark rocket, SL 781, was instrumented with nine ion chambers which were mounted in three banks such that their look directions were normal to the rocket roll axis. Each detector bank consisted of a LiF-NO, a S-X and a Q-T ion chamber as well as aspect sensors of the type described in Section 4.3.3(c). The ion chambers were a mixture of the copper-bodied type flown previously by Carver et al. (1969) (Figure 3.1) and the more recent glass-bodied type shown in Figure 3.3.

The main objectives of this experiment were to measure the vertical distribution of molecular oxygen in the height range 70 Km to 150 Km and to measure the intensity of solar radiation both at Lyman-α and in the wavelength bands 1420Å to 1480Å and 1550Å to 1690Å. The radiation intensity in these bands has importance in establishing the value of the solar minimum temperature (Section 1.2).

As explained in Section 2.1, in the height range 70 Km to 150 Km, much more information is required on the variations of the molecular oxygen distribution with season, latitude and time of day. This is

especially true above about 90 Km where the dissociation of molecular oxygen into atomic oxygen is significant. It was hoped that useful comparisons would be made between the results of this experiment and those from the WRESAT satellite (Chapter 5) and the Long Tom rocket experiment of Carver et al. (1969).

Skylark SL 781 was launched from Woomera at 1355 hours local time* on January 21st, 1969. Due to the premature activation of the head release mechanism, the vehicle failed to reach an altitude at which useful data could be obtained.

4.3 The HAD Experiments

4.3.1 The HAD Rocket

The HAD (High Altitude Density) rocket was developed by the Flight Projects Group of the Weapons Research Establishment, Department of Supply. It is a two stage vehicle with solid fuel motors and when fully instrumented it can reach an apogee height in excess of 90 Km.

HAD rockets were used to carry LiF-NO ion chambers to heights in excess of 70 Km, to enable measurements to be made of the atmospheric absorption of Lyman-α radiation. As explained in Section 2.3 such measurements can be used to determine the vertical distribution of molecular oxygen. Below about 90 Km, where molecular dissociation is small and the major atmospheric constituents are well mixed, the vertical distribution of molecular oxygen can be inferred from

---

*Local time = Greenwich Mean Time + 0906 hours.

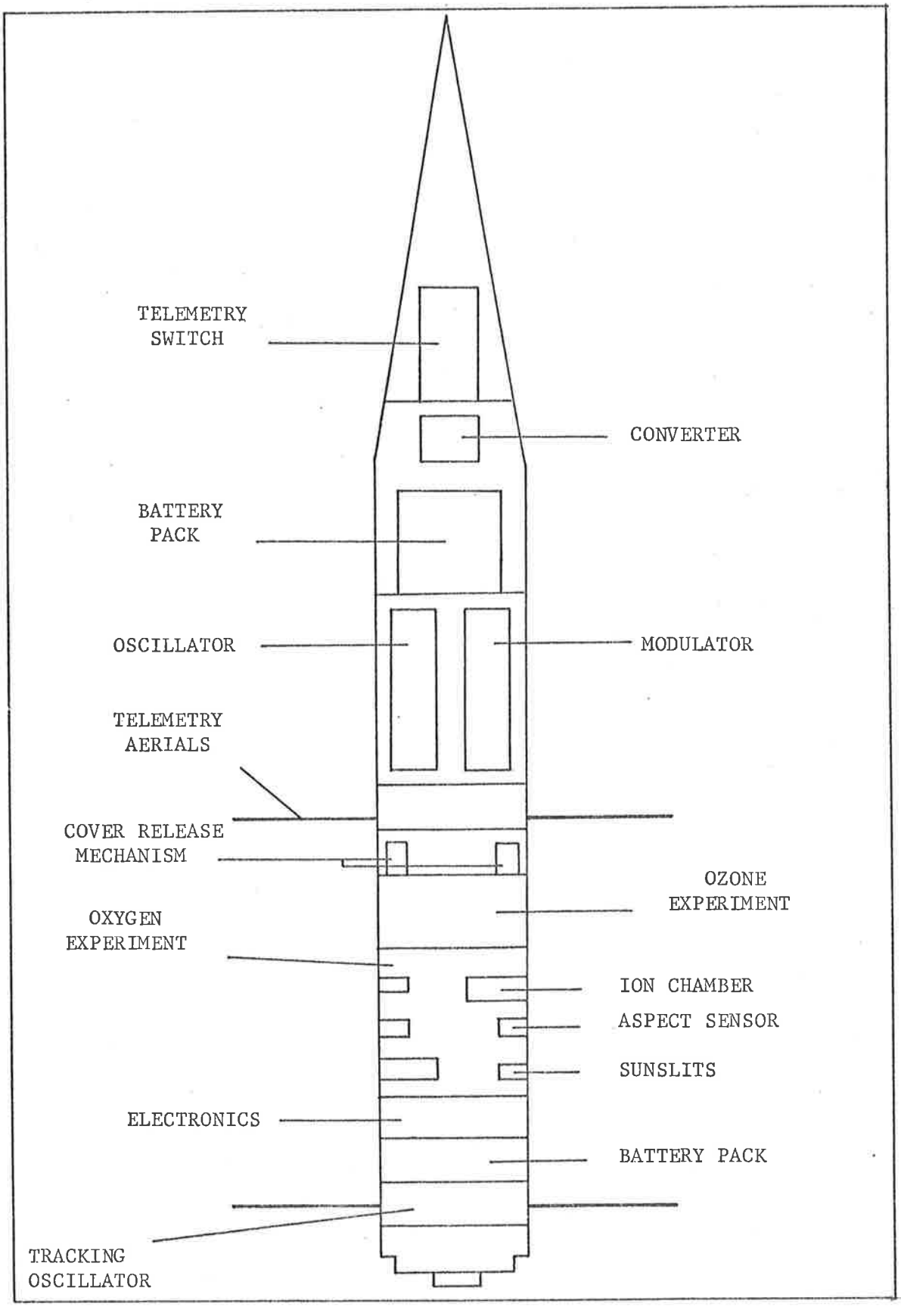

Fig. 4.1 Instrumentation layout of the HAD rocket head.

measurements of the total neutral atmosphere. However, direct measurements of molecular oxygen in this region are valuable, if only as indicators of the total atmospheric density.

An attempt was made to investigate seasonal variations of the molecular oxygen distribution, in the height range 70 Km to 100 Km, by flying LiF-NO ion chambers at different times of the year. However, only two of the HAD flights (the results of which are given in Section 4.4) were successful. The results of these experiments are discussed in Section 6.2.1 in relation to similar measurements made by other workers.

4.3.2 Instrumentation Layout of the Rocket Head

Space for instrumentation is provided in the HAD rocket in the forward section of the second stage which has a diameter of 5 inch and a length, including the nosecone, of 48 inch. The distribution of the payload in the rocket head is shown in Figure 4.1, while Figure 4.2 shows the various sections of the head prior to its assembly.

As can be seen from Figure 4.1, the detectors, and their associated electronics, were contained in the section of the rocket immediately below the telemetry aerials. The section above the aerials, including the nosecone, housed the telemetry equipment. An "ackaid" oscillator, used to assist the radar in tracking the rocket, was mounted below the experiment section.

Signals from the detectors (0V to 1.5V) were fed to a 24 pin

Fig. 4.2 A view of the various sections of the HAD head prior to its assembly. The section on the far right housed the telemetry equipment and was later mounted inside the nosecone section of the skin shown on the far left. The radiation detectors and their associated electronics were housed in the section second from the right which was later mounted inside the section of black anodized skin shown second from the left.

rotating switch, the wiper arm of which rotated at about 80 rev/sec. The voltages on the wiper arm were fed to a voltage controlled oscillator, the frequency modulated output of which was used to amplitude modulate a 465 MHz carrier wave. The telemetry signals were received at the ground and recorded on magnetic tape.

The detectors were arranged in two banks which were mounted on opposite sides of the rocket. The look direction of the detectors in each bank was normal to the rocket roll axis. Each bank contained a glass-bodied LiF-NO ion chamber (Figure 3.3) which was potted in silicone rubber inside a copper holder suitable for mounting in the rocket. The potting material mechanically protected the ion chamber and also electrically isolated it from the rocket, enabling the required voltage to be applied to the chamber body. In addition to an ion chamber, each detector bank contained sunslits and an amplitude ratio aspect sensor. These detectors, which are described in Section 4.3.3, were needed to determine the solar aspect angle.

The current from each ion chamber was fed through a 10MΩ resistor connected between the input of a linear amplifier and ground. The gain of the amplifier, the circuit of which is shown in Figure 4.3, could be varied between 1 and 10 to allow for variations in the quantum efficiencies of the ion chambers. The input of the amplifier was a dual p-channel MOS field effect transistor which gave an input impedance of greater than $10^{16}\Omega$. The maximum amplifier temperature recorded in the HAD flights was $60^{o}C$. In the laboratory, the change

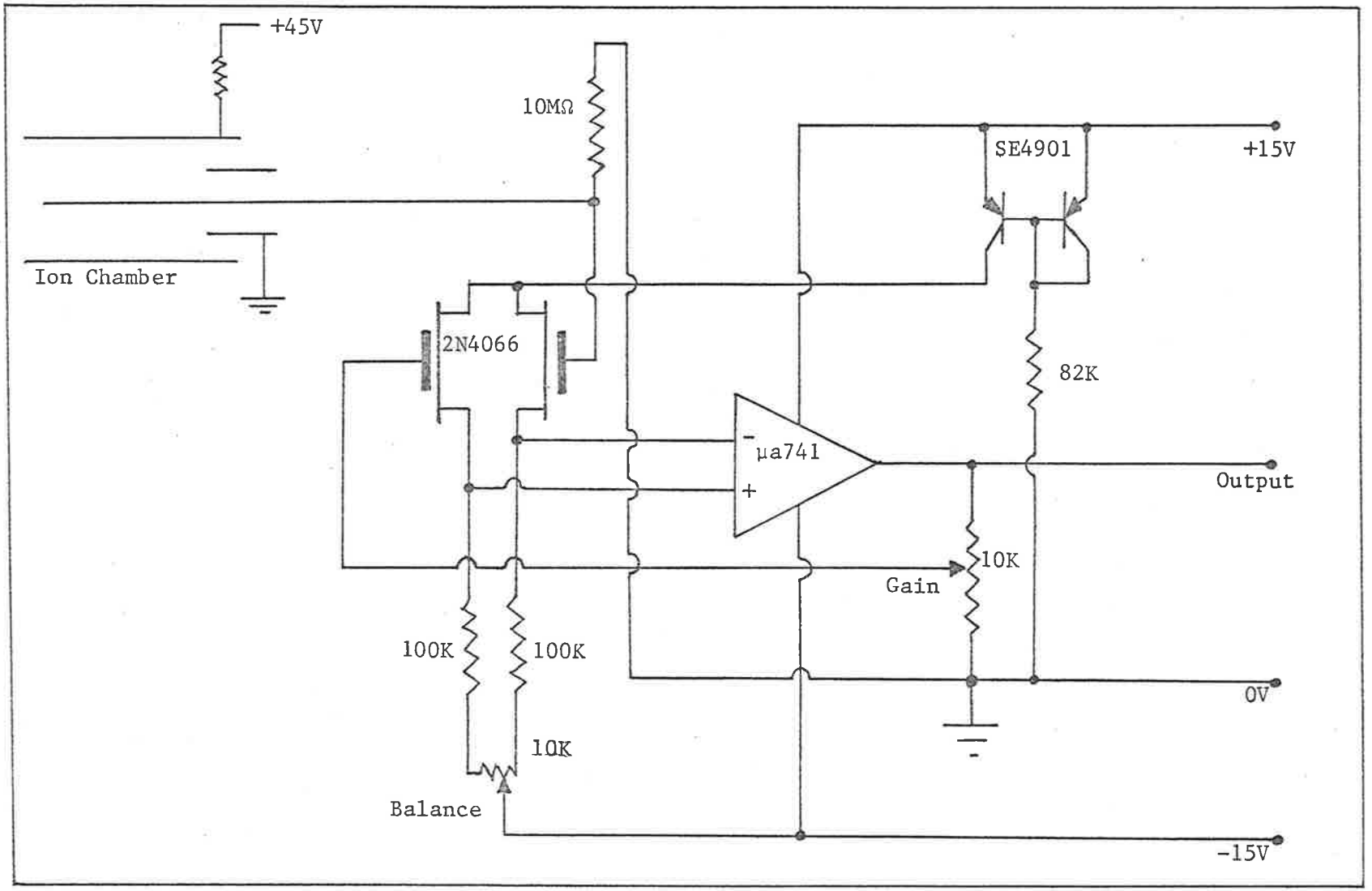

Fig. 4.3 The circuit of the ion chamber linear amplifier used in the HAD experiments.

in the zero level of an amplifier, when heated from room temperature to 60°C, was always found to be less than 15 mV (which represents 1% of the telemetry range).

4.3.3 Solar Aspect Sensors

(a) The solar aspect angle.

The aspect angle of an ion chamber is defined as the angle between its look direction and the direction of the incident radiation. Since the output of an ion chamber changes as the aspect angle varies (Section 3.7), it is essential to know the solar aspect angle during a rocket flight. This allows the signal to be corrected to what it would have been if the ion chamber had been pointing directly at the sun.

Usually, the roll rate is greater than the rate at which the roll axis changes its orientation in space, and so an ion chamber will show one peak in its output for each roll of the rocket. The peak value occurs when the solar aspect angle is a minimum and it is this angle, termed the rocket aspect angle, α, which must be measured. For an ion chamber with a look direction normal to the rocket roll axis, α is the complement of the angle between the roll axis and the direction of the sun.

The two different types of aspect sensor flown with each ion chamber are described below.

(b) Sunslits.

One of the aspect sensors flown on the HAD rockets was a modification of the sunslits used in Skylark rockets and described by Gross and Heddle (1964). Sunslits only respond when the sun crosses one of several planes fixed relative to the rocket body. The solar aspect angle is deduced from the time interval between the pulses produced in this way. In the HAD sunslits, these planes were defined by three slits, 0.3mm wide, cut in an aluminium hemisphere (inset Figure 4.4). One plane contained the rocket roll axis while the other two made an angle of 45^{o} with the roll axis (Figure 4.4). The three planes intersected along a line that was perpendicular to the rocket roll axis and passed through the centre of the detector. The light detector was a small silicon photovoltaic cell (Mullard type BPY 10) which was mounted behind a pinhole fixed at the centre of curvature of the aluminium hemisphere.

In Figure 4.4, which illustrates the operation of the sunslits, β represents the angle between the planes of the sunslits ($\beta = 45^{o}$ in this case) and α is the rocket aspect angle. It is assumed that the ion chamber is pointing in the same direction as the sunslits. If the rocket rolls through an angle γ, in the time interval between two pulses from the sunslits, then the angle α is given by

$$\tan\alpha = \sin\gamma \cot\beta = \sin\gamma$$

Therefore, by measuring the roll rate and the time between successive pulses from the sunslits, γ and hence α can be determined.

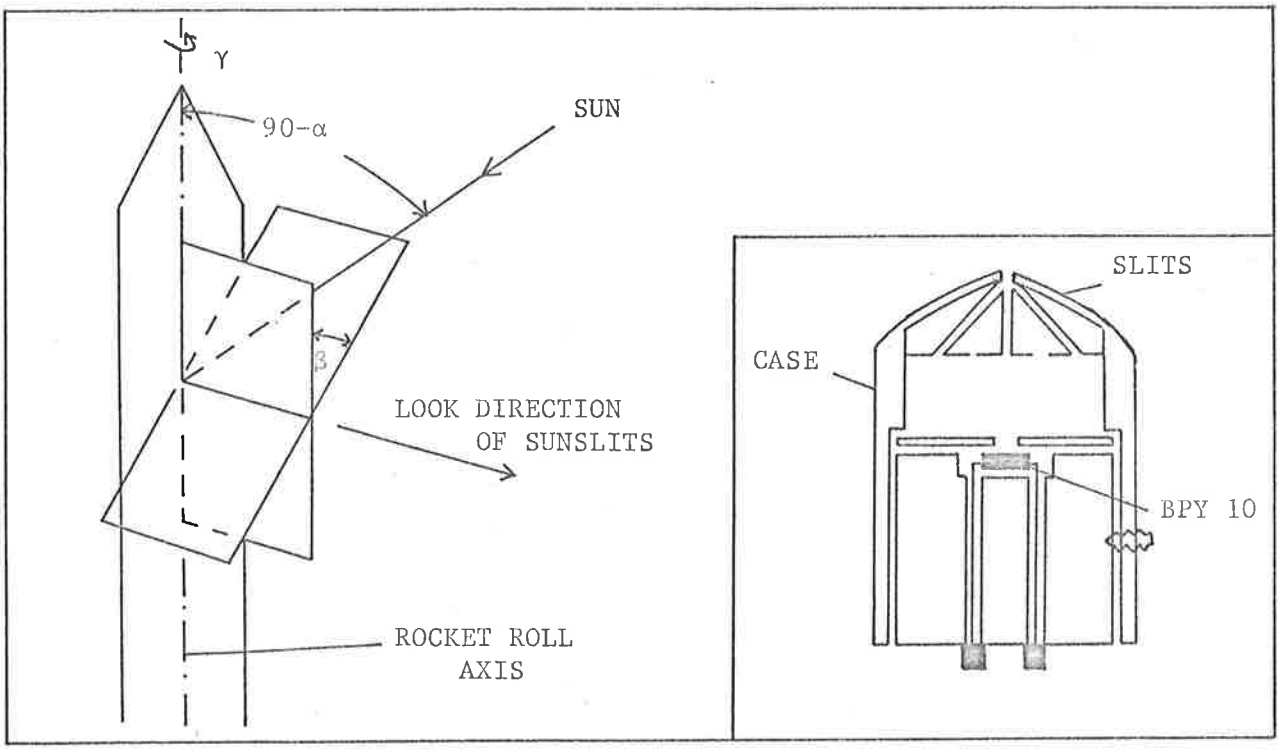

Fig. 4.4 Diagram illustrating the operation of the sunslits. The inset shows a cross-sectional diagram of a typical sensor.

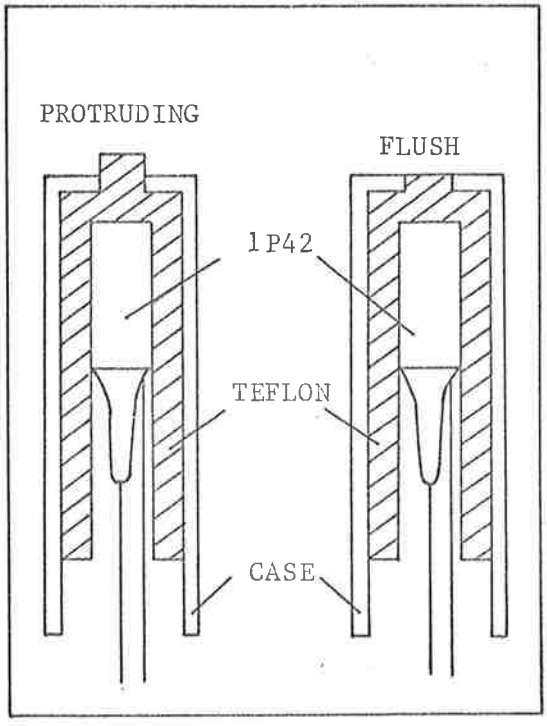

Fig. 4.5 Cross-sectional diagram of an amplitude ratio aspect sensor pair.

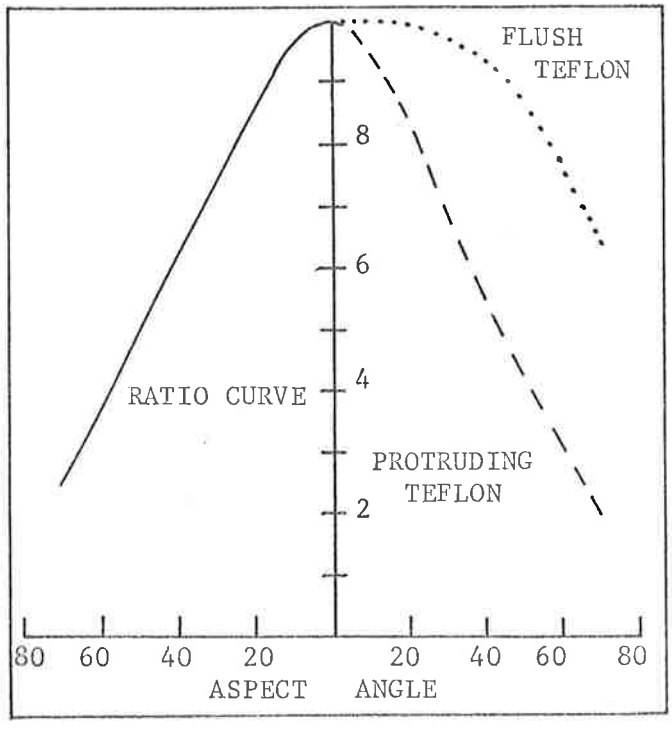

Fig. 4.6 Laboratory angular response curves for an amplitude ratio aspect sensor pair.

Each set of sunslits was calibrated by rotating it in front of a mercury-iodide lamp placed behind an aperture. The distance between the aperture and the sunslits was adjusted so that the aperture subtended an angle at the sensor equal to the angular diameter of the sun. The above relationship was found to hold for aspect angles up to about 40°. At greater angles no signal was obtained through the 45° slits.

If the roll axis of the rocket does not coincide with its longitudinal axis, or if the roll axis changes its position in space significantly during the time interval between the pulses from the 45° slits, then the above relationship will not hold. This type of rocket behaviour is made obvious by the use of three slits, as under these conditions the three pulses will not be evenly spaced. Sunslits may also become useless when the rocket roll rate is too fast. For example, if the roll rate of the rocket is 2 cps then, as the HAD telemetry rate is about 80 samples sec^{-1}, the error in determining the angular separation of the two 45° slits is $\pm 4.5^{\circ}$. The error in γ is therefore $\pm 2.25^{\circ}$ which may lead to an error in α that would cause serious errors in the corrected ion chamber signal. In all of the HAD flights, two telemetry channels were allocated to each sunslit thus giving an effective sampling rate of about 160 samples sec^{-1}.

(c) Amplitude ratio aspect sensor

The second type of aspect sensor used was a modification of the aspect sensor designed by Mitchell (1966). Two light detectors, with

different angular responses, were needed for each aspect sensor. Each detector consisted of a small vacuum phototube (RCA type 1P42) surrounded by a teflon insert inside an aluminium holder. As shown in Figure 4.5, the teflon insert was flush with the front face of the aluminium holder for one detector and protruded past the front face for the other. As the teflon acted as a diffuser, the response of each detector depended mainly on the effective area of the exposed teflon. This resulted in an almost flat response for the detector with the protruding teflon piece, while the flush teflon piece resulted in a response strongly peaked in the forward direction (Figure 4.6). A 0.1 inch deep hole of 0.014 inch diameter was drilled down the centre of the flush teflon piece to enhance the peaked nature of the response. As the spectral responses of the two detectors were the same, and as they responded to the same intensity of light, the ratio of their outputs was a unique function of the aspect angle and was independent of the light intensity. The aspect sensor was mounted in the rocket so that the detector pair pointed in the same direction as the ion chamber.

The angular response of each detector was measured in the laboratory by rotating it in front of a xenon lamp. The lamp was placed behind an aperture and the distance between the aperture and the detector adjusted until the aperture subtended an angle at the detector equal to the angular diameter of the sun.

The output signal from each detector was obtained by connecting

the 1P42 and a variable resistor, R, in series with a +45V supply. The voltage developed across R was then taken to the telemetry switch. The absolute level of each detector was adjusted prior to launch by pointing the aspect sensor directly at the sun and then varying the value of R until the output voltage was +1V. This ensured that the telemetry limit of + 1.5V would not be exceeded during the flight when the detector was exposed to unattenuated solar radiation. Once the absolute level of each detector had been set, the angular response curves were normalized and the ratio of the detector outputs plotted as a function of aspect angle (Figure 4.6). This calibration curve was independent of the light intensity and so aspect angles could be derived in flight, even in regions where considerable scattering and absorption of solar visible light occurred.

In the original aspect sensor designed by Mitchell (1966), the light detectors were silicon photodiodes (Phillips type LS 400), the outputs of which were very temperature dependent. In the present work, it was found to be difficult to obtain pairs of these photodiodes with exactly the same temperature response and so it was decided to replace them with 1P42 vacuum phototubes. This latter detector is insensitive to temperature variations in the range 15^{o}C to 90^{o}C.

The LS 400 has a wavelength response that peaks at 9800Å. Each detector has a wide field of view and so it is possible for it to respond to light reflected and scattered from the earth and clouds (earthshine), as well as the direct solar radiation. This results

in a varying background level that has to be considered when determining the output of each detector. Mitchell (1966) has reported a maximum signal due to earthshine that was 10% of the signal due to the direct sun. To minimize the effect of earthshine, the detector should be sensitive to the wavelength region where the ratio of the intensity of the earthshine to the intensity of the direct solar radiation is a minimum. The spectral distribution of the earthshine is not accurately known however, so it is not possible to say where this region is. It was hoped that as the 1P42 has a different spectral response (peak response at 4700Å) to the LS 400, the earthshine signal would be less. However, on the HAD 310 flight (Section 4.3.6) the maximum background level due to earthshine was again nearly 10% of the direct sun signal.

(d) Summary.

Two types of aspect sensor were flown with each ion chamber. Sunslits are the preferred method of determining aspect angles due to their ease of calibration and the fact that response to earthshine does not affect the aspect angle determinations. However, as sunslits are useless when the rocket motion is unstable or irregular, amplitude ratio aspect sensors, which do not rely on a suitable roll rate, were included.

4.3.4 The Form of the HAD Trajectory

Part of the trajectory information derived from the radar tracking data is the height, h, of the rocket above sea level, given at

0.5 sec intervals from launch. When the tracking is incomplete, the heights in the missing portions of the trajectory must be interpolated. To do this, the mathematical form of the trajectory must be known.

If, in this section, we let t represent the time from apogee, then the trajectory can be represented by the simple ballistic form

$$h(t) = h(0) - \tfrac{1}{2}gt^2 \ .$$

The two most important factors that cause the trajectory to deviate from this form are air drag and variations in the acceleration due to gravity, g. As shown in Section 4.3.6, the effect of air drag is negligible when the rocket is above an altitude of about 50 Km and as the oxygen density determinations take place above 70 Km this effect need not be considered.

The value of g varies inversely as the square of the distance from the centre of the earth, but over a height range of about 50 Km the decrease in g with height will be very closely linear. We may therefore write

$$a(t) = -(g_o + k[h(0) - h(t)]$$

where a(t) is the vertical acceleration of the rocket, g_o is the value of g at apogee and k is a small positive constant. If a(t) and g_o are in units of Km sec^{-2} and h(0) and h(t) are in units of Km, then k has the value 3.0866×10^{-6} sec^{-2} (CIRA, 1965). Because k is

small we may, to a good approximation, put

$$a(t) = -(g_o + \tfrac{1}{2} k g_o t^2) \ .$$

If $v(t)$ is the vertical velocity of the rocket then, as $v(0) = 0$,

$$v(t) = \int_o^t a(t)dt = -(g_o t + \frac{1}{6} k g_o t^3)$$

and therefore

$$\begin{aligned} h(t) &= h(0) + \int_o^t v(t)\, dt \\ &= h(0) - \tfrac{1}{2} g_o t^2 (1 + \frac{1}{12} k t^2) \\ &= h(0) - \tfrac{1}{2} g_o t^2 (1 + 2.572 \times 10^{-7} t^2) \qquad \ldots(1) \end{aligned}$$

This equation accurately describes the trajectory of a HAD rocket above 50 Km. If we assume an apogee height of 100 Km then the difference between the values of $h(t)$ determined from equation (1) and the equation

$$h(t) = h(0) - \tfrac{1}{2} g_o t^2 \qquad \ldots(2)$$

amounts to only 0.05 Km at a height of 70 Km. As the density determinations are made above 70 Km, and this difference decreases with increasing height, we can use equation (2) to describe the HAD trajectory with no significant loss of accuracy in the determination of oxygen densities.

4.3.5 The HAD 309 Flight

The rocket HAD 309, was fired from Woomera (latitude $30^{\circ}35'S$,

longitude 136°31"E) on July 24th, 1969, at 1615 hours local time when the solar zenith angle was 78°. It carried two LiF-NO ion chambers with their associated equipment as described in Sections 4.3.2 and 4.3.3. The apogee height of 121.3 Km was reached 172.5 sec after launch. A 1P42 phototube in one of the ratio aspect sensors failed soon after launch, but good telemetry signals were received from the remaining detectors until the loss of telemetry 204 sec after launch. As the telemetry failure occurred soon after apogee, no information was received from the downward portion of the flight.

Above 72 Km, Lyman-α radiation was detected by the ion chambers each time the rocket, which rolled once every 3.7 sec, pointed them towards the sun. No response was seen from the ion chambers below 72 Km indicating that their long wavelength sensitivity (Section 3.9) was negligible.

The tracking of the rocket was poor, with the radar never locking onto the vehicle. However, during the period from 100 sec to 200 sec after launch the radar was slave to the signals from the ackaid tracking oscillator mounted in the rocket head (Section 4.3.2). This meant that the azimuth and elevation of the rocket were known relative to the location of the radar station. Also, the range of the rocket was determined on five occasions during this period. From these five sightings it was possible to establish the plane of the rocket trajectory. Using the azimuth and elevation information and the position of the radar station it was then possible

to calculate the rocket's altitude as a function of time from 100 sec to 200 sec after launch. The apogee height was estimated in this way to be 121.3 ± 1.0 Km and to have been attained 172.5 sec after launch. Using these values the rocket trajectory above 70 Km was derived from equation (2) in Section 4.3.4.

As the rocket rolled, each ion chamber showed a peak in its telemetry output voltage as it looked towards the sun. The peak value occurred when the aspect angle was equal to the rocket aspect angle (Section 4.3.3.(a)) and it was this value that had to be determined. The sunslits (Section 4.3.3(b)) were used to determine the rocket aspect angle values. The rocket roll period of 3.7 sec, coupled with the sampling rate of 143 samples sec^{-1} (two telemetry channels were used for each set of sunslits), resulted in a maximum error in the derived aspect angle of ± 0.25^{o}. Additional uncertainties resulting from the laboratory calibrations and alignment of the detectors in the rocket increased the error to about ± 1^{o}. The amplitude ratio aspect sensors showed almost no response due to earthshine (Section 4.3.3(c)) and so they were used to check the sunslit determinations of the rocket aspect angle at a few points. The difference between the aspect angles derived by the two types of aspect sensor never exceeded 1^{o}. This demonstrates the accuracy of the laboratory calibration procedures for these sensors.

As the rocket aspect angle was not zero at any stage of the flight, it was not possible to obtain an in-flight calibration of the

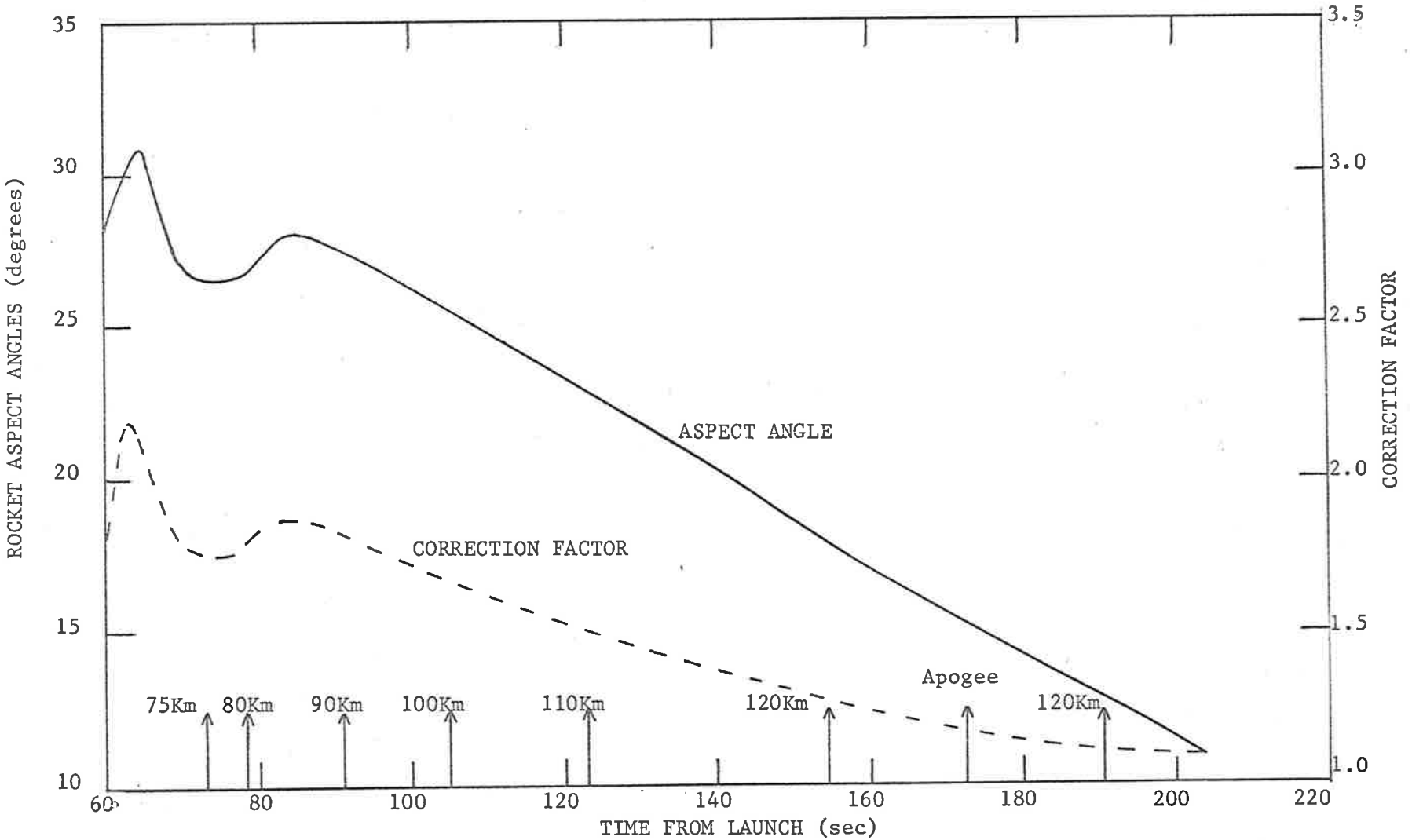

Fig. 4.7 Aspect angles and correction factors for the HAD 309 flight, plotted against time from launch.

angular response of the ion chambers (Section 4.3.6). Therefore, the laboratory angular response curves were used to derive the factors needed to correct the peak telemetry voltages from the ion chambers to their values at zero aspect angle. The rocket aspect angles and the corresponding correction factors are plotted in Figure 4.7 as a function of time from launch, for the period during which the height of the rocket was above 65 Km. The rocket altitude is also shown at a few points.

The aspect corrected values of peak ion chamber voltage were converted to currents, using the known input resistance and gain of each ion chamber amplifier. Figure 4.8 shows a semi-logarithmic plot of the individual currents versus altitude. This response curve includes data from both ion chambers but the values refer only to the upward portion of the flight due to the failure of the telemetry sender shortly after apogee. Molecular oxygen densities and the absolute solar Lyman-α flux were determined from this response curve as described in Section 4.4.

4.3.6 The HAD 310 Flight

The rocket, HAD 310, was fired from Woomera on December 9th, 1969, at 0726 hours local time when the solar zenith angle was 59^{o}. It carried two LiF-NO ion chambers in an experimental package identical to that carried by HAD 309. Good telemetry signals were received throughout the flight and all of the instrumentation performed satisfactorily. However, due to the very large rocket aspect angles that

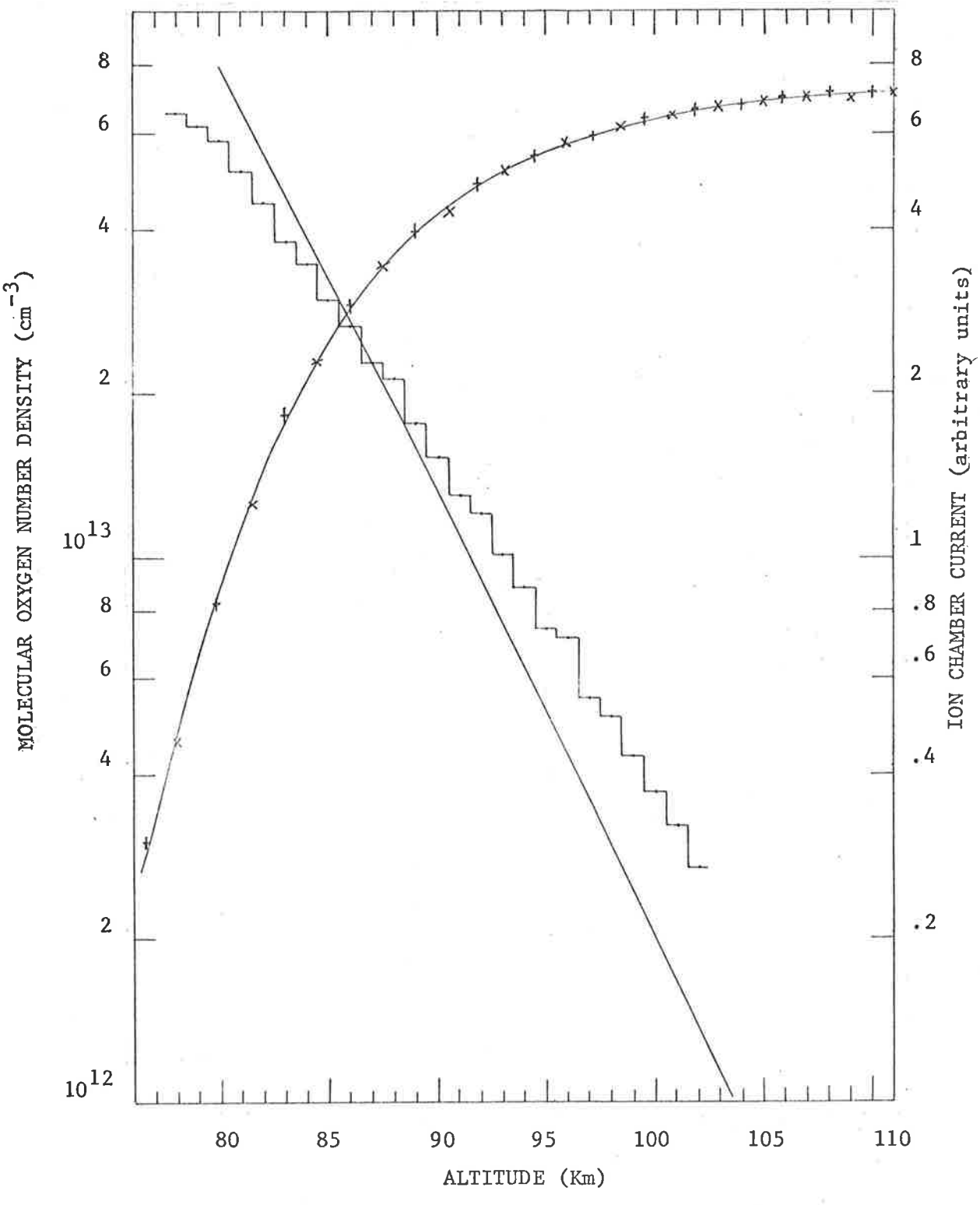

Fig. 4.8 Ion chamber currents and derived molecular oxygen density profile (histogram) for the HAD 309 flight. The 1965 mean CIRA atmosphere (full curve) is shown for comparison.

occurred on the downward portion of the flight, only the results obtained from the upward portion were reduced.

The rocket was tracked by FPS16 radar from 19 sec before apogee until impact. The apogee height of 98.3 ± 0.02 Km and the apogee time of 151.1 sec after launch were directly determined from the tracking data. Using these values the rocket trajectory was derived from equation (1) in Section 4.3.4. The derived trajectory was then compared with the actual trajectory (as given by the tracking data) for the downward portion of the flight. At low altitudes, due to air drag, the actual trajectory heights were higher than those of the derived trajectory for the same time from apogee. The height difference was about 0.1 Km at an altitude of 50 Km and decreased rapidly with increasing altitude. Therefore, for the purpose of molecular oxygen density determinations, the effect of air drag on a HAD vehicle can be ignored.

The amplitude ratio aspect sensors responded to earthshine (Section 4.3.3(c)) as well as the direct solar radiation, with the earthshine signal at times reaching about 10% of that due to the sun at zero aspect angle. Because of the resultant uncertainty in the output levels of these sensors, only the sunslits were used to determine the rocket aspect angles. As two telemetry channels were employed for each set of sunslits, the roll period of 0.82 sec resulted in a maximum uncertainty in the derived aspect angles of $\pm 1^{\circ}$. Figure 4.9 shows the rocket aspect angle as a function of time

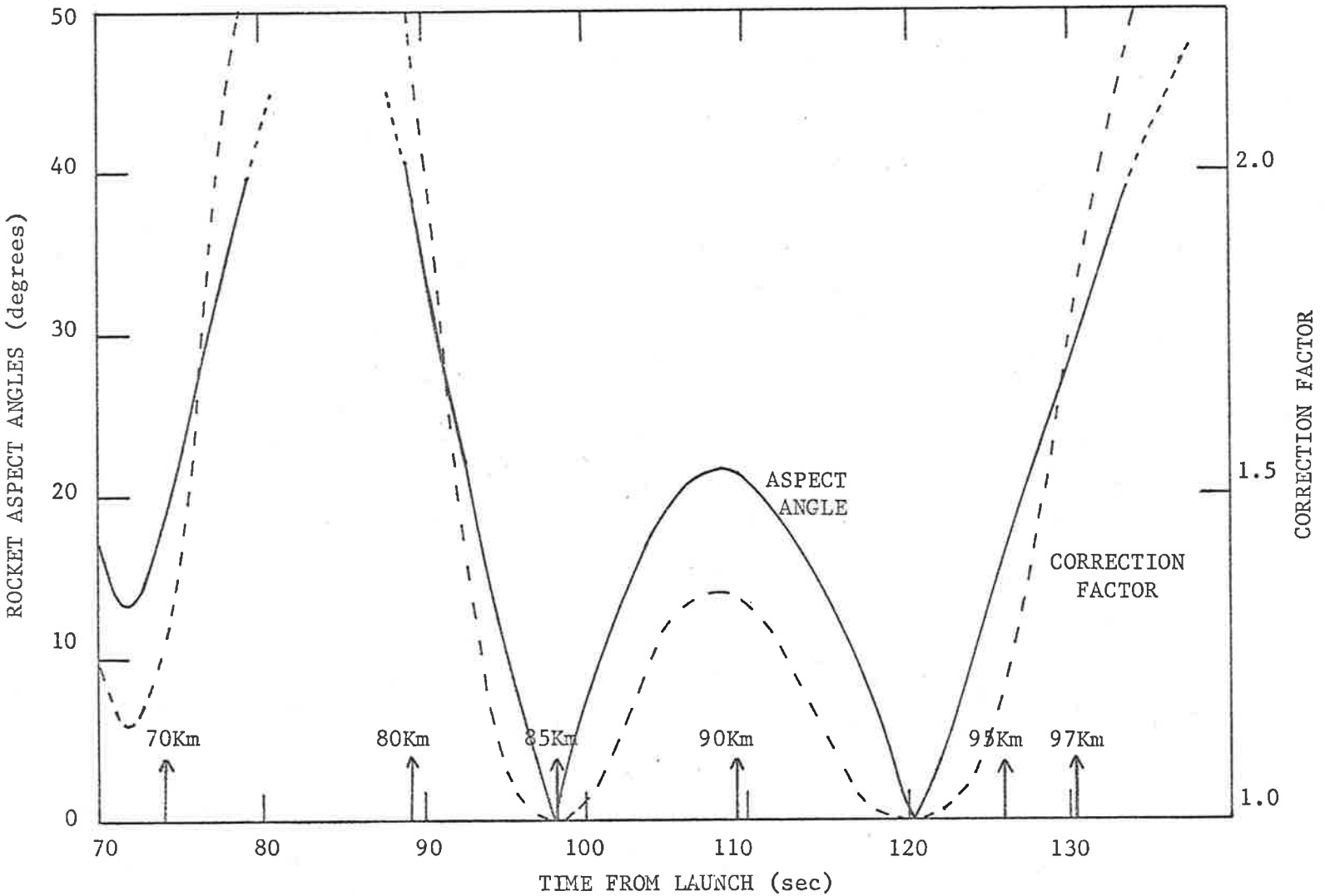

Fig. 4.9 Aspect angles and the corresponding correction factors plotted against time from launch for the upward portion of the HAD 310 flight.

from launch for the upward portion of the flight, during the period when the rocket was between 68 Km and 98 Km. As can be seen from Figure 4.9, at 121 sec from launch the rocket aspect angle was 0^{o}. The angular response curve of each ion chamber was determined from the signals obtained during one roll of the rocket at this time. Good agreement was found between these in-flight curves and the laboratory calibrations described in Section 3.7, with the difference being less than 3% for aspect angles less than 40^{o}. The in-flight calibrations were used to derive the factors needed to correct the peak telemetry voltages from the ion chambers to their values at zero aspect angle. It can be seen from Figure 4.9 that between 82 Km and 96 Km the correction factors were always less than 1.6. However, both between 72 Km and 82 Km and above 96 Km the rocket aspect angle rapidly increased and the correction factors became large. Rocket aspect angles greater than 40^{o} could not be measured with the sunslits. No ion chamber signals were detected below 70 Km indicating that the long wavelength sensitivity of the ion chambers (Section 3.9) was negligible.

Ion chamber currents were derived as described in Section 4.3.5 for the HAD 309 detectors. The individual current values from both ion chambers are plotted in Figure 4.10 as a function of the rocket altitude. The data refers only to the upward portion of the flight as the very large aspect angles on the downward portion made accurate aspect corrections impossible. The data points can be seen to follow a smooth curve except where the aspect angles are large and the

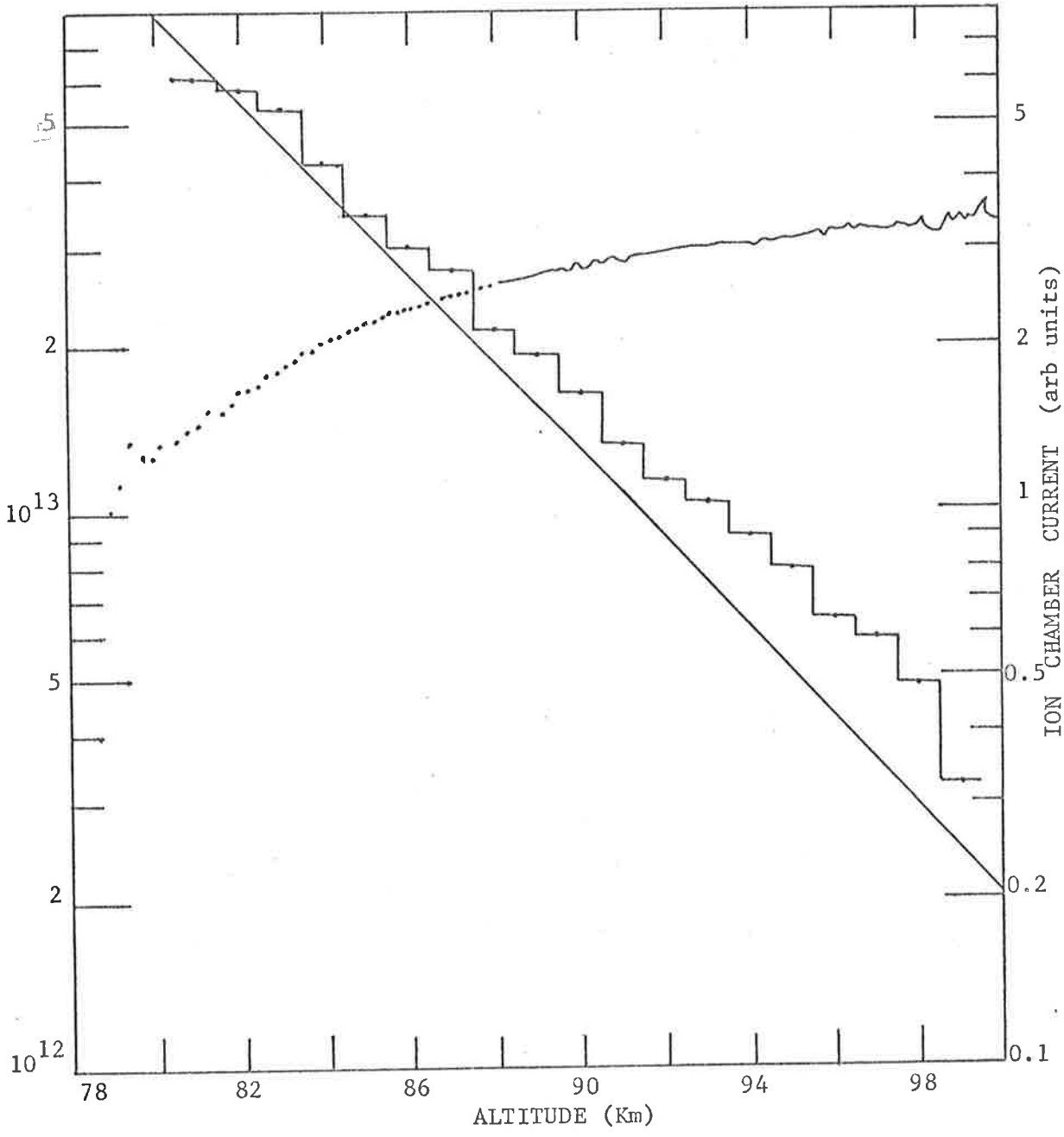

Fig. 4.10 Ion chamber current and derived molecular oxygen density profile (histogram) for the HAD 310 flight. The 1965 mean CIRA atmosphere (full curve) is shown for comparison.

correction factors consequently of greater uncertainty.

4.4 Results from HAD 309 and HAD 310

4.4.1 Molecular Oxygen Densities

As shown in Section 2.3, when the solar zenith angle, Z, is not too large, the number density is proportional to the slope of a semi-logarithmic plot of ion chamber signal versus height. In practice, the analysis is best carried out by determining the average number densities in a series of equal height intervals in the following way.

To a good approximation, it may be assumed that over a limited height range near the height, h, the density distribution of molecular oxygen is of the form

$$n(h_1) = n(h) \exp [-(h_1-h)/H] .$$

If we consider the atmosphere to be divided into layers of equal height interval, Δh, then, provided Δh is less than H, the density at the height $(h + \Delta h/2)$ can be taken with high accuracy to be the average number density over the height range h to $h + \Delta h$. Equation (10) of Chapter 2 then becomes

$$n(h+\Delta h/2) = \frac{1}{\sigma \sec Z} \frac{\ln [I(h+\Delta h)] - \ln [I(h)]}{\Delta h} \qquad \ldots(3)$$

Two main assumptions were made when deriving densities from the Lyman-α absorption profiles:-

(i) The ion chamber was assumed to be responding only to Lyman-α radiation (Section 2.3).

(ii) Molecular oxygen was assumed to be the only atmospheric constituent contributing to the absorption of Lyman-α radiation (Section 2.5).

The density profiles obtained from the HAD 309 and HAD 310 flights are discussed separately below.

(a) HAD 309.

Figure 4.8 shows the vertical distribution of molecular oxygen (histogram) derived as described above assuming a layer height of 1 Km. The 1965 mean CIRA atmosphere (CIRA, 1965) is also shown (full curve) for comparison. The value of the zenith angle used in equation (3) was $78^{\circ}14'$ which occurred when the rate of change of signal with height was a maximum. The density values follow closely those of an exponential distribution with a scale height of 7.5 Km.

Random errors in the densities are due to uncertainties arising from the data reduction and noise on the telemetry records. In this flight the errors due to telemetry noise are less than ± 2%. As shown in Section 2.4, errors in the data reduction are generally a minimum in the vicinity of the penetration height where the rate of change of the signal with height is a maximum. In this flight, the probable

errors in the density values arising from the data reduction, in the height range 80 Km to 100 Km, are estimated to be less than ± 5% with the greatest error occurring near 85 Km where the aspect angles are largest. An additional error results from the inaccuracy of the flat earth approximation (Section 2.3) at large zenith angles. For an aspect angle of 78^{o} Weeks and Smith (1968) have shown that this approximation results in an error of approximately ± 2% for a species having a scale height of 6.5 Km. The total probable random error in the density values between 80 Km and 100 Km is therefore not expected to exceed ± 7%.

As shown in Section 2.2, there is an uncertainty of about ± 14% in the value of 1.0×10^{-20} cm^2 taken for the absorption cross-section of molecular oxygen at Lyman-α. As can be seen from equation (3) above, this results in a systematic error of ± 14% in the number densities.

There is also a systematic error of ± 1 Km in the height values of the data points due to an uncertainty of ± 1 Km in the estimated apogee height. As the scale height of the density distribution is about 7.5 Km, this error is significant and must be considered when comparing these results with similar measurements by other workers (Section 6.2.1).

(b) HAD 310.

A layer height of 1 Km was used to derive a molecular oxygen distribution from the HAD 310 absorption data. The results are

shown as a histogram in Figure 4.10 which also shows (full line) the 1965 mean CIRA atmosphere (CIRA, 1965) for comparison. The density profile is well represented by an exponential distribution with a scale height of 6.5 Km.

Random errors in the density values due to noise on the telemetry records are estimated to be about ± 2%. The random errors resulting from uncertainties in the data reduction vary widely due to the rapid change of aspect angles that occurred. Between 82 Km and 96 Km, where the aspect angles are less than 22^{o}, the probable errors are less than ± 8%. Outside of this height range the aspect angles become rapidly larger and the errors therefore increase. If the systematic error of ± 14% due to the uncertainty of the value of the absorption cross-section is included, the total error in the density values between 82 Km and 96 Km is not expected to exceed ± 22%. Errors in the trajectory heights are estimated to be less than 0.1 Km.

The HAD 310 density results are compared in Section 6.2.1. with those from the HAD 309 flight and with similar results obtained by other workers.

4.4.2 Lyman-α Flux Values

The individual aspect corrected currents from each ion chamber were converted to Lyman-α flux values by using the known effective area of the detector (1.60 cm^2) and its absolute quantum efficiency at Lyman-α, measured as described in Section 3.6.

To obtain the Lyman-α flux above the atmosphere for each flight, it was necessary to assume that the derived molecular oxygen distribution could be extrapolated to higher altitudes with the same scale height. A plot was then made of the logarithm of the flux as a function of the columnar density (Section 2.3) in units of the columnar density at a chosen height (90 Km for HAD 309 and 85 Km for HAD 310). The straight line graph that resulted was then extrapolated to zero columnar density. The values of the solar Lyman-α flux obtained in this way for the HAD 309 and HAD 310 flights were 3.9 ± 0.4 erg cm^{-2} sec^{-1} and 4.2 ± 0.4 erg cm^{-2} sec^{-1} respectively. These values are compared with other measurements in Section 6.3.

In the HAD 309 flight, the flux values at heights in excess of 110 Km were found to lie above the extrapolation of the straight line fitted to the points below this height. This additional signal was due to radiation other than Lyman-α in the 1050Å to 1350Å bandpass of the ion chambers. At the apogee height of 121.3 Km this additional signal was about 7% of the extrapolated Lyman-α flux.

CHAPTER 5

THE WRESAT 1 ION CHAMBER EXPERIMENT

5.1 Introduction

WRESAT 1, a small scientific satellite, was launched from Woomera in November 1967. It was designed and developed by the Weapons Research Establishment, Department of Supply and the Department of Physics, University of Adelaide. The launch vehicle was provided by the U.S. Department of Defence, while the launch facilities were provided by the U.K. Ministry of Technology. Satellite tracking and data acquisition were performed by the STADAN network of the U.S. National Aeronautics and Space Administration (NASA).

Included in the experiments flown on WRESAT 1 were six ion chambers of the types described in Chapter 3. The two objectives of the ion chamber experiment were:-

(i) The measurement of molecular oxygen densities by utilizing the occultation of the sun by the earth's atmosphere at satellite sunrise and sunset (Section 5.3).

(ii) The determination of the solar flux in the wavelength bands 1420Å to 1480Å and 1550Å to 1690Å and at the wavelength of hydrogen Lyman-α (Section 5.6).

It was hoped that the density determinations would lead to information on possible day-to-day and geographical variations in the vertical molecular oxygen density profile. The solar flux measurements

Fig. 5.1 A view of the WRESAT 1 satellite undergoing environmental testing at Weapons Research Establishment. The side-facing detector package can be seen to the left of the aperture formed by the removal of a section of the skin. The side of the forward-facing package can be seen at the apex of the cone.

were expected to give important information relating to the solar temperature minimum (Section 1.2).

The satellite (Figure 5.1) was conical in shape with a base diameter of 30 inch and a height of 62 inch. All of the instrumentation units were thermally isolated from the main structure which consisted of a framework and skin of aluminium alloy. By painting the bulk of the external surfaces black and the interior surfaces white, it was possible to ensure that the temperature of the internal equipment remained within satisfactory limits as the satellite orbited the earth.

The satellite structure and equipment were subjected to environmental tests by the Weapons Research Establishment. These tests included static and dynamic loading, vibration testing, impact loading and testing at elevated temperatures. In addition, the complete satellite was tested in a high vacuum chamber at the Physics Department, University of Adelaide. The satellite was held at a pressure of 10^{-4} mm of Hg while being cycled in temperature between +50°C and -15°C over a period of about 4 days. All units survived this test without observable permanent changes in their operation.

WRESAT 1 (also given the COSPAR designation 1967-118A) was launched on 29th November, 1967 at 1425 hours Australian Central Standard Time. The launch vehicle was a Redstone missile boost motor modified to accept two solid fuel upper stages. A nearly polar elliptical orbit was achieved with a perigee of 170 Km and an apogee of 1249 Km. The orbital inclination was 83.3° and the orbital period 99 min. The sub-satellite track of WRESAT 1 is shown in Figure 5.2 for the first 8 orbits.

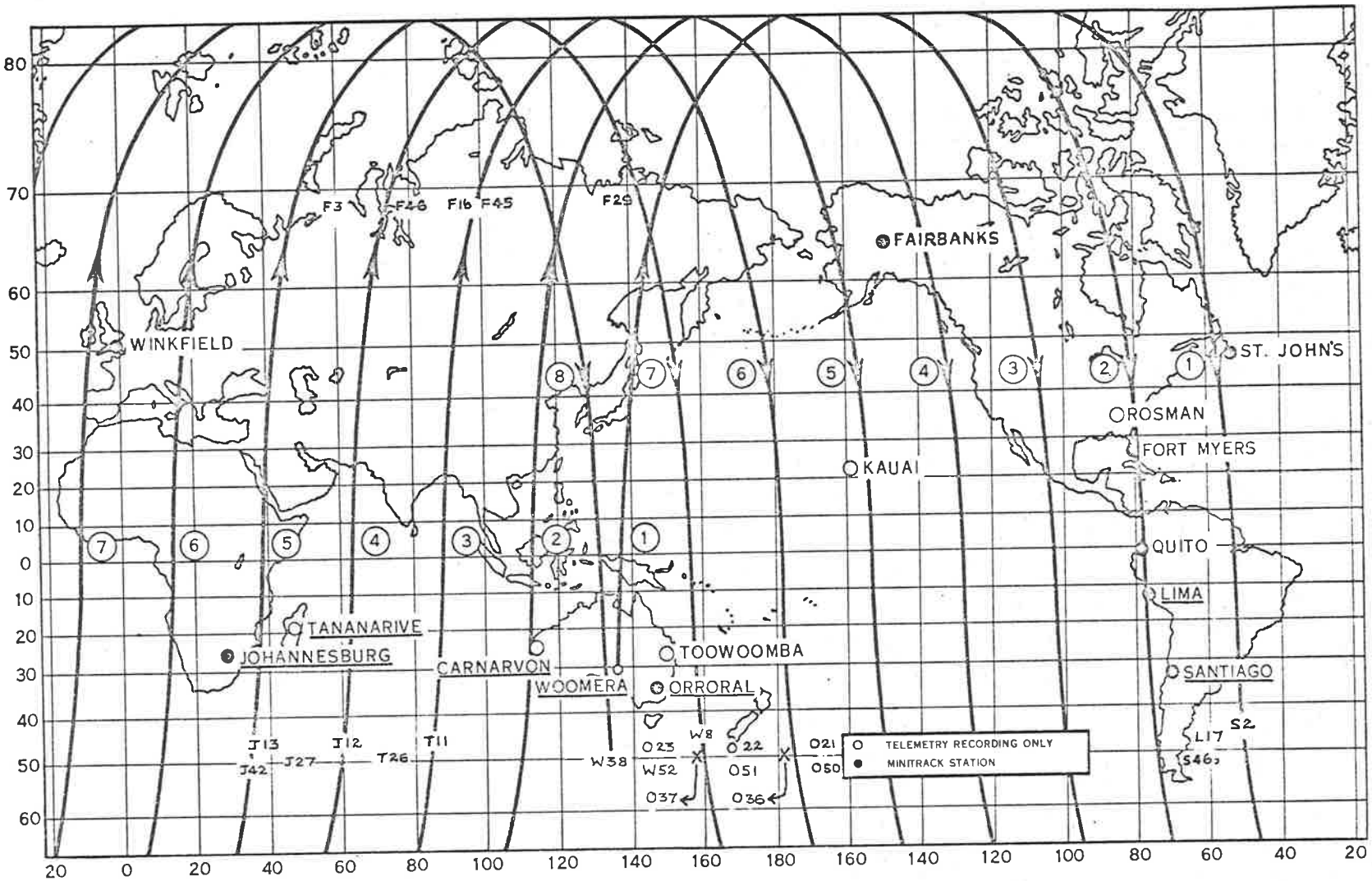

Fig.5.2 The sub-satellite track of WRESAT 1 for the first 8 orbits.

The satellite entered orbit with a spin rate of 2.5 rev sec^{-1} about the cone axis which was inclined at approximately 27° to the earth's rotational axis. Due to the lack of infinite rigidity of the satellite, and other factors, the axis of spin nutated and the motion became that of a flat spin about the axis of maximum moment of inertia. This latter axis, which was designed to be at right angles to the cone axis, was parallel to the original spin axis of the satellite on its insertion into orbit. As the ratio of the moments of inertia about the cone axis and the flat spin axis was 1:5, the final flat spin rotation rate was about 0.5 rev sec^{-1}. The conversion to the flat spin mode was accelerated by the use of an energy dissipator mounted inside the satellite. As a result, the conversion was complete 35 min from launch.

The orbital lifetime of WRESAT 1 was 42 days, re-entry occurring on 10th January, 1968. However, the use of batteries for satellite power limited the useful transmitting life to 53 orbits, i.e., approximately 3 days.

5.2 Satellite Instrumentation

5.2.1. The Ion Chambers and Amplifiers

Figure 5.3 shows the layout of the WRESAT 1 instrumentation. The radiation detectors were mounted in two separate packages. The front-facing package was located near the apex of the cone (the tip of which was separated after the injection of the satellite into orbit) with the look direction of the sensors being forward along the cone axis. The side-facing package was located near the surface of the cone,

Fig. 5.3 The layout of the WRESAT 1 instrumentation.

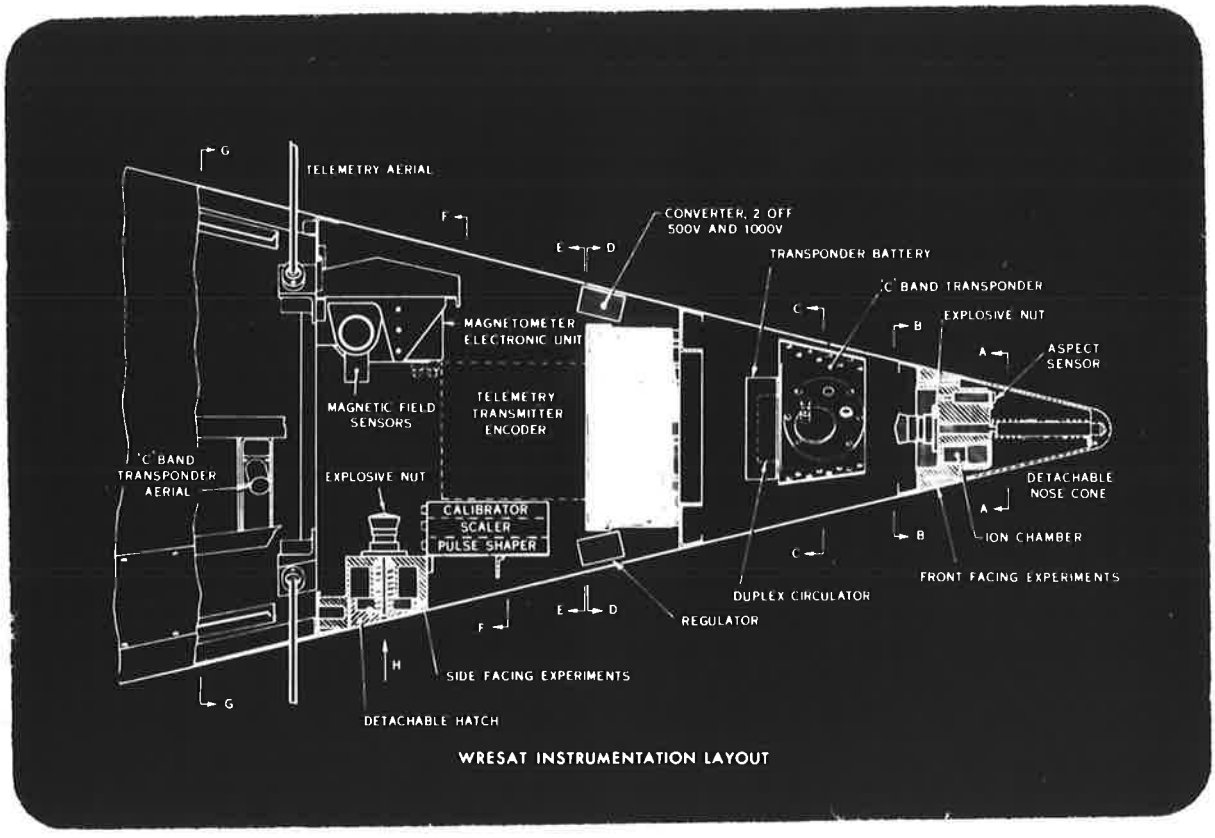

WRESAT INSTRUMENTATION LAYOUT

30 inch from the apex (Figure 5.1), such that the look direction of the sensors was at right angles to both the cone axis and the anticipated axis of the flat spin mode. With this geometry, first the front-facing ion chambers and then the side-facing ion chambers were expected to scan directly across the solar disk as the satellite rotated. However, the actual axis of the flat spin mode was at right angles to the cone axis but rotated approximately 30° about the cone axis relative to its predicted position. As a result, the front-facing detectors scanned directly across the sun while the minimum solar aspect angle for the side-facing detectors was 30° (Section 5.4.3).

The ion chamber experiment consisted of two LiF-NO, two Q-T and two S-X copper bodied ion chambers of the type shown in Figure 3.1. Both detector packages contained three ion chambers (one of each type) and a set of optical aspect sensors. These three combinations of window material and filling gas were chosen because the resulting effective molecular oxygen absorption cross-sections (Section 2.3) are such that an almost continuous density profile can be obtained over the height range 90 Km to 220 Km at satellite sunrise and sunset. The importance of such measurements has been pointed out in Section 4.1.

All of the ion chambers were operated at unity gain with positive voltage applied to the chamber walls to minimize long wavelength photoelectric effects (Section 3.9). The ion chamber currents were fed to logarithmic amplifiers. Those amplifiers fed by the LiF-NO ion chambers developed output voltages from 0V to +5V for input currents from 10^{-10} amp to 10^{-6} amp, while those fed by the Q-T and S-X ion

chambers produced the same range of voltage for input currents from 10^{-12} amp to 10^{-8} amp.

5.2.2. Optical Aspect Sensors and Magnetometers

A set of amplitude ratio aspect sensors similar to those flown in the rocket experiments (Section 4.3.3) was included in each of the detector packages for the purpose of measuring solar aspect. Originally, three mutually perpendicular flux-gate magnetometers were included in the payload to determine the attitude of the satellite and to provide a check on the measurements of the optical aspect sensors. Owing to weight limitations, two of the magnetometers had to be removed from the satellite prior to launch, leaving one with its axis parallel to the cone axis. This remaining magnetometer enabled an independent check to be made on the solar aspect angle for the front-facing detector package. However, the solar aspect angle determined for the side-facing package relied entirely on the optical aspect sensors (Section 5.4.3).

5.2.3. The Telemetry System

The WRESAT 1 telemetry system was purchased commercially and was compatible with the NASA STADAN network. As there were no facilities for data storage in the satellite, only those observations made within range of a telemetry station are available. The sampling rate was 256 samples sec^{-1} with the sampling format being a 16x8array. Each position was sampled in turn and the complete array scanned in half a second. This meant that there were 128 sampling positions available for the radiation detectors and the general voltage and engineering

monitor levels. The ion chamber and aspect sensor outputs were allocated to positions in the telemetry matrix such that each detector was sampled at intervals of 1/16 sec. This gave sufficient data points to define the shape of the signal pulses from the detectors as they scanned across the sun. Sunslits were not included in the detector packages owing to the high sampling rate demanded by them (Section 4.3.3) which could only have been achieved at the expense of the other experiments involved.

5.3 The Atmospheric Occultation Experiment

5.3.1. The Principle of the Experiment

Observations of the orbital drag on artificial satellites have yielded information on atmospheric densities down to an altitude of about 180 Km. However, for lower altitudes this technique is limited by the short lifetime of satellites (e.g. Champion et al., 1969). Knowledge of atmospheric densities between 90 Km and 180 Km has been derived from a relatively small number of widely scattered rocket flights. One of the main objectives of the WRESAT 1 ion chamber experiment was to make repeated measurements of molecular oxygen density over the height range from 90 Km to 220 Km. It was hoped that important information would be obtained on the expected day-to-day and geographical variations in the molecular oxygen density profile over this height range. Such information is needed to improve existing thermospheric models and to provide a better understanding of the relationship between the thermosphere and the underlying atmosphere.

The principle of the experiment is shown in Figure 5.4. At times near satellite sunrise and sunset, the intensity of the solar ultraviolet radiation detected at the satellite, S, will vary as the sun is occulted by the earth's atmosphere. As shown in Section 2.5, molecular oxygen is the only effective absorbing constituent of the atmosphere at the wavelengths to which the ion chambers respond. Therefore, as the decrease of molecular oxygen density with height is approximately exponential, most of the absorption along a ray from the sun to the satellite, takes place in the near vicinity of the point where the ray approaches closest to the earth. The height of closest approach is known as the minimum ray height and in this work is taken to have the value h for the central solar ray (Figure 5.4).

To determine molecular oxygen number densities from the absorption data we may, as a first approximation, consider the sun to be a point source. We may then (Section 5.3.2) extend the theory derived in Section 2.3 for the rocket experiments, to apply to the situation where the solar zenith angle, Z, is greater than 90°. It will then be possible (Section 5.3.3) to include the effect of the finite size of the sun in the analysis.

5.3.2. The Point-Sun Approximation

Let us assume that the sun is a point source located at the centre of the solar disk. As can be seen from Figure 5.4, the solar zenith angle at the minimum ray height point, P, is always 90°. However, the solar zenith angle at the satellite is greater than this and for the WRESAT 1 satellite varied from approximately 119° to 116° as the minimum

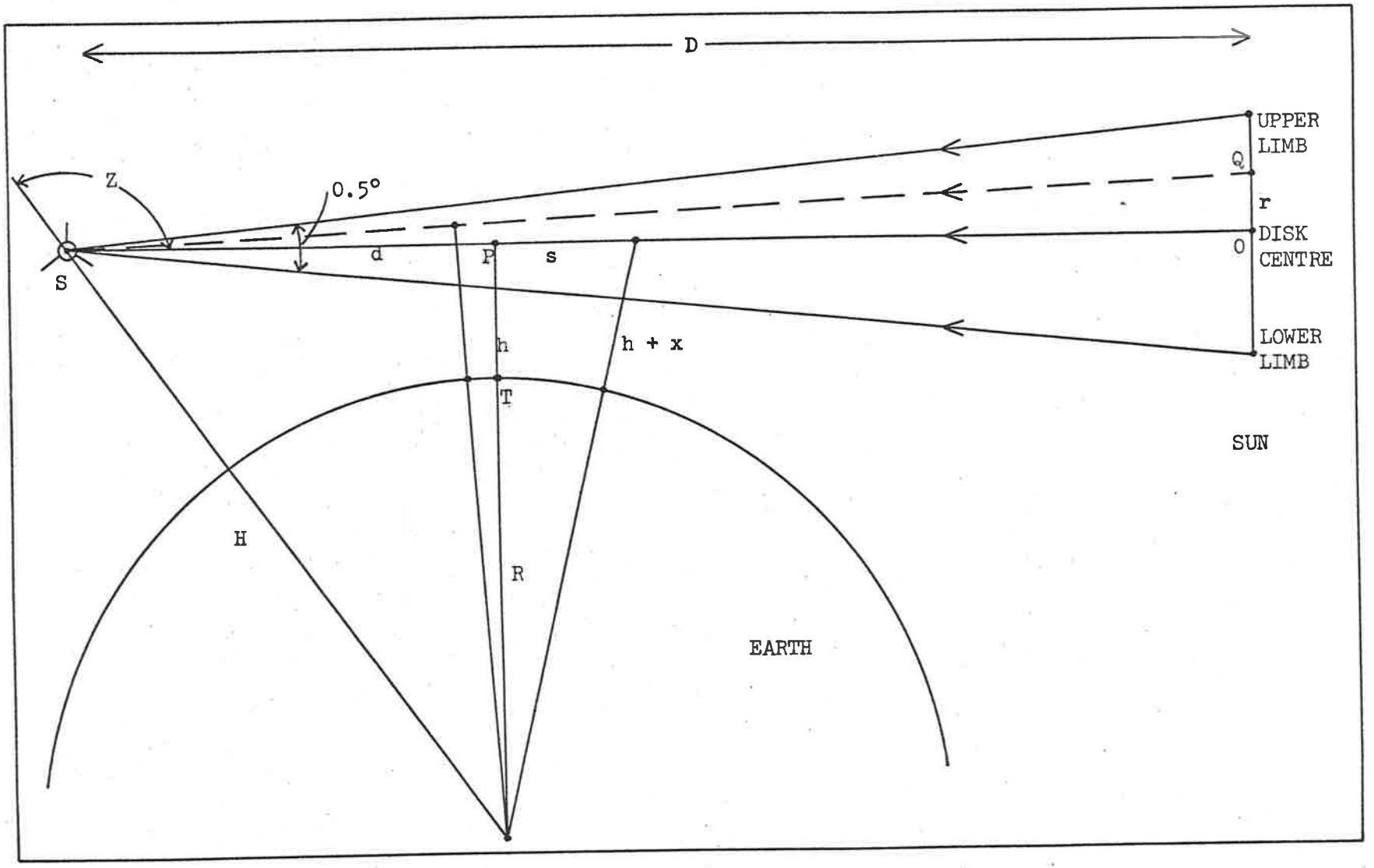

Fig.5.4 The geometry of the satellite atmospheric occultation experiment.

ray height of the central solar ray varied over the height range 100 Km to 200 Km. Equations (1) to (4) and equation (8) in Chapter 2 were derived for the situation where the solar zenith angle at the observing point is less than 90°. These equations are also valid for the satellite sunrise-sunset experiment provided that the rocket height, h, is now considered as the minimum ray height of the central solar ray. Therefore, if I(h) is the ion chamber current when the minimum ray height is h, we have, from equation (8) in Chapter 2, the expression

$$\frac{d}{dh}[\ell n\ I(h)] = -\sigma \frac{d\ N(h)}{dh} \qquad \ldots(1)$$

The columnar density, N(h), can be found by integrating along the ray from the satellite to the sun. If s is the distance along the ray from the point P, then, with reference to Figure 5.4, we have

$$N(h) = \int_P^\infty n\ ds + \int_P^S n\ ds \qquad \ldots(2)$$

where n is the number density of molecular oxygen.

At satellite sunrise and sunset, the satellite was at an altitude of about 900 Km above the earth's surface. It was therefore above the effective absorbing atmosphere and so the second integral in equation (2) may also be taken to infinity with no loss of accuracy. Therefore equation (2) becomes

$$N(h) = 2\int_P^\infty n\ ds \qquad \ldots(3)$$

To evaluate this integral the variation of n with height must be specified. If we assume an exponential distribution of scale height, H,

we may write

$$n(x) = n(h)\ \exp(-x/H) \qquad \ldots(4)$$

where n(x) is the number density at the height (h + x) above the earth's surface and n(h) is the value at the height h. As most of the absorption is taking place at heights less than two scale heights above h, the assumption that the scale height is constant does not introduce significant errors into the calculations unless the scale height gradient, $\frac{dH}{dh}$, is large.

From Figure 5.4 we see that

$$s^2 = (R + h + x)^2 - (R + h)^2$$

i.e.

$$s^2 = x(2R + 2h + x).$$

It follows that

$$\int_P^\infty n\ ds = n(h)\int_o^\infty \frac{(R + h + x)\ \exp(-x/H)}{x^{\frac{1}{2}}(2R + 2h + x)^{\frac{1}{2}}}\ dx \qquad \ldots(5)$$

Since, over the range of importance, (R + h) >> x, equation (5) may be simplified to the form

$$\int_P^\infty n\ ds = \left(\frac{R + h}{2}\right)^{\frac{1}{2}} n(h) \int_o^\infty \frac{\exp(-x/H)}{x^{\frac{1}{2}}}\ dx \qquad \ldots(6)$$

If we put t = x/H, equation (6) can be rewritten as

$$\int_P^\infty n\ ds = \left[\frac{H(R + h)}{2}\right]^{\frac{1}{2}} n(h) \int_o^\infty \frac{e^{-t}}{t^{\frac{1}{2}}}\ dt \qquad \ldots(7)$$

Now

$$\int_0^\infty \frac{e^{-t}}{t}\, dt = \Gamma(-\tfrac{1}{2}) = \sqrt{\Pi}$$

and so, substituting equation (7) into equation (3) gives

$$N(h) = [2\Pi H\ (R + h)]^{\frac{1}{2}}\ n(h) \qquad \ldots(8)$$

The differential form of equation (8) is, to a very good approximation,

$$\frac{d\ N(h)}{dh} = [2\Pi\ H\ (R + h)]^{\frac{1}{2}}\ \frac{d\ n(h)}{dh} \qquad \ldots(9)$$

But, from equation (4)

$$\frac{d\ n(h)}{dh} = -n(h)/H \qquad \ldots(10)$$

Substituting equation (10) into equation (9) and re-arranging gives

$$\frac{d\ N(h)}{dh} = -\left[\frac{2\Pi(R + h)}{H}\right]^{\frac{1}{2}} n(h)$$

and so, from equation (1), we may write

$$n(h) = \frac{H^{\frac{1}{2}}}{\sigma[2\Pi(R + h)]^{\frac{1}{2}}}\ \frac{d}{dh}\ [\ell n\ I(h)] \qquad \ldots(11)$$

A constant value of 6520 Km was taken for (R + h) in the present work. The maximum error in n(h) introduced by this assumption is less than 0.5% over the height range 90 Km to 220 Km.

5.3.3. Correction for the Effect of the Finite Size of the Solar Disk

In Section 5.3.2, theory was developed for a point sun, but in

reality each ion chamber responds to the integrated radiation over a cone of angle 0.5° (Figure 5.4).

The distance, d, from the satellite to the point P was about 3300 Km, at both satellite sunrise and sunset. The difference in the minimum ray height of the rays reaching the satellite from the upper and lower limbs of the solar disk was therefore approximately 29 Km. As this difference is considerably greater than the scale height of molecular oxygen over much of the height range from 90 Km to 220 Km, the attentuation of radiation along these extreme rays will be very different.

In developing a method of analysis that allows for the finite size of the sun, we will make the assumption that the sun is a uniformly bright disk subtending an angle of 0.5° at the satellite. The possible errors introduced by assuming the solar disk to be uniformly bright are discussed in Section 6.2. The variation in absorption along rays emitted from a horizontal line across the solar disk (i.e. a line tangential to the earth's horizon as seen from the satellite) will be small. Therefore, we can replace the solar disk by a vertical line source such that the intensity at any point on this source is proportional to the width of the solar disk at that point.

Consider the situation shown in Figure 5.4, where the minimum ray height of the ray from a point, Q, a distance r from O along the solar line source, is (h + p). Let I_o represent the ion chamber current due to radiation emitted from the entire unobscured disk. Then, the current due to radiation emitted from a section of the line source of

length dr, at Q is given by

$$I_Q = 2(R_s^2 - r^2)^{\frac{1}{2}}\, dr\, \frac{I_o}{\Pi R_s^2}$$

$$= 2(t^2 - p^2)^{\frac{1}{2}}\, \frac{R_s^2}{t^2}\, \frac{I_o}{\Pi R_s^2}\, dp$$

where R_s is the solar radius and t is the difference in the minimum ray height of the central solar ray and a ray from either extremity of the line source. The total ion chamber current observed when the minimum ray height of the central solar ray is h, is therefore given by

$$I(h) = \int_{-t}^{+t} \frac{I_o}{\Pi R_s^2} \cdot 2(t^2 - p^2)^{\frac{1}{2}}\, \frac{R_s^2}{t^2} \exp[-\sigma N(h+p)]dp$$

$$= \frac{2I_o}{\Pi t^2} \int_{-t}^{+t} (t^2 - p^2)^{\frac{1}{2}} \exp[-\sigma N(h+p)]dp \qquad (12)$$

Therefore, if a theoretical model of the vertical distribution of molecular oxygen is assumed, a plot of I(h) versus h can be derived from equation (12). This computed attenuation curve can be compared with the experimentally determined attenuation curve. Then, by an iteration procedure, a density profile can be obtained which gives a computed attenuation curve in accord with the observations. Note that although absolute values of I(h) are not required, the values relative to I_o are essential for the determination of a density profile. This is in contrast to the point-sun approximation method (Section 5.3.2) where density determinations are not dependent on any knowledge of I_o but

are instead dependent on the local gradient $(\frac{dI}{dx})$ of the flux.

In the method adopted here, the solar line source is considered to be divided into an odd number of sections, (2m + 1), such that the length of each section is $2R_s/(2m + 1)$. If the sections are numbered sequentially from the lower limit of the line source (as seen from the satellite) from -m to +m, then we may replace equation (12) by

$$I(h) = \sum_{i=-m}^{+m} A_i \frac{I_o}{\pi R_s} \exp[-\sigma N(h + p_i)] \qquad ...(13)$$

where $h + p_i$ is the minimum ray height of the ray from the centre of the i th section of the line source and A_i is the area of the strip of the solar disk replaced by the i th section. From Figure 5.4, it can be seen that

$$p_i = \frac{r_i d}{D} = \frac{d}{D} \frac{2iR_s}{(2m + 1)}$$

The value of m to be used in equation (13) must be such that for any assumed density distribution, an increase in this value produces no significant change in the resultant computed attenuation curve. The individual sections of the line source are then behaving as point sources. For the data from the Q-T and S-X ion chambers, a value of 2 was found to be sufficient for m. However, due to the much smaller density scale height of molecular oxygen in the height range where solar Lyman-α radiation is absorbed, a value of 7 was required for m for the LiF-NO ion chamber data.

The model chosen in this work to represent the vertical distribution of molecular oxygen is of the form

$$n(h) = \tfrac{1}{2}n(h_c)\{\exp[(h_c - h)/H_1] + \exp[(h_c - h)/H_2]\} \qquad \ldots(14)$$

where H_1 and H_2 are scale heights and h_c is the minimum ray height of the central solar ray when the rate of change of the ion chamber current is a maximum (Stewart and Wildman, 1969). A single exponential model (obtained by putting $H_2 = H_1$ in equation (14)) was tried initially but was found to be inadequate for the data from the Q-T and S-X ion chambers. If H_1 is smaller than H_2, then the model given by equation (14) is one in which the scale height at low altitudes approaches H_1 while the scale height at high altitudes approaches H_2.

It can be shown that when the point-sun approximation is valid the maximum rate of change of I(h) occurs at the penetration height (i.e., at the height where $I(h)/I_o = e^{-1} = 0.370$). For the data from the Q-T and S-X ion chambers, h_c was found to be close to the penetration height. The value taken for h_c was 150 Km for all the Q-T ion chamber data and 180 Km for all the S-X ion chamber data. However, for the LiF-NO ion chamber data, where the point-sun approximation is least valid (Section 5.5), h_c was found to be higher than the penetration height and in fact was close to the height at which the ion chamber current had been attenuated by 50%. This height varied from about 100 Km to 106 Km for the different sets of data.

For the density model given in equation (14), the columnar density for the ray from the centre of the i th section of the line source (which, as shown on page 103,can be considered as a point source) is given by

$$N(h_i) = \tfrac{1}{2}n(h_c)[2\Pi(R + h)]^{\frac{1}{2}}\left[(\exp[(h_c - h_i)/H_1]\ H_1^{\frac{1}{2}} + \exp[(h_c - h_i)/H_2]\ H_2^{\frac{1}{2}}\right] \qquad \ldots(15)$$

This equation is obtained by considering the right hand side of equation (14) to consist of two separate terms of the same form as the right hand side of equation (4). The steps shown in equations (5) to (8) can then be applied to each term and the results added to give equation (15).

Once the values of the parameters $n(h_c)$, H_1 and H_2 have been selected, columnar densities calculated from equation (15) can be used in equation (13) to generate a computed attenuation curve which may then be compared with the observations.

The alteration of the model parameters to improve the agreement between the experimental and computed attenuation curves is carried out in two steps:

(i) The central number density, $n(h_c)$, is multiplied by a scaling factor, A, such that the next computed curve generated is normalized to the experimental curve near the height h_c. The agreement between the two curves is then checked by means of the "chi-squared" test.

(ii) When the two curves have been normalized, H_1 and H_2 are adjusted to improve the agreement between the computations and the observations, at heights well below and above h_c respectively, and a new attenuation curve computed.

These two steps are repeated until no further improvement in the agreement between the computed and observed attenuation curves, as indicated by the chi-squared test, is possible. These steps are considered separately below and, for simplicity, only their application to the S-X ion chamber data will be considered in detail. The curve

fitting procedures used for the data from the LiF-NO and Q-T ion chambers were very similar to the one used for the S-X ion chamber data.

(a) Normalization of the theoretical curve

Each experimentally determined attenuation curve for the S-X ion chamber consisted of values of ion chamber current plotted as a function of the minimum ray height of the central solar ray, h, at height intervals of 5 Km (Section 5.4). As explained on page 104, the value of h_c taken for all the S-X ion chamber data was 180 Km. The effective molecular oxygen absorption cross-section for this ion chamber was taken to be 1.45×10^{-17} cm^2 (Section 2.3).

The first step in the normalization procedure is to calculate the mean relative error of the computed current values over the height range 175 Km to 190 Km. This is given by

$$S = 1/4 \sum_{h=175}^{190} \frac{I(h) - I'(h)}{I(h)}$$

where I(h) and I'(h) represent the experimental and computed ion chamber currents respectively. We require a new computed attenuation curve such that the current values are given by

$$I''(h) = I'(h)(1 + S)$$

and in particular we require

$$I''(180) = I'(180)(1 + S) \qquad \ldots(16)$$

This new computed curve will be in better agreement with the observations near 180 Km than the initial computed curve.

Suppose that when deriving the initial computed attenuation curve it is found that the i th section of the solar line source provides the greatest contribution to the value of I'(180). Then for the purpose of determining the scaling factor, A, the sun may be approximated to a point source located at the centre of the i th section of the solar line source. The minimum ray height of the ray from this point on the line source to the ion chamber is $180 + p_i$ (equation 13) and so we may write

$$I'(180) = I_o \exp[-\sigma N'(180 + p_i)] \qquad \ldots(17)$$

and

$$I''(180) = I_o \exp[-\sigma N''(180 + p_i)] \qquad \ldots(18)$$

where N' and N'' are the respective columnar densities of the initial and required density models. From equations (16), (17) and (18) we have

$$\ln\left[\frac{I'(180)}{I''(180)}\right] = \ln\left(\frac{1}{1+S}\right) = \sigma\,[N''(180 + p_i) - N'(180 + p_i)]$$

and so

$$N''(180 + p_i) = N'(180 + p_i)\left[1 + \frac{1}{\sigma N'(180 + p_i)} \ln\left(\frac{1}{1+S}\right)\right] \qquad \ldots(19)$$

$$= N'(180 + p_i)\, A$$

Therefore, from equation (15), we may write

$$n''(180) = n'(180)\, A \qquad \ldots(20)$$

where n'(180) and n''(180) are the respective number densities of the initial and required density models. This normalization procedure is repeated until the value of the factor A becomes within 0.5% of unity,

or reaches some minimum value. The chi-squared test is then applied to the whole of the normalized computed curve to test its agreement with the observations.

(b) Adjustment of the scale heights

For the S-X ion chamber data, H_1 is generally about a factor of three less than H_2 (Appendix A). Therefore for values of h much less than 180 Km the last exponential term in both equations (14) and (15) will become vanishingly small. As a result, a substantial change in H_2 will have little effect on the computed ion chamber currents at heights well below 180 Km. Similarly, a substantial change in H_1 will not greatly affect the computed ion chamber currents at heights well in excess of 180 Km. Therefore, essentially independent adjustments can be made to H_1 and H_2 to improve the agreement between the experimental and computed attenuation curves at altitudes well below and above 180 Km respectively.

Suppose that the values of current for the computed attenuation curve (normalized to the experimental curve as described in (a) above) are given by I'(h). Suppose also that the mean relative error in these theoretical current values over the height range 150 Km to 170 Km is T. Then, to improve the agreement between the computed and experimental attentuation curves over this height range, we require a new computed curve with current values over this height range given by

$$I''(h) = I'(h)\,(1 + T)$$

in particular we require

$$I''(160) = I'(160)\,(1 + T)$$

Suppose that when deriving the normalized computed attenuation curve, it is found that the i th section of the solar line source provides the greatest contribution to the value of I'(160). Then, for the purpose of determining the change required in H_1, the sun may be approximated to a point source located at the centre of the i th section of the line source. Therefore, we can see from equation (19) that

$$\frac{N''(160 + p_i)}{N'(160 + p_i)} = \left[1 + \frac{1}{\sigma N'(160 + p_i)} \ln\left(\frac{1}{1 + T}\right)\right] = B \quad \ldots(21)$$

where N" and N' are the respective columnar densities of the required density model and the density model producing the normalized computed attenuation curve.

As explained above, the last exponential term of equation (15) is small for heights well below 180 Km and so we may use the approximation

$$\frac{N''(160 + p_i)}{N'(160 + p_i)} = \exp[(20 - p_i)(1/H_1'' - 1/H_1')]\,(H_1''/H_1')^{\frac{1}{2}}$$

where the scale heights H_1'' and H_1' refer respectively to the required density model and the density model producing the normalized computed attentuation curve. If we assume that the change required in H_1 is small, we may make the approximation $(H_1''/H_1')^{\frac{1}{2}} = 1$. Therefore, from equation (22) we have

$$\ln\left[\frac{N''(160 + p_i)}{N'(160 + p_i)}\right] = (20 - p_i)(1/H_1'' - 1/H_1') \qquad \ldots(23)$$

Substituting equation (21) into equation (23) and re-arranging results in the expression

$$H_1'' = \frac{H_1'}{1 + \frac{H_1'}{(20 - p_i)} \ln B} \qquad \ldots(24)$$

Similarly, an improvement in the agreement between the computed and experimental attenuation curves, over the height range 195 Km to 220 Km, will occur if the scale height, H_2', of the density model producing the normalized theoretical curve, is changed to the value

$$H_2'' = \frac{H_2'}{1 - \frac{H_2'}{(30 + p_i)} \ln C} \qquad \ldots(25)$$

In this expression, C is given by

$$C = \frac{N''(210 + p_i)}{N'(210 + p_i)} = 1 + \frac{1}{\sigma N'(210 + p_i)} \ln\left(\frac{1}{1 + V}\right)$$

where V is the mean relative error in the computed current values between 195 Km and 220 Km and N''(210) and N'(210) are the respective columnar densities of the required density model and the density model producing the normalized theoretical curve.

The point-sun method of deriving molecular oxygen densities (Section 5.3.2) is shown in Section 5.5 to be of insufficient accuracy.

When using the finite-sun method described above, it was found that the changes required in the values of the parameters of the density model were generally small. Even though a point-sun approximation was used in their derivation, equations (20), (24) and (25) were found to be accurate enough to define a density profile in accord with the experimental data.

In the experimentally determined attenuation curves of the Q-T ion chamber (Section 5.4), values of ion chamber current were also given at 5 Km intervals and the fitting procedure used for this data was very similar to that described above. The value of h_c used was 150 Km while the comparison heights used for adjusting H_1 and H_2 were 130 Km and 180 Km respectively. The effective molecular oxygen cross-section was taken as 3.4×10^{-18} cm^2 (Section 2.3).

Ion chamber currents were determined at 2 Km intervals in the experimental attenuation curves of the LiF-NO ion chamber (Section 5.4). The value taken for h_c varied over the range 98 Km to 104 Km for the different sets of data considered. The effective molecular oxygen absorption cross-section was taken as 1.0×10^{-20} cm^2 (Section 2.3). A fitting procedure similar to that used for the S-X ion chamber data was tried, but it was found that to within the experimental error, an exponential model ($H_2 = H_1$ in equation (14)) was sufficient to fit the data. The comparison heights used to adjust the scale height were 14 Km above and 14 Km below h_c. The two correction factors obtained in this way were combined to produce an average correction factor for the scale height.

A computer program, compatible with the CDC 6400 digital computer of the University of Adelaide, was devised to carry out automatically the iterative fitting processes described above. The input for each density profile determination consisted of the experimentally derived ion chamber currents (at 5 Km or 2 Km height intervals), the appropriate values of A_i and p_i (equation (13)), the effective molecular oxygen absorption cross-section, σ (Section 2.3), and the initial values of the density model parameters $n(h_c)$, H_1 and H_2. After each normalization stage of the fitting procedure, the experimental and computed attenuation curves were printed out. Also printed out, was the attenuation curve that would have resulted if the sun was in fact a point source located at the centre of the solar disk. This latter curve was obtained by only considering the contribution to the ion chamber signal due to the central section of the solar line source. Also, solar intensity profiles were printed out for various values of h. Each profile consisted of a list of the contributions to the ion chamber signal due to the various sections of the line source. These values (which are given relative to a value of 1 for the contribution due to the unobscured centre section) are proportional to the intensity of each section of the line source (Figures 5.9 and 5.12). The solar intensity profiles made it simple to determine which section of the line source was contributing most to the ion chamber signal at a given value of h (Section 5.5).

5.4. Determination of the Attenuation Curves

5.4.1. Data Acquisition

Real-time telemetry signals from the satellite were recorded on magnetic tape at the various tracking stations shown in Figure 5.2. The satellite experienced both sunrise and sunset on every orbit but only those observations made within range of a telemetry station are available. All of the satellite sunrises occurred in the southern hemisphere as the satellite crossed the sunrise line on the earth. The satellite sunsets were confined to the northern hemisphere and occurred when the satellite crossed the sunset line. The Fairbanks, Alaska, telemetry station was the only station far enough north to be able to monitor the satellite as it experienced sunset. Those stations with their location names underlined in Figure 5.2 recorded telemetry data from the satellite as it passed through one or more sunrise. In Figure 5.2, an alpha-numeric system has been used to denote the location of the mean position of the sub-minimum ray height point of the central solar ray (the point T in Figure 5.4) for a recorded satellite sunrise or sunset. The letter represents the first letter of the recording station name and the number represents the number of the orbit. This number is referred to as the station pass number. During the time taken for h to vary from 90 Km to 240 Km at satellite sunrise, the latitude of the point T changes by about 2° while its longitude changes by about 1.8°. At satellite sunset these changes are about 0.2° and 7.0° respectively. In all, 17 usable satellite sunrises and 5 usable satellite sunsets were recorded during the period from

0738 hours U.T. on 29th November to 1758 hours U.T. on 2nd December, 1967.

The tracking station tapes were decoded by Weapons Research Establishment staff who then provided the Physics Department, University of Adelaide, with computer print-outs of the ion chamber currents as functions of time. The conversion of the telemetry voltages to ion chamber currents was made using the laboratory amplifier calibration curves (Section 5.4.2).

5.4.2. Amplifier Calibrations

Over the current ranges given for the ion chamber amplifiers described in Section 5.2.1, a plot of the logarithm of the input current of an amplifier versus its output voltage, results in a straight line graph. The slope of this graph is independent of the environmental conditions but the whole graph can shift as the ambient temperature varies. For this reason a system was included on the satellite to provide an in-flight calibration of each amplifier.

For an amplifier fed by a Q-T or S-X ion chamber a current of 2.03×10^{-9} amp was fed through a standard resistance to its input once every 30 seconds. For the less sensitive amplifiers, fed by the LiF-NO ion chambers, the calibration current was 1.67×10^{-7} amp. The conversion of the telemetry voltages on the tracking station tapes to ion chamber currents was performed using the laboratory calibration graphs. These currents were then corrected for amplifier drift by simply multiplying them by the ratio of the laboratory calibration current to the apparent in-flight calibration current.

This latter current was found by averaging over a pass the calibration current pulses given every 30 seconds in the computer print-out derived from the telemetry tapes.

5.4.3. Aspect Angle Determinations

As mentioned in Section 5.2.2, one magnetometer and two amplitude ratio optical aspect sensors were used to determine solar aspect relative to the detector packages. The aspect sensor pair in the front-facing package performed satisfactorily for the transmitting lifetime of the satellite and indicated minimum aspect angles between 0° and 5° for all of the passes investigated. Minimum solar aspect angles between 0° and5° were also found by Johnson (1970) from an analysis of the data from the flux-gate magnetometer, the axis of which was parallel to the satellite cone axis. Acting independently, the Royal Radar Establishment, Malvern, England, tracked WRESAT 1 during orbit 36 with a high powered tracking radar. From their radar data, they were able to determine the orientation in space of the rotational axis of the satellite. Assuming the spin axis of the satellite and the axis of the magnetometer are perpendicular, the radar measurements imply a minimum solar aspect angle for the front-facing package of about 2° (Johnson, 1970). This value is in excellent agreement with the aspect sensor and magnetometer determinations. These results indicate that the solar aspect relative to the front-facing package was changing by at most $\pm$2.5° with the mean value close to 2°. Variations of the aspect angle over this range will not produce a significant change in the output of an ion chamber (Figure 3.13).

It was not possible to obtain solar aspect information from the side-facing optical aspect sensor pair. This was a result of the break-down of the flush-teflon detector (Figure 4.5) in an early satellite pass. However, it was possible to derive aspect information for the side-facing package by using the side-facing protruding-teflon detector and the front-facing flush-teflon detector as a pair. This could be done as the ratio of the outputs of these two detectors, when exposed to the sun at zero aspect angle, had been determined in laboratory calibrations before launch. The in-flight zero aspect response of the side-facing protruding-teflon detector could therefore be determined from the in-flight zero aspect response of the forward-facing flush-teflon detector. The laboratory determined angular response curve of the side-facing detector could then be used to determine the minimum solar aspect angle for the side-facing package. This aspect angle, which varied very little throughout a pass and from pass to pass, was found to have a mean value of $30° \pm 3°$.

Provided the solar aspect angle is constant, it is not necessary to know its absolute value when making density determinations. However, the value of the aspect angle is essential for the measurement of absolute solar fluxes (Section 5.6).

5.4.4. Minimum Ray Height and Sub-Minimum Ray Height Point Determinations

Satellite orbital parameters for WRESAT 1 were provided at time intervals of 1 min by Goddard Space Flight Centre, Maryland, U.S.A. Included in these parameters were the latitude and longitude of the

sub-satellite point, the distance of the satellite from the centre of the earth (H in Figure 5.4) and the solar zenith angle at the satellite, Z.

As can be seen from Figure 5.4, the minimum ray height of the central solar ray is given by

$$h = H \sin Z - R$$

Owing to the deviation of the earth from a perfectly spherical shape, R cannot be assumed to be the radius of the earth at the sub-satellite point. For example, at satellite sunrise the sub-minimum ray height point is approximately 20° further south than the sub-satellite point. This results in R being approximately 7 Km less than the earth's radius at the sub-satellite point. Therefore, it is essential that the latitude, λ_{ray}, of the sub-minimum ray height point be known. The following expression was derived to calculate this value

$$\lambda_{ray} = \arcsin \left[\frac{\sin \lambda_{sat} = \cos Z \sin \lambda_{sun}}{\sin Z} \right]$$

In this expression λ_{sat} is the latitude of the sub-satellite point and λ_{sun} is the declination of the sun as determined from ephemeris tables. As the geographical location of each density determination was required, an expression was also derived whereby the longitude, θ, of the sub-minimum ray height point could be calculated.

The earth model used to calculate R was that used by Goddard Space Flight Centre (equatorial radius 6378.166 Km and flatness coefficient 1/298.25).

A computer program was developed to calculate h, λ_{ray}, θ, R, H and d (Figure 5.4) at 10 sec intervals throughout each satellite sunrise and sunset. As inputs the program had satellite orbital parameters at 1 min intervals, and solar ephemerides at 1 day intervals. Stirling's formula to second degree was used to interpolate between these values.

5.4.5. The Attenuation Curves

A peak was produced in the current output from each ion chamber as the detector looked towards the sun once every revolution of the satellite. These peak values were read from the computer print-out (derived from the telemetry tapes as described in Section 5.4.1) and tabulated as a function of time. The corresponding values of minimum ray height of the central solar ray, h, were determined from the print-out of the computer program described in Section 5.4.4. Plots of I(h) versus h were then produced and smooth curves fitted. As the variation in aspect angle throughout a sunrise or sunset was negligible (Section 5.4.3) no aspect corrections were applied to the currents.

Figure 5.5 shows the variation of ion chamber current with minimum ray height for Santiago pass 2, the first recorded WRESAT 1 sunrise. Data from all the ion chambers are shown. The ion chamber currents, which have not been aspect corrected nor corrected for amplifier drift, are plotted in arbitrary units. As pointed out on page 102, it is not necessary to know the absolute values of the ion chamber currents when determining number densities. However, their

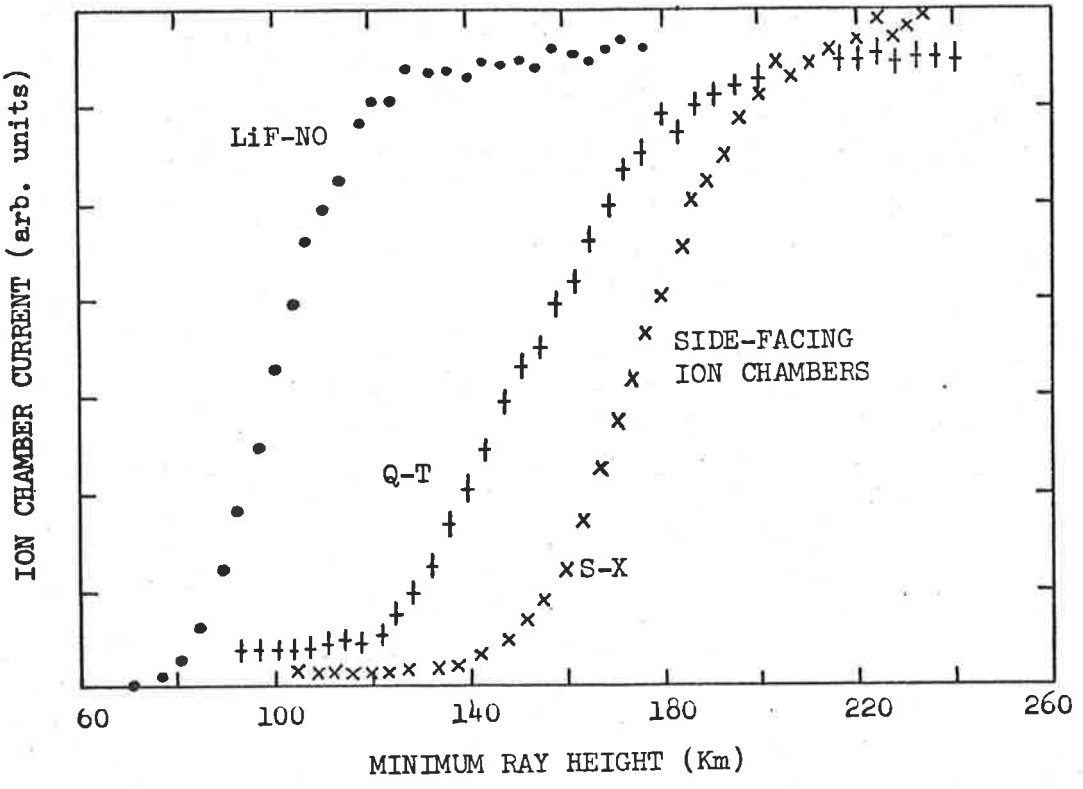

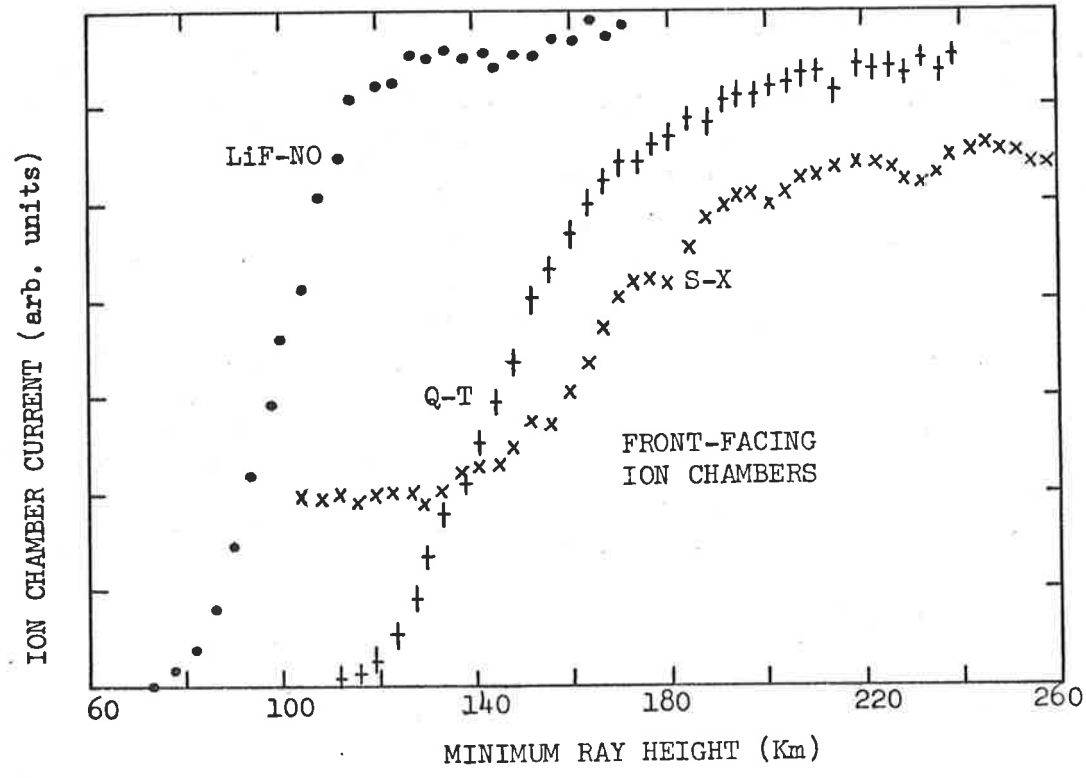

Fig.5.5 Response curves for both the front-facing and side-facing ion chambers for Santiago pass 2.

values relative to I_o the current due to the unobscured solar disk, must be known.

The signal from each ion chamber at very low values of h was less than 10^{-13}amp and represented the leakage current between the centre electrode and the guard ring (Section 3.2). For values of h between 50 Km and 70 Km an increase in the ion chamber signal was noted. This is thought to be a result of photoemission from the centre electrode and the back seal (which were both close to ground potential) caused by long wavelength radiation near 2100Å. This long wavelength signal, which has also been noted in the ion chambers carried by the U.K. ARIEL 3 satellite (Stewart and Wildman, 1969) reached a constant value for values of h above about 80 Km. The full-sun signal of each ion chamber was therefore I_o plus the long wavelength signal and the leakage signal. Due to the high values of I_o given by them, the long wavelength signal was negligible for the LiF-NO ion chambers (less than 0.2% of I_o) for all passes.

For the Santiago 2 pass, the long wavelength signal of the front-facing Q-T and S-X ion chambers and the side-facing Q-T and S-X ion chambers was respectively 1.0%, 32%, 6.0% and 2.5% of the full-sun signal. The very high long wavelength signal of the front-facing S-X ion chamber, coupled with the large differences noted in this chamber's full-sun signal at sunrise and sunset (Section 5.6), indicated that this detector was malfunctioning. Therefore, it was not used for the determination of molecular oxygen densities or absolute solar flux.

As explained in Section 5.6, the side-facing LiF-NO and Q-T ion chambers were also suspected of malfunctioning and so only the front-facing LiF-NO and Q-T ion chambers and the side-facing S-X ion chamber were used for density and flux measurements. The long wavelength signal of all the ion chambers was found to increase, as a percentage of the full-sun signal, as the orbit number increased. This was partially due to a decrease in the main short wavelength signal but was mainly a result of an absolute increase in the long wavelength signal.

Figures 5.6 and 5.7 show the variation of output current with minimum ray height for the front-facing LiF-NO and Q-T ion chambers and the side-facing S-X chamber. The data of Figure 5.6 apply to the satellite sunset, Fairbanks pass 16, while the data of Figure 5.7 apply to the satellite sunrise, Orroral pass 22. By orbit 22, the long wavelength levels of the front-facing Q-T and side-facing S-X ion chambers had increased to 6.2% and 14.5% of the full-sun signal respectively. For orbit numbers in excess of 26, the long wavelength signal of the Q-T ion chamber continued to increase above 80 Km and did not reach a constant value before the onset of the main short wavelength signal. It was therefore impossible to estimate accurately the level of the background signal to be removed from the main short wavelength signal and so this ion chamber was not used for density or flux determinations from orbit 27 onwards. For the same reason it was not possible to use the side-facing S-X ion chamber from orbit 36 onwards.

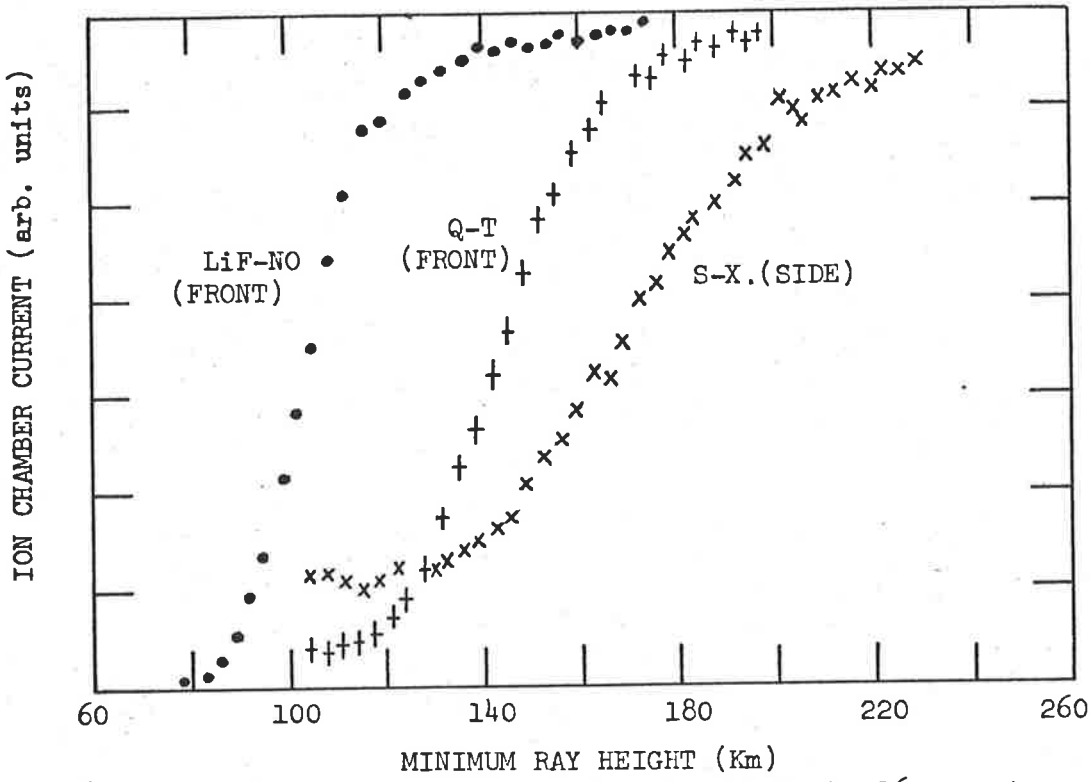

Fig.5.6 Ion chamber response curves for the Fairbanks 16 sunset pass.

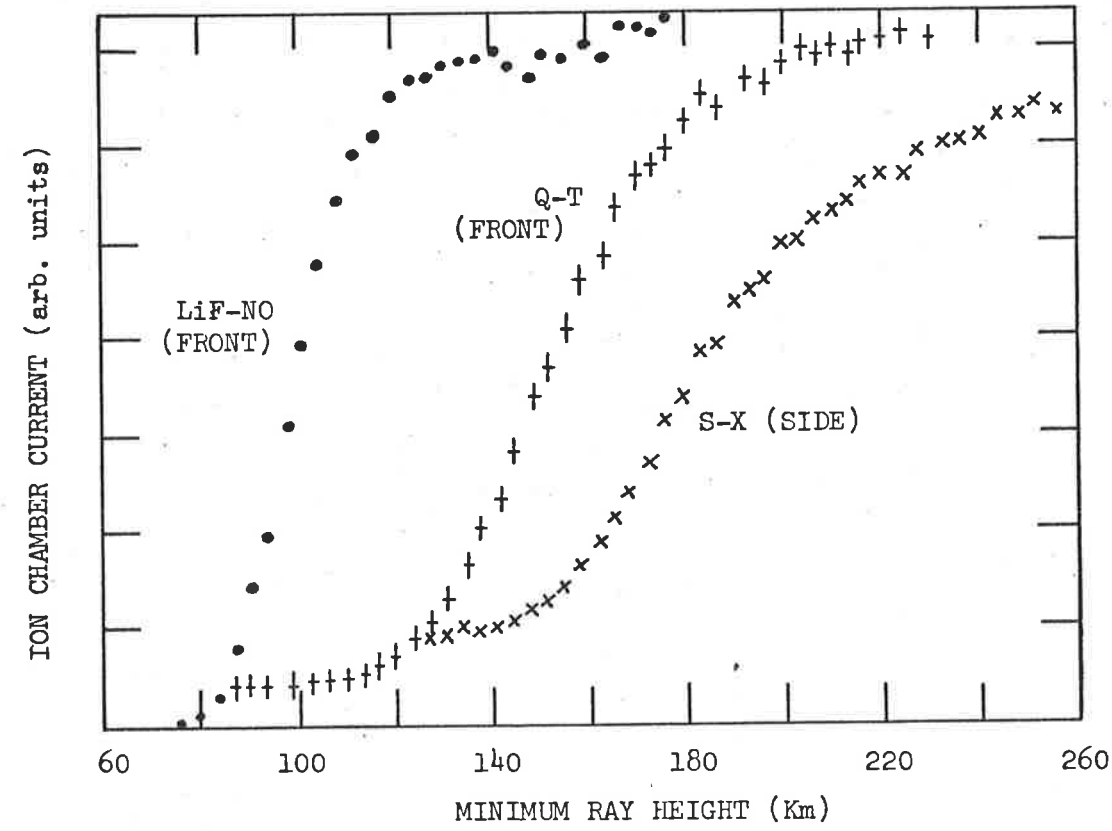

Fig.5.7 Ion chamber response curves for the Orroral 22 sunrise pass.

As can be seen from Figures 5.5, 5.6 and 5.7 the LiF-NO ion chamber signal reaches an almost constant level at heights near 140 Km. However, as expected (pages 29 and 90) an increase of about 10% in the ion chamber current is observed at greater heights. This increase is due to wavelengths other than Lyman-α in the pass-band of the detector. Owing to the much greater molecular oxygen absorption cross-section at these wavelengths, this radiation is absorbed at much greater altitudes than the Lyman-α radiation. The signal level near 140 Km is taken as the value of I_o for Lyman-α.

Attenuation curves were obtained from plots such as those shown in Figures 5.6 and 5.7 by subtracting the background levels (due to leakage and long wavelength effects) from the ion chamber currents. Each curve was then normalized to that I_o had the value 1. Values were read from the Q-T and S-X ion chamber attenuation curves at height intervals of 5 Km and from the LiF-NO ion chamber curves at height intervals of 2 Km.

5.5. Molecular Oxygen Density Results

The point-sun method of deriving molecular oxygen densities from the experimental attenuation curves (Section 5.3.2) was found to be of insufficient accuracy. The greatest errors occur for the data from the LiF-NO ion chamber, due to the small molecular oxygen density scale heights (approximately 6 Km) that prevail in the height range where solar Lyman-α radiation is absorbed. The errors are somewhat less for the Q-T ion chamber data and even less for the S-X ion chamber

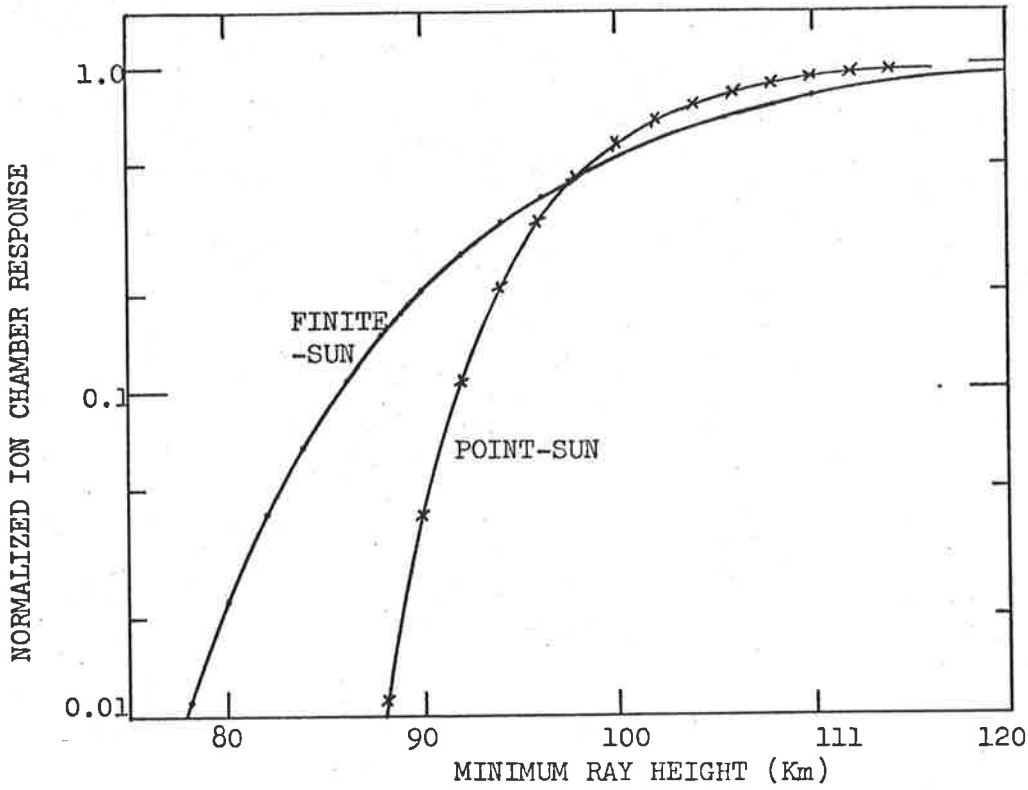

Fig.5.8 Computed attenuation curves for the LiF-NO ion chamber for Orroral pass 22.

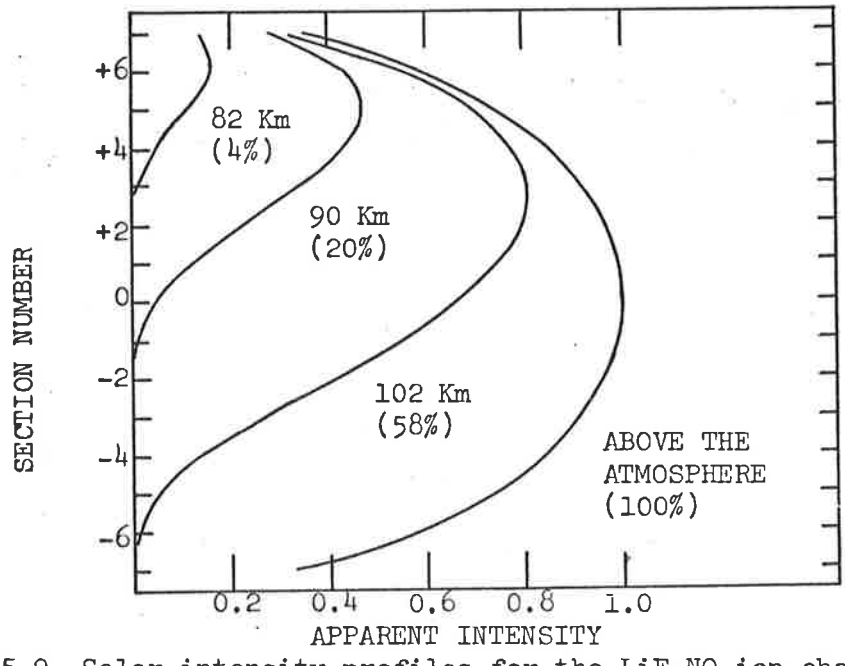

Fig.5.9 Solar intensity profiles for the LiF-NO ion chamber for Orroral pass 22.

data. The degree of inaccuracy introduced by the employment of the point-sun approximation is discussed below.

Figure 5.8 shows the computed attenuation curve which gives the best fit to the experimental data obtained from the front-facing LiF-NO ion chamber during the satellite sunrise, Orroral pass 22. This curve was obtained from the print-out of the fitting program used in the finite-sun method of analysis (Section 5.3.3). Shown for comparison is the attenuation curve computed for the same molecular oxygen density profile, assuming that the sun is a point source located at the centre of the solar disk (i.e., assuming that only the centre section of the solar line source is contributing to the ion chamber signal). This curve was also obtained from the fitting program (page 112). The explanation for the great disparity between these two curves can be seen from Figure 5.9 which shows the corresponding solar intensity profiles (page 112) for several values of h and also for the unobscured sun. The difference in the minimum ray height for rays to the satellite from the centres of adjacent sections of the line source is 2.19 Km. For each value of h, the corresponding value of ion chamber signal is shown as a percentage of I_o. It is clear from Figure 5.9, that even for ion chamber signals with values well in excess of 60% of I_o, the central section of the line source is still not the main contributor to the ion chamber signal. The point-sun approximation method developed in Section 5.3.2 is therefore completely inadequate.

The density profiles resulting from a finite-sun and point-sun analysis of the LiF-NO ion chamber data for the Orroral pass 22 sunrise are shown in Figure 5.10. As can be seen from Figure 5.10, the

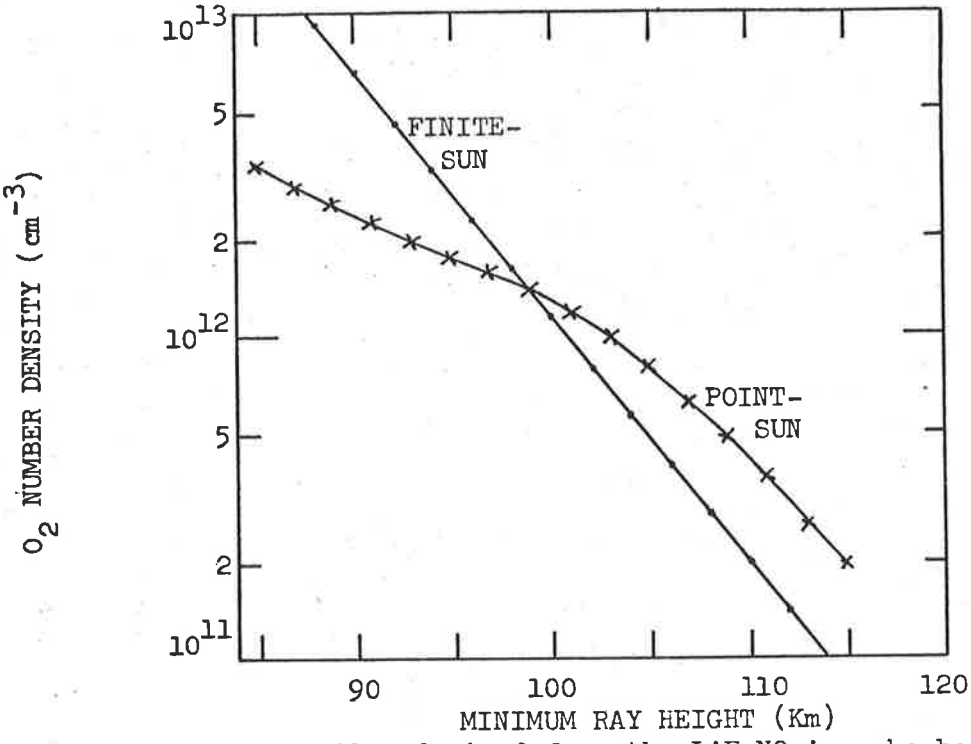

Fig.5.10 Density profiles derived from the LiF-NO ion chamber data of the Orroral pass 22 by both finite-sun and point-sun analysis.

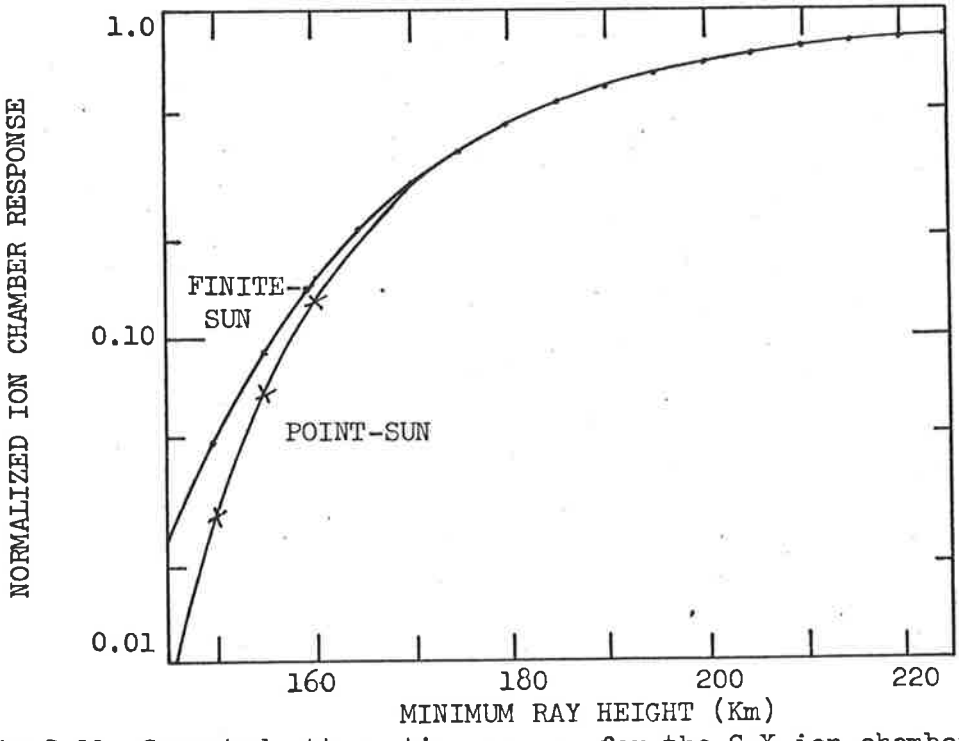

Fig.5.11 Computed attenuation curves for the S-X ion chamber for Orroral pass 22.

errors in the number densities resulting from the use of the point-sun approximation are large across almost the entire height range over which the LiF-NO ion chamber responds. The best agreement between the profiles occurs near the height where the ion chamber current is approximately 50% of I_o. This height corresponds closely to h_c, the height at which the ion chamber signal is changing most rapidly with height (page 104).

Figure 5.11 shows finite-sun and point-sun computed attenuation curves for the S-X ion chamber data from the satellite sunrise, Orroral pass 22. These curves were obtained in the same way as those shown in Figure 5.8 for the LiF-NO ion chamber data from the same sunrise pass. Figure 5.12 shows some of the corresponding solar profiles. By comparing Figures 5.11 and 5.12 with Figures 5.8 and 5.9, it can be seen that the point-sun approximation is much more valid for the S-X ion chamber data than for the LiF-NO ion chamber data. This is due to the much greater density scale height of molecular oxygen (approximately 20 Km) across the height range where the solar radiation in the wavelength range 1420Å to 1470Å is being absorbed.

Figure 5.13 shows the density profiles obtained from a finite-sun and point-sun analysis of the S-X ion chamber data for the Orroral pass 22 sunrise. The agreement between these profiles is much better than for the corresponding LiF-NO ion chamber profiles but the point-sun approximation still introduces significant errors below about 190 Km.

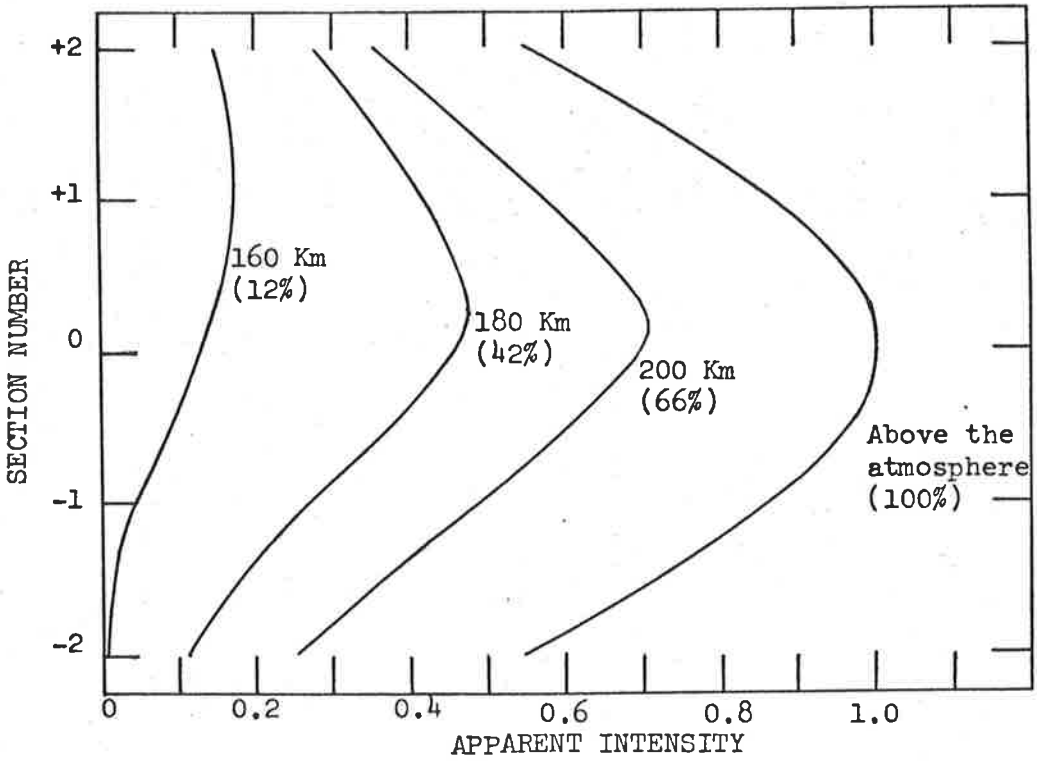

Fig.5.12 Solar intensity profiles for the S-X ion chamber for Orroral pass 22.

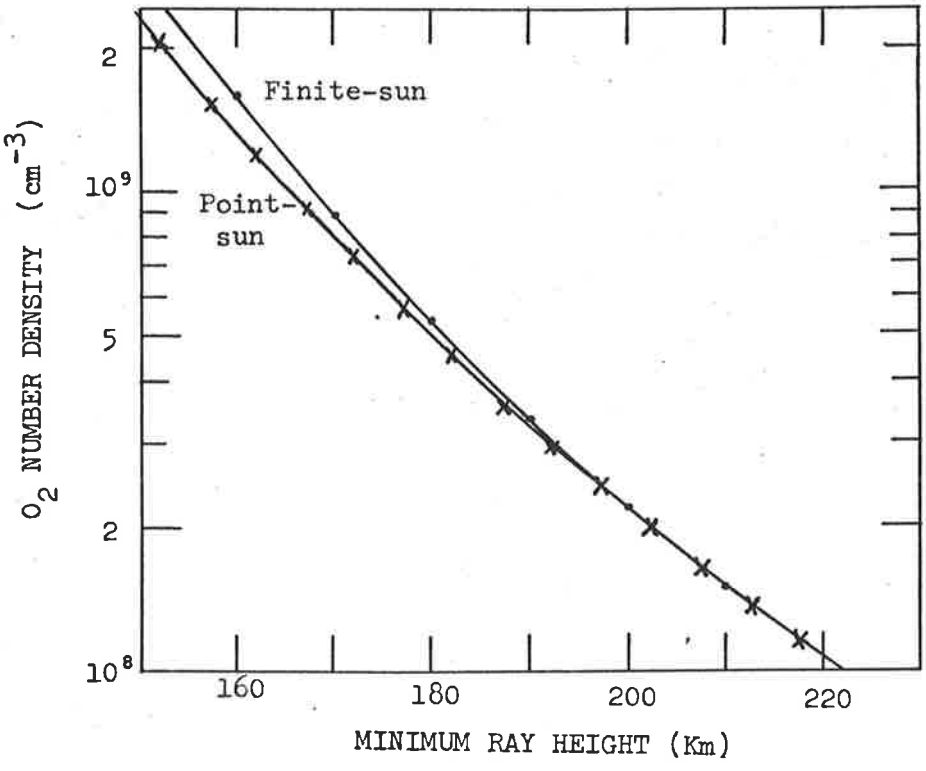

Fig.5.13 Density profiles derived from the S-X ion chamber data of Orroral pass 22 by both finite-sun and point-sun analysis.

For the Q-T ion chamber data the errors introduced by the point-sun approximation are intermediate between those for the LiF-NO and S-X ion chamber data.

Due to the inaccuracy of the point-sun method, only the finite-sun fitting procedure described in Section 5.3.3 was used to derive molecular oxygen number density profiles. The results are given in Appendix A in order of the pass number of the observations. The date of each observation is given together with the time, t_{150}, at which h was 150 Km. The mean geographical position of each observation is given by the values of the latitude and longitude of the sub-minimum ray height point of the central solar ray at t_{150}. These values, obtained from the print-out of the computer program described on page 118, were used to display the positions of the recorded satellite sunrise and sunset density measurements in Figure 5.2.

The number density results have been presented both in tabular form and in the form of the final values of the density model parameters $\hat{n}(h_c)$, H_1 and H_2 ($H_1 = H_2 = H$ for the LiF-NO ion chamber results). No real physical significance can be given to the values obtained for H_1 and H_2 as these scale heights refer to altitudes well outside the range over which the experiment gives accurate results. The values of H_1 and H_2 are not obtained with great precision by the fitting procedure. However, the local scale height at the altitude h_c, $H(h_c)$, is determined with greater precision and is given by

$$H(h_c) = 2H_1H_2/(H_1 + H_2)$$

Therefore, for the Q-T and S-X ion chamber results the local scale height is given at 150 Km and 180 Km respectively.

In presenting the density results, the notation a(b) has been used as an abbreviation for a x 10^b. The probable error, E, of the density values, has been given in the tables at the height h_c and at the extremities of the height range over which each density profile has been given. These errors, which do not include errors due to height uncertainties and uncertainties in the values of the effective molecular oxygen absorption cross-sections used, are discussed in Section 6.2. Also given in the tables are the values of the vertical columnar density* (VCD).

The WRESAT I density results are compared with the rocket results described in Chapter 4 and with the results of other workers, in Section 6.2.

5.6. Solar Flux Results

As stated in Section 5.4.5, a peak was produced in the current output from each ion chamber as the detector looked towards the sun once every revolution of the satellite. The total signal in full sunlight (or the full-sun signal) was derived for each Q-T and S-X ion chamber by averaging the peak currents over a period of at least 2 minutes for times when h was greater than 350 Km. The value of I_o was then obtained by subtracting the background signal, due to leakage

---

*The vertical columnar density at the height, h, is the number of oxygen molecules in a vertical column, of cross-sectional area 1 cm^2, above the height h.

and long wavelength effects (Section 5.4.5), from the full-sun signal. As the background level was negligible for the LiF-NO ion chambers (page 119) the value of I_o for each of these detectors was obtained simply by averaging the peak current values for heights near 140 Km (page 121).

The values of I_o obtained in this way were corrected for amplifier drift (as described in Section 5.4.2) and also corrected to their zero aspect values. As shown in Section 5.4.3, the minimum solar aspect angle could be taken as 0° for the front-facing detectors with negligible error. An in-flight calibration curve could therefore be obtained for the angular response of the front-facing ion chambers. All of the ion chambers had the same geometry except for slight differences in window thickness which had only a minor effect on the angular response. Therefore, the in-flight calibration curves could be used to derive an aspect correction factor for the side-facing ion chambers. In this way, the minimum solar aspect angle of 30° $\pm$3° that was determined for the side-facing detector package (Section 5.4.3), was found to result in an aspect correction factor of 1.66 $\pm$0.13.

Figure 5.14 shows, as a function of time, the values of I_o obtained for each ion chamber after corrections for amplifier drift and aspect corrections had been made. It was generally difficult to estimate accurately the background signal level for the Q-T and S-X ion chambers on those passes where the satellite was always in full sunlight. For this reason, the values of I_o given in Figure 5.14 for the Q-T and S-X ion chambers refer only to satellite sunrise and sunset passes. The background signal for the LiF-NO ion chambers was

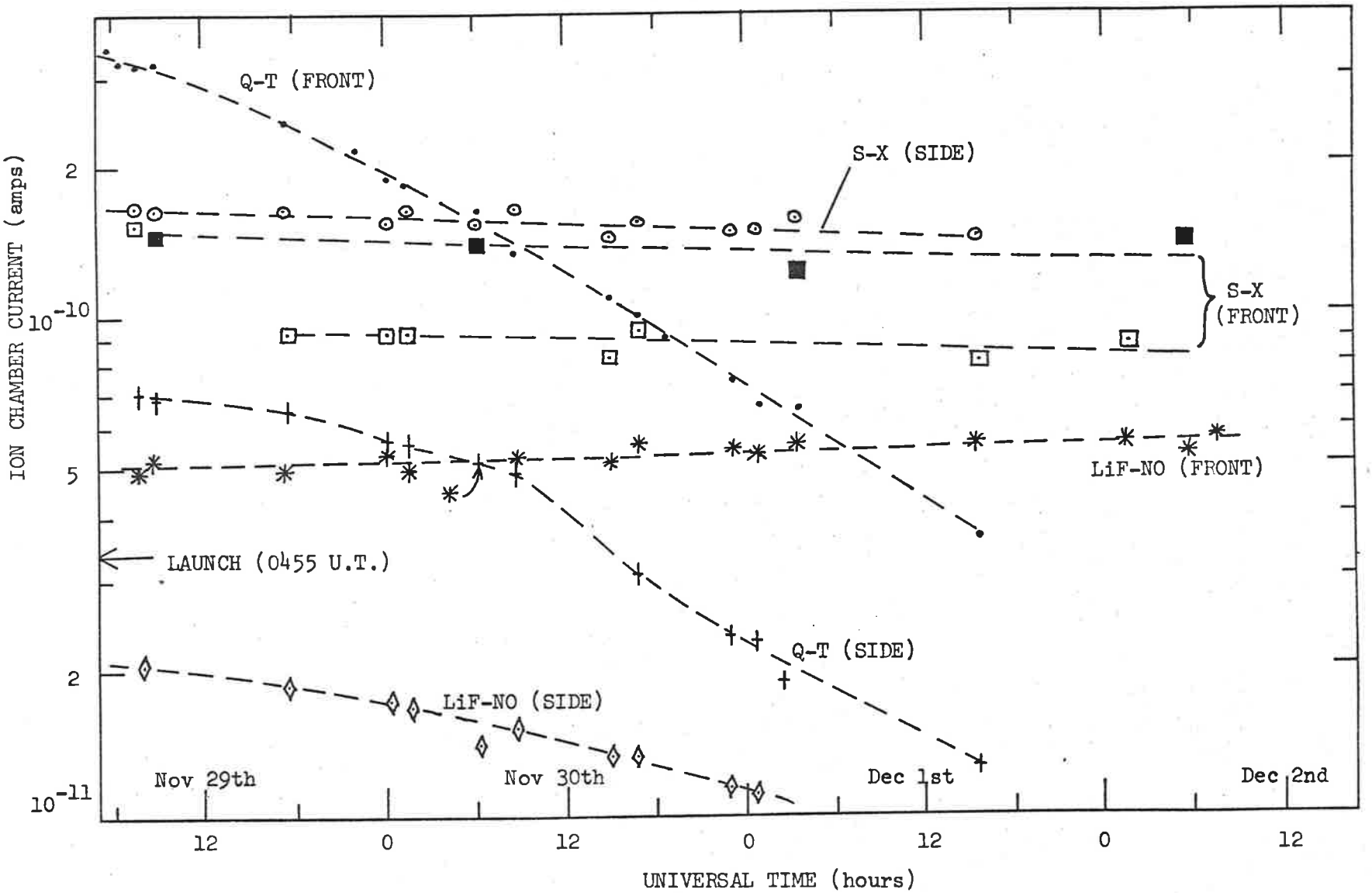

Fig.5.14 Output current as a function of time for the WRESAT 1 ion chambers.

negligible on all passes. However, to determine the value of I_o for a pass in which the satellite was always in full sunlight, the contribution to the LiF-NO ion chamber signal due to Lyman-α alone had to be estimated. The contribution to the total signal due to wavelengths other than Lyman-α was determined for all of the sunrise and sunset passes. The average contribution was found to be 11% with a standard deviation of approximately 2%. Therefore, on passes where the satellite was always in full sunlight, I_o was derived for each LiF-NO ion chamber by multiplying the full-sun signal by 0.89. As Figure 5.14 is only intended to show the general trend with time of the ion chamber signals only the I_o values for the sunrise and sunset passes are shown for the LiF-NO ion chambers.

Apart from a small difference, due to a difference in their quantum efficiencies, ion chambers of the same type should have given the same value of I_o for the same satellite pass. From Figure 5.14 it can be seen that the side-facing LiF-NO and Q-T ion chambers gave much smaller values of I_o than did their front-facing counterparts. For this reason, these detectors were not used for the solar flux or atmospheric density determinations. The reason for the initially low value, and the decrease with time, of the output of each of these detectors is not known. Loss of the filling gas due to a small leak developed during launch of the satellite could explain this behaviour.

The values of I_o obtained for the front-facing S-X ion chamber have been presented in Figure 5.14 in two groups. Those values indicated by open squares refer to sunrise observations while those indicated by solid squares refer to sunset observations. It can be

seen that for all but the first recorded satellite sunrise (Santiago pass 2) the value of I_o is much less at sunrise than at sunset. A thermistor attached to the mounting block of the front-facing detector package was used to monitor the temperature of the front-facing ion chambers. This thermistor indicated that from orbit 8 onwards, the temperature of the front-facing package cycled between 8°C at satellite sunrise and 20°C at satellite sunset (Hind and Beach, 1969). However, for the first seven orbits, the satellite was cooling down from the high temperatures reached during the launch phase. As a result, the temperature of the front-facing package was approximately 25°C during the Santiago pass 2 sunrise and during the Fairbanks pass 3 sunset. The temperatures prevailing during all subsequent recorded satellite sunrise and sunset passes were 8°C and 20°C respectively. Therefore, the output from the front-facing S-X ion chamber seems to be temperature dependent, giving a much higher value of I_o at temperatures near 20°C than at temperatures near 8°C. As can be seen from Table 3.3, the change in sensitivity of a S-X ion chamber over this temperature range is expected to be very small. This is verified by the fact that to within the experimental error, no significant systematic difference could be found between the sunrise and sunset values of I_o obtained from the side-facing S-X ion chamber. The front-facing S-X ion chamber was not used for solar flux or density determinations owing to its very large long wavelength signal (Section 5.4.5) and to the large difference between its values of I_o at sunrise and sunset.

The front-facing Q-T ion chamber showed a rapid decrease in its output with time. The reason for this is not known but it seems likely that it is a result of the decay of the triethylamine filling gas under the action of ultraviolet radiation. Another possible cause of the decrease is the loss of transmission of the quartz window due to X-ray irradiation (Friedman, 1960a). That the spectral response of this ion chamber was not substantially changed by these effects, is demonstrated by the good agreement between the molecular oxygen density profiles obtained from this detector and from the side-facing S-X ion chamber (Appendix A).

Both the side-facing S-X ion chamber and the front-facing LiF-NO ion chamber showed relatively small changes in output with time. The side-facing S-X ion chamber showed a gradual decrease in the value of I_o. This was to be expected, as the outputs of the S-X ion chambers flown on the British satellite ARIEL 3 (Stewart and Wildman, 1969) were found to decrease owing to the deterioration of the p-xylene filling gas under the action of ultraviolet radiation. The front-facing LiF-NO ion chamber was the only detector to show an increase in output during the transmitting lifetime of the satellite. The output of this detector showed a gradual rise of about 8% over the 3-day period indicated in Figure 5.14.

For the purpose of determining solar flux values, smooth curves were fitted to plots of I_o versus time for the front-facing Q-T and side-facing S-X ion chambers. These curves were then extrapolated back to the time of the first satellite orbit. This extrapolation was assisted for the Q-T ion chamber by including values of I_o measured in

orbits 1 and 2 for passes where the satellite was always in full sunlight. As the background signal level for this ion chamber was only about 1% of the full-sun signal for the early passes (Page 119) it was possible to accurately estimate the value of I_o from the full-sun value. The first orbit values of I_o, obtained by extrapolation, were 3.40×10^{-10} amp and 1.68×10^{-10} amp for the Q-T and S-X ion chambers respectively.

The S-X and Q-T ion chambers respond to radiation in the wavelength bands 1420Å to 1480Å (i.e. a full width at half maximum, FWHM, response of 1430Å to 1470Å) and 1550Å to 1690Å (1580Å to 1640Å FWHM) respectively (Figures 3.11 and 3.12). To obtain solar flux values from the Q-T and S-X ion chamber current measurements, obtained as described above,it was assumed that the solar continuum spectrum in these wavelength bands could be represented by that of a black body at temperature T. The laboratory calibrations of the efficiency (Section 3.6.3) and spectral response (Section 3.6.2) of each ion chamber were then used to calculate the ion chamber current which would be produced for different values of T. In this way, a brightness temperature was deduced which agreed with the satellite observations. The contributions of emission lines to the ion chamber currents were estimated using the solar spectral data of Detwiler et al. (1961 a and b), page 3, a portion of which has been presented in a convenient digitalized form by Brinkman et al. (1966)(Figure 3.14). These contributions were 4.5% for the Q-T ion chamber and 12% for the S-X ion chamber. After making these comparatively small corrections

for the effects of emission lines, the brightness temperature for the continuum was found to be 4590°K for the wavelength region 1580Å to 1640Å (Q-T ion chamber) and 4540°K for the region 1430Å to 1470Å (S-X ion chamber).

As can be seen from Figure 3.14, the percentage of the ion current that is contributed by emission lines will vary as the temperature of a S-X ion chamber changes. However, no significant variation is expected over the temperature range from 8°C (satellite sunrise) to 20°C (satellite sunset). For this reason, the laboratory derived spectral response curve, determined at room temperature, was used in the solar flux determinations for the side-facing S-X ion chamber.

The uncertainty in the estimated solar flux values, arising from errors in the laboratory calibrations, errors in the telemetry transmission and errors in estimating the first orbit values of I_o, amounted to $\pm$ 15%. An additional uncertainty of $\pm$ 8% in the intensity levels resulted from errors in the aspect correction factor for the side-facing S-X ion chamber (page 126).

An ion chamber responding to radiation in the wavelength band 1440Å to 1660Å (1470Å to 1570Å FWHM) has been orbited on the SOLRAD 10 satellite (Chubb et al., 1971). Using laboratory calibrations provided by the U.S. Naval Research Laboratory, some of the SOLRAD 10 observations were analysed in the same way as was done for the WRESAT 1 data. In the case of the SOLRAD 10 ion chamber, the results of Detwiler et al. (1961b) indicate that emission lines contribute about 25% of the

observed signal. After making this correction, the SOLRAD 10 ion chamber data indicated a brightness temperature of 4525°K for the solar continuum in the wavelength region 1470Å to 1570Å FWHM.

As the front-facing LiF-NO ion chamber showed no signs of deterioration during the transmitting lifetime of the satellite (Figure 5.14), the individual values of I_o were converted to Lyman-α flux values using the known effective area of the detector (1.60 cm^2) and its absolute quantum efficiency at Lyman-α (Section 3.6). The uncertainty in the Lyman-α flux values, due to random errors in the telemetry transmission and errors in determining the values of I_o, is estimated to be $\pm$ 6%. There is also a systematic uncertainty of approximately $\pm$ 6% due to errors in the laboratory calibration of absolute efficiency.

The WRESAT 1 and SOLRAD 10 solar flux values are discussed and compared with other measurements in Section 6.3.

CHAPTER 6

DISCUSSION AND COMPARISON OF THE SATELLITE AND ROCKET RESULTS

6.1. Measurements of Molecular Oxygen Density

6.1.1. Introduction

As mentioned in Section 2.1, the two basic methods for determining the concentration of molecular oxygen in the upper atmosphere are ultraviolet absorption spectroscopy and mass spectroscopy. Some measurements that have been made by other workers, using these techniques, are discussed in Sections 6.1.2 and 6.1.3. The discussion is limited to those results most suitable for comparison with measurements made in the present work.

6.1.2. Measurements by Absorption Spectroscopy

Both narrow-band dispersive instruments and broad-band non-dispersive instruments have been used in the application of absorption spectroscopy. The most successful non-dispersive detector that has been employed is the ultraviolet ion chamber.

Ion chambers of various types have been used by Weeks and Smith (Smith and Weeks, 1965, Weeks and Smith, 1968) in a series of ten rocket flights between 15th July, 1964 and 31st January, 1967. The use of solar zenith angles in the range 19° to 95° made possible the determination of molecular oxygen densities over the height range 62 Km to 154 Km (page 38). Eight of the flights were made in the northern hemisphere at latitudes between 38°N and 40°N. The other two flights

were made in the southern hemisphere at latitudes 44°S (9th April,1965) and 32°S (12th November,1966). As the density measurements were made at different times of day and in different seasons, Weeks and Smith (1968) have been able to draw some tentative conclusions regarding seasonal and diurnal variations. Some of the results of Weeks and Smith (1968) are compared with the present results in Figures 6.1, 6.2, and 6.4.

There have been very few determinations of molecular oxygen density in the southern hemisphere. In rocket flights from Woomera in December 1963 and February 1965 (Carver et al., 1964, 1965) LiF-NO ion chambers were used to determine molecular oxygen densities in the height range 70 Km to 90 Km. The results of the 1965 flight are compared with the present rocket results in Figure 6.1. In a rocket flight from Woomera in November 1966, molecular oxygen densities were determined from 70 Km to 150 Km using ion chambers of six different types (Carver et al., 1969). Wildman et al. (1969) have flown S-X ion chambers on sun-stabilized Skylark rockets in a series of three experiments launched from Woomera in March and November 1967 and March 1968. From the data of these flights, molecular oxygen density profiles have been derived over the height range 100 Km to 150 Km. One of these profiles is compared in Figure 6.4 with the present satellite results.

Ion chambers have also been used in satellite occultation experiments, similar to the WRESAT I experiment, to determine molecular oxygen densities at satellite sunrise and sunset. Norton and Warnock

(1968) have analysed SOLRAD 8 LiF-NO ion chamber data from winter (December 1966) and summer (June to August 1967) satellite passes over the Boulder, U.S.A. telemetry station (40°N, 105°W) and from summer (December 1966) passes over the Orroral, Australia, telemetry station (36°S, 149°E). Although there is some scatter in the data, a preliminary analysis has indicated a seasonal variation in the molecular oxygen number density near 100 Km. The summer data are a mixture of sunrise and sunset observations and to within the experimental error no systematic difference was detected between the density values determined at sunrise and sunset (Norton, 1970). Also, unpublished winter data measured at sunset fall within the same scatter as the winter sunrise data (Norton, 1970). The SOLRAD 8 results are compared with the WRESAT I results on page 144.

Stewart and his co-workers (Stewart and Wildman, 1968, 1969 and Parker and Stewart, 1972) have analysed S-X ion chamber data received from the ARIEL 3 satellite during the period from May to November 1967. Preliminary results indicate geomagnetic,diurnal and longitutinal variations in the molecular oxygen density at 180 Km. A comparison between the ARIEL 3 and WRESAT 1 results is given in Figure 6.3.

More recently, Felske et al. (1970) have reported the determination of molecular oxygen density using data received from LiF-NO ion chambers orbited on the INTERKOSMOS I satellite. Uncertainties in the satellite orbit led to a height uncertainty of $\pm$ 5 Km. However, from Lyman-α absorption data obtained on 15th October 1969, it was concluded that the molecular oxygen densities in the height

range 90 Km to 105 Km were significantly lower than the corresponding mean 1965 CIRA model atmosphere values (CIRA, 1965). A comparison is made between the INTERKOSMOS I and the WRESAT I results on page 144.

Hinteregger and his co-workers (Hall et al., 1965, 1967) have used the photoelectric monochromators described in Section 1.1.2 to measure the atmospheric absorption of solar ultraviolet radiation. These instruments could only be used above an altitude of about 120 Km owing to the effect of the atmospheric gases on the open photomultiplier. Absorption analysis was carried out at the wavelengths of nine strong solar emission lines between 304Å and 1207Å. Molecular oxygen density profiles were derived directly from the measurements of the 1207Å (Si III) line while measurements of the other emission lines were combined to give O_2, N_2 and O density profiles. Results obtained by Hall et al. (1965) are compared in Figure 6.3 with the WRESAT I results.

Molecular oxygen density determinations by absorption spectroscopy have been discussed above for two different types of instrument. Of these instruments, the photoelectric monochromator provides the most detailed information. However, the operation of this instrument is limited to altitudes above 120 Km and it requires the use of a pointing control. Also, the density determinations rely on an accurate knowledge of the absorption cross-sections of the atmospheric constituents. Ion chambers have the advantage of not requiring a pointing control and their ruggedness and small size allow them to be used in small (and relatively inexpensive) unstabilized sounding rockets. Although the information provided by ion chambers is less detailed than that provided

by spectrometers, the height resolution of the data is generally better. As for the spectrometer, the ion chamber density determinations rely on an accurate knowledge of absorption cross-sections (Section 2.3).

6.1.3. Measurements by Mass Spectroscopy

In a completely different approach to the problem of the measurement of atmospheric composition, Nier and his co-workers have flown mass spectrometers in a number of rockets. On 30th November,1966 (night) and 2nd December,1966 (day) mass spectrometers were flown to investigate diurnal effects in the lower thermosphere (Kasprzak et al., 1968). Very little difference was found between the daytime and nighttime molecular oxygen densities in the height range 120 Km to 220 Km. A further flight on 21st June,1967 and two more flights on 20th July,1967 were made by the same group (Krankowsky et al., 1968). The flights on 20th July were a true day-night pair and it was found that the daytime molecular oxygen densities were substantially higher than the nighttime densities (Figure 6.3). However, the very small difference observed between the daytime and nighttime densities measured in the 1966 flights indicates that day-to-day variations in the altitude range 120 Km to 200 Km are at least as important as the diurnal effect.

The mass spectrometer does not require a pointing control; it can be operated at night and the density determinations are independent of any knowledge of absorption cross-sections. Its main disadvantages are that it can only be used above 120 Km and it is very difficult to

calibrate absolutely (Nier et al., 1964). Difficulties also arise from the dependence of its response on the orientation of the rocket and from its susceptibility to contamination.

6.2. Discussion of the Density Results

6.2.1. The Rocket Measurements

In Figure 6.1, the molecular oxygen density profiles obtained from the HAD 309 (winter) and HAD 310 (summer) rocket flights at Woomera (Section 4.4.1) are compared with the mean 1965 CIRA model atmosphere (CIRA, 1965).

The uncertainties in the HAD results are discussed in Section 4.4.1. The maximum random uncertainty in the HAD 309 density values is $\pm$ 7% over the height range 80 Km to 100 Km. There is also a height uncertainty of $\pm$ 1 Km which results from uncertainties in the rocket trajectory (Section 4.3.5). The maximum random uncertainty in the HAD 310 density values is $\pm$ 8% over the height range 82 Km to 96 Km. As shown in Section 4.4.1, there is a systematic uncertainty of $\pm$ 14% in the results from both of the HAD flights owing to an uncertainty of $\pm$ 14% in the value of 1.0×10^{-20} cm^2 taken for the absorption cross-section of molecular oxygen at Lyman-α.

The HAD 309 results represent the first winter measurement of molecular oxygen density below 100 Km that has been made in the southern hemisphere. The most obvious difference between the HAD 309 and HAD 310 results is that the average scale height of the former (7.5 Km) is considerably greater than that of the latter (6.5 Km). The two HAD

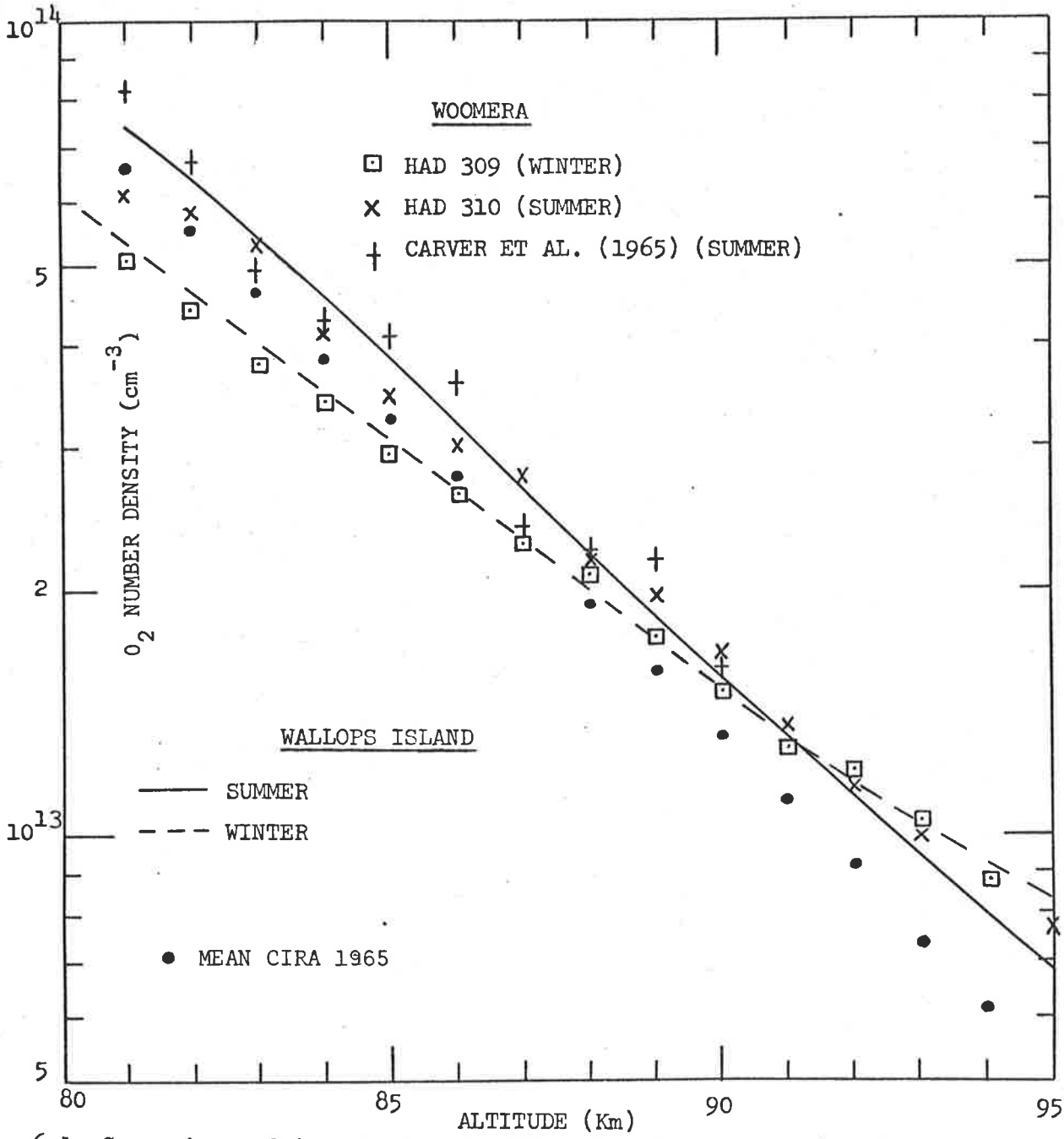

Fig.6.1 Comparison of ion chamber density determinations in the 80-95 Km altitude range.

profiles taken together suggest a region near 91 Km where the density is the same in summer and in winter. Models of the total neutral atmosphere given by the U.S. Standard Atmosphere Supplements (1966), are in agreement with the HAD results in indicating a larger scale height in winter and a region near 90 Km where the density is essentially the same in winter and summer.

Also shown in Figure 6.1 is a density profile obtained by Carver et al. (1965) from a summer rocket flight at Woomera and two smooth curves representing average daytime profiles obtained from rocket flights at Wallops Island (38°N) in winter and summer by Weeks and Smith (1968). The results of Carver et al. (1965) and Weeks and Smith (1968) were also obtained by the use of LiF-NO ion chambers. It can be seen from Figure 6.1 that the summer profiles measured by Carver et al. (1965) and Weeks and Smith (1968) are in good agreement with the summer profile from HAD 310. The winter profile measured by Weeks and Smith (1968) is in good agreement with the winter profile from HAD 309. Other summer measurements from Woomera (Carver et al., 1964, Carver et al., 1969) are also in substantial agreement with the HAD 310 results.

Below approximately 85 Km the present results are, on the average, in agreement with the values given by the mean 1965 CIRA model atmosphere (CIRA, 1965). However, at greater altitudes the observed values are significantly higher than those of the mean CIRA model. The local scale height of the mean CIRA model at 85 Km is 5.6 Km which is substantially lower than that observed in the present measurements.

6.2.2. The Satellite Measurements

The uncertainties in the molecular oxygen densities determined from the WRESAT I data varied greatly from pass-to-pass. The most accurately determined parameters for each profile given in Appendix A are the number density and local scale height at the height h_c ($n(h_c)$ and $N(h_c)$ respectively). The random uncertainties in the density values arising from telemetry errors and errors in the fitting procedure are given in Appendix A for each pass. However, there are other important uncertainties which must be considered.

As pointed out in Section 6.2.1, there is a systematic uncertainty of $\pm$ 14% in the number densities determined from the LiF-NO ion chamber data, owing to uncertainties in the value of the absorption cross-section of molecular oxygen at Lyman-α. Similarly there are systematic uncertainties of $\pm$ 20% and $\pm$ 10% respectively in the number densities determined from the Q-T and S-X ion chamber data owing to corresponding uncertainties in the effective absorption cross-sections for these detectors (Section 2.3).

Another important source of uncertainty in the results arises from uncertainties in the satellite position. These uncertainties, due mainly to uncertainties in the atmospheric drag on the satellite, lead to a probable error in the minimum ray height of $\pm$ 2 Km with the maximum error not expected to exceed $\pm$ 3.5 Km. The effect of these height errors is much more significant for the LiF-NO ion chamber results than for the Q-T and S-X ion chamber results, owing to the greater scale height of the molecular oxygen density distribution in the altitude range where solar Lyman-α radiation is absorbed (Appendix A).

In the finite-sun analysis described in Section 5.3.3, it is assumed that the solar disk is uniformly bright at the wavelengths to which the ion chambers respond. However, the solar Lyman-α radiation is chromospheric in origin and as shown in Section 1.1.4 there can be considerable plage enhancement. The error involved in assuming the solar disk to be uniformly bright will depend on the fraction of the total radiation that comes from plage regions. It will also depend on the distances of these regions from the centre of the solar disk measured in the direction in which the earth's horizon, as seen from the satellite, moves across the solar disk.

No direct evidence is available concerning the Lyman-α plage regions on the solar disk during the period from 29th November to 2nd December, 1967. Although Mercure et al. (1956), Purcell et al. (1959) and others have shown that there is a strong correlation between CaK and Lyman-α plage regions (Section 1.1.4), it is difficult to estimate the Lyman-α intensities associated with these regions of high activity. In general the earth's horizon, as seen from the satellite, sweeps across the solar disk at different angles to the solar rotation axis for sunrise and sunset passes. It follows that in the presence of plage regions on the solar disk, the errors incurred in the derived number densities will be different for sunrise and sunset passes and in fact may be of opposite sign.

In the wavelength regions to which the Q-T and S-X ion chambers respond, plage enhancement is not expected to be as important as it is at Lyman-α. This is especially true for wavelengths greater than 1525Å

as the continuum here is photospheric (Section 1.2) and no plage enhancement is seen in the visible or near ultraviolet continuum wavelengths except close to the limb. In addition, for the determination of number densities, the finite size of the solar disk is much less important for the Q-T and S-X ion chambers than for the LiF-NO ion chambers (Section 5.5). For these reasons, errors in the density values derived from the Q-T and S-X ion chamber data, arising from non-uniformity of the brightness of the solar disk, are assumed to be small and are not considered in the present work.

Figure 6.2 shows a comparison of the mean 1965 CIRA model atmosphere (CIRA, 1965) with the Fairbanks 16 and the Orroral 50 satellite passes. These profiles are representative of the LiF-NO ion chamber sunset and sunrise results respectively. As stated above, the most accurately determined number density in each profile is $n(h_c)$. The value of h_c varied from pass-to-pass between 96 Km and 104 Km with the mean value being 100 Km. The vertical bar in Figure 6.2 represents the range of values of n(100) determined from the WRESAT 1 data.

Owing to height uncertainties and uncertainties resulting from possible non-uniformity of the Lyman-α brightness of the solar disk, it is not certain to what extent the observed variations in the value of n(100) represent actual changes in the molecular oxygen density at this height. The mean value of n(100) is 1.39×10^{12} cm^{-3} for the sunrise data and 1.96×10^{12} cm^{-3} for the sunset data (cf. 1.99×10^{12} cm^{-3} for the mean 1965 CIRA model), with all of the sunset values being greater than the sunrise mean. The sunrise observations were made in

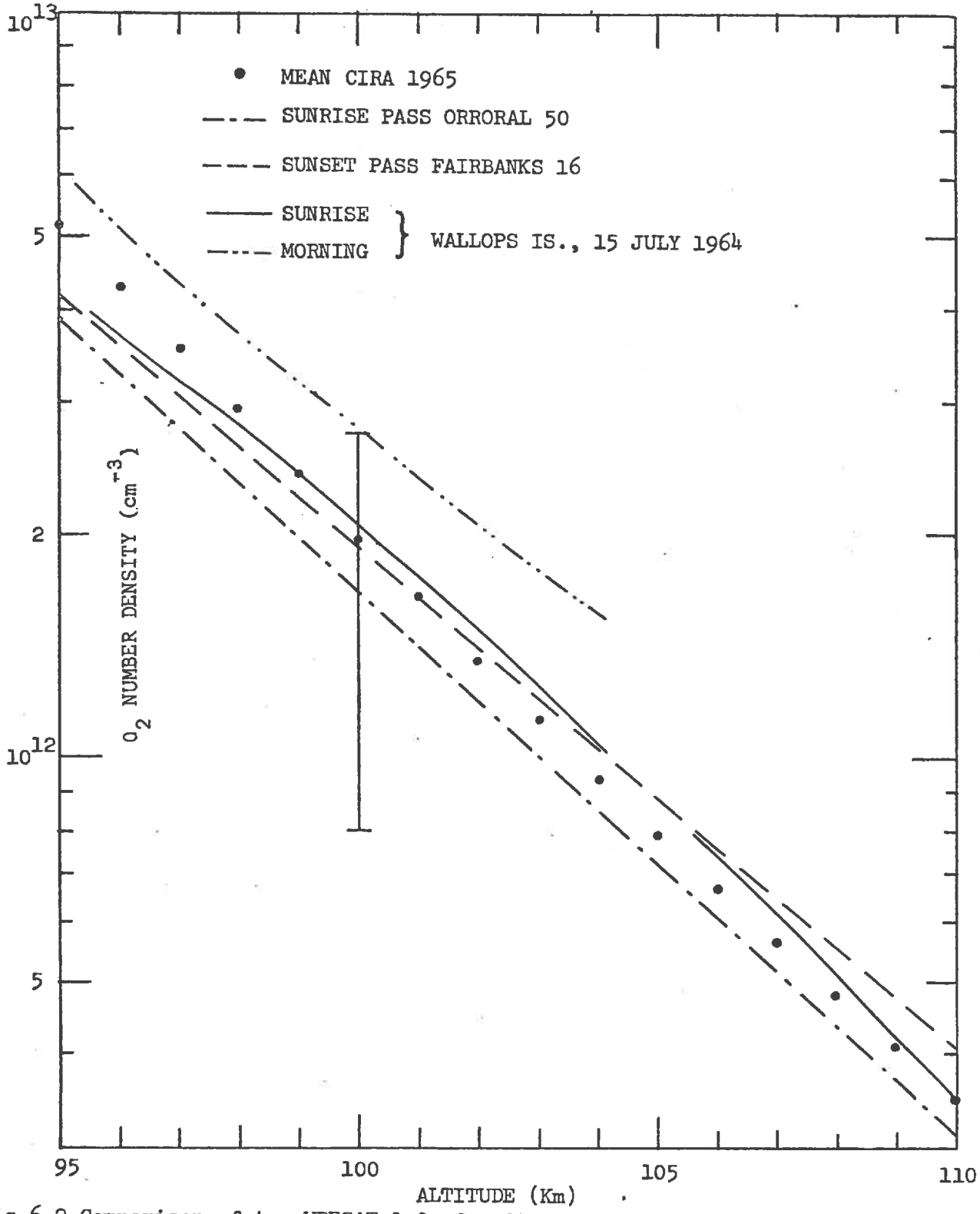

Fig.6.2 Comparison of two WRESAT 1 O_2 density determinations with the mean 1965 CIRA model and with sunrise and early morning determinations by Weeks and Smith (1968) at Wallops Island.

late spring-early summer at a local time of approximately 4 hours and at latitudes between 44.5°S and 46.9°S. The sunset observations were made in late autumn-early winter at a local time of approximately 13 hours and at latitudes between 67.5°N and 68.0°N (Figure 5.2). The difference seen between the mean sunrise and sunset observations could therefore reflect seasonal, diurnal or geographical variations or some combination of these. Alternatively, as described above, it could be a consequence of non-uniformity of the Lyman-α brightness of the solar disk. However, if the latter effect is assumed to be negligible, the difference between the sunrise and sunset results is in agreement with both the seasonal and diurnal variations suggested by rocket observations.

The results of Weeks and Smith (1968) (page 133) suggest a significant diurnal variation near 100 Km with lower concentrations at sunrise than in the early morning and afternoon. An example of their results is shown in Figure 6.2 for a case in which the two flights were only one hour and five minutes apart. From 94 Km to 104 Km the average change between sunrise and daytime at a particular height was found to be approximately 33% of the average concentration at that height. This variation is in good agreement with the difference seen between the WRESAT 1 sunrise and sunset measurements.

However, the mean scale height at 100 Km for the WRESAT 1 results is 6.3 Km for the summer (sunrise) observations and 7.2 Km for the winter (sunset) observations. This and the greater average number density for the winter observations seems more in agreement with the seasonal variations suggested by the results displayed in Figure 6.1.

The only other extensive satellite measurements of molecular oxygen density near 100 Km are the SOLRAD 8 results reported by Norton and Warnock (1968) (page 135). No evidence was found of a difference between sunrise and sunset observations for the same season (Norton, 1970). The average number density* at 100 Km was found to be 1.80×10^{12} cm^{-3} for the winter data and 2.76×10^{12} cm^{-3} for the summer data indicating a seasonal difference opposite to that suggested by the WRESAT 1 results.

A single molecular oxygen density profile was obtained from the INTERKOSMOS 1 LiF-NO ion chamber data (page 135). Over the height range from 90 Km to 105 Km this profile, determined in October 1969, at a latitude of 40°N, showed essentially the same scale height as the mean 1965 CIRA model atmosphere (CIRA, 1965). However, the density values were more than a factor of three below those of the CIRA model and so significantly lower than the WRESAT 1 values.

The widely different number densities derived from the LiF-NO ion chamber data from the three satellite experiments indicate the difficulties associated with the use of this type of ion chamber in the satellite sunrise-sunset experiment. Possible ways of improving this experiment are discussed in Section 6.4.

Considering the uncertainties in the data and the fitting procedure, the WRESAT I LiF-NO ion chamber density values at 100 Km

---

*The density values given in the paper by Norton and Warnock (1968) have been changed to correspond to a value of 1.0×10^{-20} cm^2 for the absorption cross-section of molecular oxygen at Lyman-α.

are in general agreement with the mean 1965 CIRA model atmosphere value. However, the mean values of the scale height at 100 Km for the sunrise and sunset results are considerably greater than the mean CIRA model value of approximately 5.1 Km.

In a preliminary analysis of the WRESAT I LiF-NO ion chamber data (Lockey, Horton and Rofe, 1969), a different fitting procedure to that described in Section 5.3.3 was used and an attempt was made to extend the density determinations above an altitude of approximately 110 Km. The resulting profiles indicated a region from approximately 110 Km to 120 Km where the molecular oxygen density was almost constant. This effect, also reported by Groebecker (1971), is now thought to be a result of wavelengths other than Lyman-α (e.g. the Si III line at 1206.5Å) contributing significantly to the ion chamber signal at these altitudes (Section 2.2).

Figure 6.3 shows the number density profiles derived from the Q-T and S-X ion chamber data obtained on the Woomera 8 sunrise pass and the Fairbanks 16 sunset pass. These results are representative of the extreme profiles obtained. Considering the random uncertainties in the density values (Appendix A) and the height uncertainties discussed above, it can be seen from Figure 6.3 that there is a significant difference between the mean profiles suggested for these two passes.

As stated above, the most accurately determined parameters of each profile are the number density and local scale height at the height h_c. For the Q-T and S-X ion chamber data h_c was approximately

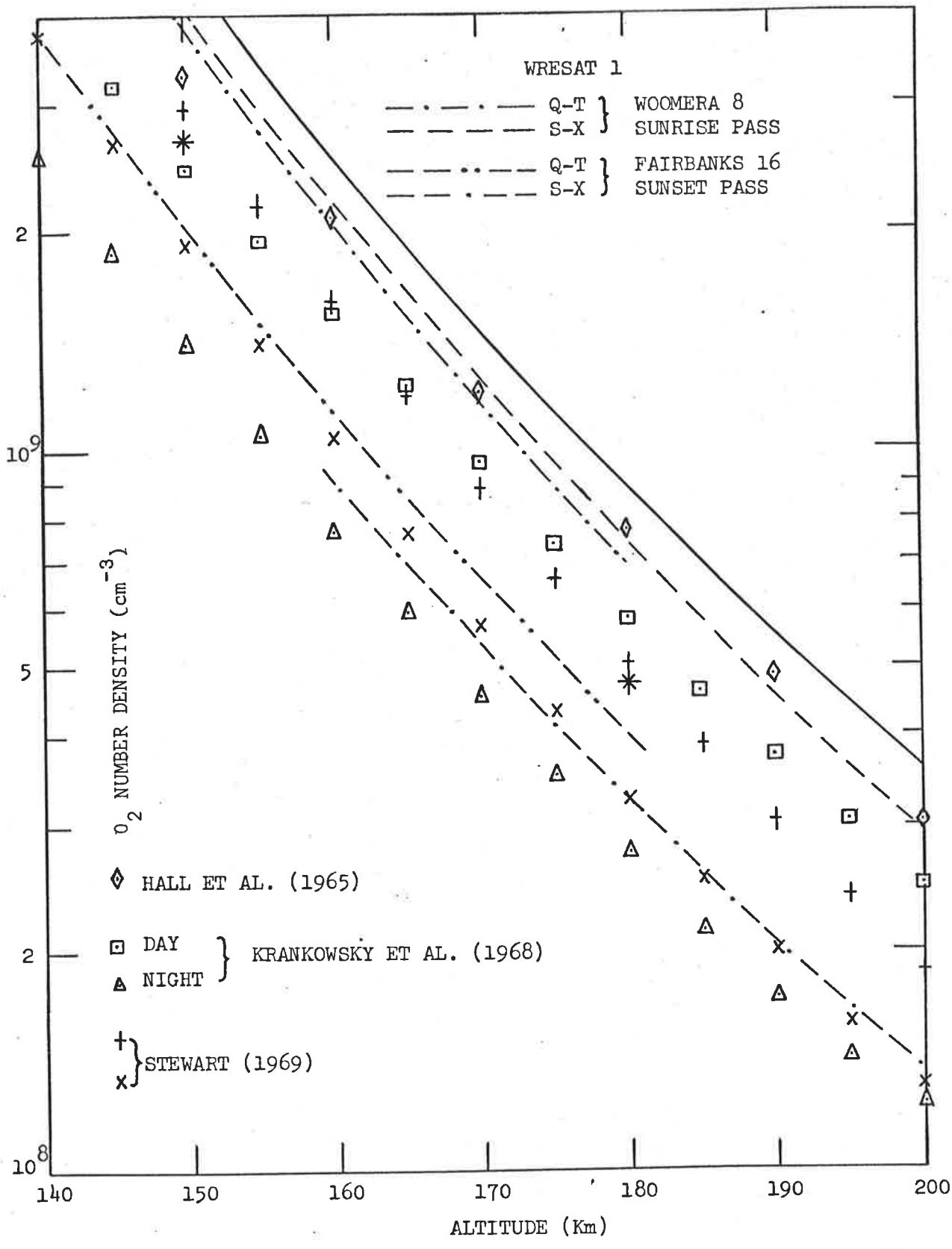

Fig.6.3 Comparison of WRESAT 1 O_2 density determinations with ARIEL 3 S-X ion chamber determinations (Stewart, 1969) and with ultraviolet spectrometer (Hall et al., 1965) and mass spectrometer (Krankowsky et al., 1968) determinations.

150 Km and 180 Km respectively. The few sunset observations (two Q-T ion chamber and three S-X ion chamber observations) fall within the scatter of the sunrise observations. The mean value of molecular oxygen number density at 150 Km, as determined from the sunrise and sunset Q-T ion chamber data, is 2.7×10^{9} cm^{-3} with extreme density values of 1.8×10^{9} cm^{-3} and 3.9×10^{9} cm^{-3}. The mean value of the number density at 180 Km, as determined from the sunrise and sunset S-X ion chamber data, is 4.7×10^{8} cm^{-3} with extreme values of 3.3×10^{8} cm^{-3} and 7.5×10^{8} cm^{-3}. The mean density values at 150 Km and 180 Km are indicated in Figure 6.3 by asterisks. In comparison, the number densities at 150 Km and 180 Km given by the mean 1965 CIRA model atmosphere (shown in Figure 6.3) are 4.78×10^{9} cm^{-3} and 8.83×10^{8} cm^{-3} respectively. The mean WRESAT 1 values are therefore a factor of 1.8 lower than the mean CIRA model values at 150 Km and a factor of 1.9 lower at 180 Km.

The mean scale height at 150 Km, determined from the sunrise and sunset Q-T ion chamber data, is 16.3 Km while the mean value at 180 Km, determined from the sunrise and sunset S-X ion chamber data, is 20.3 Km. The scale heights given at 150 Km and 180 Km by the mean CIRA model are 15.4 Km and 20.5 Km respectively. Therefore, the WRESAT 1 mean scale heights, which can be interpreted as temperatures if diffusive equilibrium is assumed, are somewhat higher than the mean CIRA model values at 150 Km and almost the same at 180 Km.

The ARIEL 3 satellite sunrise-sunset experiment described on page 135, showed variations in the number density at 180 Km from

2.0×10^8 cm^{-3} to 8.8×10^8 cm^{-3} with one exceptionally high value of 1.12×10^9 cm^{-3} (Parker and Stewart, 1972). Two density profiles, representative of the profiles obtained from ARIEL 3 (Stewart, 1969) are shown in Figure 6.3.

Also shown in Figure 6.3 are results obtained using the other techniques for determining molecular oxygen density described in Section 6.1. A single profile obtained by Hall et al. (1965) using a rocket-borne photoelectric monochromator (page 136) is shown along with two profiles (a day-night pair) obtained by Krankowsky et al. (1968) using rocket-borne mass spectrometers (page 137). Considering the uncertainties in the various techniques of measuring molecular oxygen density (Section 6.1) there is broad agreement between the results shown in Figure 6.3. The results are all in accord in showing that there are substantial variations in the molecular oxygen density profile over the range 130 Km to 220 Km and that the mean densities are a factor of two or more lower than those given by the mean CIRA model values.

Insufficient Q-T and S-X ion chamber sunset data were obtained to allow a meaningful comparison of the WRESAT 1 sunrise and sunset results to be made over the height range 130 Km to 220 Km. As shown by Krankowsky et al. (1968), day-to-day variations in this height range are at least as important as diurnal variations. Therefore, an observational period considerably longer than that of WRESAT 1 would be needed to definitely establish the existence or otherwise of a diurnal variation in this height range. The ARIEL 3 experiment (363 observations)

has indicated that at 180 Km the molecular oxygen density is higher at sunrise than at sunset.

The variations in the WRESAT 1 density profiles over the height range 130 Km to 220 Km are greater than those given by the CIRA model atmospheres (CIRA, 1965). The small variations predicted by the CIRA models are a result of the fixed boundary conditions of constant density and temperature at 120 Km. Jacchia (1969) has suggested that the height of the boundary layer be lowered to 90 Km and be made isopycnic but not isothermal.

Figure 6.4 demonstrates the overall character of the WRESAT 1 results. The density profiles from the LiF-NO, Q-T and S-X ion chamber data obtained on the Johannesburg 13 sunrise pass are compared with the mean 1965 CIRA model atmosphere (CIRA, 1965). The vertical bars at 100, 110, 130 and 160 Km represent the range of number densities obtained at these heights from the WRESAT 1 data. Table 6.1 summarizes the mean WRESAT 1 results. For comparison, the corresponding values of number density and scale height for the 1965 mean CIRA atmosphere (CIRA, 1965) are given in parentheses. At 100 Km the WRESAT 1 results are given separately for sunrise (S.R.) and sunset (S.S.).

As stated above, at altitudes below approximately 110 Km, the WRESAT 1 LiF-NO ion chamber number densities are in agreement with the mean CIRA model to within the experimental uncertainties. However, above 130 Km the WRESAT 1, Q-T and S-X ion chamber number densities are, on average, a factor of almost two below those of the mean CIRA model.

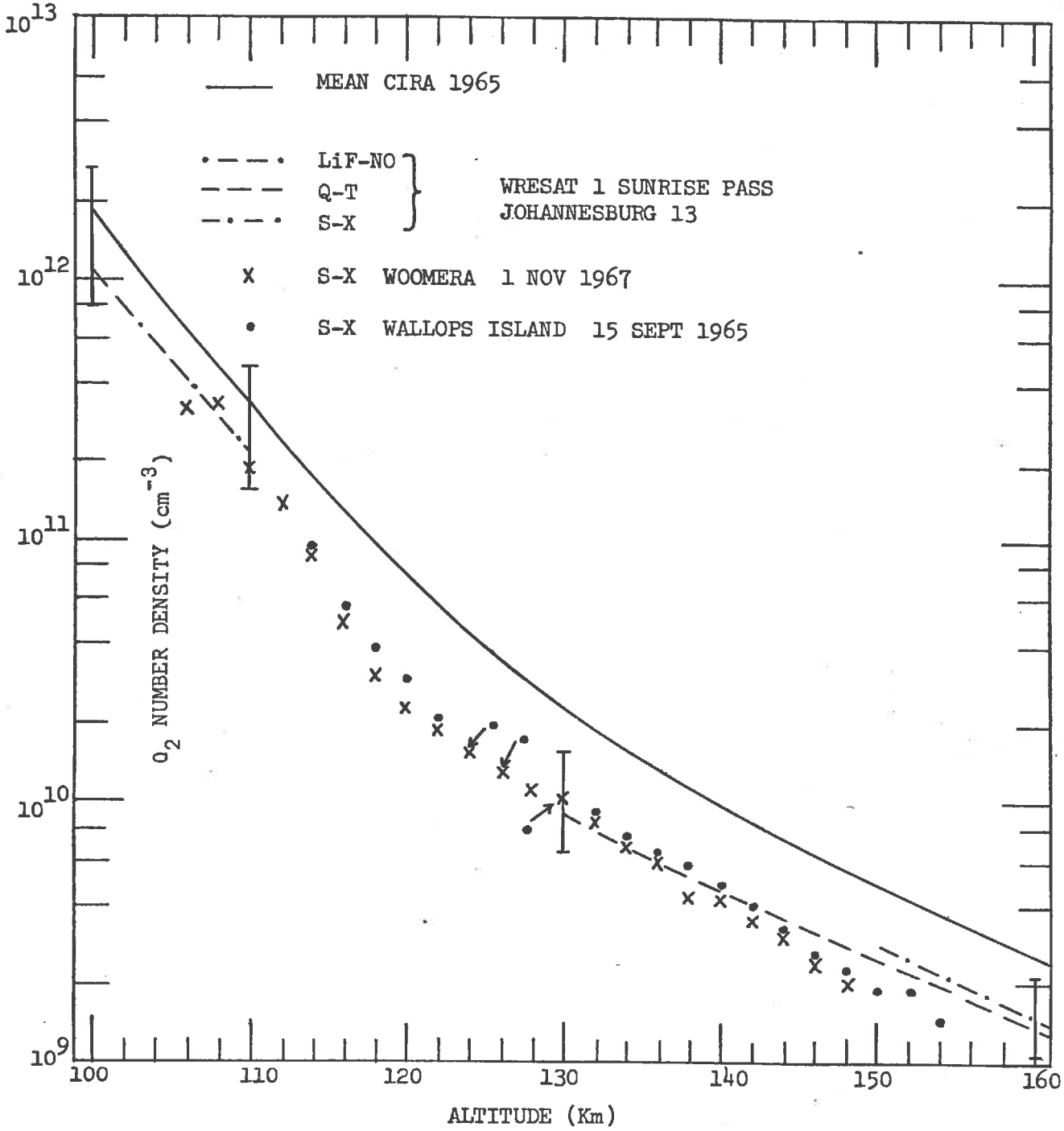

Fig.6.4 Comparison of some O_2 density determinations with the mean 1965 CIRA model for the altitude range 100-160 Km. , Woomera, Wildman et al. (1969); Wallops Island, Weeks and Smith (1968).

TABLE 6.1

MEAN WRESAT 1 RESULTS

Height (Km)	Mean number density (cm^{-3})	Mean scale height (Km)
100	1.39×10^{12} (S.R.) 1.96×10^{12} (S.S.) (1.99×10^{12})	6.3 (S.R.) 7.2 (S.S.) (5.1)
150	2.7×10^{9} (4.78×10^{9})	16.3 (15.4)
180	4.7×10^{8} (8.86×10^{8})	20.3 (20.5)

In the altitude region from approximately 110 Km to 130 Km there are no results from WRESAT 1. Shown in Figure 6.4 are density profiles obtained from two rocket flights of S-X ion chambers (Weeks and Smith, 1968 and Wildman et al. , 1969). These results span the gap in the WRESAT I results and indicate that in the region of the atmosphere near 110 Km there is a sudden decrease in the number densities, to a value of two or more below those of the mean CIRA model.

6.3. Discussion of the Solar Flux Results

The region of the solar temperature minimum (Section 1.2) between the upper photosphere and lower chromosphere is of considerable importance for the theory of the solar atmosphere. The value of the

temperature minimum may be inferred from measurements of the brightness temperature of radiation emitted from this region. As explained in Section 1.2, both observation (Tousey, 1964) and theory (Gingerich et al., 1971) suggest that the wavelength range 1525Å to 1682Å is the part of the spectrum most clearly showing the properties of the solar temperature minimum.

As can be seen from Figure 3.12, the spectral response of a Q-T ion chamber of the type orbited in WRESAT 1 is particularly well suited to a determination of the solar continuum flux over the above wavelength range. The solar fluxes determined (as described in Section 5.6) from the WRESAT 1 and SOLRAD 10 ion chambers are represented in Figure 6.5 as black body curves plotted over wavelength ranges equal to the full width at half maximum (FWHM) response of the ion chambers. Black body curves for various temperatures are also shown in Figure 6.5 for comparison with the observations. The flux values refer to the integrated radiation from the entire solar disk. Combining the results for the WRESAT 1 ion chambers, and giving greater weight to the Q-T ion chamber data, suggests a value of $(4570 \pm 50)^{\circ}K$ for the minimum solar brightness temperature. These results are consistent with the value of $4525^{\circ}K$ obtained from the SOLRAD 10 ion chamber and with the value of $4500^{\circ}K$ reported previously for similar rocket ion chamber observations from Woomera (Carver et al., 1969).

The ion chamber determinations are compared in Figure 6.5 with spectroscopic observations of the solar flux made using dispersing

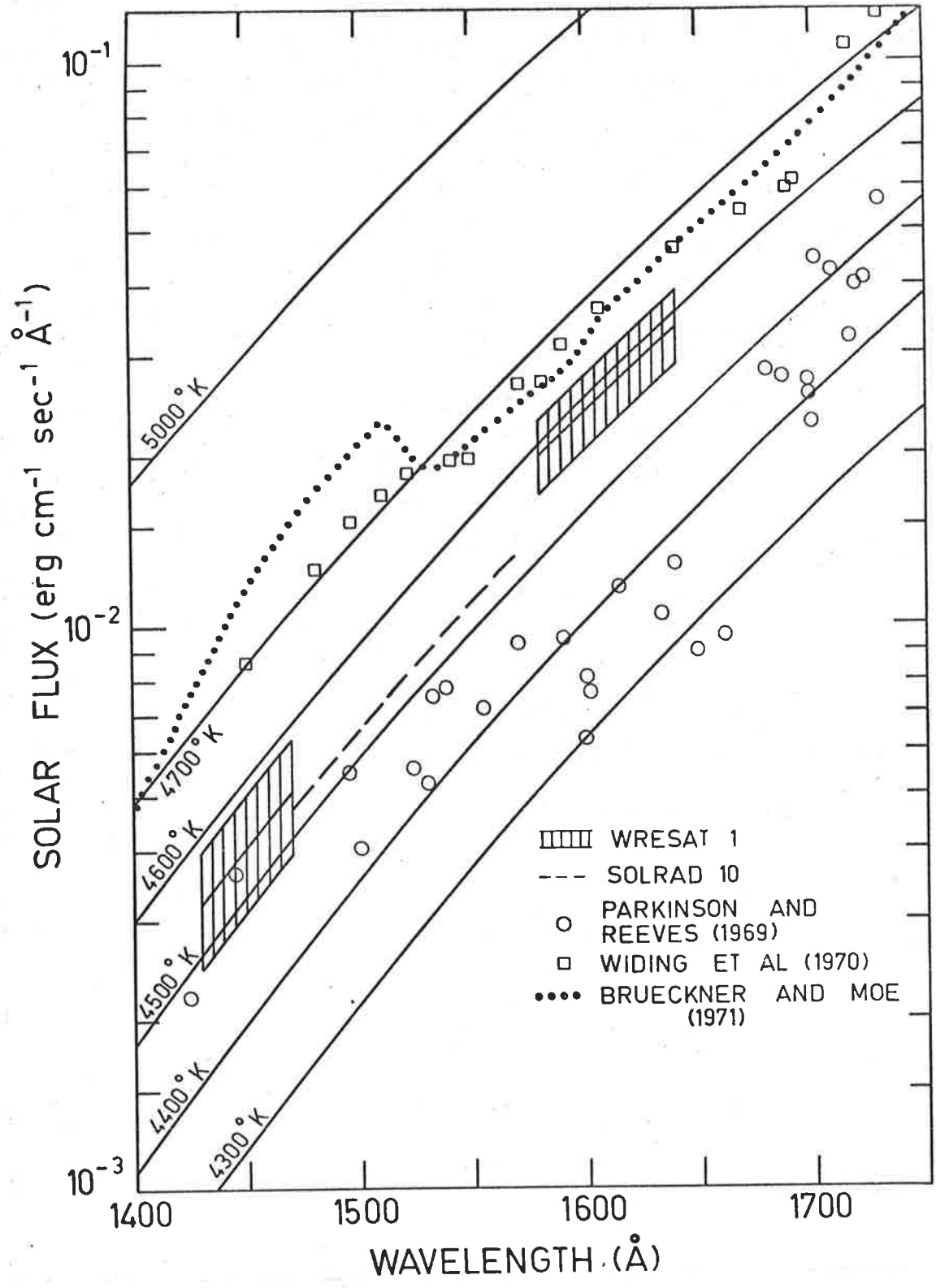

Fig.6.5 Solar flux measurements near the region of the solar temperature minimum.

instruments by Parkinson and Reeves (1969), Widing et al. (1970) and Brueckner and Moe (1972). All of these observations have been discussed fully in Section 1.1.2. Widing et al. (1970), using photographic recording techniques, have found that the brightness temperature of the ultraviolet continuum emerging near the centre of the solar disk, passes through a minimum in the region of the silicon ^1D continuum with a value of $(4670 \pm 100)°K$. Parkinson and Reeves (1969) have used a photoelectric recording technique to study the spectral region between 1400Å and 1875Å. The observations of Parkinson and Reeves (1969), also made near the centre of the solar disk, suggest a minimum brightness temperature of 4400°K (or lower) and therefore some 300°K lower than the value obtained by Widing et al. (1970). Hinteregger (1970) has reported that the results of a second flight in August 1969 tend to confirm those of the earlier flight of Parkinson and Reeves. More recently Brueckner and Moe (1972), also using photographic recording techniques, have determined the intensity distribution of the continuum radiation emerging from four localized areas on the solar disk at positions 7, 24, 40 and 300 arc sec from the limb. The intensity distribution for the region nearest the centre of the disk is shown in Figure 6.5 and indicates a minimum brightness temperature in agreement with that obtained by Widing et al. (1970). The observations taken closer to the limb indicate a minimum radiation temperature of 4550°K in the wavelength region from 1660Å to 1740Å. The spectroscopic observations all refer to localized areas of the solar disk, and to make the comparison shown in Figure 6.5 the observations have been converted

to total disk emissions, assuming that the disk is uniformly bright in the wavelength region concerned (Section 6.2).

As explained in Section 1.2, information about the solar temperature minimum region can also be obtained from observations in the infrared portion of the spectrum. The most recent measurements in the infrared, carried out at wavelengths spanning the region of the solar temperature minimum, yield a mean brightness temperature of $(4370 \pm 260)°K$ for the spectral range 238μ to 312μ (Eddy et al., 1969). This value, recorded at aircraft altitude, is in agreement with the ultraviolet measurements of Parkinson and Reeves (1969). However, the nature of the Plank function is such that observations of the ultraviolet continuum intensity should be the most sensitive indicator of the precise value of the minimum temperature.

The difference of approximately 300°K in the value of the brightness temperature determined near 1600Å by the use of photographic and photoelectric recording techniques, represents a difference of a factor of three in the measured solar flux. As explained in Section 1.1.2, the absolute calibration of dispersive instruments is difficult. The ion chamber measurements provide an independent estimate of the solar minimum brightness temperature using simple detectors which are very straight forward to calibrate (Section 3.6). In the important region of the temperature minimum near 1600Å, the present ion chamber observations are inconsistent with the very low flux values reported by Parkinson and Reeves (1969).

Figure 6.6 shows, as a function of time, the Lyman-α flux values obtained from the front-facing LiF-NO ion chamber carried on WRESAT 1.

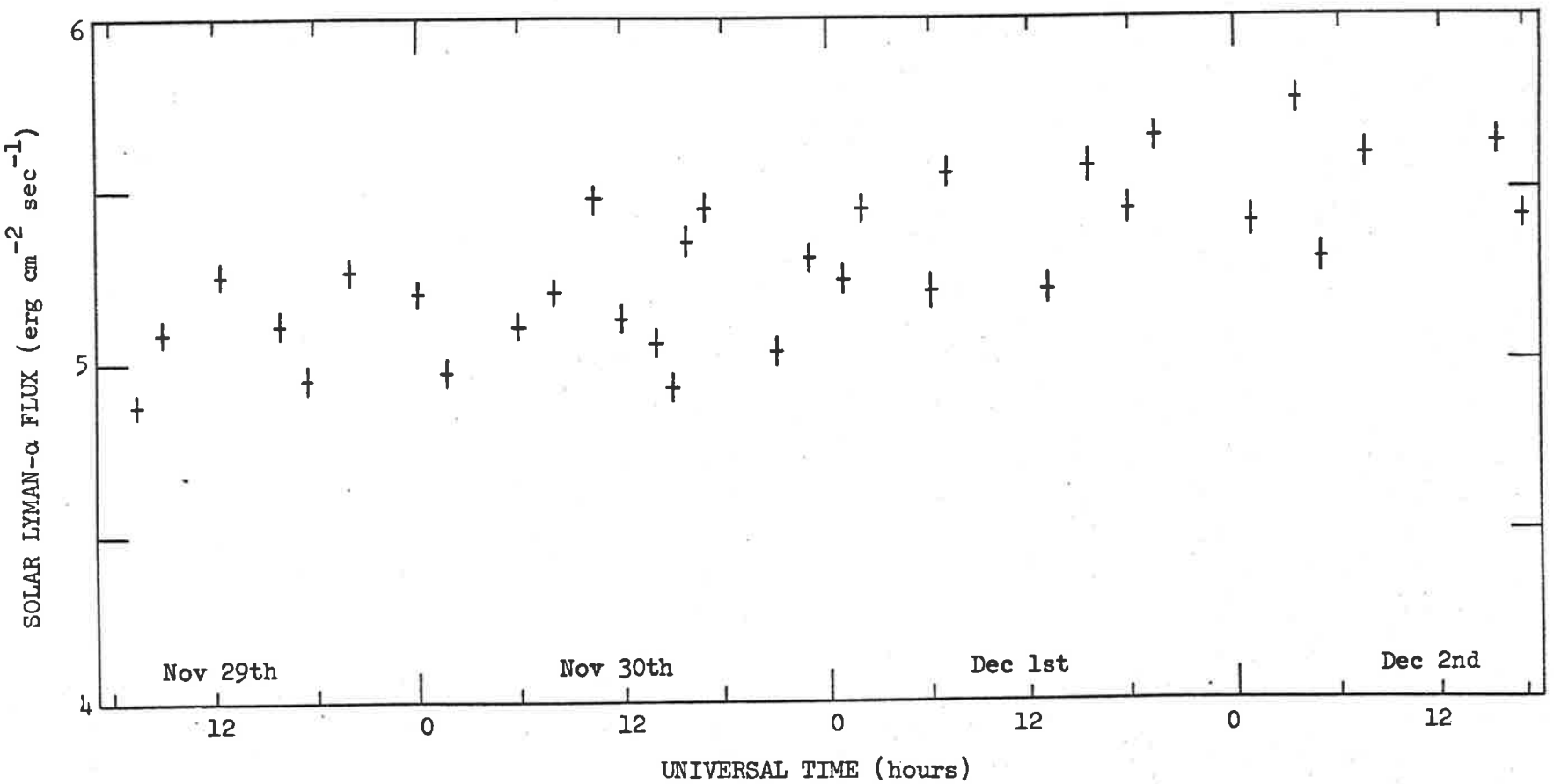

Fig.6.6 Solar Lyman-α flux measurements determined from the front-facing LiF-NO ion chamber data.

For those passes where the satellite was always in full sunlight, the flux level has been estimated using the method described on page 127. The uncertainty of the flux values due to errors in the telemetry transmission and errors in determining the values of I_o is estimated to be $\pm$ 6%. Apart from this random uncertainty, there is also a systematic uncertainty of approximately $\pm$ 6% due to errors in the laboratory calibration of the ion chamber's quantum efficiency at Lyman-α. From Figure 6.6 it can be seen that to within the random uncertainty of $\pm$ 6% there is no evidence of short term variations in the Lyman-α flux level. However, there is evidence of a gradual increase in the flux level over the 3-day period of the observations. The mean flux level increased from approximately 5.1 erg cm^{-2} sec^{-1} on 29th November to a value of approximately 5.5 erg cm^{-2} sec^{-1} on 3rd December (i.e. a rise of about 8%). This longer period variation is in accord with the satellite observations of Hall and Hinteregger (1970) which showed a 27-day periodicity in the solar Lyman-α line intensity with a variation over one period of approximately 30% (page 8).

As described on page 9, Timothy and Timothy (1970) used a photoelectric monochromator on the satellite OSO 4 to monitor the intensity of the solar hydrogen Lyman-α line over the period from October 1967 to December 1967. The value of the Lyman-α flux was found to be constant over this period, to within the estimated experimental uncertainty of $\pm$ 30%, with a mean value of 5.9 erg cm^{-2} sec^{-1}. This mean value is in good agreement with the mean WRESAT 1 value of approximately 5.3 erg cm^{-2} sec^{-1}.

The Lyman-α flux values determined in 1969 from the HAD 309 and HAD 310 rocket flights (Section 4.4.2), are considerably lower than the values obtained in the period November to December 1967 from WRESAT 1 and OSO 4 observations. However, the Lyman-α flux level was monitored from 15th October,1969 to 23rd October,1969 by LiF-NO ion chambers carried on the INTERKOSMOS 1 satellite (page 15). During this period the flux level showed variations from 3.7 to 4.7 erg cm^{-2} sec^{-1} with a mean value of 4.1 erg cm^{-2} sec^{-1}. These values are in good agreement with the value of 3.9 ± 0.4 erg cm^{-2} sec^{-1} determined by HAD 309 on 24th July,1969 and with the value of 4.2 ± 0.4 erg cm^{-2} sec^{-1} determined by HAD 310 on 9th December,1969.

6.4 Conclusions and Comments

A comparison of the present results, obtained from rocket flights of LiF-NO ion chambers, with the results of other workers has indicated seasonal variations in the atmospheric distribution of molecular oxygen in the altitude range 80 Km to 95 Km. The seasonal variations are clearly seen in the average scale height which is larger in winter than in summer. As a result, in the region near 90 Km the number density of molecular oxygen is almost the same in summer and winter. Below 85 Km the present results are, on the average, in agreement with the mean 1965 CIRA model atmosphere (CIRA, 1965). However, at greater altitudes the observed values are significantly higher than those of the mean CIRA model. The average scale heights of both the summer (6.5 Km) and winter (7.5 Km) results are substantially greater than the mean CIRA model value of 5.6 Km.

Recent atmospheric models (Moe, 1970, Jacchia, 1971) have replaced the fixed boundary conditions at 120 Km of earlier models (e.g. the 1965 CIRA models) with time varying boundary conditions at 90 Km. More information about seasonal and other variations near 90 Km is needed if realistic models are to be produced. To determine fully the seasonal variations near 90 Km, a series of rocket experiments similar to the HAD experiments of the present work are required at regular (e.g. two monthly) intervals over a period of at least two years.

Results obtained from the WRESAT 1 LiF-NO ion chambers are complicated by height uncertainties and by unknown but potentially significant uncertainties arising from non-uniformity of the Lyman-α brightness of the solar disk. To within the uncertainties in the data, the observed molecular oxygen densities at 100 Km are in agreement with the mean CIRA model value. However, the average scale height at 100 Km of both the sunrise (6.3 Km) and sunset (7.2 Km) results is considerably greater than the mean CIRA model value of 5.1 Km.

A systematic difference was found between the WRESAT 1 LiF-NO ion chamber sunrise (summer) and sunset (winter) data. This difference could be explained as a seasonal effect. However, results obtained from a similar experiment orbited on the SOLRAD 8 satellite indicate a seasonal difference near 100 Km which is the reverse of that suggested by the WRESAT 1 results.

The large differences in the results obtained near 100 Km by the WRESAT 1, SOLRAD 8 and INTERKOSMOS 1 experiments indicate the

difficulties involved in the use of LiF-NO ion chambers in satellite atmospheric occultation experiments. The effect of the finite size of the sun could be greatly diminished by limiting the field of view of each ion chamber so that it could only receive radiation from a small area of the solar disk. An accurate pointing control would be needed to ensure that the detectors remained pointed at the same region of the solar disk.

The WRESAT 1 Q-T and S-X ion chamber results showed that there are substantial day-to-day variations in the molecular oxygen distribution in the altitude range 130 Km to 220 Km. These variations are greater than those given by the CIRA model atmospheres. The mean densities in the altitude range 130 Km to 220 Km were found to be almost a factor of two lower than those of the mean 1965 CIRA model.

The satellite atmospheric occultation experiment gives data only during sunrise and sunset periods but is useful for studying changes in density from day-to-day, with season, with geographical position and during geomagnetic storms. To distinguish between these various effects, satellite measurements over a period of greater than one year are required. Unfortunately, ultraviolet ion chambers suffer a loss of sensitivity with time owing to ultraviolet degradation of their filling gases. However, the useful lifetime of ion chambers could be prolonged by extreme limitation of the exposed window areas and the use of high gain amplifiers.

The solar minimum temperature between the photosphere and low chromosphere is an important parameter of theoretical models of the

solar atmosphere. The nature of the Plank function is such that observations of the ultraviolet continuum intensity should be the most sensitive indicator of the precise value of the solar minimum temperature. However, there is a difference of approximately 300°K in the values of the brightness temperature determined at wavelengths near 1600Å by the use of dispersive instruments with photographic and photoelectric recording techniques. This temperature difference represents a difference of approximately a factor of three in the absolute flux level. The WRESAT 1 ion chamber measurements provide an independent estimate of the solar minimum brightness temperature using simple detectors which are much easier to calibrate than the dispersive instruments. In the important region of the temperature minimum near 1600Å, the present ion chamber determination of (4570 ± 50)°K is inconsistent with that made using photoelectric recording techniques. Further satellite and rocket flights of Q-T and S-X ion chambers will help in determining more precisely the value of the solar minimum temperature.

APPENDIX A

THE WRESAT 1 DENSITY RESULTS

This appendix contains a summary of the molecular oxygen density results obtained from the WRESAT 1 ion chamber experiment. The tables are discussed on pages 124 and 125.

Note that throughout this appendix the notation a(b) has been used as an abbreviation for $a \times 10^{b}$.

APPENDIX B

PUBLICATIONS

Lockey, G.W.A., Horton, B.H. and Rofe, B.: 1969, "Satellite Measurement of Upper Atmospheric Molecular Oxygen Densities," Nature 223, 387.

Carver, J.H., Horton, B.H. and Lockey, G.W.A.: 1972, "The Temperature of the Solar Photosphere - Chromosphere Transition Region," Proceedings of the Astronomical Society of Australia 2, 94.

Carver, J.H., Horton, B.H. and Lockey, G.W.A.: 1972, "Ultraviolet Ion Chamber Measurements of the Solar Minimum Brightness Temperature," Solar Physics. In press.

SUNRISE PASS SANTIAGO 2

Date: 29 November 1967 Time: 7h 38m 45s U.T.

Ray latitude: 44.6°S Ray longitude: 50.2°W

LiF - Nitric Oxide				Quartz - Triethylamine				Sapphire - p-Xylene			
Model parameters: $n(100) = 9.91(11)\,cm^{-3}$, $H = 6.52$ Km				Model parameters: $n(150) = 2.09(9)\,cm^{-3}$, $H_1 = 12.3$ Km, $H_2 = 26.1$ Km, $H(150) = 16.7$ Km				Model parameters: $n(180) = 4.54(8)\,cm^{-3}$, $H_1 = 13.1$ Km, $H_2 = 39.0$ Km, $H(180) = 19.6$ Km			
h(Km)	n	E(%)	VCD	h(Km)	n	E(%)	VCD	h(Km)	n	E(%)	VCD
92	3.38(12)	28	2.20(18)	130	7.83(9)	20	1.29(16)	150	2.74(9)	22	4.86(15)
94	2.49		1.62	140	4.03		7.16(15)	160	1.43		2.85
96	1.83		1.19	150	2.17	11	4.17	170	7.81(8)		1.78
98	1.35	17	8.80(17)	160	1.22		2.53	180	4.54	13	1.18
100	9.91(11)		6.46	170	7.18(8)		1.58	190	2.82		8.24(14)
102	7.29		4.75	180	4.39		1.02	200	1.86		5.95
104	5.37		3.50	190	2.77(8)	18	6.65(14)	210	1.28		4.40
106	3.95		2.58					220	9.21(7)	21	3.31(14)
108	2.90		1.89								
110	2.14(11)	28	1.40(17)								

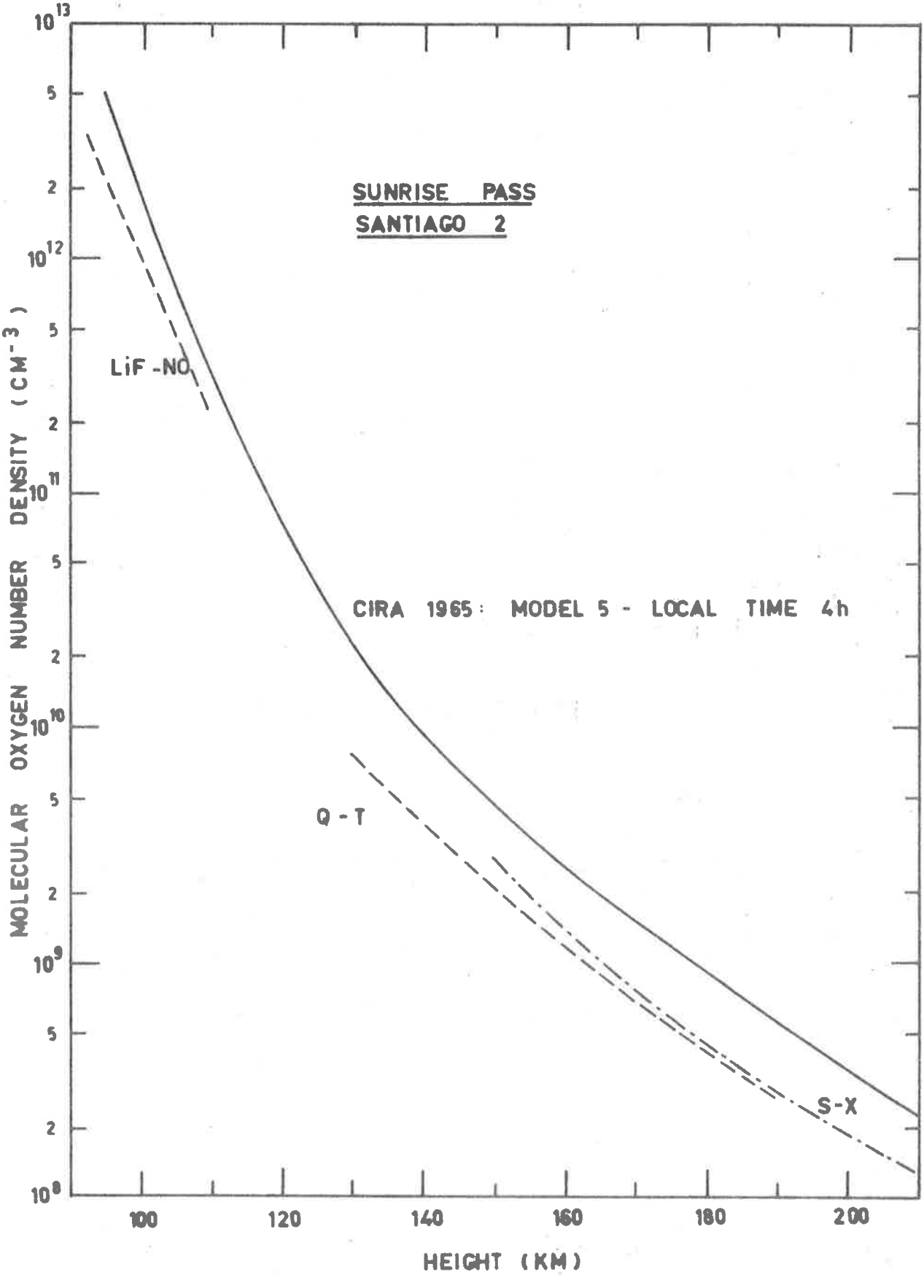
SUNRISE PASS
SANTIAGO 2
LiF - NO
CIRA 1965 : MODEL 5 - LOCAL TIME 4h
Q - T
S - X
MOLECULAR OXYGEN NUMBER DENSITY (CM⁻³)
HEIGHT (KM)
10¹³
5
2
10¹²
5
2
10¹¹
5
2
10¹⁰
5
2
10⁹
5
2
10⁸
100
120
140
160
180
200

SUNSET PASS FAIRBANKS 3

Date: 29 November 1967 Time: 8h 42m 10s U.T.

Ray latitude: 68.0°N Ray longitude: 60.2°E

LiF - Nitric Oxide				Quartz - Triethylamine				Sapphire - p-Xylene			
Model parameters: $n(100) = 2.17(12)\,cm^{-3}$ $H = 7.60$ Km				Model parameters: $n(150) = 3.13(9)\,cm^{-3}$ $H_1 = 12.4$ Km $H_2 = 22.2$ Km $H(150) = 15.9$ Km				Model parameters: $n(180) = 5.86(8)\,cm^{-3}$ $H_1 = 13.1$ Km $H_2 = 43.2$ Km $H(180) = 20.1$ Km			
h(Km)	n	E(%)	VCD	h(Km)	n	E(%)	VCD	h(Km)	n	E(%)	VCD
98	2.82(12)	25	2.14(18)	130	1.17(10)	19	1.83(16)	150	3.48(9)	18	6.31(15)
100	2.17		1.65	140	5.97(9)		9.80(15)	160	1.81		3.77
102	1.67		1.27	150	3.13	10	5.42	170	9.99(8)		2.42
104	1.28	15	9.73(17)	160	1.70		3.08	180	5.86	11	1.65
106	9.85(11)		7.49	170	9.48(8)		1.80	190	3.69		1.18
108	7.57		5.75	180	5.45		1.07	200	2.48		8.80(14)
110	5.82		4.42	190	3.20(8)	17	6.50(14)	210	1.76		6.71
112	4.47		3.40					220	1.30(8)	19	5.19(14)
114	3.44		2.61								
116	2.64(11)	26	2.01(17)								

SUNRISE PASS WOOMERA 8

Date: 29 November 1967 Time: 17h 33m 25s U.T.

Ray latitude: 45.8°S Ray longitude: 159.9°E

LiF - Nitric Oxide				Quartz - Triethylamine				Sapphire - p-Xylene			
Model parameters: $n(100) = 2.72(12)\,cm^{-3}$, $H = 5.79$ Km				Model parameters: $n(150) = 3.87(9)\,cm^{-3}$, $H_1 = 11.5$ Km, $H_2 = 23.5$ Km, $H(150) = 15.4$ Km				Model parameters: $n(180) = 7.45(8)\,cm^{-3}$, $H_1 = 13.9$ Km, $H_2 = 34.6$ Km, $H(180) = 19.9$ Km			
h(Km)	n	E(%)	VCD	h(Km)	n	E(%)	VCD	h(Km)	n	E(%)	VCD
98	3.85(12)	29	2.23(18)	130	1.56(10)	18	2.33(16)	150	4.09(9)	19	7.53(15)
100	2.72		1.57	140	7.58(9)		1.23	160	2.23		4.48
102	1.93		1.12	150	3.87	10	6.77(15)	170	1.26		2.79
104	1.37	17	7.93(17)	160	2.08		3.90	180	7.45(8)	11	1.81
106	9.66(11)		5.59	170	1.17		2.33	190	4.61		1.22
108	6.84		3.96	180	6.82(8)		1.43	200	2.98		8.47(14)
110	4.84		2.80	190	4.12(8)	17	8.96(14)	210	2.00		6.02
112	3.43		1.99					220	1.38(8)	19	4.35(14)
114	2.43		1.41								
116	1.72(11)	28	9.96(16)								

SUNRISE PASS TANANARIVE 11

Date: 29 November 1967 Time: 22h 30m 30s U.T.

Ray latitude: 46.3°S Ray longitude: 85.3°E

LiF - Nitric Oxide				Quartz - Triethylamine				Sapphire - p-Xylene
Model parameters: $n(100) = 1.94(12)\,cm^{-3}$ $H = 5.82$ Km				Model parameters: $n(150) = 2.87(9)\,cm^{-3}$ $H_1 = 12.0$ Km $H_2 = 23.4$ Km $H(150) = 15.8$ Km				not available
h(Km)	n	E(%)	VCD	h(Km)	n	E(%)	VCD	
96	3.86(12)	28	2.25(18)	130	1.10(10)	22	1.70(16)	
98	2.74		1.59	140	5.50(9)		9.10(15)	
100	1.94		1.13	150	2.87	12	5.07	
102	1.38	18	8.03(17)	160	1.56		2.93	
104	9.77(11)		5.69	170	8.80(8)		1.75	
106	6.93		4.03	180	5.15		1.07	
108	4.91		2.86	190	3.10(8)	20	6.68(14)	
110	3.48		2.03					
112	2.47		1.44					
114	1.75(11)	29	1.02(17)					

SUNRISE PASS JOHANNESBURG 12

Date: 30 November 1967 Time: 0h 9m 30s U.T.

Ray latitude: 46.5°S Ray longitude: 60.4°E

LiF - Nitric Oxide				Quartz - Triethylamine				Sapphire - p-Xylene			
Model parameters: $n(100) = 1.26(12)\,cm^{-3}$, $H = 7.11$ Km				Model parameters: $n(150) = 2.78(9)\,cm^{-3}$, $H_1 = 12.1$ Km, $H_2 = 23.1$ Km, $H(150) = 15.9$ Km				Model parameters: $n(180) = 4.89(8)\,cm^{-3}$, $H_1 = 13.8$ Km, $H_2 = 33.9$ Km, $H(180) = 19.6$ Km			
h(Km)	n	E(%)	VCD	h(Km)	n	E(%)	VCD	h(Km)	n	E(%)	VCD
92	3.89(12)	24	2.77(18)	130	1.06(10)	17	1.64(16)	150	2.74(9)	18	4.99(15)
94	2.93		2.08	140	5.33(9)		8.79(15)	160	1.48		2.94
96	2.21		1.57	150	2.78	9	4.89	170	8.33(8)		1.82
98	1.67	14	1.19	160	1.51		2.81	180	4.89	10	1.17
100	1.26		8.96(17)	170	8.50(8)		1.67	190	3.00		7.84(14)
102	9.52(11)		6.77	180	4.95		1.01	200	1.93		5.41
104	7.19		5.11	190	2.96(8)	16	6.27(14)	210	1.29		3.82
106	5.42		3.85					220	8.86(7)	19	2.75(14)
108	4.09		2.91								
110	3.09(11)	24	2.20(17)								

SUNRISE PASS JOHANNESBURG 13

Date: 30 November 1967 Time: 1h 48m 30s U.T.

Ray latitude: 46.7°S Ray longitude: 35.5°E

LiF - Nitric Oxide				Quartz - Triethylamine				Sapphire - p-Xylene			
Model parameters: $n(100) = 1.14(12)\,cm^{-3}$ $H = 6.00$ Km				Model parameters: $n(150) = 2.54(9)\,cm^{-3}$ $H_1 = 12.9$ Km $H_2 = 21.7$ Km $H(150) = 16.2$ Km				Model parameters: $n(180) = 5.10(8)\,cm^{-3}$ $H_1 = 14.0$ Km $H_2 = 35.1$ Km $H(180) = 20.0$ Km			
h(Km)	n	E(%)	VCD	h(Km)	n	E(%)	VCD	h(Km)	n	E(%)	VCD
92	4.34(12)	27	2.60(18)	130	9.20(9)	20	1.47(16)	150	2.77(9)	20	5.14(15)
94	3.11		1.87	140	4.78		7.93(15)	160	1.51		3.07
96	2.23		1.34	150	2.54	11	4.39	170	8.59(8)		1.92
98	1.60	17	9.60(17)	160	1.39		2.49	180	5.10	12	1.25
100	1.14		6.84	170	7.75(8)		1.44	190	3.17		8.48(14)
102	8.20(11)		4.92	180	4.43		8.52(14)	200	2.05		5.92
104	5.87		3.52	190	2.58(8)	19	5.11(14)	210	1.38		4.23
106	4.21		2.53					220	9.63(7)	21	3.07(14)
108	3.02		1.81								
110	2.16(11)	26	1.30(17)								

SUNSET PASS FAIRBANKS 16

Date: 30 November 1967 Time: 6h 9m 10s U.T.

Ray latitude: 67.9°N Ray longitude: 97.8°E

LiF - Nitric Oxide				Quartz - Triethylamine				Sapphire - p-Xylene			
Model parameters: $n(100) = 1.92(12)\,cm^{-3}$ $H = 6.53$ Km				Model parameters: $n(150) = 2.03(9)\,cm^{-3}$ $H_1 = 12.6$ Km $H_2 = 24.9$ Km $H(150) = 16.7$ Km				Model parameters: $n(180) = 3.26(8)\,cm^{-3}$ $H_1 = 14.8$ Km $H_2 = 37.2$ Km $H(180) = 21.2$ Km			
h(Km)	n	E(%)	VCD	h(Km)	n	E(%)	VCD	h(Km)	n	E(%)	VCD
96	3.55(12)	23	2.32(18)	130	7.29(9)	23	1.19(16)	150	1.60(9)	23	3.19(15)
98	2.61		1.70	140	3.77		6.61(15)	160	9.08(8)		1.97
100	1.92		1.25	150	2.03	12	3.81	170	5.35		1.27
102	1.42	14	9.27(17)	160	1.14		2.27	180	3.26	13	8.49(14)
104	1.04		6.79	170	6.62(8)		1.39	190	2.07		5.87
106	7.67(11)		5.01	180	3.98		8.75(14)	200	1.38		4.17
108	5.65		3.69	190	2.46(8)	22	5.60(14)	210	9.42(7)		3.03
110	4.16		2.72					220	6.67(7)	21	2.23(14)
112	3.06		2.00								
114	2.25(11)	25	1.47(17)								

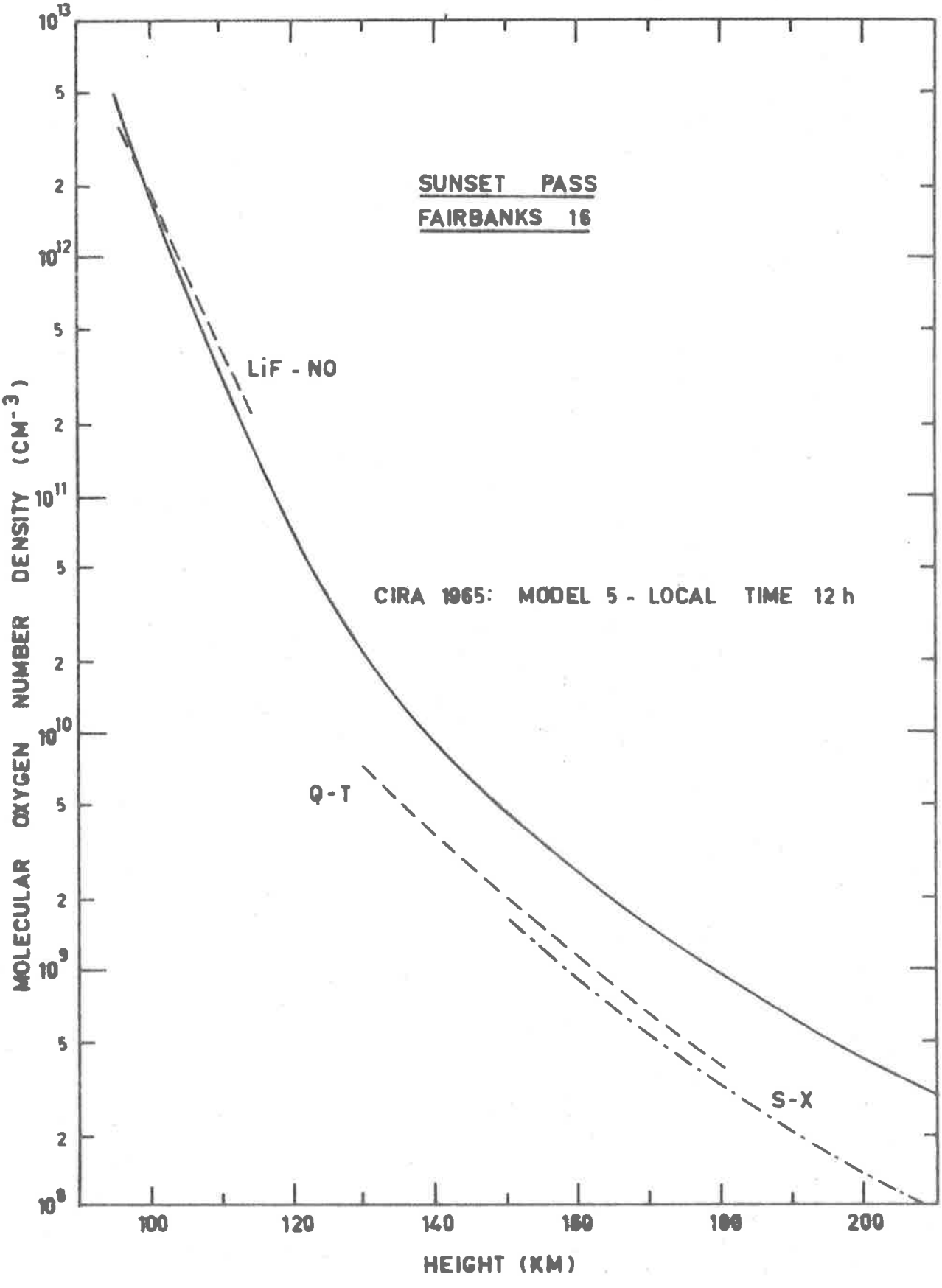
SUNSET PASS
FAIRBANKS 16
LiF - NO
CIRA 1965: MODEL 5 - LOCAL TIME 12 h
Q-T
S-X
MOLECULAR OXYGEN NUMBER DENSITY (CM⁻³)
HEIGHT (KM)
10¹³
5
2
10¹²
5
2
10¹¹
5
2
10¹⁰
5
2
10⁹
5
2
10⁸
100
120
140
160
180
200

SUNRISE PASS LIMA 17

Date: 30 November 1967 Time: 8h 24m 20s U.T.

Ray latitude: 47.4°S Ray longitude: 64.2°W

LiF - Nitric Oxide				Quartz - Triethylamine				Sapphire - p-Xylene			
Model parameters: $n(100) = 1.28(12)\,cm^{-3}$ $H = 6.00$ Km				Model parameters: $n(150) = 2.39(9)\,cm^{-3}$ $H_1 = 12.0$ Km $H_2 = 24.9$ Km $H(150) = 16.2$ Km				Model parameters: $n(180) = 3.54(8)\,cm^{-3}$ $H_1 = 14.4$ Km $H_2 = 37.3$ Km $H(180) = 20.7$ Km			
h(Km)	n	E(%)	VCD	h(Km)	n	E(%)	VCD	h(Km)	n	E(%)	VCD
94	3.47(12)	30	2.08(18)	130	9.01(9)	25	1.42(16)	150	1.81(9)	25	3.53(15)
96	2.49		1.49	140	4.54		7.75(15)	160	1.02		2.15
98	1.78		1.07	150	2.39	14	4.39	170	5.88		1.37
100	1.28	19	7.68(17)	160	1.32		2.61	180	3.54(8)	15	9.14(14)
102	9.16(11)		5.50	170	7.61(8)		1.60	190	2.23		6.31
104	6.56		3.94	180	4.56		1.01	200	1.48(8)		4.49
106	4.70		2.82	190	2.82(8)	23	6.45(14)	210	1.01		3.27
108	3.37		2.02					220	7.15(7)	23	2.41(14)
110	2.41		1.45								
112	1.73(11)	29	1.04(17)								

SUNRISE PASS ORRORAL 21

Date: 30 November 1967 Time: 14h 59m 50s U.T.

Ray latitude: 47.9°S Ray longitude: 163.6°W

LiF - Nitric Oxide				Quartz - Triethylamine				Sapphire - p-Xylene			
Model parameters: $n(100) = 9.02(11)\,cm^{-3}$ $H = 5.70$ Km				Model parameters: $n(150) = 1.83(9)\,cm^{-3}$ $H_1 = 12.7$ Km $H_2 = 23.8$ Km $H(150) = 16.6$ Km				Model parameters: $n(180) = 3.49(8)\,cm^{-3}$ $H_1 = 13.9$ Km $H_2 = 37.0$ Km $H(180) = 20.3$ Km			
h(Km)	n	E(%)	VCD	h(Km)	n	E(%)	VCD	h(Km)	n	E(%)	VCD
92	3.67(12)	26	2.09(18)	130	6.51(9)	17	1.06(16)	150	1.89(9)	18	3.54(15)
94	2.59		1.48	140	3.40		5.86(15)	160	1.03		2.13
96	1.82		1.04	150	1.83	9	3.33	170	5.86(8)		1.34
98	1.28	15	7.30(17)	160	1.02		1.96	180	3.49	10	8.89(14)
100	9.02(11)		5.14	170	5.84(8)		1.18	190	2.18		6.12
102	6.35		3.62	180	3.45		7.24(14)	200	1.43		4.34
104	4.47		2.55	190	2.09(8)	18	4.53(14)	210	9.79(7)		3.16
106	3.15		1.80					220	6.91(7)	18	2.33(14)
108	2.22		1.27								
110	1.56(11)	25	8.89(16)								

SUNRISE PASS ORRORAL 22

Date: 30 November 1967 Time: 16h 38m 45s U.T.

Ray latitude: 48.0°S Ray longitude: 171.4°E

LiF - Nitric Oxide				Quartz - Triethylamine				Sapphire - p-Xylene			
Model parameters: $n(100) = 1.14(12)\,cm^{-3}$, $H = 5.70$ Km				Model parameters: $n(150) = 3.04(9)\,cm^{-3}$, $H_1 = 14.7$ Km, $H_2 = 20.8$ Km, $H(150) = 17.2$ Km				Model parameters: $n(180) = 5.30(8)\,cm^{-3}$, $H_1 = 14.1$ Km, $H_2 = 37.6$ Km, $H(180) = 20.5$ Km			
h(Km)	n	E(%)	VCD	h(Km)	n	E(%)	VCD	h(Km)	n	E(%)	VCD
92	4.63(12)	25	2.64(18)	130	9.91(9)	18	1.70(16)	150	2.82(9)	19	5.35(15)
94	3.26		1.86	140	5.46		9.52(15)	160	1.55		3.24
96	2.29		1.31	150	3.04	10	5.39	170	8.84(8)		2.06
98	1.61	14	9.21(17)	160	1.71		3.08	180	5.30	11	1.37
100	1.14		6.49	170	9.70(8)		1.78	190	3.33		9.47(14)
102	8.00(11)		4.57	180	5.56		1.04	200	2.20		6.75
104	5.63		3.22	190	3.22(8)	18	6.09(14)	210	1.51		4.93
106	3.97		2.26					220	1.07(8)	18	3.65(14)
108	2.79		1.59								
110	1.97(11)	26	1.12(17)								

SUNRISE PASS CARNARVON 23

Date: 30 November 1967 Time: 18h 17m 35s U.T.

Ray latitude: 48.2°S Ray longitude: 146.5°E

LiF - Nitric Oxide				Quartz - Triethylamine				Sapphire - p-Xylene
Model parameters: $n(100) = 1.66(12)\,cm^{-3}$, $H = 7.10$ Km				Model parameters: $n(150) = 2.76(9)\,cm^{-3}$, $H_1 = 12.8$ Km, $H_2 = 24.2$ Km, $H(150) = 16.7$ Km				not available
h(Km)	n	E(%)	VCD	h(Km)	n	E(%)	VCD	
96	2.91(12)	27	2.07(18)	130	9.75(9)	19	1.61(16)	
98	2.20		1.56	140	5.10		8.90(15)	
100	1.66		1.18	150	2.76	11	5.10	
102	1.25	18	8.88(17)	160	1.54		3.02	
104	9.44(11)		6.70	170	8.92(8)		1.83	
106	7.12		5.06	180	5.31		1.14	
108	5.38		3.82	190	3.25(8)	19	7.17(14)	
110	4.06		2.88					
112	3.06		2.17					
114	2.31(11)	25	1.64(17)					

SUNRISE PASS TANANARIVE 26

Date: 30 November 1967 Time: 23h 14m 0s U.T.

Ray latitude: 48.7°S Ray longitude: 72.0°E

LiF - Nitric Oxide				Quartz - Triethylamine				Sapphire - p-Xylene			
Model parameters: $n(100) = 1.53(12)\,cm^{-3}$, $H = 5.30$ Km				Model parameters: $n(150) = 2.81(9)\,cm^{-3}$, $H_1 = 13.0$ Km, $H_2 = 22.7$ Km, $H(150) = 16.5$ Km				Model parameters: $n(180) = 4.02(8)\,cm^{-3}$, $H_1 = 13.3$ Km, $H_2 = 42.2$ Km, $H(180) = 20.2$ Km			
h(Km)	n	E(%)	VCD	h(Km)	n	E(%)	VCD	h(Km)	n	E(%)	VCD
94	4.76(12)	34	2.52(18)	130	9.96(9)	26	1.62(16)	150	2.33(9)	24	4.28(15)
96	3.26		1.73	140	5.22		8.89(15)	160	1.23		2.56
98	2.24		1.19	150	2.81	15	5.01	170	6.81(8)		1.64
100	1.53	24	8.11(17)	160	1.55		2.89	180	4.02	16	1.11
102	1.05		5.57	170	8.82(8)		1.71	190	2.53		7.94(14)
104	7.21(11)		3.82	180	5.13		1.03	200	1.70		5.86
106	4.94		2.62	190	3.05(8)	25	6.31(14)	210	1.20		4.44
108	3.39		1.80					220	8.77(7)	25	3.41(14)
110	2.32		1.23								
112	1.59(11)	33	8.43(17)								

SUNRISE PASS JOHANNESBURG 27

Date: 1 December 1967 Time: 0h 52m 50s U.T.

Ray latitude: 48.9°S Ray longitude: 47.1°E

LiF - Nitric Oxide

Model parameters:

$n(100) = 1.32(12)\,cm^{-3}$

$H = 7.00$ Km

h(Km)	n	E(%)	VCD
94	3.12(12)	28	2.18(18)
96	2.34		1.64
98	1.76		1.23
100	1.32	16	9.24(17)
102	9.94(11)		6.96
104	7.47		5.23
106	5.61		3.93
108	4.22		2.95
110	3.17		2.22
112	2.38(11)	27	1.67(17)

Quartz - Triethylamine

Sapphire - p-Xylene

Model parameters:

$n(180) = 5.65(8)\,cm^{-3}$

$H_1 = 13.8$ Km

$H_2 = 41.6$ Km

$H(180) = 20.7$ Km

h(Km)	n	E(%)	VCD
150	3.06(9)	20	5.84(15)
160	1.66		3.56
170	9.42(8)		2.30
180	5.65	12	1.57
190	3.59		1.11
200	2.41		8.18(14)
210	1.70		6.15
220	1.24(8)	20	4.70(14)

SUNSET PASS FAIRBANKS 29

Date: 1 December 1967 Time: 3h 33m 45s U.T.

Ray latitude: 67.7°N Ray longitude: 136.7°E

LiF-Nitric Oxide				Quartz - Triethylamine	Sapphire - p-Xylene			
Model parameters: $n(100) = 1.51(12)\,cm^{-3}$, $H = 7.81$ Km					Model parameters: $n(180) = 3.69(8)\,cm^{-3}$, $H_1 = 14.1$ Km, $H_2 = 40.4$ Km, $H(180) = 20.9$ Km			
h(Km)	n	E(%)	VCD		h(Km)	n	E(%)	VCD
94	3.25(12)	29	2.54(18)		150	1.94(9)	22	3.75(15)
96	2.52		1.97		160	1.07		2.30
98	1.95		1.52		170	6.12(8)		1.48
100	1.51	18	1.18		180	3.69	13	1.01
102	1.17		9.14(17)		190	2.35		7.10(14)
104	9.04(11)		7.06		200	1.57		5.17
106	7.00		5.47		210	1.10		3.86
108	5.42		4.23		220	7.94(7)	21	2.92(14)
110	4.19		3.27					
112	3.25(11)	28	2.54(17)					

LITHIUM FLUORIDE - NITRIC OXIDE ION CHAMBER RESULTS

Sunrise Pass Orroral 36

Date: 1 December 1967
Time: 15h 41m 15s U.T.
Ray latitude: 50.3°S
Ray longitude: 176.6°W

Model parameters:

$n(100) = 8.02(11)\,cm^{-3}$
H = 6.80 Km

h(Km)	n	E(%)	VCD
90	3.49(12)	25	2.37(18)
92	2.60		1.77
94	1.94		1.32
96	1.44	14	9.79(17)
98	1.08		7.34
100	8.02(11)		5.45
102	5.97		4.06
104	4.45		3.03
106	3.32		2.26
108	2.47(11)	24	1.68(17)

Sunrise Pass Johannesburg 42

Date: 2 December 1967
Time: 1h 32m 55s U.T.
Ray latitude: 51.0°S
Ray longitude: 34.6°E

Model parameters:

$n(100) = 1.79(12)\,cm^{-3}$
H = 7.00 Km

h(Km)	n	E(%)	VCD
96	3.17(12)	26	2.06(18)
98	2.38		1.67
100	1.79		1.25
102	1.34	15	9.41(17)
104	1.01		7.07
106	7.59(11)		5.31
108	5.71		3.99
110	4.29		3.00
112	3.22		2.26
114	2.42(11)	27	1.69(17)

Sunset Pass Fairbanks 45

Date: 2 December 1967
Time: 5h 51m 30s U.T.
Ray latitude: 67.5°N
Ray longitude: 102.1°E

Model parameters:

$n(100) = 1.59(12)\,cm^{-3}$
H = 7.50 Km

h(Km)	n	E(%)	VCD
96	2.71(12)	29	2.04(18)
98	2.07		1.56
100	1.59		1.19
102	1.22	18	9.14(17)
104	9.34(11)		7.01
106	7.15		5.37
108	5.48		4.11
110	4.20		3.15
112	3.22		2.41
114	2.46(11)	29	1.85(17)

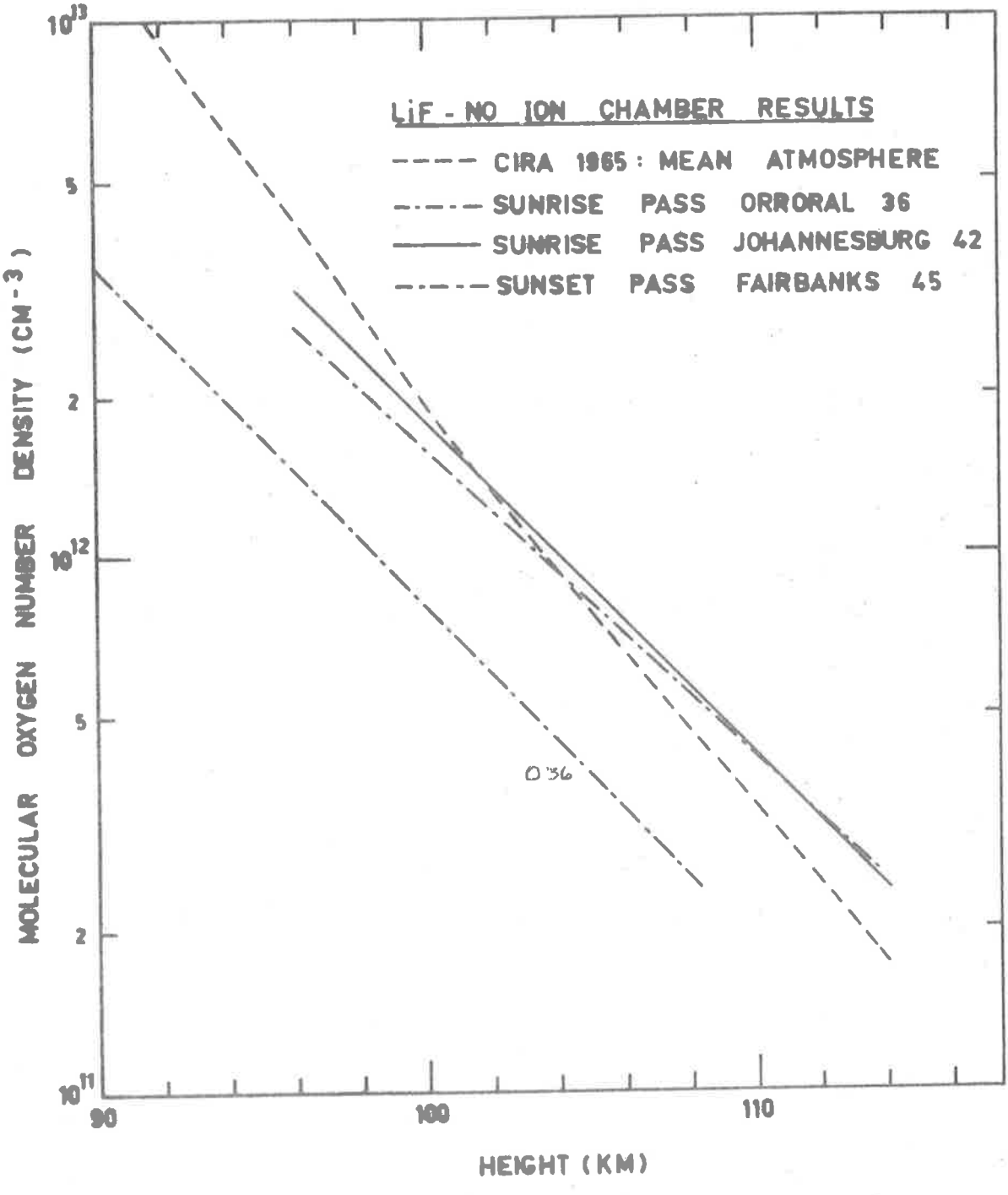
LiF - NO ION CHAMBER RESULTS
CIRA 1965 : MEAN ATMOSPHERE
SUNRISE PASS ORRORAL 36
SUNRISE PASS JOHANNESBURG 42
SUNSET PASS FAIRBANKS 45
O 36
MOLECULAR OXYGEN NUMBER DENSITY (CM⁻³)
HEIGHT (KM)
10¹³
5
2
10¹²
5
2
10¹¹
90
100
110

LITHIUM FLUORIDE - NITRIC OXIDE ION CHAMBER RESULTS

Sunset Pass Fairbanks 46

Date: 2 December 1967
Time: 7h 30m 5s U.T.
Ray latitude: 67.5°N
Ray longitude: 78.7°E

Model parameters:
n(100) = 2.62(12) cm^{-3}
H = 6.50 Km

h(Km)	n	E(%)	VCD
98	3.56(12)	27	2.31(18)
100	2.62		1.70
102	1.92		1.25
104	1.41	16	9.18(17)
106	1.04		6.76
108	7.64(11)		4.97
110	5.62		3.65
112	4.13		2.68
114	3.04		1.97
116	2.23(11)	27	1.45(17)

Sunrise Pass Santiago 46

Date: 2 December 1967
Time: 8h 7m 2s U.T.
Ray latitude: 51.5°S
Ray longitude: 64.6°W

Model parameters:
n(100) = 1.62(12) cm^{-3}
H = 6.10 Km

h(Km)	n	E(%)	VCD
94	4.34(12)	29	2.65(18)
96	3.13		1.91
98	2.25		1.37
100	1.62	18	9.88(17)
102	1.17		7.14
104	8.42(11)		5.14
106	6.07		3.70
108	4.37		2.67
110	3.15		1.92
112	2.27(11)	30	1.38(17)

Sunrise Pass Orroral 50

Date: 2 December 1967
Time: 4h 41m 3s U.T.
Ray latitude: 52.2°S
Ray longitude: 163.9°W

Model parameters:
n(100) = 1.31(12) cm^{-3}
H = 5.50 Km

h(Km)	n	E(%)	VCD
94	3.91(12)	27	2.15(18)
96	2.72		1.50
98	1.89		1.04
100	1.31	15	7.21(17)
102	9.12(11)		5.02
104	6.34		3.49
106	4.41		2.43
108	3.06		1.68
110	2.13		1.17
112	1.48(11)	26	8.14(16)

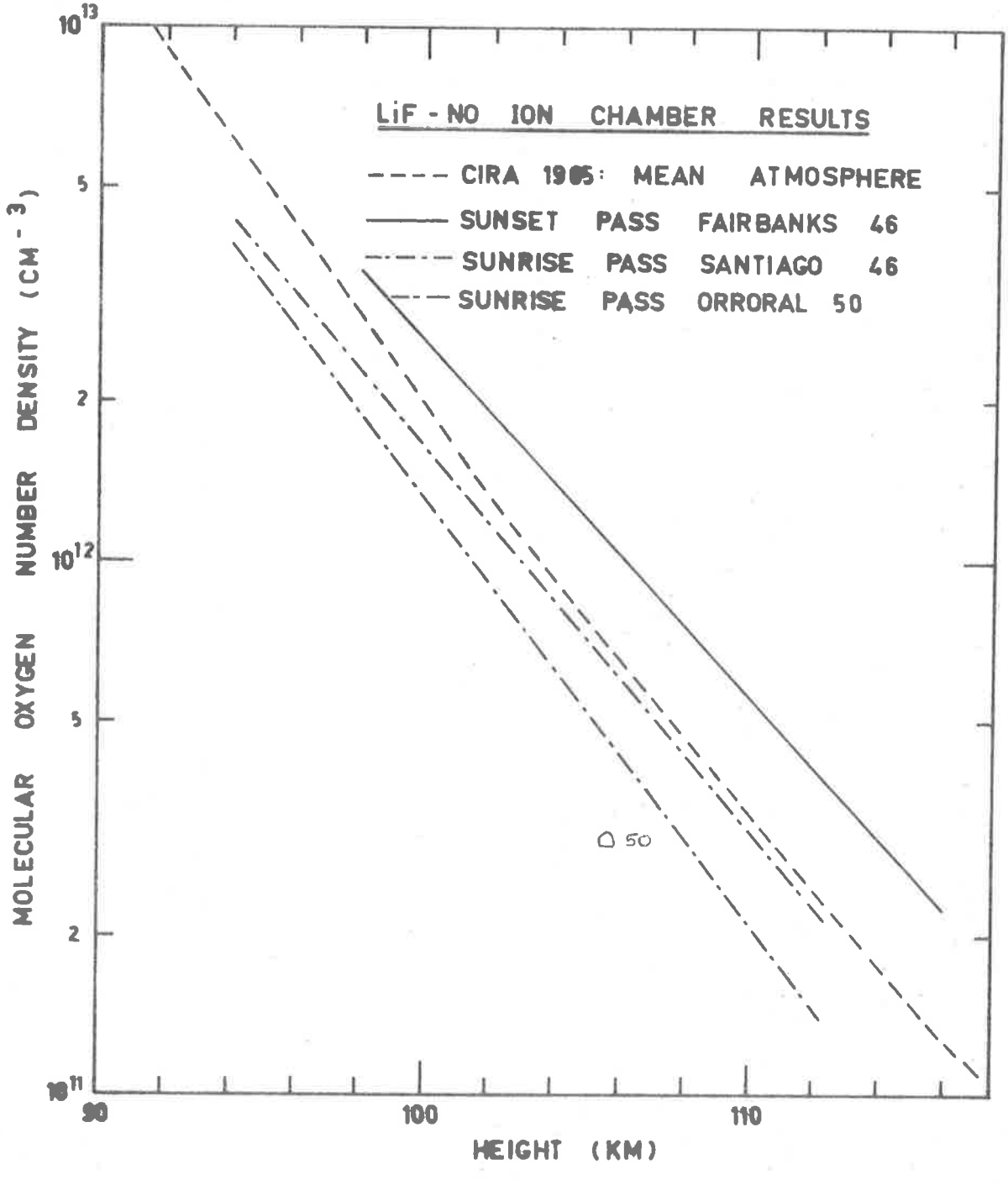
LiF - NO ION CHAMBER RESULTS
CIRA 1965: MEAN ATMOSPHERE
SUNSET PASS FAIRBANKS 46
SUNRISE PASS SANTIAGO 46
SUNRISE PASS ORRORAL 50
D 50
MOLECULAR OXYGEN NUMBER DENSITY (CM⁻³)
HEIGHT (KM)
10¹³
5
2
10¹²
5
2
10¹¹
90
100
110

LITHIUM FLUORIDE - NITRIC OXIDE ION CHAMBER RESULTS

Sunrise Pass Orroral 51				Sunrise Pass Woomera 52			
Date: 2 December 1967 Time: 16h 19m 26s U.T. Ray latitude: 52.3°S Ray longitude: 171.4°E Model parameters: n(100) = 9.87(11) cm^{-3} H = 6.80 Km				Date: 2 December 1967 Time: 17h 57m 51s U.T. Ray latitude: 52.4°S Ray longitude: 146.7°E Model parameters: n(100) = 1.23 (12) cm^{-3} H = 6.80 Km			
h(Km)	n	E(%)	VCD	h(Km)	n	E(%)	VCD
92	3.20(12)	24	2.18(18)	92	3.99(12)	26	2.72(18)
94	2.39		1.62	94	2.98		2.02
96	1.78		1.21	96	2.22		1.51
98	1.32	14	9.01(17)	98	1.65	15	1.12
100	9.87(11)		6.71	100	1.23		8.37(17)
102	7.36		5.00	102	9.18(11)		6.24
104	5.48		3.73	104	6.84		4.65
106	4.09		2.78	106	5.10		3.47
108	3.04		2.07	108	3.80		2.58
110	2.27(11)	25	1.54(17)	110	2.83(11)	26	1.92(17)

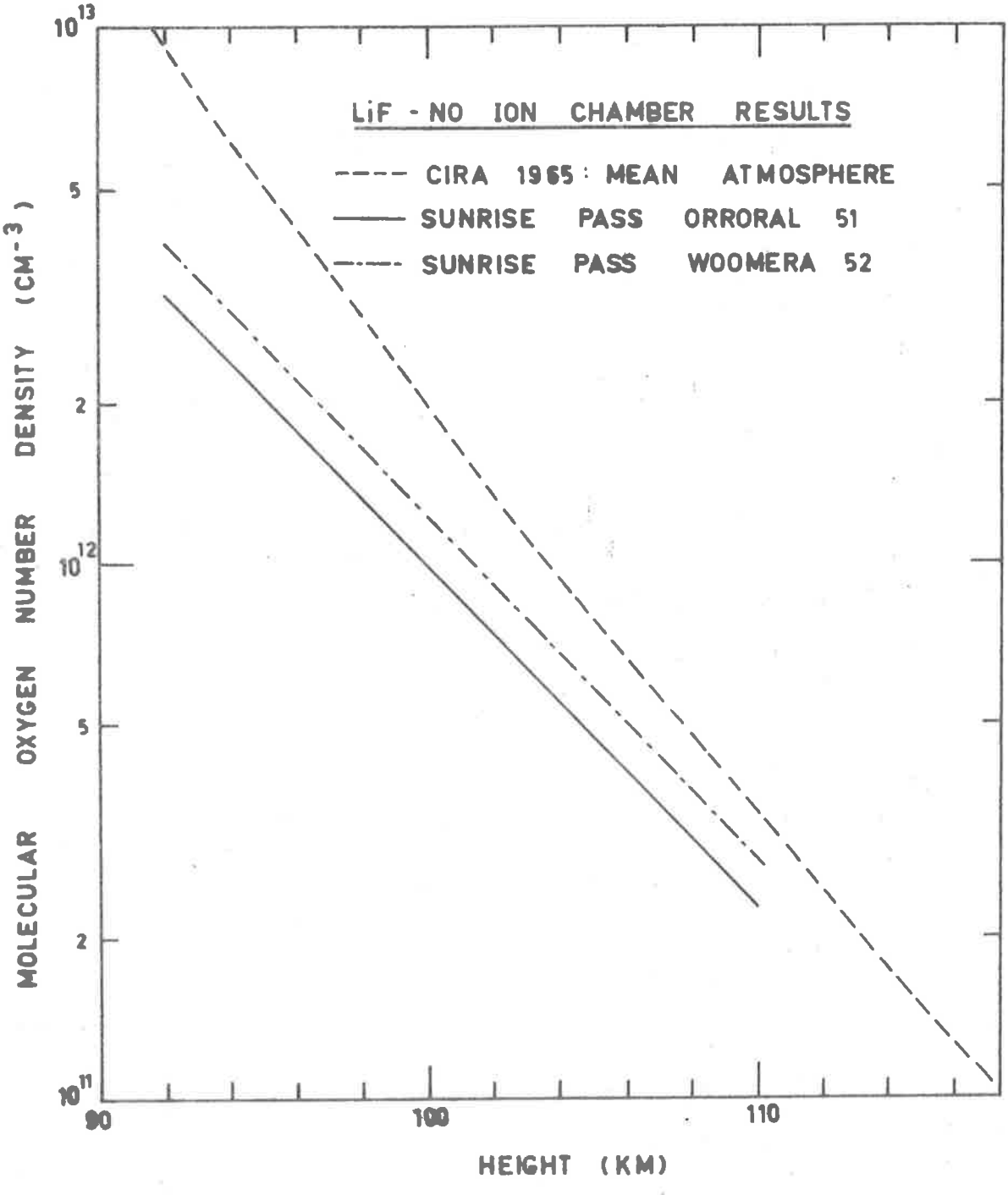
LiF - NO ION CHAMBER RESULTS
CIRA 1965 : MEAN ATMOSPHERE
SUNRISE PASS ORRORAL 51
SUNRISE PASS WOOMERA 52
MOLECULAR OXYGEN NUMBER DENSITY (CM-3)
10^13
5
2
10^12
5
2
10^11
90
100
110
HEIGHT (KM)

BIBLIOGRAPHY

Allison, R., Burns, J. and Tuzzolini, A.J.: 1964, J. Opt. Soc. Am., 54, 747.

Bates, D.R. and Nicolet, M.: 1950, J. Geophys. Res., 55, 301.

Bates, D.R. and Witherspoon, A.E.: 1952, Mon. Not. R. Astr. Soc., 112, 101.

Baum, W.A., Johnson, F.S., Oberly, J.J., Rockwood, C.C., Strain, C.V. and Tousey, R.: 1946, Phys. Rev., 70, 781.

Blake, A.J., Carver, J.H. and Haddad, G.N.: 1966, J. Quant. Spectrosc. Radiat. Transfer, 6, 451.

Brandt, J.C.: 1969, Solar Phys., 6, 490.

Brinkman, R.T., Green, A.E.S. and Barth, C.A.: 1966, NASA Tech. Report No.32-951.

Brueckner, G.E. and Moe, O.K.: 1972, Space Research 11.

Brueckner, G.E., Bartoe, J.F., Nicolas, K.R. and Tousey, R.: 1970, Nature, 226, 1132.

Bruner, E.C. and Parker, R.W.: 1969, J. Geophys. Res., 74, 107.

Bruner, E.C. and Rense, W.A.: 1969, Astrophys. J., 157, 417.

Burton, W.M. and Ridgeley, A.: 1970, Solar Phys, 14, 3.

Byram, E.T., Chubb, T., Friedman, H. and Gailar, N.: 1953, Phys. Rev., 91, 1278.

Byram, E.T., Chubb, T., Friedman, H. and Kupperian, J.E.: 1956, Astrophys. J., 124, 480.

Byram, E.T., Chubb, T.A., Friedman, H., Kupperian, J.E. and Kreplin, R.W.: 1958, Astrophys. J., 128, 738.

Carver, J.H. and Mitchell, P.: 1964, J. Scient. Instrum., 41, 555.

Carver, J.H. and Mitchell, P.: 1967, J. Opt. Soc. Amer., 57, 738.

Carver, J.H., Mitchell, P., Murray, E.L. and Hunt, B.G.: 1964, J. Geophys. Res., 69, 3755.

Carver, J.H., Mitchell, P., Murray, E.L. and Rofe, B.: 1965, Space Research, 6, 373.

Carver, J.H., Edwards, P.J., Gough, P.L., Gregory, A.G., Rofe, B. and Johnson, S.G.: 1969, J. Atmos. Terr. Phys., 31, 563.

Champion, K.W.S., Marcos, F.A. and Schweinfurth, R.A.: 1969, Space Research, 10, 459.

Chapman, S. and Kendall, P.C.: 1965, Quart. J. Roy. Meteorol. Soc., 91, 115.

Chubb, T.A., Kreplin, R.W., Horan, D.M. and Taylor, R.G.: 1971, Private communication.

Chubb, T.A. and Friedman, H.: 1955, Rev. Sci. Instrum., 26, 493.

C.I.R.A. (Cospar International Reference Atmosphere): 1965, North-Holland Publ. Co., Amsterdam.

Cook, G.R. and Ching, B.K.: 1965, Rep. No. TDR-469 (9260-01)-4 (Aerospace Corp.).

Cuny, Y.: 1971, Solar Phys., 16, 293.

Detwiler, C.R., Purcell, J.D. and Tousey, R.: 1961a, Mem. Soc. Roy. Sci. Liege, ser.5, 4, 253.

Detwiler, C.R., Garrett, D.L., Purcell, J.D. and Tousey, R.: 1961b, Annls. Geophys., 17, 9.

Ditchburn, R.W.: 1962, J. Quant. Spectrosc. Radiat, Transfer, 2, 361.

Ditchburn, R.W., Bradley, J.E.S., Cannon, G.G. and Munday, G.: 1954, Rocket Exploration of the Upper Atmosphere, Ed. R.L.F. Boyd and M.J. Seaton (London: Pergamon Press), p.327.

Dunkelman, L., Fowler, W.B. and Hennes, J.P.: 1962, Applied Optics, 1, 695.

Dunkelman, L., Hennes, J.P. and Fowler, W.B.: 1963, Space Research, 3, 1174.

Dupree, A.K. and Reeves, E.M.: 1971, Astrophys, J., 165, 599.

Dupree, A.K., Goldberg, L., Huber, M.C.E., Noyes, R.W., Parkinson, W.H., Reeves, E.M. and Withbroe, G.L.: 1970, BAAS, 2, 191.

Eddy, J.A., Léna, P.J. and MacQueen, R.M.: 1969, Solar Physics, 10, 330.

Felske, D., Martini, L., Stark, B. and Taubenheim, J.: 1970, Nature, 228, 1298.

Fossi, B.C., Poletto, G. and Tagliaferri, G.L.: 1970, Space Research, 10, 903.

Friedman, H.: 1960a, I.R.E. Transactions on Military Electronics, pg. 18.

Friedman, H.: 1960b, Physics of the Upper Atmosphere, Ed. J.A. Ratcliffe (New York: Academic Press), p.133.

Friedman, H.: 1961, Ann. Geophys., 17, 245.

Friedman, H., Lichtman, S.W. and Byram, E.T.: 1951, Phys. Rev., 83, 1025.

Friedman, H., Chubb, T.A., Kupperian, J.E. and Lindsay, J.C.: 1958, Annals. of the I.G.Y., 6, 316.

Friedman, H., Chubb, T.A. and Siomkejlo, J.M.: 1964, Sounding Rocket Research Techniques, Instruction Manual No.9, IQSY (Secretariat, London), pp.88-104.

Gaily, T.D.: 1969, J. Opt. Soc. Am., 59, 536.

Gingerich, O., Noyes, R.W., Kalkofen, W. and Cuny, Y.: 1971, Solar Phys., 18, 347.

Goldberg, L.: 1967, Ann. Rev. Astron. Ap., 5, 279.

Groebecker, A.J.: 1971, Solar Flux and "Total" Particle and O_2 Density in Upper Atmosphere, I.D.A. Science and Technology Division, Paper P-695.

Gross, M.J. and Heddle, D.W.O.: 1964, Proc. Roy. Soc. A, 279, 523.

Hall, L.A. and Hinteregger, H.E.: 1970, J. Geophys. Res., 75, 6959.

Hall, L.A., Schweizer, W. and Hinteregger, H.E.: 1965, J. Geophys. Res., 70, 105.

Hall, L.A., Chagnon, C.W. and Hinteregger, H.E.: 1967, J. Geophys. Res., 72, 3425.

Hall, L.A., Higgins, J.E., Chagnon, C.W. and Hinteregger, H.E.: 1969, J. Geophys. Res., 74, 4181.

Hind, A.D. and Beach, C.J.: 1969, Weapons Research Establishment Tech. Note, HSA 160.

Hinteregger, H.E.: 1961a, Space Astrophysics, Ed. W. Liller (New York: McGraw-Hill), p.34.

Hinteregger, H.E.: 1961b, Mem. Soc. Roy. Sci. Liege, ser.5, 4, 111.

Hinteregger, H.E.: 1962, J. Atmos. Sci., 19, 351.

Hinteregger, H.E.: 1965, Space Sci. Rev., 4, 461.

Hinteregger, H.E.: 1970, Annals. Geophys., 26, 547.

Hinteregger, H.E. and Hall, L.A.: 1965, Space Research, 5, 1175.

Hughes, E.E.: 1961, J. Chem. Phys., 35, 1531.

Inn, E.C.Y., Watanabe, K. and Zelikoff, M.: 1953, J. Chem. Phys., 21, 1648.

Jacchia, L.G.: 1969, Space Research, Presented at 12th COSPAR meeting, Prague, May 1969.

Jacchia, L.G.: 1971, Spec. Rep. Smithson. Astrophys. Obs. No.332.

Johnson, F.S., Purcell, J.D. and Tousey, R.: 1954, Phys. Rev., 95, 621.

Johnson, F.S., Malitson, H.H., Purcell, J.D. and Tousey, R.: 1958, Astrophys. J., 127, 80.

Johnson, S.G.: 1970, Weapons Research Establishment Tech. Note, HSA 180.

Jursa, A.S., Nakamura, M. and Tanaka, Y.: 1963, J. Geophys. Res., 68, 6145.

Jursa, A.S., Nakamura, M. and Tanaka, Y.: 1965, J. Geophys. Res., 70, 2699.

Kasprzak, W.T., Krankowsky, D. and Nier, A.D.: 1968, J. Geophys. Res., 73, 6765.

Knapp, R.A. and Smith, A.M.: 1964, Appl. Opt., 3, 637.

Krankowsky, D., Kasprzak, W.T. and Nier, A.O.: 1968, J. Geophys. Res., 73, 7291.

Kreplin, R.W., Chubb, T.A. and Friedman, H.: 1962, J. Geophys. Res., 67, 2231.

Lee, P.: 1955, J. Opt. Soc. Amer., 45,703.

Lockey, G.W.A., Horton, B.H. and Rofe, B.: 1969, Nature, 223, 387.

Marmo, F.F.: 1953, J. Opt. Soc. Amer., 43, 1186.

Mercure, R., Miller, S.C., Rense, W.A. and Stuart, F.J.: 1956, J. Geophys. Res., 61, 573.

Metzger, P.H. and Cook, G.R.: 1964, J. Quant. Spectrose. Radiat. Transfer, 4, 107.

Mitchell, P.: 1966, Ph.D. Thesis, University of Adelaide.

Moe, K.: 1970, Orbital Atmospheric Model Development, NASA Tech. Report MDC - G0574.

Nier, A.O., Hoffman, J.H., Johnson, C.Y. and Holmes, J.C.: J. Geophys. Res., 69, 979.

Norton, R.B.: 1970, Private communication.

Norton, R.B. and Warnock, J.M.: 1968, J. Geophys. Res., 73, 5798.

Noyes, R.W.: 1971, Ann. Rev. Astron. Ap., 9, 209.

Ogawa, M.: 1968, J. Geophys. Res., 73, 6759.

Pagel, B.E.J.: 1963, Planet. Space Sci., 11, 333.

Parker, A.E. and Stewart, K.H.: 1972, J. Atmos. Terr. Phys., 34, 1223.

Parkinson, W.H. and Reeves, E.M.: 1969, Solar Phys., 10, 342.

Pearce, J.B.: 1969, J. Geophys. Res., 74, 853.

Preston, W.M.: 1940, Phys. Rev., 57, 887.

Purcell, J.D. and Tousey, R.: 1960, J. Geophys. Res., 65, 370.

Purcell, J.D. and Tousey, R.: 1961, Mem. Soc. Roy. Sci. Liege, ser.5, 4, 274, 283.

Purcell, J.D., Packer, D.M. and Tousey, R.: 1959, Nature, 184, 8.

Purcell, J.D., Packer, D.M. and Tousey, R.: 1960, Space Research, 1, 581.

Rawcliffe, R.D., Meloy, G.E., Friedman, R.M. and Rogers, E.H.: 1963, J. Geophys. Res., 68, 6425.

Reeves, E.M. and Parkinson, W.H.: 1970, Astrophys. J. Suppl., ser.181, 21, 1.

Rense, W.A.: 1953, Phys. Rev., 91, 299.

Rense, W.A.: 1961, Space Astrophysics, Ed. W. Liller (New York: McGraw-Hill), p.17.

Samson, J.A.R.: 1964, J. Opt. Soc. Am., 54, 6.

Schilling, G.F.: 1968, Meteorological Monographs, vol.8, no.31, 82.

Shardanand: 1967, Absorption Coefficients of O_4 at Oxygen Windows, NASA TN D-4225.

Sloan, W.A.: 1968, Solar Phys., 5, 329.

Smith, L.G. and Weeks, L.: 1965, G.C.A. Tech. Report No.65-10-N.

Speer, R.J., Garton, W.R.S., Goldberg, L., Parkinson, W.H., Reeves, E.M., Morgan, J.F., Nicholls, R.W., Jones, T.J.L., Paxton, H.J.B., Shenton, D.B. and Wilson, R.: 1970, Nature, 226, 249.

Stewart, K.H. and Wildman, P.J.L.: 1968, Nature, 219, 714.

Stewart, K.H. and Wildman, P.J.L.: 1969, Proc. Roy. Soc. A., 311, 591.

Stober, A.K.: 1962, Ceramic Vacuum Ultra-Violet Ion Chambers, NASA Tech. Note D-1180.

Tanaka, Y., Inn, E.C.Y. and Watanabe, K.: 1953, J. Chem. Phys., 21, 1651.

Timothy, A.F. and Timothy, J.G.: 1970, J. Geophys. Res., 75, 6950.

Tousey, R.: 1963, Space Sci. Rev., 2, 3.

Tousey, R.: 1964, Quart, J. Roy. Astron. Soc., 5, 123.

Tousey, R.: 1967, Astrophys. J., 149, 239.

Tousey, R. Watanabe, K. and Purcell, J.D.: 1951, Phys. Rev., 83, 792.

Tousey, R., Purcell, J.D., Austin, W.E., Garrett, D.L. and Widing, K.G.: 1964, Space Research, 4, 703.

U.S. Standard Atmosphere: 1962 (Washington, D.C.: U.S. Govt. Printing Office).

Violett, T. and Rense, W.A.: 1959, Astrophys. J., 130, 954.

Watanabe, K.: 1957, J. Chem. Phys., 26, 542.

Watanabe, K. and Inn, E.C.Y. : 1953, J. Opt. Soc. Am., 43, 32.

Watanabe, K. and Zelikoff, M.: 1953, J. Opt. Soc. Am., 43, 753.

Watanabe, K., Inn, E.C.Y. and Zelikoff, M.: 1953a: J. Chem. Phys., 21, 1026.

Watanabe, K., Marmo, F.F. and Inn, E.C.Y.: 1953b, Phys. Rev., 90, 155.

Watanabe, K., Nakayama, T. and Mottl, J.: 1962, J. Quant. Spectrosc. Radiat. Transfer, 2, 361.

Watanabe, K., Matsunaga, F.M. and Sakai, H.: 1967, Appl. Opt., 6, 391.

Weeks, L.H.: 1967, Astrophys. J., 147, 1203.

Weeks, L.H. and Smith, L.G.: 1968, J. Geophys. Res., 73, 4835.

Widing, K.G., Purcell, J.D. and Sandlin, G.D.: 1970, Solar Phys., 12, 52.

Wildman, P.J.L., Kerley, M.J. and Shaw, M.S.: 1969, J. Atmos. Terr. Phys., 31, 951.

Willmore, P.: 1961, Mem. Soc. Roy. Sci. Liege, ser.5, 4, 103.